

Spring 2007

# Uncertainty and error in laser triangulation measurements for pipe profiling

Michael Kenneth Swanbom  
*Louisiana Tech University*

Follow this and additional works at: <https://digitalcommons.latech.edu/dissertations>



Part of the [Civil Engineering Commons](#), and the [Mechanical Engineering Commons](#)

---

## Recommended Citation

Swanbom, Michael Kenneth, "" (2007). *Dissertation*. 489.  
<https://digitalcommons.latech.edu/dissertations/489>

This Dissertation is brought to you for free and open access by the Graduate School at Louisiana Tech Digital Commons. It has been accepted for inclusion in Doctoral Dissertations by an authorized administrator of Louisiana Tech Digital Commons. For more information, please contact [digitalcommons@latech.edu](mailto:digitalcommons@latech.edu).

UNCERTAINTY AND ERROR IN LASER  
TRIANGULATION MEASUREMENTS  
FOR PIPE PROFILING

by

Michael Kenneth Swanbom, B.S.

A Dissertation Presented in Partial Fulfillment  
Of the Requirements for the Degree  
Doctor of Philosophy

COLLEGE OF ENGINEERING AND SCIENCE  
LOUISIANA TECH UNIVERSITY

May 2007

UMI Number: 3270933

### INFORMATION TO USERS

The quality of this reproduction is dependent upon the quality of the copy submitted. Broken or indistinct print, colored or poor quality illustrations and photographs, print bleed-through, substandard margins, and improper alignment can adversely affect reproduction.

In the unlikely event that the author did not send a complete manuscript and there are missing pages, these will be noted. Also, if unauthorized copyright material had to be removed, a note will indicate the deletion.

**UMI**<sup>®</sup>

---

UMI Microform 3270933

Copyright 2007 by ProQuest Information and Learning Company.

All rights reserved. This microform edition is protected against unauthorized copying under Title 17, United States Code.

ProQuest Information and Learning Company  
300 North Zeeb Road  
P.O. Box 1346  
Ann Arbor, MI 48106-1346

LOUISIANA TECH UNIVERSITY

THE GRADUATE SCHOOL

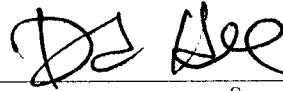
April 5, 2007

Date

We hereby recommend that the dissertation prepared under our supervision  
by Michael Kenneth Swanborn

entitled Uncertainty and Error in Laser Triangulation Measurements for Pipe Profiling

be accepted in partial fulfillment of the requirements for the Degree of  
Doctor of Philosophy, Engineering



Supervisor of Dissertation Research

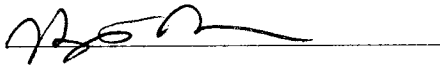


Head of Department

College of Engineering and Science

Department

Recommendation concurred in:



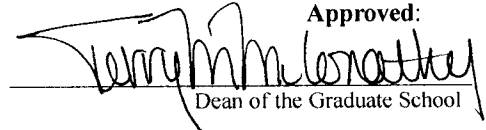
Advisory Committee

Approved:

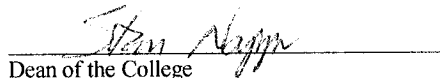


Director of Graduate Studies

Approved:



Dean of the Graduate School



Dean of the College

## ABSTRACT

Underground pipeline infrastructure often receives insufficient attention and maintenance. Those responsible for ensuring the continuing functionality of this infrastructure primarily use subjective information in their decision making, and standards defining the level of damage acceptable before repair or replacement are difficult to implement. Laser pipe profiling is a relatively new technology that has emerged to take a step toward the objective assessment of buried assets. A laser profiler is a device that traverses a section of pipe, taking measurements of radius around the circumference of the inner pipe wall at multiple locations along the length of the pipe. The accuracy of the measurements obtained by a profiler is a critical piece of knowledge for the evaluation of its usefulness.

Analytical measurement and uncertainty models were developed for three laser profiling configurations. These configurations involved a digital camera and a laser whose relative position and orientation were fixed relative to one another. The three configurations included (1) a conically projected laser aligned with the pipe axis, (2) a planar laser placed perpendicular to the pipe axis, and (3) a side-facing laser that projected a line onto the pipe wall parallel to the axis of the pipe. The models utilized normalized system parameters to compute pipe geometry from digital images that reveal the intersection of the laser light and the pipe wall; error propagation techniques were

applied to compute the variation in measurement uncertainty as a function of position in the measurement space.

Analytical evaluation of the conical projection configuration revealed infinite measurement error for a region of the measurement space; the unbounded error was eliminated by utilizing two conical lasers. The accuracy and uncertainty of the perpendicular plane and side facing configurations were much better than for the conical configuration. Physical models of these two configurations were constructed, and measurements were collected for a pipe section to validate the measurement and uncertainty predictions of the analytical models. The difference between observed worst-case laser measurement error and predicted uncertainty was on the order of 0.1% of nominal pipe radius. This work provides pipe profiler designers the analytical detail required to understand the relationship between system geometry, camera parameters and measurement accuracy. The work provides asset managers with a reference against which to evaluate laser profiling for their infrastructure condition monitoring needs.

### APPROVAL FOR SCHOLARLY DISSEMINATION

The author grants to the Prescott Memorial Library of Louisiana Tech University the right to reproduce, by appropriate methods, upon request, any or all portions of this Dissertation. It is understood that "proper request" consists of the agreement, on the part of the requesting party, that said reproduction is for his personal use and that subsequent reproduction will not occur without written approval of the author of this Dissertation. Further, any portions of the Dissertation used in books, papers, and other works must be appropriately referenced to this Dissertation.

Finally, the author of this Dissertation reserves the right to publish freely, in the literature, at any time, any or all portions of this Dissertation.

Author Michael P. Swank

Date APRIL 20, 2007

## TABLE OF CONTENTS

ABSTRACT .....	iii
LIST OF TABLES.....	xiii
LIST OF FIGURES.....	xiv
ACKNOWLEDGEMENTS.....	xx
CHAPTER 1 INTRODUCTION .....	1
1.1 Background and Need.....	2
1.2 Objective and Scope.....	3
CHAPTER 2 LITERATURE REVIEW.....	7
2.1 Introduction.....	7
2.2 Objective Sewer Condition Assessment .....	8
2.2.1 Regulations and Directives .....	9
2.2.2 Commercialized Profilers .....	10
2.3 Structured Light Measurements .....	12
2.3.1 Differing Geometries for Pipe Assessment.....	13
2.3.2 Camera Models and Calibration .....	20
2.3.3 Pixel Identification Techniques .....	23
2.3.4 Accuracy Assessments.....	26
2.3.5 Common Problems and Novel Solutions.....	27
2.3.6 Speckle: The Fundamental Limit on Accuracy.....	30

2.4 Qualitative Damage Detection.....	32
2.4.1 Flattened Image Processing .....	32
2.4.2 Reflectometric Technique.....	34
2.4.3 Shape Detection and Analysis.....	34
2.5 Conclusions.....	36
<b>CHAPTER 3 ANALYTICAL EVALUATION OF TRIANGULATION ACCURACY FOR A CONICALLY PROJECTED LASER PROFILER.....</b>	<b>37</b>
3.1 Introduction.....	37
3.2 Derivation of Triangulation Equations .....	38
3.2.1 Geometrical Assumptions.....	38
3.2.2 Non-Dimensionalization of Parameters .....	39
3.2.3 Aim and Fan Angle of Laser Module .....	40
3.2.4 Spherical Coordinate Camera Model.....	43
3.2.5 Triangulation Equations.....	46
3.2.6 Inversion Frontiers .....	51
3.2.7 Measurement Limits and Camera Field of View.....	58
3.3 Uncertainty Analysis.....	63
3.3.1 Evaluation of Partial Derivatives .....	63
3.3.2 Uncertainty in Geometric Parameters .....	67
3.3.3 Uncertainty in Camera Parameters .....	71
3.3.4 Overall Uncertainty.....	73
3.3.5 Modification to Method .....	75
3.4 Design Process .....	77

3.4.1 Projection Parameter .....	79
3.4.2 Baseline Parameter.....	80
3.4.3 Resulting System Characteristics.....	81
3.5 Observations.....	83
3.5.1 Profiling Apparatus .....	83
3.5.2 Collected Images.....	84
3.6 Conclusions.....	86
<b>CHAPTER 4 ANALYTICAL EVALUATION OF TRIANGULATION ACCURACY FOR PERPENDICULAR PLANE LASER PROFILERS .....</b>	<b>87</b>
4.1 Introduction.....	87
4.2 Derivation of Triangulation Equations .....	88
4.2.1 Geometrical Assumptions .....	88
4.2.2 Laser Misalignment.....	91
4.2.3 Triangulation Equations.....	91
4.2.4 Measurement Limits and Camera Field of View .....	93
4.2.5 Visualization of Measurements.....	94
4.3 Uncertainty Analysis.....	97
4.3.1 Evaluation of Partial Derivatives .....	97
4.3.2 Uncertainty in Geometrical Parameters .....	98
4.3.3 Uncertainty in Camera Parameters .....	99
4.3.4 Overall Uncertainty Visualization .....	100
4.3.5 Overall Uncertainty Versus Measurement.....	102
4.3.6 Effects of Angular Misalignment.....	103

4.4 Design Process .....	104
4.4.1 Occlusion Versus Accuracy .....	105
4.4.2 Physical Dimensions .....	107
4.5 Conclusions.....	107
<b>CHAPTER 5 ANALYTICAL EVALUATION OF TRIANGULATION ACCURACY FOR SIDE-FACING LASER PROFILERS .....</b>	<b>109</b>
5.1 Introduction.....	109
5.2 Derivation of Triangulation Equations .....	110
5.2.1 Geometrical Assumptions.....	110
5.2.2 Triangulation Equations.....	112
5.2.3 Measurement Limits and Camera Field of View.....	115
5.2.4 Visualization of Measurements.....	118
5.3 Uncertainty Analysis.....	120
5.3.1 Evaluation of Partial Derivatives.....	120
5.3.2 Uncertainty in Geometrical Parameters .....	121
5.3.3 Uncertainty in Camera Parameters .....	123
5.3.4 Overall Uncertainty.....	124
5.3.5 Measurement Uncertainty Versus Measurement .....	126
5.4 Measurement System Design.....	127
5.5 Conclusions.....	128
<b>CHAPTER 6 OBTAINING PIPE PROFILES USING THE PERPENDICULAR PLANE PROFILING METHOD.....</b>	<b>129</b>
6.1 Introduction and Overview .....	129

6.2 Extrinsic Camera Calibration.....	130
6.2.1 Calibration Methodology .....	130
6.2.2 Calibration Fixture .....	132
6.2.3 Calibration Images and Data.....	133
6.2.4 Curve Fitting .....	135
6.3 Profiling .....	140
6.3.1 Profiling Methodology .....	140
6.3.2 Hardware and Automated Axial Position .....	141
6.3.3 Image Collection.....	144
6.3.4 Image Processing .....	147
6.3.4.1 Initial Processing.....	150
6.3.4.2 Peak Finding .....	151
6.3.4.3 Center Finding.....	151
6.3.4.4 Real-Time Visualization and Output .....	152
6.3.4.5 Parsing Multiple Images .....	153
6.3.5 Application of Calibration .....	155
6.4 Profile Visualization .....	156
6.4.1 Output for Various Baseline Lengths.....	158
6.4.2 Observations.....	159
6.5 Conclusions.....	162
<b>CHAPTER 7 OBTAINING PIPE PROFILES USING THE SIDE- FACING PROFILING METHOD.....</b>	<b>163</b>
7.1 Introduction and Overview .....	163
7.2 Determining the Location of the Entrance Pupil .....	163

7.2.1 Methodology .....	164
7.2.2 Testing Fixture .....	166
7.2.3 Procedure .....	166
7.3 Rotating Profiling Head .....	168
7.3.1 Physical Arrangement .....	169
7.3.2 Angular Indexing .....	171
7.4 Extrinsic Measurement Calibration .....	171
7.4.1 Calibration Methodology .....	172
7.4.2 Calibration Fixture .....	174
7.4.3 Calibration Images and Data.....	176
7.4.4 Calibration Curve Fitting .....	183
7.5 Profiling .....	187
7.5.1 Profiling Methodology .....	187
7.5.2 Hardware .....	188
7.5.3 Image Collection .....	189
7.5.4 Parsing Images .....	192
7.5.5 Application of Calibration .....	195
7.5.6 Removal of Invalid Data and Calculation of Independent Coordinates.....	201
7.6 Profile Visualization .....	205
7.7 Conclusions .....	208
<b>CHAPTER 8 COMPARISON OF LASER-BASED PROFILES WITH TACTILE MEASUREMENTS.....</b>	<b>209</b>
8.1 Introduction and Overview .....	209

8.2 Automated Tactile Profile Measurements.....	209
8.2.1 Hardware.....	210
8.2.2 Control and Automation.....	214
8.2.3 Calibration of Tactile System .....	220
8.2.4 Visualization .....	222
8.3 Conditioning of Profiles.....	224
8.3.1 Rotation by Interpolation .....	226
8.3.2 Translation Using Coordinate Transformations.....	227
8.3.3 Intrinsic Calibration Corrections.....	227
8.3.3.1 Perpendicular Plane Method .....	228
8.3.3.2 Side-Facing Method.....	228
8.3.4 Summary of Necessary Conditioning .....	231
8.4 Error Analysis .....	231
8.4.1 Quantification of Measurement Error .....	232
8.4.2 Perpendicular Plane Error .....	233
8.4.2.1 Error Versus Baseline Distance .....	234
8.4.2.2 Error Versus Radius .....	236
8.4.3 Side-Facing Error.....	238
8.5 Conclusions.....	240
<b>CHAPTER 9 CONCLUSIONS, BROADER IMPACT AND FUTURE DIRECTIONS.....</b>	<b>241</b>
9.1 Research Conclusions .....	241
9.2 Broader Impact and Future Directions.....	244
<b>REFERENCES .....</b>	<b>246</b>

## LIST OF TABLES

Table 3.1	Radius Parameter Measurements.....	57
Table 3.2	Measurements with Limited Field of View .....	62
Table 3.3	Uncertainty in Radius Parameter .....	74
Table 4.1	Visualization of Measurements.....	96
Table 4.2	Uncertainty Visualization .....	101
Table 5.1	Measurement Visualization.....	119
Table 5.2	Uncertainty Visualization .....	125
Table 6.1	Fitted Curve Parameters and Errors.....	139
Table 7.1	Designed Versus Actual Parameters .....	185
Table 8.1	Extrinsic Versus Intrinsic Calibration.....	230
Table 8.2	Conditioning Performed by Profile.....	231
Table 8.3	Predicted Uncertainty and Worst-Case Error for Perpendicular Plane Method .....	235
Table 8.4	Errors Versus Radii.....	237

## LIST OF FIGURES

Figure 1.1	Triangulation Schemes to be Analyzed .....	4
Figure 2.1	Principle of Structured Light Measurements .....	13
Figure 2.2	Single Spot Profiling.....	14
Figure 2.3	Planar Light Projection .....	15
Figure 2.4	Radially Symmetric Lighting.....	16
Figure 2.5	Asymmetric Conical Projection.....	17
Figure 2.6	Reversed Conical Projection.....	19
Figure 2.7	Laser Spot Array Method.....	20
Figure 2.8	Perspective Projection Model .....	21
Figure 2.9	Wide-Angle Image Distortion.....	22
Figure 2.10	Intensity Distribution .....	24
Figure 2.11	Segmentation of Circular Laser Line Image .....	25
Figure 2.12	Error from Surface Discontinuities.....	28
Figure 2.13	Multiple Detectors for Signal Averaging.....	29
Figure 2.14	Speckle Effects.....	31
Figure 2.15	Image Flattening and Defect Identification .....	33
Figure 2.16	Reflectometric Defect Location Technique .....	34
Figure 2.17	Pipe Collapse Identified by Image Processing.....	35
Figure 3.1	Conical Laser Light Projection .....	37

Figure 3.2	Triangulation Setup.....	39
Figure 3.3	Fan Angle Versus Projection Parameter .....	42
Figure 3.4	Aim Angle Versus Projection Parameter .....	43
Figure 3.5	Zenith and Azimuth Angles .....	44
Figure 3.6	Loci of Constant Zenith Angles .....	44
Figure 3.7	Refraction of Light Through a Lens and onto a CCD Sensor.....	45
Figure 3.8	Image of Concentric Cones of Light onto the CCD Image Plane.....	45
Figure 3.9	Spherical Coordinates .....	47
Figure 3.10	Frontiers of Change.....	53
Figure 3.11	Conjugate Solutions for the Radius Parameter .....	54
Figure 3.12	Unified Solution for Radius Parameter .....	55
Figure 3.13	Limits on Field of View.....	59
Figure 3.14	Field of View and Implications.....	60
Figure 3.15	Estimated Uncertainty in Aim Angle.....	69
Figure 3.16	Estimated Uncertainty in Fan Angle.....	70
Figure 3.17	Expected Uncertainty Profile .....	75
Figure 3.18	Two-Laser Conical System.....	76
Figure 3.19	Composite Uncertainty Profile.....	77
Figure 3.20	Uncertainty Versus Baseline Parameter for Dual Laser System.....	78
Figure 3.21	Uncertainty Versus Projection Parameter .....	79
Figure 3.22	Design Tradeoff .....	81
Figure 3.23	Uncertainty Versus Measurement.....	82
Figure 3.24	Conical Profiling Apparatus.....	84

Figure 3.25	Image Collected Over Track .....	85
Figure 3.26	Pixel Detail Over Track .....	85
Figure 4.1	Perpendicular Plane Triangulation Setup.....	89
Figure 4.2	Laser Module Misalignment .....	90
Figure 4.3	Uncertainty Versus Measurement .....	102
Figure 4.4	Uncertainty Versus Misalignment .....	104
Figure 4.5	Occlusion Effects .....	105
Figure 4.6	Design Chart for Baseline Parameter.....	106
Figure 4.7	Length Constraint for Deployment .....	107
Figure 5.1	Side-Facing Triangulation Setup .....	111
Figure 5.2	Range of Measurement .....	116
Figure 5.3	Aim and Field of View Selection Versus Baseline Distance.....	118
Figure 5.4	Uncertainty in Aim Angle.....	123
Figure 5.5	Uncertainty Versus Measurement.....	126
Figure 5.6	Design Chart for Baseline Parameter.....	127
Figure 6.1	Camera Calibration Stand .....	133
Figure 6.2	Calibration Images .....	134
Figure 6.3	Extrinsic Camera Calibration Data .....	135
Figure 6.4	Perspective Projection Fit .....	136
Figure 6.5	Stereographic Curve Fit .....	137
Figure 6.6	Equidistant Curve Fit .....	137
Figure 6.7	Sine-Law Curve Fit.....	138
Figure 6.8	Equi-Solid Curve Fit .....	138

Figure 6.9	Coordinates for Profiling .....	140
Figure 6.10	Rail for Holding Camera and Laser .....	142
Figure 6.11	Rail Spacings of 3, 6, 12 and 30 Inches (Top to Bottom).....	143
Figure 6.12	Axial Positioning System.....	144
Figure 6.13	Front Panel of Image Collection VI.....	145
Figure 6.14	Block Diagram of the Image Collection VI.....	146
Figure 6.15	Front Panel of Image Processing VI.....	148
Figure 6.16	Image Processing Block Diagram.....	149
Figure 6.17	Parsing Multiple Images VI.....	154
Figure 6.18	Calibration VI .....	156
Figure 6.19	Profile Visualization VI.....	157
Figure 6.20	Pipe Test Section.....	158
Figure 6.21	Three Dimensional Visualizations.....	159
Figure 6.22	Top and Front Views of Profiles.....	161
Figure 7.1	Pivoting Behind Entrance Pupil.....	164
Figure 7.2	Pivoting In Front of Entrance Pupil.....	165
Figure 7.3	Fixture for Determining the Location of the Entrance Pupil .....	166
Figure 7.4	Pivot Behind Pupil .....	167
Figure 7.5	Pivot In Front of Pupil .....	167
Figure 7.6	Axis of Rotation Coincides with the Entrance Pupil .....	168
Figure 7.7	Rotating Profiling Fixture .....	170
Figure 7.8	Setting the Location of the Entrance Pupil .....	171
Figure 7.9	Side-Facing Calibration Setup .....	173

Figure 7.10	Side-Facing Calibration Fixture.....	175
Figure 7.11	Collecting Measurements for Calibration.....	176
Figure 7.12	Calibration Image Collection Tool .....	177
Figure 7.13	Calibration Tool Block Diagram.....	178
Figure 7.14	Peak-Finding Sub-VI .....	180
Figure 7.15	Calibration Image Set Parsing VI .....	182
Figure 7.16	Side-Facing Measurement Calibration.....	186
Figure 7.17	Profiling Hardware.....	188
Figure 7.18	Front Panel of Image Collection VI.....	189
Figure 7.19	Block Diagram of Image Collection VI.....	191
Figure 7.20	Ring Parsing VI.....	194
Figure 7.21	Image Coordinates of a Point on the Laser Line.....	196
Figure 7.22	World Coordinate Calculation VI Front Panel .....	198
Figure 7.23	World Coordinate Calculation VI Block Diagram .....	200
Figure 7.24	Front Panel of Data Sorting VI .....	202
Figure 7.25	Data Sorting VI Block Diagram.....	204
Figure 7.26	Profile Visualization VI .....	206
Figure 7.27	Front and Top Views of Profile .....	207
Figure 8.1	Positional Feedback Air Cylinder.....	211
Figure 8.2	Top View of Tactile Hardware .....	212
Figure 8.3	Tactile Measurement Hardware .....	213
Figure 8.4	Schematic of Tactile Measurement System.....	215
Figure 8.5	Pneumatic Control Components .....	216

Figure 8.6	Tactile Experiment VI Front Panel .....	217
Figure 8.7	Tactile Experiment VI Block Diagram .....	218
Figure 8.8	Tactile Calibration Measurements .....	220
Figure 8.9	Tactile Probe Calibration .....	221
Figure 8.10	Visualization Front Panel and Block Diagram .....	223
Figure 8.11	Data Conditioning VI.....	225
Figure 8.12	Intrinsic Calibration Curve Fit .....	230
Figure 8.13	Experimental Error Comparison .....	234
Figure 8.14	Error Versus Radius .....	239
Figure 9.1	Triangulation Schemes Studied .....	242

## ACKNOWLEDGEMENTS

I would like to thank my wife Gwen for her support and patience during this long and difficult process. She has been faithful and understanding of the many hours it has taken to complete this work, and I am very grateful for her. I would also like to thank my close friend, Dr. Andy Dettmer, with whom I had the privilege of taking the Ph.D. journey. Andy has not only played a key role in keeping my curious wanderings on track, he has offered encouragement and a motivating spirit in a way that few people can.

I would like to thank my co-advisors Dr. David Hall and Dr. Hisham Hegab. Dr. Hall has been a very great encourager and friend to me; his sacrificial attitude towards developing achievement in others is a trait I aspire to emulate. The numerous projects with which he has encouraged me to become involved have served to strengthen many facets of my development as an engineer and educator. Dr. Hegab has played a vital role both in the inception and continued direction of this project, and I am very grateful for his expertise and involvement.

Others who have provided encouragement and assistance along the way are the director of the Trenchless Technology Center Dr. Ray Sterling, Industrial Engineering Professor Dr. Jun-Ing Ker, and a recently developed friend and Professor of Mechanical Engineering Dr. Heath Tims. I am grateful to Dr. Sterling for the classes I had the privilege of taking from him, and the unparalleled breadth of his understanding of Trenchless industries that he is always willing to share. I am grateful to Dr. Ker for the

expertise in computer vision he lent to this project, and for the advanced robotics class he instructed. I am grateful to Dr. Tims for the great discussions we have about common interests, and his ability to dream big.

I would like to thank Jimmy Cook, Ray McKinney, and Murray Rasbury for their expert assistance in the machine shop at Louisiana Tech. I would also like to thank Estevan Garcia for assisting me to produce a calibration target suitable to my needs.

I would also like to express my gratitude to my parents, my brother and my sister, my aunts and uncles and my grandparents, and my in-laws for their continuing prayers. It is truly amazing that we have a God who likes for us to ask for help, and I appreciate all those who have asked on my behalf. Finally, I want to thank Jesus for hearing my cries and interceding for me. It is not by my strength that this has been completed, but by the strength of the One who works through me.

## CHAPTER 1

### INTRODUCTION

Buried infrastructure represents one of the public's biggest investments, yet quite frequently it receives insufficient attention. Often it takes a catastrophic failure to generate enough public concern to force adequate expenditures toward the repair and maintenance of these buried assets. Understandably, to make decisions on how to best spend limited resources, information regarding the current state of the infrastructure must be gathered. The tools available to gather helpful information have become more sophisticated in recent years. The most commonly used technique is closed-circuit television (CCTV) wherein a video camera is affixed to a platform designed to move through the pipe. The video collected is analyzed by technicians in a process that is both time consuming and subjective. Some newer techniques for pipe inspection are designed to provide more objective data, while using more automated processes. These techniques may include the use of ultrasound, sonar, ground penetrating radar, microwave sensors, and a host of other sensors. These more advanced techniques have not seen vast use in actual practice. One technique that shows promise for widespread usage is laser profiling. Laser profiling most commonly uses a principle called structured light triangulation to gather radius measurements of pipes. The collected measurements may be assembled into wireframe models or point clouds in three dimensions to visualize pipe

geometry, defects and deformation. Eventually, multiple scans of the same pipe over time may be overlaid to track changes in pipe geometry.

### **1.1 Background and Need**

There are infinitely many different ways to arrange a structured light projector (such as a laser) relative to a light detector (such as a camera) for the purpose of performing range measurements. Different shapes of projected light may be utilized and different angles and distances may be used in orienting the chosen light shape relative to the camera. There are advantages and disadvantages for each arrangement, all of which must be considered when designing a measurement system. Regardless of what arrangement is used, minimizing measurement uncertainty is a significant design consideration.

Relatively little work has been published to quantify the uncertainty in the measurements obtained by pipe profilers. Most of the evaluations of uncertainty have been based on experimental testing of physical devices. This empirical design approach utilizes trial and error along with intuition to arrive at the “best” design configuration for the profiling unit. No definitive analytical models relating measurement uncertainty to the geometric relationships between the camera and laser are available in the open literature. The empirical design approach is cumbersome since custom hardware must be developed for each design considered.

An analytical method is needed to evaluate and guide profiler design. The analytical method should not be overly complex, but should take into account key issues which affect the fundamental uncertainty in the measurements obtained by simple laser and camera measurement schemes. The first step toward developing these methods

should be the development of analytical measurement models that predict the expected behavior of the system. Once the models are developed, further analysis should be performed to evaluate the effects of certain parameters on the overall uncertainty of the schemes. In this way, the designs can be directed in such a way as to minimize uncertainty. The predicted uncertainty for a given system configuration can be compared to other configurations to judge the relative merit of the designs. The predicted uncertainties should subsequently be compared with the error observed from physically constructed systems to validate the analytical method and the assumptions contained therein.

## **1.2 Objective and Scope**

The objective of this research is to develop and test an analytical method for quantifying the uncertainty inherent in laser triangulation systems for pipe profiling. Three triangulation schemes will be analyzed, one utilizing a conically shaped laser mounted beside a camera, one utilizing a planar laser mounted in front of a camera and perpendicular to the pipe axis, and one utilizing a planar laser mounted beside a side-facing camera and projected parallel to the pipe axis. Figure 1.1 shows diagrams illustrating each triangulation scheme to be analyzed.

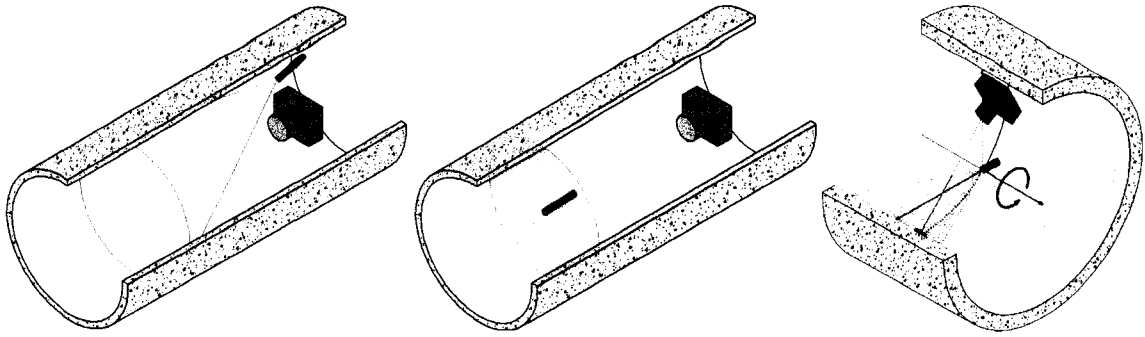


Figure 1.1 — Triangulation Schemes to be Analyzed.

Analytical models will be developed to characterize each of the three triangulation schemes. Values for some of the parameters that define the geometry of the system will be left variable to allow a particular design to be “optimized” to a certain extent. Examples of parameters that will be allowed to vary include the distance between the laser and the camera and the angles defining the orientation of the camera and laser relative to one another and to the robot. Other parameters, such as the camera resolution, will be held constant. As much as possible, the fixed parameters will be chosen for each of the three schemes to make comparison across the schemes possible. An uncertainty analysis will be performed for each scheme, and critical design tradeoffs will be identified for each scheme.

Physical models will be constructed of each profiling scheme for the purpose of comparison of the analytical models with physical systems. Software will be written to control the physical models and to process the data retrieved. The completed measurement systems will be deployed in a controlled environment, and the measurements will be compared with measurements taken by a precise tactile measurement device. The resulting error will be compared with the uncertainty

predictions found analytically, and conclusions will be drawn about the suitability of the analytical method.

Specific activities that were completed to achieve the research objectives are listed below:

- A literature review was completed that demonstrates the need for objective assessment of pipe condition and details current pipe profiler technology and research.
- Equations were derived to characterize the measurements taken by the three structured light triangulation schemes.
- The overall uncertainty for each measurement scheme was estimated using the Kline-McClintock uncertainty propagation method based on the uncertainties of each model parameter.
- Visualizations of the predicted measurements and the uncertainties in the measurements were provided as color contour plots.
- Design considerations and tradeoffs for each scheme were identified.
- Physical models of each triangulation scheme were constructed and tested.
- Software was written to interface with the profiling hardware and to automate the profiling process and data processing.
- A precision tactile measurement profiling tool and the accompanying software was developed to provide a set of high-confidence measurements of a test section of pipe.
- Measurements of the same section of pipe taken with two of the laser profiling schemes were compared with the tactile measurements to calculate error.

- The error between the laser and tactile measurements was compared with the analytical uncertainty predictions to validate the analytical methods developed in this research.

The results of the study provide important information for the designers of laser profilers, those considering the use of laser profiling for asset management, and those attempting to determine the limitations of laser profiling.

## CHAPTER 2

### LITERATURE REVIEW

#### **2.1 Introduction**

A literature review was completed to assess the need for pipe profiling and the current state of the art for laser triangulation techniques. Literature regarding specific mandates and other motivators for objective pipe condition data were reviewed. In response to the need for objective data, several commercial pipe profilers have been produced; the general operational principles and characteristics of these systems were reviewed. Studies regarding analytical models used for pipe measurement and the uncertainty of the measurements retrieved from pipe profilers were of particular interest in this literature review. Most of the profilers were found to operate on the principle of laser (or other structured light) triangulation. Several different configurations of laser profiling systems have been proposed, including different shapes for the projected laser light as well as different camera/laser arrangements. However, very few have been treated with analytical evaluations of the uncertainty of the measurements they obtain. The work presented in subsequent chapters is novel because it examines the effects that the geometries of certain triangulation schemes have on measurement uncertainty. This information will help designers of profiling systems identify good (and poor) geometrical schemes and parameters for the construction of pipe profilers. The work also provides

potential consumers of pipe profiling technology a baseline by which to judge the merits of particular profilers.

## **2.2 Objective Sewer Condition Assessment**

Laser profiling may have application for many different types of buried infrastructure, but the group which seems to be furthest along in adopting the method is the wastewater industry. Therefore, to demonstrate the most immediate need for this research, the needs of the wastewater industry will be reviewed. There are approximately 4.2 billion feet of sanitary sewer in the United States alone. It is difficult to estimate the value of this asset, but some have estimated it to be between \$1 - \$2 trillion [1, 2]. Despite its high value, maintenance for these assets is quite often lacking, most obviously due to the fact that they are invisible to the general public. A very large portion of the sewer collection systems were installed in the early 1900s [3]. The design life of the sewer collection infrastructure is rarely above 50 years, and many of these systems have been functioning nearer to 100 years with little repair [4].

Because so much of the sewer collection system is in poor repair, groundwater often inadvertently enters the collection system, adding to the volume of wastewater that must be treated and often causing overflows. Each year, an estimated 3 to 10 billion gallons of raw sewage is unintentionally released from sanitary sewer systems in more than 23,000 overflow incidents in the United States. Clearly, this represents a public health concern. In light of the poor condition of the sewer systems, the EPA has made recommendations to congress regarding the reduction of these incidents. One of these recommendations is that better technology be developed to measure pipe defects [5]. Chae and Abraham further state that “the accuracies and precisions of these infrastructure

inspection technologies must be analyzed in order to quantify the variances of various technologies” [6]. The thrust of this research is the development of a method of evaluating the quality of measurements achieved with a family of advanced pipe inspection tools.

### **2.2.1 Regulations and Directives**

There are already some laws and guidelines being enacted which have begun to further motivate the need for objective pipe assessment data. The EPA has developed programs called CMOM, which stands for “Capacity, Management, Operations and Maintenance.” The focus of these programs is to encourage and at times coerce municipalities to adopt best industry practices for the maintenance of their sewer infrastructure. CMOM places a great deal of emphasis on the inspection and condition monitoring of sewer systems [7]. The evaluations should be as objective and quantitative as possible, thus providing new opportunities for advanced pipeline measurement systems [8]. Therefore, as profiling measurements become more refined and proven, they will likely already have the support of the agencies which oversee the inspection practices of municipal underground asset owners.

Perhaps a more specific motivator for objective pipe assessment data arises from the need for public agencies to accurately account for all of their assets. In 1999, the Governmental Accounting Standards Board (GASB) released a directive called Statement 34. This statement created a new requirement that the condition (and thus value) of all sewer assets had to be assessed every three years on a scale that was consistent and repeatable [9]. This new standard has many sewer asset owners looking closely at adopting laser profiling to achieve the repeatability specified by Statement 34. The

proposed research will help to better quantify the uncertainty of the measurements achieved with laser profiling, and thus provide some information to those evaluating options to achieve the requirements of this new accounting directive.

One state in the USA has already adopted a direct mandate for laser profiling. The state of Florida has specified that all new installations of large diameter rigid and flexible pipe must be laser profiled upon completion. The goal of the profiling is to measure the ovality of the pipes after installation to ensure proper methods are used during the backfill [10]. Perhaps in a first move towards a similar requirement, the state of Arizona is recommending that all new installations of corrugated HDPE pipe be laser profiled upon completion [11].

### **2.2.2 Commercialized Profilers**

A few companies have developed products designed to fill the need for the collection of pipe profiles. These companies include CleanFlow Systems Ltd. from New Zealand, Colmatec Inc. out of Canada, the Optical Metrology Center from the United Kingdom, and RedZone Robotics from the United States.

CleanFlow Systems Ltd. produces an attachment that can be attached to the front of an existing CCTV pipe inspection robot. The attachment shoots a ring of laser light onto the wall of the pipe, and measurements are taken of that section of the pipe using video processing software produced by CleanFlow Systems. The software can display three-dimensional models of the inner surface of the pipe and calculate pipe ovality [12]. The profiler has been tested by an independent research group in the UK and has been approved for use. The research group made no mention of an analytical evaluation of the uncertainty of the measurements, but did provide descriptions of the experimental error in

the profiler's measurements, which it estimated to be about 0.5% of the pipe diameter [13]. There are several case studies which have been performed with this profiler in several countries with good results reported [12, 14].

Colmatec, Inc, has developed a laser profiler that operates using the same principles as the profiler from CleanFlow. A rotating spot laser is projected on the inner surface of the pipe wall in the same geometrical arrangement as the ClearLine profiler. The CoolVision software produced by Colmatec can display three-dimensional models of the inner surface of the pipes scanned. A total of three case studies have been reported using this profiler, all of which seemed to have good results [15]. No documentation could be located regarding the uncertainty or error in the measurements achieved by this profiler.

The Optical Metrology Centre offers a profiler called the OMC Laser Profiler 15/50 that also uses a rotating spot laser; however, this system uses a one-dimensional detector that rotates along with the laser, rather than a two-dimensional detector such as a camera. The product literature advertises an error profile that is near zero at close measurements and up to about 0.8 mm at long range measurements (~200 mm) [16]. The OMC 15/50 profiler has been tested by Thames Water Research and Technology; however, the only results reported were that the profiler could measure up to 400 points in a few seconds and function 95 meters from the operator [17]. The profiler can display three-dimensional plots of the measurements obtained and ovality calculations. A significant amount of analysis has been performed on this profiler by Clarke and Gooch [18-20], much of which will be discussed in Section 2.3.1.

RedZone Robotics has developed some custom pipe profiling tools. The RedZone profiler is extremely accurate due to its use of laser interferometry for the execution of the measurements. Laser interferometry tends to deliver more accurate measurements than laser triangulation, but tends to be much more expensive. The output of the device is in the form of a cloud of points representing the inner surface of the pipe wall [21].

### **2.3 Structured Light Measurements**

Structured lighting can be coupled with optical sensors to produce accurate geometric measurements. A light source is set up such that its illumination falls on a surface within the view of an optical sensor. The shape of the structured light is precisely known. The optical sensor can distinguish precisely the angle of trajectory with which the reflected light approaches the sensor. An array of photosensitive elements composes the image sensor, and the location in this array where the light falls tells the system the angle of trajectory of the light. Figure 2.1 illustrates the concept of structured light measurements [22].

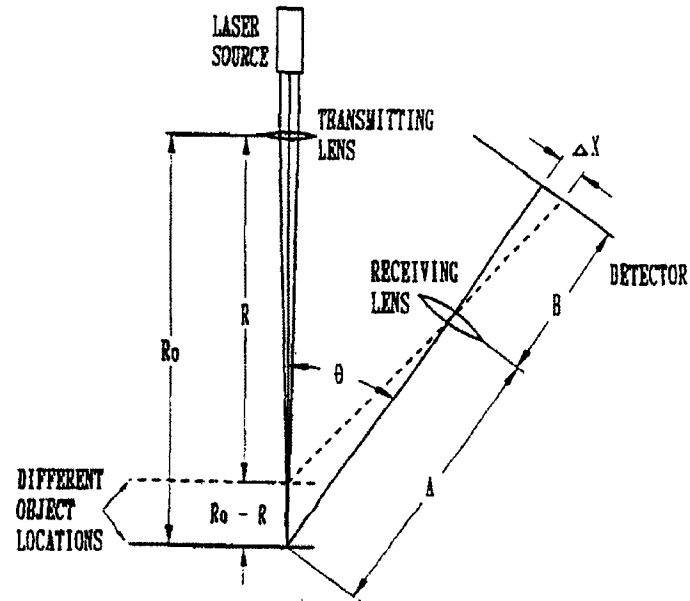


Figure 2.1 — Principle of Structured Light Measurements.

By detecting the angle of trajectory of the reflected light, the distance from the source of the emitted light to the object on which it falls can be determined. For the example shown in Figure 2.1, a one-dimensional detector array is sufficient to detect the trajectory angle. Digital cameras are usually made with two-dimensional detector arrays, and cameras are frequently deployed on pipe assessment equipment [23].

### 2.3.1 Differing Geometries for Pipe Assessment

The basic structured light triangulation arrangement shown in Figure 2.1 must be set up in a special way to provide profiles of the inner surfaces of pipelines. This type of system only measures one point at a time; thus arrangements must be made to sweep the point of measurement around the circumference and length of the pipeline [18]. The movement along the length of the pipeline is accomplished by mounting the entire measurement system on a moveable platform. On this platform, accommodations are made for the rotation of the measurement device about an axis parallel with the pipe axis.

This rotation as well as the movement of the measurement platform must be precisely monitored for the system to correctly identify the angular and translational position of the radial measurements being taken [24]. A schematic of how this type of system is set up is shown in Figure 2.2.

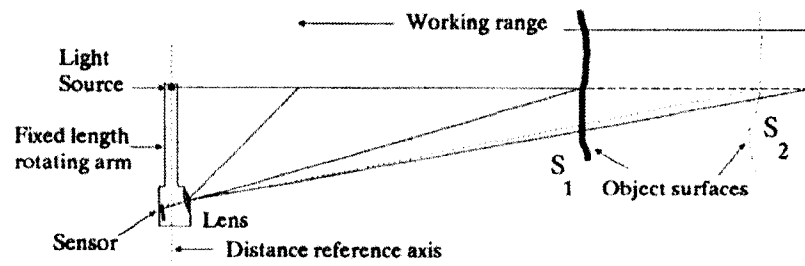


Figure 2.2 — Single Spot Profiling.

Since the geometry for this type of system is so simple, the authors did not even include an analytical model of the profiler, but rather performed an overall system calibration to which later measurements could be compared. The relationship between the location of the spot in the linear array and the distance of the object from the reference axis was found to be very non-linear [20].

A group from Japan describes the use of a single spot system like this for pipe profiling. A very simple analytical relationship exists between the location in the linear sensor and the measurement range which the group derives. The group tested a device constructed with this model and reports the accuracy to be  $\pm 0.2\text{mm}$  in the range of 33 to 42.5 mm radius measurements. No mention is made of an analytical uncertainty model [25].

If a two-dimensional image is to be employed for pipe profiling, more complicated shapes may be used for the structured lighting. Probably the most common

arrangement for pipe profiling is a plane of light placed in front of the camera, parallel with the image sensor. Figure 2.3 shows a sample of this setup [23].

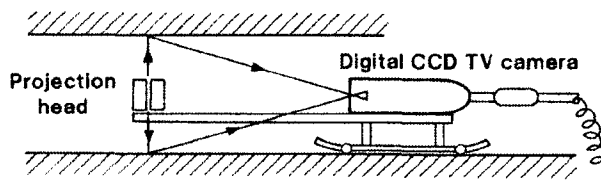


Figure 2.3 — Planar Light Projection.

A system known as the Flexiprobe which employs this concept uses a standard halogen light bulb with a cylindrical mask [23]. Another system known as the PIRAT (Pipe Inspection Real-time Assessment Technique) also employs this illumination geometry, but the light source consists of a single-spot laser which points perpendicular to the pipe axis and is spun about an axis parallel with the pipe axis [26]. A third system utilizing this geometry that is more commercially popular is marketed by Cleanflow Systems, LTD. The system is known as the Clearline Profiler, and it uses proprietary prismatic optics to split a laser beam into a plane [12]. Another profiler with a spinning spot laser head was produced and used on several pipelines by a company called Colmatec. None of the literature discusses the analytical geometric model used by these types of systems, likely because of the proprietary nature of the profiling business.

Another light shape that several groups have investigated is a cone. It is more difficult to fully describe the orientation of a cone of light relative to a camera; thus, more has been written on the analytical models of the geometry. One method of arrangement of the laser projector is with the axis of the cone coincident with the center axis of the

camera. This arrangement is illustrated in Figure 2.4 with the overall system shown on the left, and the geometry defining the analytical model shown on the right [27].

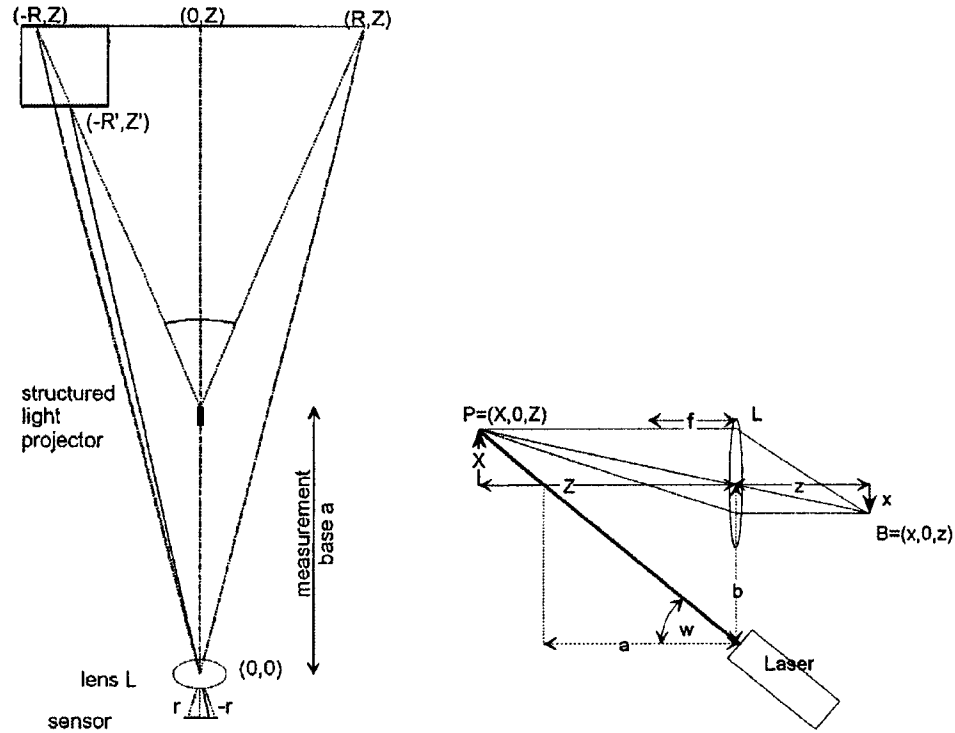


Figure 2.4 — Radially Symmetric Lighting.

Equations were derived for this arrangement of structured lighting. The equations consisted of a pipe radius measurement  $R$  and an axial distance measurement  $Z$ , both of which are determined by the radius  $r$  of the image of the laser line on the image plane.

Equations (2-1) and (2-2) give these two measurements:

$$R = \frac{r \cdot \tan(w)(f - a)}{r - f \cdot \tan(w)} \quad (2-1)$$

$$Z = \frac{f[r - a \cdot \tan(w)]}{r - f \cdot \tan(w)} \quad (2-2)$$

where  $f$  is the focal length,  $z$  is the distance from the lens to the image plane,  $a$  is the baseline distance from the lens to the laser vertex, and  $w$  is the angle defining the orientation of the laser with respect to the pipe axis. This research compares the merits of the radially symmetric projection technique with another type of conical laser projection wherein the origin of the cone and the lens of the camera lie in the same plane. A diagram illustrating this arrangement is given in Figure 2.5 [27].

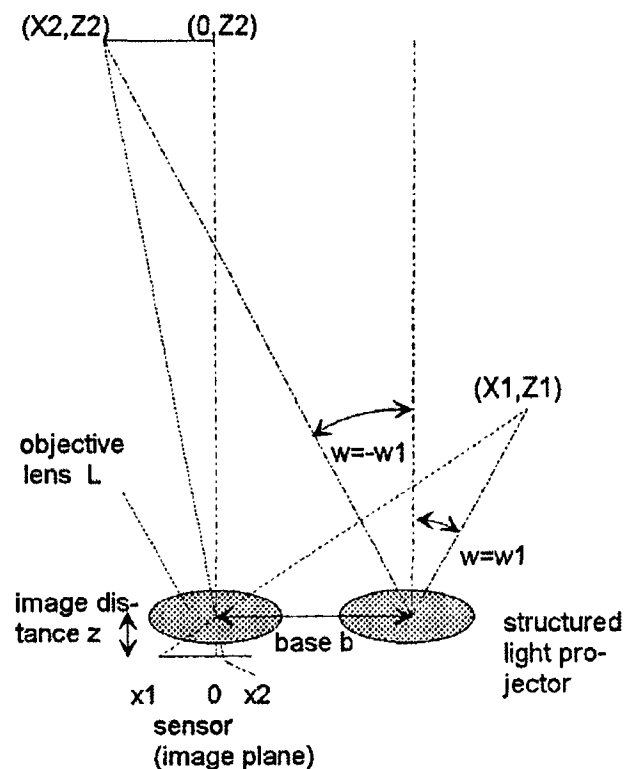


Figure 2.5 — Asymmetric Conical Projection.

Since this type of system is not radially symmetric, the analytical models describing its geometry are significantly more complicated. They cannot be reduced to simply a radius and an axial position; therefore, the authors chose to leave the model in

terms of Cartesian coordinates. Equations (2-3), (2-4), and (2-5) give the X, Y, and Z coordinates of points on the pipe wall in terms of x and y image coordinates.

$$X = x \frac{xb + \tan^2(w)f^2 \pm \sqrt{\tan^2(w)f^2[y^2 + (x+b)^2] - y^2b^2}}{y^2 + x^2 - \tan^2(w)} - \frac{b}{2} \quad (2-3)$$

$$Y = y \frac{xb + \tan^2(w)f^2 \pm \sqrt{\tan^2(w)f^2[y^2 + (x+b)^2] - y^2b^2}}{y^2 + x^2 - \tan^2(w)} \quad (2-4)$$

$$Z = f \frac{x^2 + xb + y^2 \pm \sqrt{\tan^2(w)f^2[y^2 + (x+b)^2] - y^2b^2}}{y^2 + x^2 - \tan^2(w)} \quad (2-5)$$

Since these equations were too complicated for the authors to easily find the measurement errors, the authors instead reduce the problem to a single plane, shown in Figure 2.5. When reduced to considering only this plane, the equations can reduce to equations (2-6) and (2-7):

$$X = \frac{b}{2} + \frac{f \cdot \tan(w)(x-b)}{x - f \cdot \tan(w)} \quad (2-6)$$

$$Z = f \frac{x+b}{x - f \cdot \tan(w)} \quad (2-7)$$

No mention is made of how the  $\pm$  operator was changed to a + operator for the transition from the complete equations to the reduced equations. The authors describe briefly how these optical measurement systems were implemented on a pipe assessment platform called the KARO, but they do not attempt to resolve the ambiguity presented by the “ $\pm$ ” operator in equations (2-3) through (2-5).

Another scheme utilizing conically shaped laser light turns the direction of projection of the laser cone toward the camera rather than away from it [28]. Figure 2.6 [29] illustrates this setup of the laser and camera.

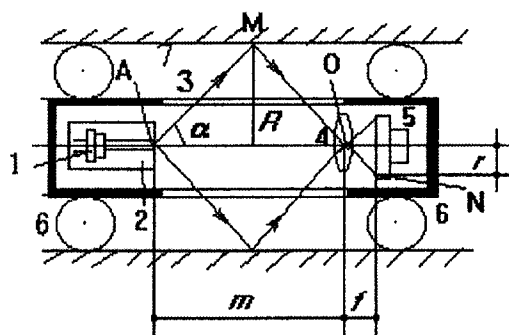


Figure 2.6 — Reversed Conical Projection.

One of the key advantages cited for setting a laser system up in such a way is that more of the illumination from the laser unit will reflect in the direction of the camera, thus allowing for a lower power laser unit. The authors also discuss two different methods of actually generating a conically shaped laser pattern: using conical mirrors and using diffraction gratings. The analytical model of measurement is given by equation (2-8).

$$r = \frac{f \cdot R}{m - R / \tan(\alpha)} \quad (2-8)$$

In this case, the equation is solved for the radius on the image plane in terms of the measured pipe radius. The author does not discuss changes in the axial location of the measurements being taken due to changes in the radial measurements. A similar system to this has also been investigated for the measurement of the inside of small circular and rectangular holes [30].

Another group has done some work on a laser profiling system that uses a laser spot array to evaluate the inside profiles of pipes. This is essentially a variation on the single spot method, but it uses a two dimensional image sensor and multiple spots to

increase the number of measurements that can be taken per image capture. Figure 2.7 [31] illustrates the laser spot array method.

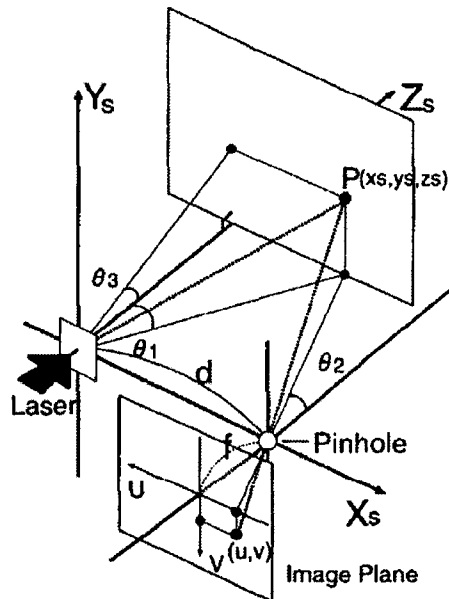


Figure 2.7 — Laser Spot Array Method.

The author's purpose for their profiler was to automatically distinguish between straight pipes and pipes with elbows or tees. The main difficulty with a laser spot array system is that the images cannot be analyzed on an individual basis. Since it is difficult to distinguish one spot from another, the image processing algorithm must employ point tracking analysis in a series of images to identify a particular spot. In addition, the geometry of this type of arrangement is inherently not well suited to the inside of pipes.

### 2.3.2 Camera Models and Calibration

With the exception of the one-dimensional laser scanners, all the profiling models discussed have utilized the perspective projection camera model. The perspective projection model can be visualized as shown in Figure 2.8 [32].

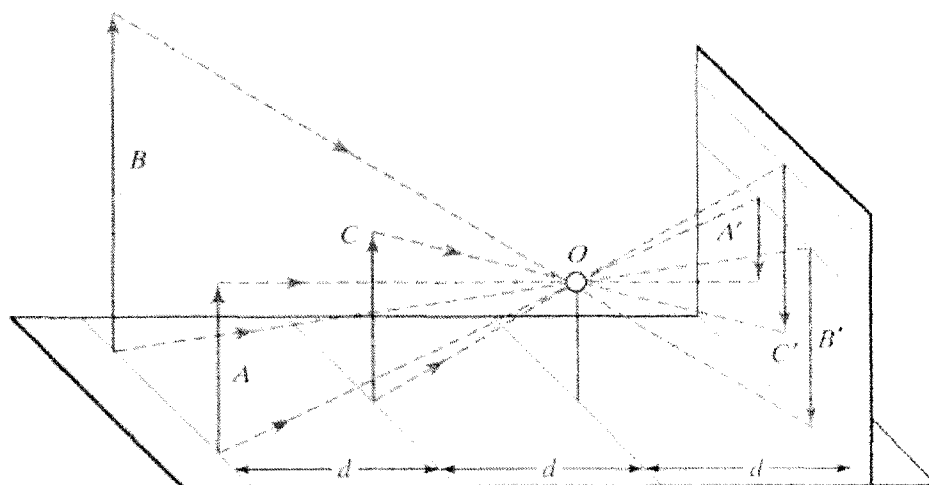


Figure 2.8 — Perspective Projection Model.

The perspective projection model is essentially a direct mapping of objects in a plane in the real world to images of those objects on the image plane. One key assumption that is made using this model is that the entrance and exit angles out of the pupil of the lens will be the same. This is a good assumption for some lenses (particularly those that have a small angle of view) however, the assumption does not work for lenses with large angles of view [33]. For larger fields of view, the world shape that is mapped to the image plane actually more closely resembles a sphere. Thus the radial location of a point within the image plane would be better modeled as a function of the entrance angle of the light illuminating that point than a location in a real-world plane. Fleck describes the perspective projection model in these terms, and also describes four other camera models that have better correspondence to the behavior of wide-angle lenses. These models are listed and their equations are given by equations (2-9), (2-10), (2-11), (2-13), and (2-14).

#### *Perspective Projection*

$$p(\alpha) = k \tan(\alpha) \quad (2-9)$$

*Stereographic Projection*

$$p(\alpha) = k \tan\left(\frac{\alpha}{2}\right) \quad (2-10)$$

*Equidistant Projection*

$$p(\alpha) = k\alpha \quad (2-11)$$

*Sine-Law Projection*

$$p(\alpha) = k \sin(\alpha) \quad (2-12)$$

*Equi-Solid Angle Projection*

$$p(\alpha) = k \sin\left(\frac{\alpha}{2}\right) \quad (2-13)$$

Here,  $p$  is the radius of a spot in from the center of the image,  $\alpha$  is the angle of trajectory of incoming light off the central axis, and  $k$  is a scaling factor related to zoom. The selection of the most suitable model for a particular application is mostly dependent on the lens chosen for the application. These models will be evaluated for suitability with respect to the specific lenses used in later chapters.

If one of these alternate camera models is not used for wide angle lenses, there will be problems with image distortion. An example of distortion may be seen in Figure 2.9, where a plane of equally spaced targets appear not to be equally spaced [34].

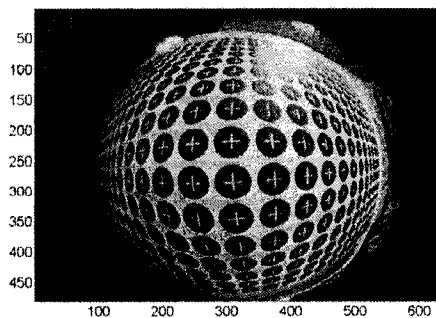


Figure 2.9 — Wide Angle Image Distortion.

The perspective projection model for this object would have maintained an image of equally spaced targets. If it is still desirable to use the perspective projection camera model, a calibration procedure must be performed to characterize the deviation of the expected locations of targets from the actual locations. Pansar and Korkealaakso use an additive model that takes the measured coordinates and adds a correction term to them to achieve actual coordinates. This correction term is formed in the calibration procedure, and is based on high order polynomials [34].

### **2.3.3 Pixel Identification Techniques**

To make the optical triangulation pipe profiling method feasible, computational methods must be used to process the images retrieved by the scanning system. This means that algorithms must be employed to identify the location in the retrieved images where the structured illumination appears. This will first be demonstrated for the one-dimensional case.

The illumination for the one-dimensional scanner previously described is a spot that is approximately circular and has an approximately Gaussian intensity distribution. This intensity distribution is propagated to the object surface and then reflected toward the light sensor [35]. As shown in Figure 2.10, the array of detector elements will pick up discrete points along this distribution [20].

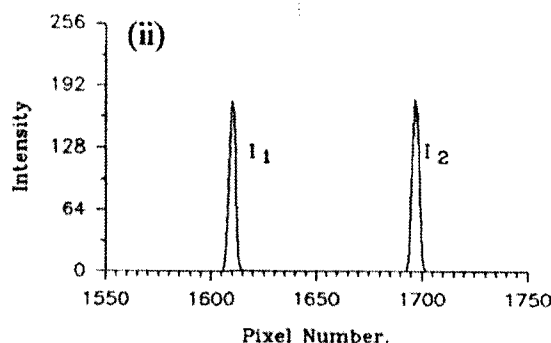


Figure 2.10 — Intensity Distribution.

Thus, to identify the location of the spot, it is first necessary to decide which portion of the intensity distribution should be used as the reference. There are two main options. One option is to take the peak as the location of the spot, and the other option is to take one of the edges as the location of the spot [35].

If the peak of the spot is used as the reference, there are several sub-techniques for identifying its location. The most simple technique is to simply find the largest value in the array. This technique has major drawbacks because it cannot produce sub-pixel accuracy and it is quite susceptible to noise. Thresholding is a similar option where all pixels above a certain intensity level are examined, and the center location is chosen between the first and last pixels that are above the threshold. Neither of these methods fully utilize the information in the image and tend to achieve less accuracy than more appropriate sub-pixel techniques [36].

Centroiding is a technique in which the intensity values of the pixels in the image are used as weights to form a weighted average of pixel locations. Thus, if many bright pixels are located in a small area, the weighted average calculation of the peak's location would fall in that area. Interpolation is a method in which the intensity of the pixels are fit to a curve, often a polynomial. The equation of this curve is calculated by least-

squares, and features (such as peaks) are located in the fitted curve. Correlation is a method in which measured intensity distributions are compared with predetermined expected intensity distributions and the error between them is evaluated. The location where the error is found to be a minimum is taken as the location of the peak [35].

Zhang and Zhuang describe a method of applying a centroiding technique to an image of a laser line to quickly determine a region of interest which contains the line but not a lot of background. Once the region of interest is established, an edge detection technique is used to identify one edge of the laser line. Since this technique is used on a circular shaped laser line, the author also describes how the image is segmented to provide discrete identified points along the line. Figure 2.11 shows an example of how the circular line is cut up into sectors, each overlapping those adjacent sectors [29].

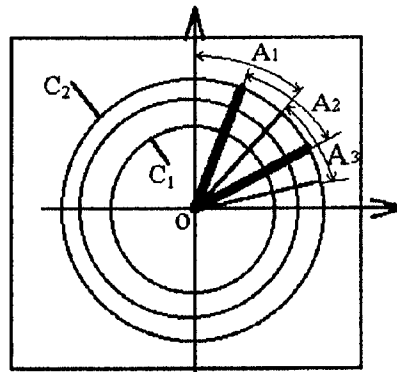


Figure 2.11 — Segmentation of Circular Laser Line Image.

Each individual sector is examined using edge detection to identify a point most likely to represent the laser line. This set of points becomes the set of measured coordinates of the pipe. Henry and Luxmoore describe a similar image segmentation process; however, instead of performing an edge detection on the light line, the maximum intensity value in a particular segment is taken as the center of the light line [23].

### 2.3.4 Accuracy Assessments

Measurement systems utilizing structured lighting use indirect measurement methods. A function of several variables is often used to evaluate a desired measurement (such as a pipe radius) using an actual measurement (such as a pixel location). In 1953, Kline and McClintock developed the model for tracking uncertainties in indirect measurement systems that has been the basis for most specific studies of such systems. These authors found that if an indirect measurement is taken that is a function of several variables ( $x_i$ ), where each variable has an uncertainty of  $U[x_i]$ , that the overall uncertainty of the measurement  $M$  can be given by equation (2-14) [37].

$$U[M] = \sqrt{\sum_{i=1}^n \left( \frac{\partial M}{\partial x_i} U[x_i] \right)^2} \quad (2-14)$$

This principle is known as error propagation and is used heavily in the analysis of the nature of measurement uncertainties using optical measurements [38].

Hartrumpf and Munser included error propagation in their analysis of radially symmetric structured light described earlier. These authors made the assumption that the bulk of the error in the system would arise from the uncertainty of the location of the image of the structured light on the image plane. This uncertainty was called  $\sigma_r$ , the uncertainty of the radius measurement being taken was called  $\sigma_R$ , and the uncertainty of the axial location of this radial measurement was called  $\sigma_z$ . The uncertainties of the measurements shown in Figure 2.4 are then given with equations (2-15) and (2-16).

$$\sigma_R = \left| \frac{(a-f) \cdot f \cdot \tan^2(w)}{[r-f \cdot \tan(w)]^2} \right| \cdot \sigma_r \quad (2-15)$$

$$\sigma_R = \left| \frac{(a-f) \cdot f \cdot \tan(w)}{[r-f \cdot \tan(w)]^2} \right| \cdot \sigma_r \quad (2-16)$$

Here  $a$ ,  $f$  and  $w$  were defined in conjunction with equations (2-1) and (2-2). It can be seen here that the authors simply found the partial derivatives of the image radius with respect to the world radius and related the errors in those two parameters as prescribed by Kline-McClintock. A similar technique was also used by the authors for the reduced measurement scenario given in Figure 2.5. In this case the equations for uncertainty are given by equations (2-17) and (2-18).

$$\sigma_x = \left| \frac{f \cdot \tan(w)[b + f \cdot \tan(w)]}{[x - f \cdot \tan(w)]^2} \right| \cdot \sigma_x \quad (2-17)$$

$$\sigma_z = \left| \frac{f \cdot [b + f \cdot \tan(w)]}{[x - f \cdot \tan(w)]^2} \right| \cdot \sigma_x \quad (2-18)$$

No other publications in which analytical treatments of measurement error for internal surface measurement systems could be located. The typical procedure used in the literature for the assessment of measurement error was to compare the profile outputs from the profiler being evaluated with dimensions known from other sources [13, 23, 28, 29].

### 2.3.5 Common Problems and Novel Solutions

There are some sources of systematic error and other problems with laser profiling. In many cases, the accuracy of the measurements depends on the surface conditions being measured. If there are discontinuities in the surface being measured, the Gaussian shape of the light may not be effectively preserved as it is transmitted from the light emitter to the surface being measured and then to the detector. Figure 2.12 illustrates the effects of several types of surface discontinuities [39].

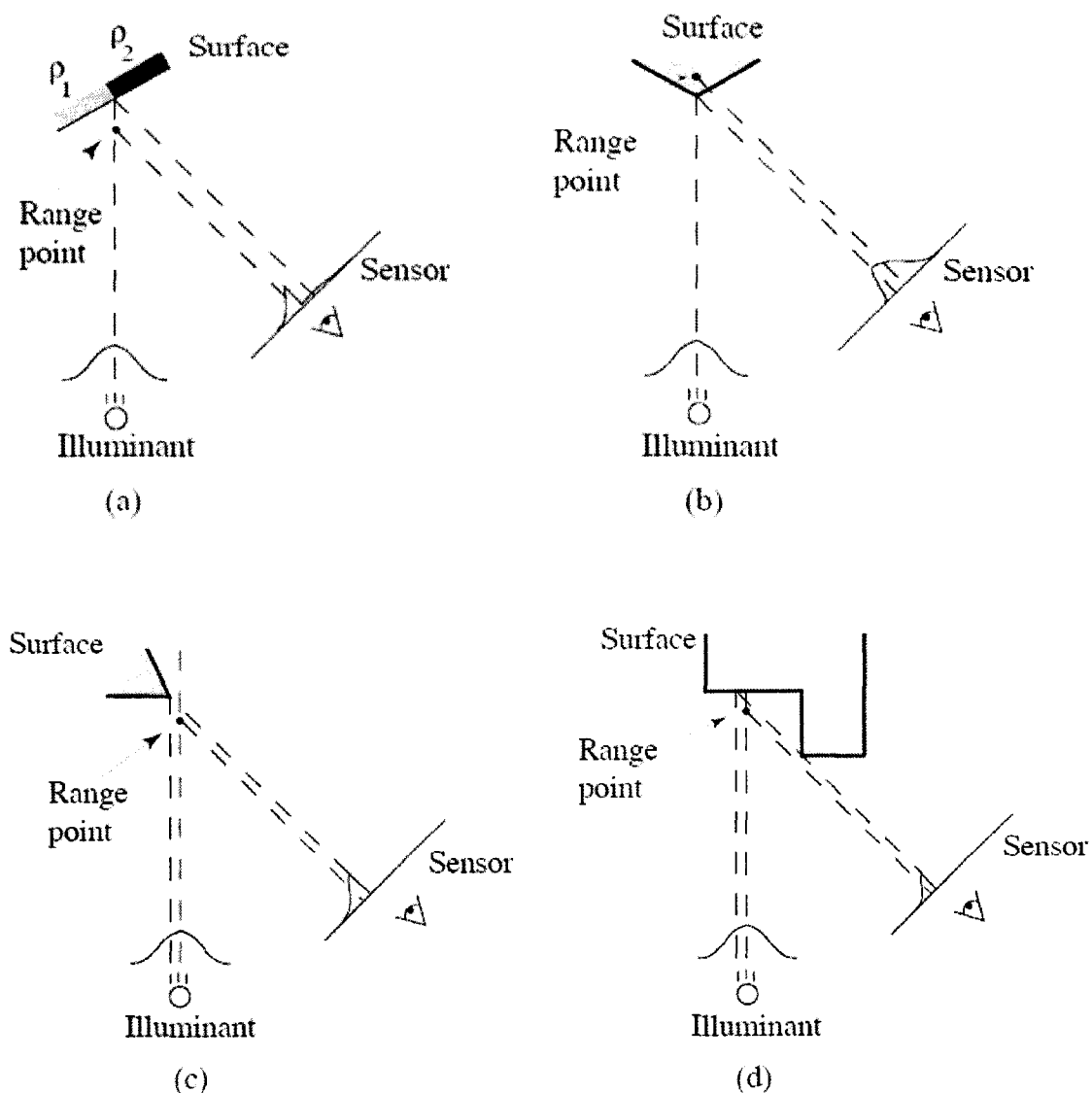


Figure 2.12 — Error from Surface Discontinuities.

From (a) through (d), the discontinuities shown in Figure 2.11 are surface reflectance discontinuities, corners, splitting of the illuminant, and sensor occlusion, respectively. To reduce the effects of these types of error, the authors propose and analyze a method in which the illuminant sweeps over the surface being measured, and measurements are taken nearly continuously. By analyzing the progressing shape of the image of the illuminant, inferences can be made about the actual shape of the geometry

being measured. Curless and Levoy call this method spacetime analysis and show great reductions in error for each of the cases listed in Figure 2.12.

When light is shined on a surface, different amounts of light will be reflected in different directions depending on varying surface conditions. Issues like the orientation of the surface relative to the direction of light projection, occlusion, and changes in the transmission medium can cause different readings for a light sensing device depending on its orientation relative to the illumination source. To compensate for these issues, a method has been proposed that uses multiple sensors in different orientations about the illumination source, and uses software to average the readings from the multiple sensors.

Figure 2.13 illustrates this type of method [40].

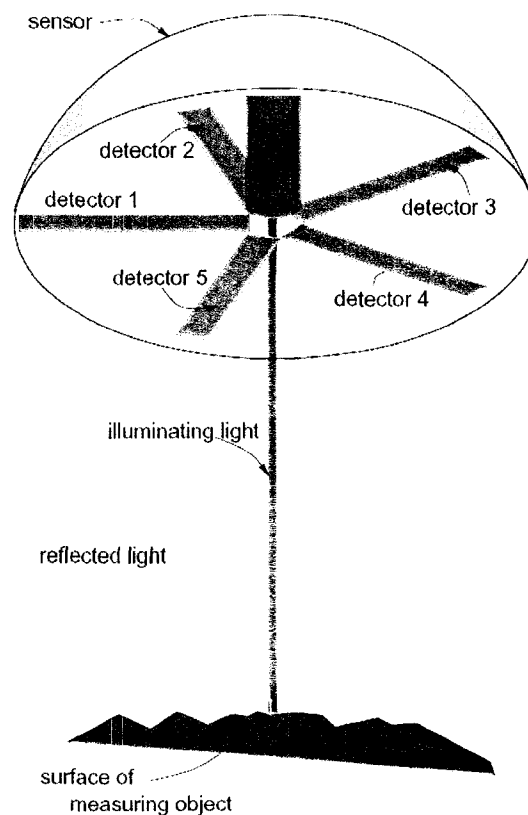


Figure 2.13 — Multiple Detectors for Signal Averaging.

Hueser and Rothe developed algorithms to use and occasionally discard information from multiple detectors simultaneously. By comparing each sensor with the consensus from all the others, better accuracy was obtained for many surface scenarios. A similar idea has also been advanced wherein multiple sources of structured lighting are used with a single detector. This type of system has been shown to provide better measurements for situations where the surface being measured varies greatly in orientation relative to the light detector [41].

### **2.3.6 Speckle: The Fundamental Limit on Accuracy**

Even if the surface being measured has uniform reflectance properties, no geometrical discontinuities, and causes no occlusion, there is still a fundamental limit on the accuracy obtainable by laser triangulation. One element of an array of light detectors detects the summation of all the points of scattered light within the limits of its view. When the surface being measured is rough on a scale relative to the wavelength of projected light, random phasors tend to combine in random ways that yield noise in the profile of light intensities over several detectors. Figure 2.14 illustrates this effect, which is known as speckle [42].

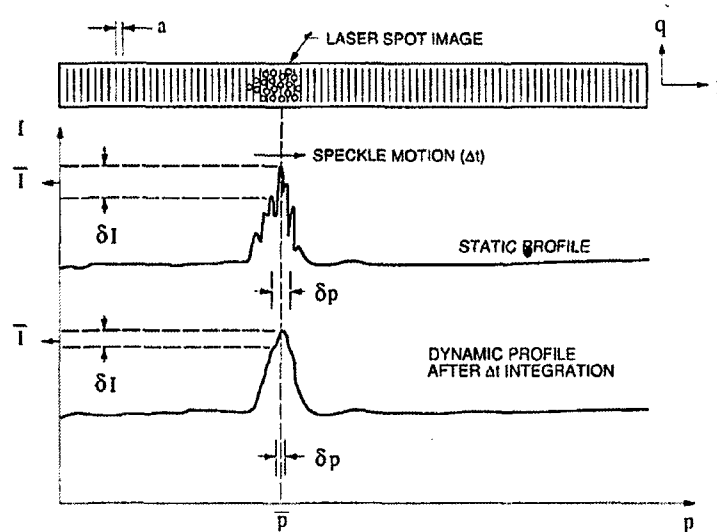


Figure 2.14 — Speckle Effects.

Baribeau and Rioux describe a method of integrating the signal from a detector over time, while the light spot is scanned over the surface to reduce the error in triangulation measurements due to speckle. In their work, the fractional pixel number of the identified peak point in the laser line is given by the expression  $p/a$  where  $p$  is the location across the image detector in length units and  $a$  is the width of one pixel in the same length units. When the detector plane in the camera is oriented perpendicular to the lens axis, the uncertainty of the location (in fractional pixels) of peak of the Gaussian light distribution is given by Equation (2-19).

$$U[p/a] = \sqrt{\frac{\lambda^2 f_0^2}{2\pi\phi^2 a^2}} \quad (2-19)$$

In this equation,  $\lambda$  is the wavelength of the projected light,  $f_0$  is the focal length of the camera, and  $\phi$  is the diameter of the lens [42]. An interesting thing to note is that the ratio of focal length to lens diameter is a quantity known in photography as the *f number*. As *f numbers* increase, the range of distances from the camera that can be sharply

focused increases. Often cameras have stops at f number values of integer powers of  $\sqrt{2}$  [43].

Dorsch, Hausler et al. examined the theoretical limit on uncertainty of the true location of the center of an image of a laser spot on a detector; they found that designing a system with low fundamental uncertainty calls for a large aperture and small temporal and spatial light coherence. Since lasers tend to be quite coherent light sources, this typically means larger uncertainties than with the use of incandescent light [44]. Hausler, Kreipl et al. describe some experience with using very incoherent light sources to perform very precise distance measurements [45].

## **2.4 Qualitative Damage Detection**

Methods other than inner wall measurements have been investigated for more automated and objective pipe assessment. There are a few pipe inspection tools available which provide flattened images of the inner walls of pipes [46, 47]. Image processing techniques can be employed on these images to identify cracks. Another research group has had success with identifying cracks using a reflectometric technique which employs a conical laser projector, but not for triangulation purposes. Still others use processing techniques on images and video from current pipe inspection techniques to try to identify collapses or laterals.

### **2.4.1 Flattened Image Processing**

There are a few groups working on image and data processing techniques to automatically identify cracks in flattened images and classify those cracks for comparison with later scans. Figure 2.15 shows the process of flattening an image and identifying the defects [6].

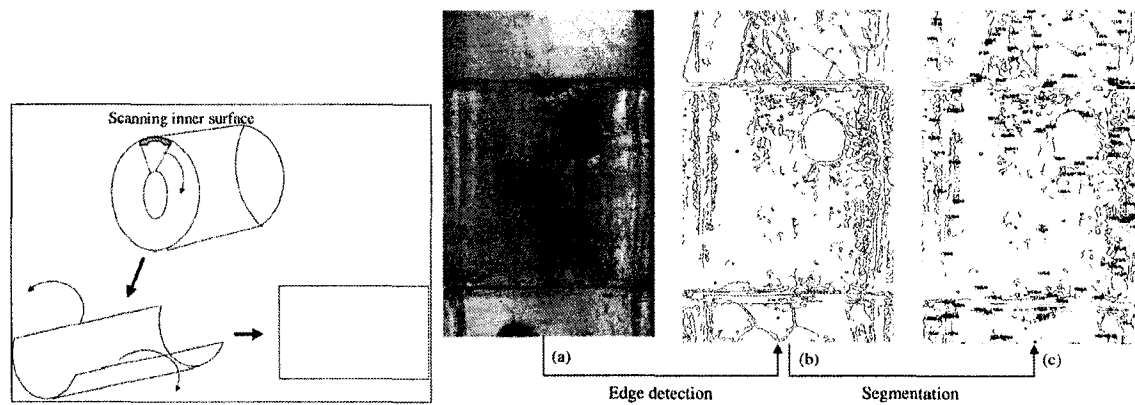


Figure 2.15 — Image Flattening and Defect Identification.

Image processing is used to detect edges in the collected images; then, the images are processed through a neural network. The neural network “learns” how to classify each type of defect based on the teaching of an experienced operator. After the neural network has learned how to identify each type of defect, it can identify defects on its own. The defects identified are then segmented for later reference, for example, to compare multiple scans of the same pipe [6]. Sinha and Karray have developed a method of linking linguistic descriptions of defects to the training of a neural network for pipe defect classification. This method has shown to produce a network that can match the assessments of an operator 92.7% of the time [48]. Several other neural network models for pipe defect classification are described and compared in another work by these authors [49]. A case study in which cracks are identified in concrete pipe is described by Sinha and Fieguth in which several different image filters are used to attempt to locate cracks. The usefulness of each filter is estimated by showing each one’s probability for false alarms and for failure of detection [50].

### 2.4.2 Reflectometric Technique

Another group has focused their work on the development of a better sensor for the detection of cracks in pipes. By projecting conically shaped laser light onto the pipe wall, cracks may be detected based on the intensity of the light which is reflected back to a camera. Figure 2.16 shows the setup of the system along with an identified defect [51].

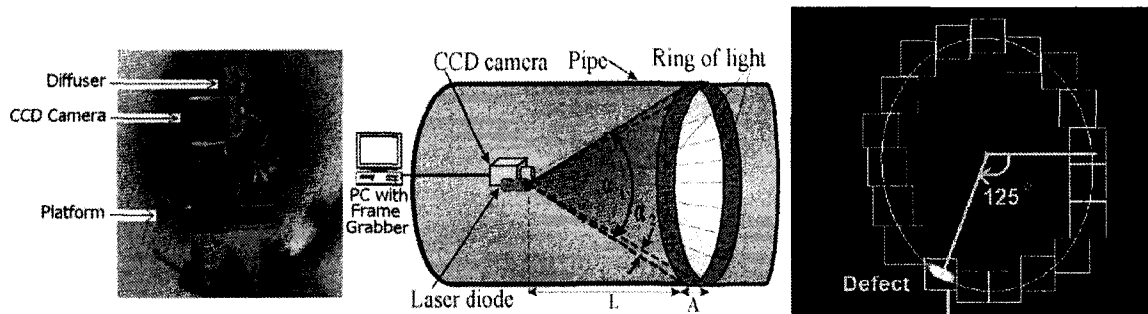


Figure 2.16 — Reflectometric Defect Location Technique.

A technique of fitting an ellipse to the image of the laser line is employed to assist in correctly identifying an appropriate location at which to analyze light intensity [52]. The system was tested for defect classification capability for various pipe colors, wall textures and pipe materials; very close correlation is reported between the types of defects reported by the system and the true nature of the defects [53]. The group has published several other works, which seem very similar to the others described [54-57].

### 2.4.3 Shape Detection and Analysis

Since the most common method of pipe inspection currently in use is the collection of video in the interior of the pipe with CCTV equipment, it would be a great boon to have the capacity to automatically process the video in some way to achieve objective data. A method is described by Xu in which the video taken at the joints of pipes may be processed to identify their shapes. When pipes collapse, often the pieces of

the pipe still retain approximately circular shapes, but they are disjointed. Image processing techniques may be used to identify edges, and those edges may be thinned. Fourier analysis is used to fit a certain number of circular arcs to the edges representing pieces of the collapsed pipe [58].

Pan describes a very similar method of identifying pieces of collapsed pipe; however, rather than the use of Fourier analysis to identify the pieces of the collapsed pipe, a method of using least-squares fitting is utilized. Circles are fit to the identified edges of pipe joints to identify collapses. Figure 2.17 shows an example of this type of extraction [59].

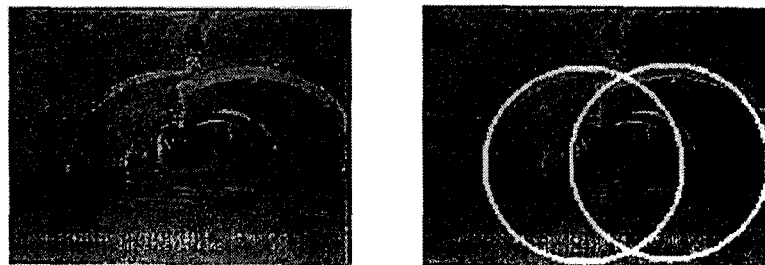


Figure 2.17 — Pipe Collapse Identified by Image Processing.

Kolesnik and Baratoff have also worked with shape recognition within sewer pipelines. Again, image processing filters are used to extract edges representing expected shapes within the sewer pipes. Ellipse fitting is used to not only extract the shape of the host pipe, but to also identify lateral inlets into the sewer. The research was performed with a focus toward autonomous navigation of a sewer robot. The work is used to identify shapes as three-dimensional landmarks to assist the robot in orientation tracking and location identification [60].

## 2.5 Conclusions

Underground infrastructure is deteriorating and frequently receives insufficient attention. More objective inspection techniques can enable better standards to be adopted regarding the upkeep of these assets. Several profilers capable of retrieving three-dimensional profiles of the inside walls of pipes have been offered, but none have yet been widely adopted. For the method to be more universally adopted, improved documentation and verifiable calibration procedures to understand and assess the accuracy and reliability of the methods are needed. This research focuses on the development and verification of rigorous models to quantify measurement uncertainty for three different laser-based pipe measurement systems.

CHAPTER 3

ANALYTICAL EVALUATION OF  
TRIANGULATION ACCURACY  
FOR A CONICALLY  
PROJECTED LASER

**3.1 Introduction**

This chapter will be devoted to the development and analysis of a triangulation scheme which uses conically projected laser light to illuminate a pipe wall. The system studied is restricted to a conical laser and a single camera that lie in a plane perpendicular to the axis of the robot, as shown in Figure 3.1. Equations are developed to relate the geometry of the camera/laser system to the coordinates of the pipe. Determination of the uncertainty in pipe coordinates as a function of system parameters is the focus of the chapter.

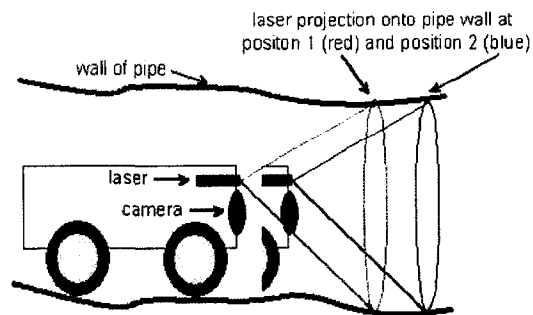


Figure 3.1 – Conical Laser Light Projection.

### 3.2 Derivation of Triangulation Equations

The laser cone will be assumed to be positioned above the camera and aimed so that the resulting ring of light on the pipe wall will fall approximately at the same distance ahead of the camera; that is, the axis of the conical laser will be pitched downward relative to the axis of the robot. The measurements will be non-dimensionalized so as to make the conclusions more universal. Values for the needed aim and fan angles of the laser cone will be derived. The camera model which will be employed will be described, and the triangulation equations will be derived in terms of the coordinates of this camera model. Some mathematical difficulties arise in the derived equations in the form of inversion of solutions, and these issues are resolved. Appropriate field of view limits are identified, and visualizations are provided of the behavior of the measurement system.

#### 3.2.1 Geometrical Assumptions

The cone of light will have its vertex in a plane which is perpendicular to the robot axis and coincident with the focal point of the camera's lens. The z-axis will be defined as the axis of the camera lens. The z-axis is assumed to coincide with the axis of the robot and with the axis of the pipe, as depicted in Figure 3.2. The y-axis lies on the line between the focal point of the camera and the vertex of the cone of light. The x-axis is perpendicular to both the y and z axes (horizontally in the pipe). The laser module produces a cone of light with an angle of  $\psi$  with respect to the cone's axis. The cone's axis lies in the y-z plane and is aimed at some angle  $\alpha$  off of the z-axis, toward the negative y-axis. The vertex of the cone of light will be placed at some distance  $D$  above the focal point of the camera. The pipe to be measured will be assumed to have a

nominal radius of  $R_0$ . The two rays of laser light which lie in the  $y$ - $z$  plane are to fall on the pipe wall in a plane which is parallel to the  $x$ - $y$  plane and offset a length  $L$  along the positive  $z$  axis. The angles  $\alpha$  and  $\psi$  are to be selected to cause these two rays to project in this fashion.

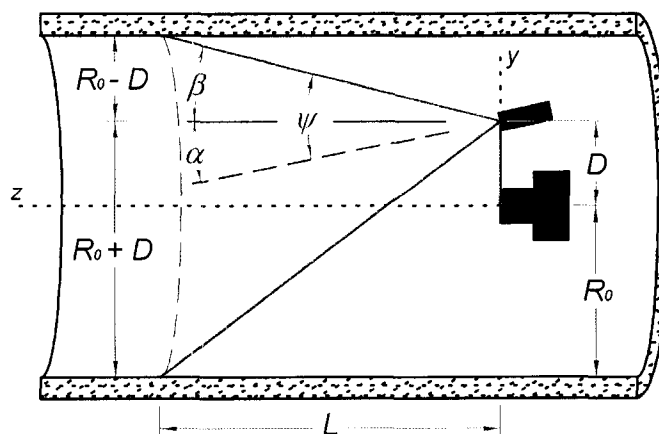


Figure 3.2 — Triangulation Setup.

### 3.2.2 Non-Dimensionalization of Parameters

Non-dimensionalizing the conical triangulation setup allows the results to be extended to any size pipe to any combination of system parameters. First, a dimensionless radius will be defined by equation (3-1).

$$\bar{R} = \frac{R}{R_0} \quad (3-1)$$

This parameter will be called the *radius parameter* and represents the ratio of the measured pipe radius to the expected or nominal radius. Thus, a number greater than one represents a radius greater than expected, or perhaps a cavity in the pipe wall. A number less than one represents a radius smaller than expected, or perhaps an obstruction or collapse.

Next, a dimensionless *baseline parameter* is defined by equation (3-2).

$$\bar{D} = \frac{D}{R_0} \quad (3-2)$$

This parameter represents the ratio of the baseline distance to the nominal pipe radius. Theoretically this value could range from zero (cone vertex at camera focal point) to one (cone vertex at pipe wall). Practically, however, there are issues with allowing the laser unit approach too close to the pipe wall or too close to the camera.

Finally, a dimensionless *projection parameter* is defined by equation (3-3).

$$\bar{L} = \frac{L}{R_0} \quad (3-3)$$

This parameter represents the ratio of the projection length to the nominal pipe radius. This value may range from zero (light ring at the x-y plane) to infinity (light ring infinitely far down the pipe). Practically, however, past a length of several pipe radii, the camera may not be able to zoom to a sufficient level to render a useful picture.

### 3.2.3 Aim and Fan Angle of Laser Module

Expressions for the aim angle  $\alpha$  and fan angle  $\psi$  will be developed as functions of the baseline distance  $D$  and the projection length  $L$ . The tangent of the angle  $\beta$  can be determined as shown in equation (3-4).

$$\tan(\beta) = \frac{R_0 - D}{L} = \frac{R_0}{L} - \frac{D}{L} = \boxed{\frac{1}{\bar{L}} - \frac{\bar{D}}{\bar{L}}} \quad (3-4)$$

Equation (3-4) can be simplified to equation (3-5).

$$\beta = \tan^{-1}\left(\frac{1 - \bar{D}}{\bar{L}}\right) \quad (3-5)$$

Now, the tangent of the angle of the lower ray can be determined by equation (3-6):

$$\tan(2\psi - \beta) = \frac{R_0 + D}{L} = \frac{R_0}{L} + \frac{D}{L} = \boxed{\frac{1}{\bar{L}} + \frac{\bar{D}}{\bar{L}}} \quad (3-6)$$

Therefore, the angle of the lower ray simplifies to equation (3-7).

$$\tan(2\psi - \beta) = \frac{1 + \bar{D}}{\bar{L}} \quad (3-7)$$

The trigonometric identity given in equation (3-8) may be applied to equation (3-7) to yield equation (3-9).

$$\tan(a \pm b) = \frac{\tan(a) \pm \tan(b)}{1 \mp \tan(a)\tan(b)} \quad (3-8)$$

$$\frac{\tan(2\psi) - \tan(\beta)}{1 + \tan(2\psi)\tan(\beta)} = \frac{1 + \bar{D}}{\bar{L}} \quad (3-9)$$

Substituting equation (3-5) into (3-9) and simplifying yields equation (3-10).

$$\tan(2\psi) = \frac{2\bar{L}}{\bar{L}^2 + \bar{D}^2 - 1} \quad (3-10)$$

Taking the inverse tangent and simplifying leads to an equation (3-11).

$$\boxed{\psi = \frac{1}{2} \tan^{-1} \left( \frac{2\bar{L}}{\bar{L}^2 + \bar{D}^2 - 1} \right)} \quad (3-11)$$

Figure 3.3 depicts the relationship between the fan angle  $\psi$  and the projection parameter  $\bar{L}$  for specific values of the baseline parameter  $\bar{D}$ .

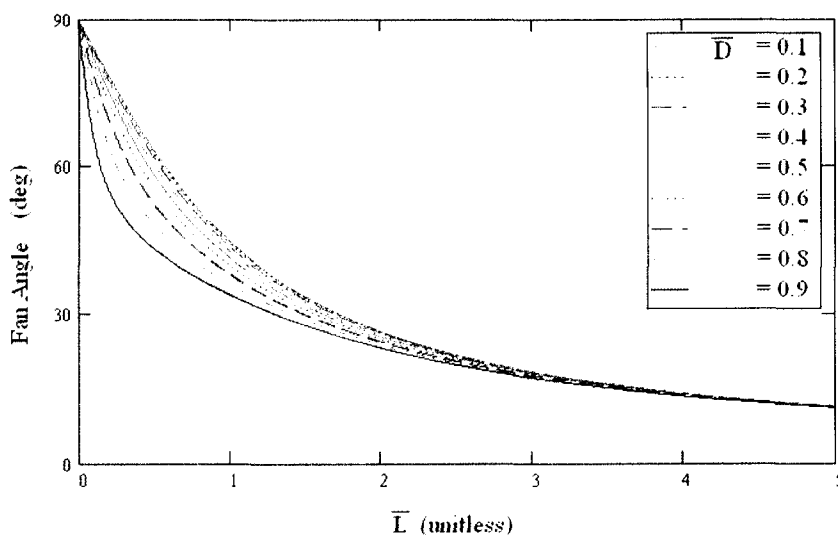


Figure 3.3 — Fan Angle Versus Projection Parameter.

The aim angle  $\alpha$  is simply the difference between the fan angle  $\psi$  and the upper ray angle  $\beta$  as shown in equation (3-13).

$$\alpha = \psi - \beta \quad (3-13)$$

Thus, substitution of equations (3-11) and (3-5) into equation (3-13) yields equation (3-14).

$$\alpha = \frac{1}{2} \tan^{-1} \left( \frac{2\bar{L}}{\bar{L}^2 + \bar{D}^2 - 1} \right) - \tan^{-1} \left( \frac{1 - \bar{D}}{\bar{L}} \right) \quad (3-14)$$

Figure 3.4 depicts the relationship between the aim angle  $\alpha$  and the projection parameter  $\bar{L}$  for specific values of the baseline parameter  $\bar{D}$ .

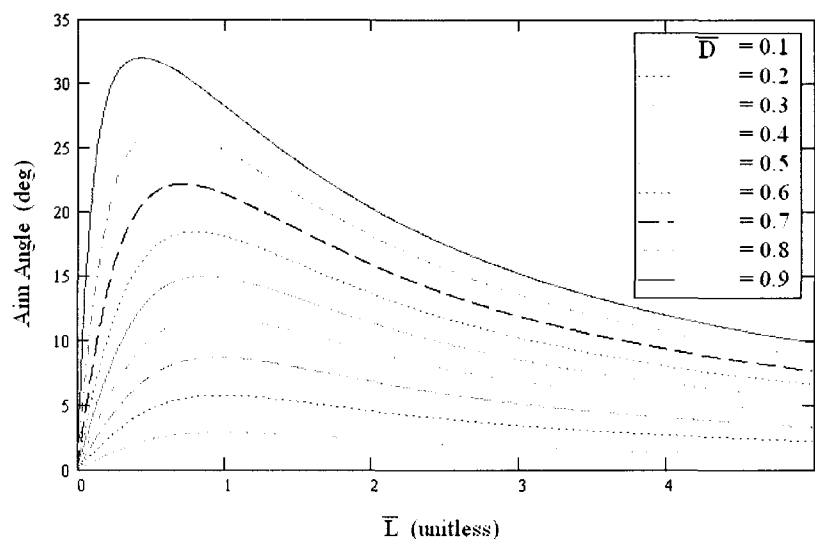


Figure 3.4 — Aim Angle Versus Projection Parameter.

### 3.2.4 Spherical Coordinate Camera Model

Cameras are devices which gather light information from their surroundings and store it in a two-dimensional array. For digital photography, each element in the array is known as a pixel. The array of pixels is typically a rectangular array, yet the light which is gathered is typically gathered based on two angles, representing two of three spherical coordinates, with the origin at the entrance pupil of the camera's lens. These two angles specify the trajectory of a particular ray of light entering the camera, responsible for the illumination of a particular pixel. One of these angles is known as the zenith angle, and is defined as the angle between the center axis of the camera and the ray of light in question. The other angle is known as the azimuth angle. This angle is defined as the angle between a reference plane passing through the center axis of the camera, and another plane which also passes through the center axis of the camera, and contains the ray of light in question. Figure 3.5 shows the zenith and azimuth angles. The center axis of the camera is shown as the z axis, and the reference plane for the azimuth angle is the x-z plane.

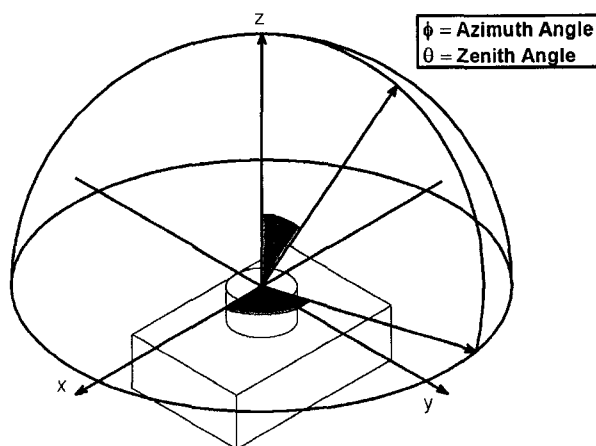


Figure 3.5 — Zenith and Azimuth Angles.

Figure 3.6 shows the loci of three discrete values of zenith angle, as they relate to the camera's surroundings. They are infinite cones (truncated for visualization in Figure 3.6) centered about the central axis of the camera. The larger the solid angle of the cone, the larger the zenith angle.

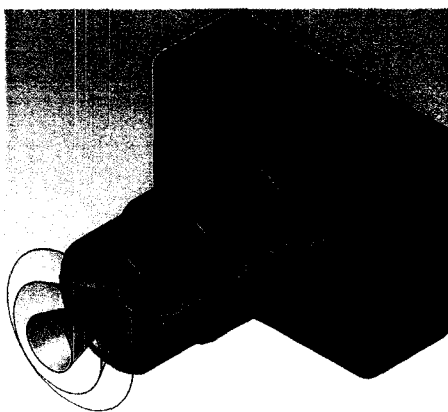


Figure 3.6 — Loci of Constant Zenith Angles.

Figure 3.7 shows a simplified model of how light with discrete zenith angles ( $\theta_1$ ,  $\theta_2$ ,  $\theta_3$ ) refracts through the lens and falls on the camera's light sensor, known as a CCD sensor.

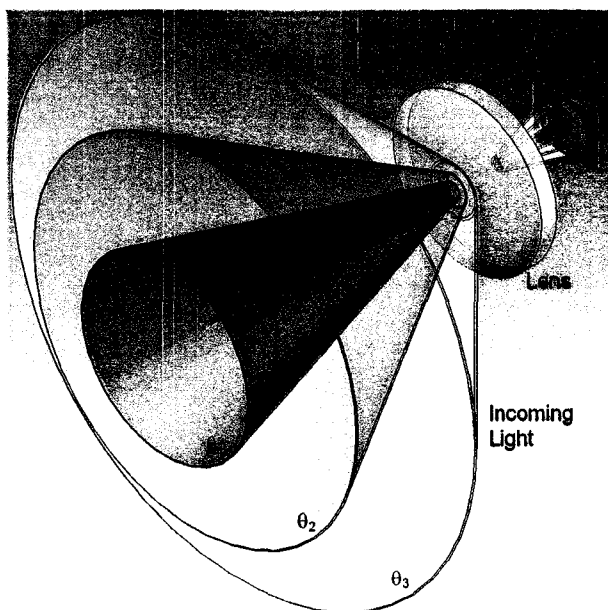


Figure 3.7 — Refraction of Light Through a Lens and onto a CCD Sensor.

Figure 3.8 shows the resulting image on the CCD sensor. The cones shown in Figure 3.7 will show up as circles on the CCD image.

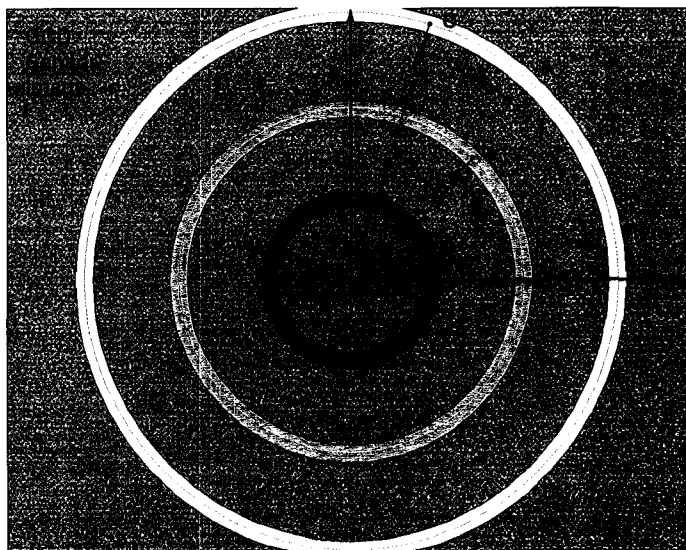


Figure 3.8 — Image of Concentric Cones of Light onto the CCD Image Plane.

The image radii of the circles ( $r_1$ ,  $r_2$ , and  $r_3$  measured in pixels) are related to the zenith angles of their sources through some proportionality relationship. This

relationship takes the form of a function which is dependent on the type of camera and lens being used. For most lenses, this relationship can be described as a function of just the image radius  $r$  as shown in equation (3-15).

$$\theta = f(r) \quad (3-15)$$

The process of determining the nature of this relationship for a particular camera and lens is known as camera calibration.

### 3.2.5 Triangulation Equations

The structure of the laser light is a cone. The basic equation for a conical surface at the origin, with its axis along the z-direction, is given by equation (3-16).

$$x^2 + y^2 = z^2 \cdot \tan^2(\psi) \quad (3-16)$$

To account for the aim angle of the cone and the baseline distance of the vertex of the cone from the camera lens, the cone must be rotated toward the negative y-axis by an angle of  $\alpha$  and translated in the positive y-direction by a distance of  $D$ . The equation of the cone after these transformations is given by equation (3-17).

$$x^2 + [(y - D) \cdot \cos(\alpha) + z \cdot \sin(\alpha)]^2 = [z \cdot \cos(\alpha) - (y - D) \cdot \sin(\alpha)]^2 \cdot \tan^2(\psi) \quad (3-17)$$

Since the entrance pupil of the camera is at the origin and uses spherical coordinates, equation (3-17) must be converted to spherical coordinates. The equations for this conversion are given by equations (3-18), (3-19) and (3-20).

$$x = d \cdot \cos(\phi) \cdot \sin(\theta) \quad (3-18)$$

$$y = d \cdot \sin(\phi) \cdot \sin(\theta) \quad (3-19)$$

$$z = d \cdot \cos(\theta) \quad (3-20)$$

In these equations,  $d$  is the distance from the entrance pupil of the camera (the point typically inside the lens where the light rays converge) to the point where the cone of light strikes the pipe wall. The angle  $\theta$  is the zenith angle of the spherical coordinate system, and the angle  $\phi$  is the azimuth angle of the spherical coordinate system, as shown in Figure 3.9.

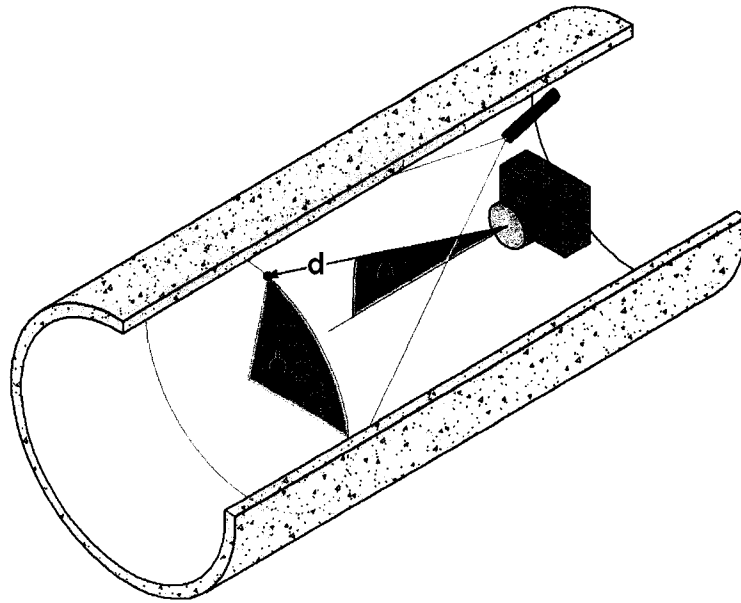


Figure 3.9 — Spherical Coordinates.

Substitution of equations (3-18) through (3-20) into equation (3-17) yields equation (3-21).

$$\begin{aligned} [d \cdot \cos(\phi) \cdot \sin(\theta)]^2 + [(d \cdot \sin(\phi) \cdot \sin(\theta) - D) \cdot \cos(\alpha) + d \cdot \cos(\theta) \cdot \sin(\alpha)]^2 = \\ [d \cdot \cos(\theta) \cdot \cos(\alpha) - (d \cdot \sin(\phi) \cdot \sin(\theta) - D) \cdot \sin(\alpha)]^2 \cdot \tan^2(\psi) \end{aligned} \quad (3-21)$$

Collecting the  $d$  terms in equation (3-21) and simplifying yields equation of the form shown in equation (3-22).

$$A \cdot d^2 + B \cdot d + C = 0 \quad (3-22)$$

Here, the terms A, B, and C are defined in equations (3-23), (3-24) and (3-25).

$$A = \sin^2(\theta) \cdot [\cos^2(\phi) + \sin^2(\phi) \cdot (\sin^2(\alpha) \cdot \tan^2(\psi) + \cos^2(\alpha))] + \cos^2(\theta) \cdot (\sin^2(\alpha) - \cos^2(\alpha) \cdot \tan^2(\psi)) + \frac{\sin(\phi) \cdot \sin(2\theta) \cdot \sin(2\alpha)}{2 \cdot \cos^2(\psi)} \quad (3-23)$$

$$B = -2D \cdot \left[ \sin(\phi) \cdot \sin(\theta) \cdot (\cos^2(\alpha) - \sin^2(\alpha) \cdot \tan^2(\psi)) + \frac{\cos(\theta) \cdot \sin(2\alpha)}{2 \cdot \cos^2(\psi)} \right] \quad (3-24)$$

$$C = D^2 (\cos^2(\alpha) - \sin^2(\alpha) \cdot \tan^2(\psi)) \quad (3-25)$$

Using the quadratic formula, equation (3-22) can be solved for  $d$  as demonstrated in equation (3-26).

$$d = \frac{-B \pm \sqrt{B^2 - 4AC}}{2A}$$

$d =$

$$\frac{D \cdot \left( \sin(\phi) \sin(\theta) (\sin^2(\psi) - \cos^2(\alpha)) - \frac{1}{2} \cos(\theta) \sin(2\alpha) \right)}{\sin^2(\theta) \sin^2(\phi) + \cos^2(\alpha) (\cos(2\theta) + \cos^2(\phi) \sin^2(\theta)) - \frac{1}{2} \sin(2\alpha) \sin(2\theta) \sin(\phi) - \cos^2(\psi)} \pm \frac{D \cdot \cos(\psi) \sqrt{\sin^2(\psi) \cos^2(\phi) + \sin^2(\phi) \cos^2(\theta) - \cos^2(\alpha) \cos^2(\phi) \sin^2(\theta)}}{\sin^2(\theta) \sin^2(\phi) + \cos^2(\alpha) (\cos(2\theta) + \cos^2(\phi) \sin^2(\theta)) - \frac{1}{2} \sin(2\alpha) \sin(2\theta) \sin(\phi) - \cos^2(\psi)} \quad (3-26)$$

This expression quantifies the distance  $d$  from the lens of the camera to a point on the cone of laser light in terms of the trajectory angle of a ray of light entering the camera ( $\theta$  and  $\phi$ ) and the geometrical constraints of the system ( $D$ ,  $\psi$  and  $\alpha$ ). The resulting spherical coordinates of the pipe wall ( $\theta$ ,  $\phi$ ,  $d$ ) can be written in cylindrical coordinates

which are better suited for pipes; the cylindrical coordinates include a radius, an angle, and a distance along the pipe axis. The radius is provided in equation (3-27).

$$R = \sqrt{x^2 + y^2} = \sqrt{(d \cdot \cos(\phi) \cdot \sin(\theta))^2 + (d \cdot \sin(\phi) \cdot \sin(\theta))^2} = d \cdot \sin(\theta) \quad (3-27)$$

Now equation (3-26) can be substituted into (3-27) to yield equation (3-28):

$$R = \frac{D \cdot \sin(\theta) \cdot \left( \sin(\phi) \sin(\theta) (\sin^2(\psi) - \cos^2(\alpha)) - \frac{1}{2} \cos(\theta) \sin(2\alpha) \right)}{\sin^2(\theta) \sin^2(\phi) + \cos^2(\alpha) (\cos(2\theta) + \cos^2(\phi) \sin^2(\theta)) - \frac{1}{2} \sin(2\alpha) \sin(2\theta) \sin(\phi) - \cos^2(\psi)} \pm \frac{D \cdot \sin(\theta) \cdot \cos(\psi) \sqrt{\sin^2(\psi) \cos^2(\phi) + \sin^2(\phi) \cos^2(\theta) - \cos^2(\alpha) \cos^2(\phi) \sin^2(\theta)}}{\sin^2(\theta) \sin^2(\phi) + \cos^2(\alpha) (\cos(2\theta) + \cos^2(\phi) \sin^2(\theta)) - \frac{1}{2} \sin(2\alpha) \sin(2\theta) \sin(\phi) - \cos^2(\psi)} \quad (3-28)$$

The angle needed to specify the desired cylindrical coordinates can simply be taken as the azimuth angle  $\phi$ . To specify the distance of a measured point down the pipe axis from the origin of the coordinate system, the z-coordinate is needed. Calling this distance down the pipe axis  $H$ , equation (3-29) is written:

$$H = z = d \cdot \cos(\theta) = \frac{D \cdot \cos(\theta) \cdot \left( \sin(\phi) \sin(\theta) (\sin^2(\psi) - \cos^2(\alpha)) - \frac{1}{2} \cos(\theta) \sin(2\alpha) \right)}{\sin^2(\theta) \sin^2(\phi) + \cos^2(\alpha) (\cos(2\theta) + \cos^2(\phi) \sin^2(\theta)) - \frac{1}{2} \sin(2\alpha) \sin(2\theta) \sin(\phi) - \cos^2(\psi)} \pm \frac{D \cdot \cos(\theta) \cdot \cos(\psi) \sqrt{\sin^2(\psi) \cos^2(\phi) + \sin^2(\phi) \cos^2(\theta) - \cos^2(\alpha) \cos^2(\phi) \sin^2(\theta)}}{\sin^2(\theta) \sin^2(\phi) + \cos^2(\alpha) (\cos(2\theta) + \cos^2(\phi) \sin^2(\theta)) - \frac{1}{2} \sin(2\alpha) \sin(2\theta) \sin(\phi) - \cos^2(\psi)} \quad (3-29)$$

The three cylindrical coordinates  $(R, \phi, H)$  are essential for generating a complete wireframe model of the pipe.

The primary quantity about which there is concern for accuracy is the radial measurements. Using the definitions established in equations (3-1) and (3-2), the radius defined in equation (3-28) can be non-dimensionalized as equation (3-30).

$$\bar{R} = \frac{\bar{D} \cdot \sin(\theta) \cdot \left( \sin(\phi) \sin(\theta) (\sin^2(\psi) - \cos^2(\alpha)) - \frac{1}{2} \cos(\theta) \sin(2\alpha) \right)}{\sin^2(\theta) \sin^2(\phi) + \cos^2(\alpha) (\cos(2\theta) + \cos^2(\phi) \sin^2(\theta)) - \frac{1}{2} \sin(2\alpha) \sin(2\theta) \sin(\phi) - \cos^2(\psi)}$$

$$\pm \frac{\bar{D} \cdot \sin(\theta) \cdot \cos(\psi) \sqrt{\sin^2(\psi) \cos^2(\phi) + \sin^2(\phi) \cos^2(\theta) - \cos^2(\alpha) \cos^2(\phi) \sin^2(\theta)}}{\sin^2(\theta) \sin^2(\phi) + \cos^2(\alpha) (\cos(2\theta) + \cos^2(\phi) \sin^2(\theta)) - \frac{1}{2} \sin(2\alpha) \sin(2\theta) \sin(\phi) - \cos^2(\psi)}$$

(3-30)

Note that the geometrical constraints are now specified in terms of the dimensionless  $\bar{D}$  parameter, the fan angle  $\psi$ , and the aim angle  $\alpha$ . As long as these values can be determined and the other geometrical constraints listed in the problem are satisfied, these three values can be selected arbitrarily within certain bounds, and the radius can be determined. The bounds must be selected such that:

- the baseline parameter  $\bar{D}$  is between 0 and 1;
- the fan angle  $\psi$  is between 0 and 90°; and
- the absolute value of the aim angle  $\alpha$  is less than the complement of the fan angle.

For the remaining portion of the analysis, the fan angle and the aim angle will be assumed to be driven by the baseline parameter  $\bar{D}$  and the projection parameter  $\bar{L}$ , as described in Section 3.2.3.

### 3.2.6 Inversion Frontiers

There are three mathematical difficulties with the expression given in equation (3-30). First, there is ambiguity as to which of the conjugate solutions yielded by the quadratic formula should be used for which ranges of variables. Second, the denominator has the potential to become zero, resulting in an infinite  $\bar{R}$ . Third, the expression under the radical (the discriminant) will yield complex solutions when negative. Each of these cases has a geometrical interpretation.

The solution represents the point or points where a line (the line representing the trajectory of a ray of light entering the camera) intersects the surface of a cone (representing the cone of laser light). The equation of the cone represents a surface that extends infinitely in both directions (a double cone in the positive and negative  $z$  directions). The case where there are two distinct real solutions represents the scenario where the trajectory line intersects the cone at two locations. The case where the denominator is zero represents the scenario where the line is parallel to the surface of the cone. The case where the discriminant is negative represents the scenario where the line does not intersect the cone at all. It will be useful to define some terms to shorten equation (3-30) and subsequent equations. Equations (3-31), (3-32) and (3-33) will be used to simplify subsequent equations.

$$\text{denominator} = \sin^2(\theta)\sin^2(\phi) + \cos^2(\alpha)(\cos(2\theta) + \cos^2(\phi)\sin^2(\theta)) - \quad (3-31)$$

$$\text{discriminant} = \sin^2(\psi)\cos^2(\phi) + \sin^2(\phi)\cos^2(\theta) - \cos^2(\alpha)\cos^2(\phi)\sin^2(\theta) \quad (3-32)$$

$$\text{discriminant} = \sin^2(\psi)\cos^2(\phi) + \sin^2(\phi)\cos^2(\theta) - \cos^2(\alpha)\cos^2(\phi)\sin^2(\theta) \quad (3-32)$$

$$B^* = \sin(\phi)\sin(\theta)(\sin^2(\psi) - \cos^2(\alpha)) - \frac{1}{2}\cos(\theta)\sin(2\alpha) \quad (3-33)$$

Using these definitions, equation (3-30) can be re-written as equation (3-34).

$$\bar{R} = \bar{D} \cdot \left( \sin(\theta) \cdot \frac{B^* \pm \cos(\psi) \cdot \sqrt{\text{discriminant}}}{\text{denominator}} \right) \quad (3-34)$$

Setting the *denominator* term equal to zero and solving for  $\theta$  will give the locus of the zenith angle where the solution goes infinite. These zenith angles are given by equation (3-35).

$$\theta|_{\text{denominator}=0} = \tan^{-1} \left( \frac{\sin(\psi)}{\cos(\phi)} \cdot \sqrt{\frac{1 - \cos^2(\psi) \cdot \sin^2(\phi) - \cos^2(\phi) \cdot \sin^2(\alpha)}{\cos^4(\alpha) \cdot \cos^2(\phi) - \cos^2(\alpha) \cdot \sin^2(\psi) \cdot \cos(2\phi) - \sin^2(\phi) \cdot \sin^4(\psi)}} \right) \quad (3-35)$$

Similarly, setting the *discriminant* term equal to zero and solving for  $\theta$  will give the locus of the zenith angle where the discriminant changes signs, which will be useful in determining the bounds of the domain where real solutions can be obtained. Equation (3-36) gives a function for zenith angles where the transition occurs.

$$\theta|_{\text{discriminant}=0} = \tan^{-1} \left( \frac{\cos^2(\alpha) - \cos^2(\psi)}{\cos(\psi) \cdot \sqrt{\sin^2(\psi) - \cos^2(\phi) \cdot \sin^2(\alpha)} + \frac{\sin(\phi) \cdot \sin(2\alpha)}{2}} \right) \quad (3-36)$$

Based on the camera model given in section 3.2.4, increasing zenith angles show up as increasing image radii in the resulting CCD image. Azimuth angles in the image directly correspond to the azimuth angle in the world cylindrical coordinates. Consequently, if zenith angles are plotted as radius coordinates and azimuth angles are

used directly as the angle coordinates in a polar plot, the resulting plot will resemble an image obtained by the camera. Equations (3-35) and (3-36) are plotted in Figure 3.10, with values for  $\alpha$  and  $\psi$  chosen using a baseline parameter of 0.5 and a projection parameter of 1.0.

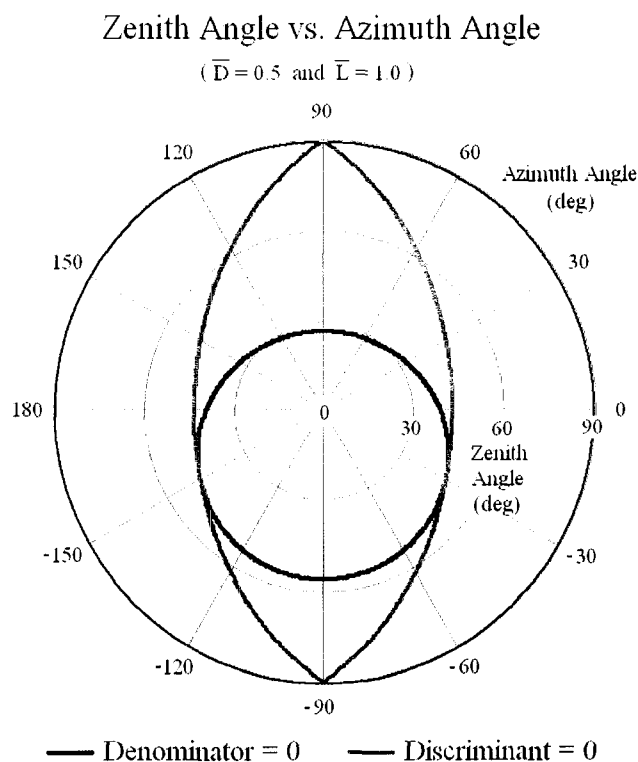


Figure 3.10 — Frontiers of Change.

This gives a good general picture of frontiers where changes (sign changes, infinite pipe radii) are likely to occur in the mathematics of this triangulation scheme. Similar plots could be prepared for other combinations of baseline parameter and projection parameter, and while they would vary slightly, the basic form of the plots would be the same. To identify the nature of each solution given in equation (3-34), both will be plotted in contour plots. Figure 3.11 shows contour plots where regions of complex solutions are shown in purple, negative solutions are shown in blue, and a color

gradient from green to red gives possible solutions. Regions of white are measurements larger than  $\bar{R} = 2$ . The frontiers of change, again in red and blue, are overlaid.

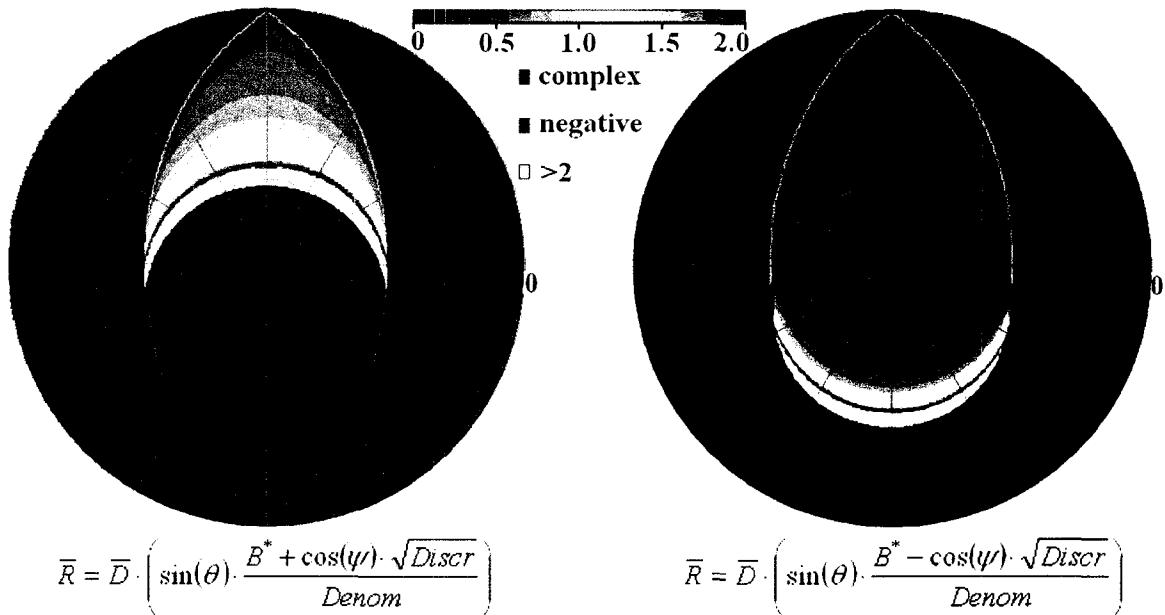


Figure 3.11 — Conjugate Solutions for the Radius Parameter.

Figure 3.11 shows that complex solutions exist outside the envelope of the red line. Below the lower section of the blue line, both solutions are negative (the point being measured actually lies behind the camera). The first solution only provides reasonable values above the upper portion of the blue line; therefore, the only allowable zenith angles for this solution are where  $\theta > \theta|_{denominator=0}$ . The second solution is always valid if  $\theta < \theta|_{denominator=0}$ ; for cases where  $\theta > \theta|_{denominator=0}$ , the solution is only valid above the upper blue line. Essentially these two solutions represent the fact that the camera has to look through the cone of laser light in the upper regions of measurement to see the portion of the laser line that strikes the pipe wall. Mathematically, both of these points of intersection will appear in the solution, and the one corresponding to the closer

intersection of the laser cone with the camera ray must be discarded. The solution seems to make good physical sense if the inversion between the two solutions occurs at the zenith angle that causes the denominator to become zero. Therefore, combining equations (3-34) and (3-35), a piecewise solution that takes into account the frontiers of inversion may be defined in equation (3-37).

$$\bar{R} = \begin{cases} \bar{D} \cdot \left( \sin(\theta) \cdot \frac{B^* + \cos(\psi) \cdot \sqrt{\text{Discriminant}}}{\text{Denominator}} \right) & \text{if } \theta > \theta|_{\text{Denominator}=0} \\ \bar{D} \cdot \left( \sin(\theta) \cdot \frac{B^* - \cos(\psi) \cdot \sqrt{\text{Discriminant}}}{\text{Denominator}} \right) & \text{if } \theta < \theta|_{\text{Denominator}=0} \\ \text{Undefined} & \text{Otherwise} \end{cases} \quad (3-37)$$

This formula was used to generate the contour plot in Figure 3.12, with a baseline parameter of 0.5 and a projection parameter of 1.0. Note once again that the inversion frontiers are overlaid.

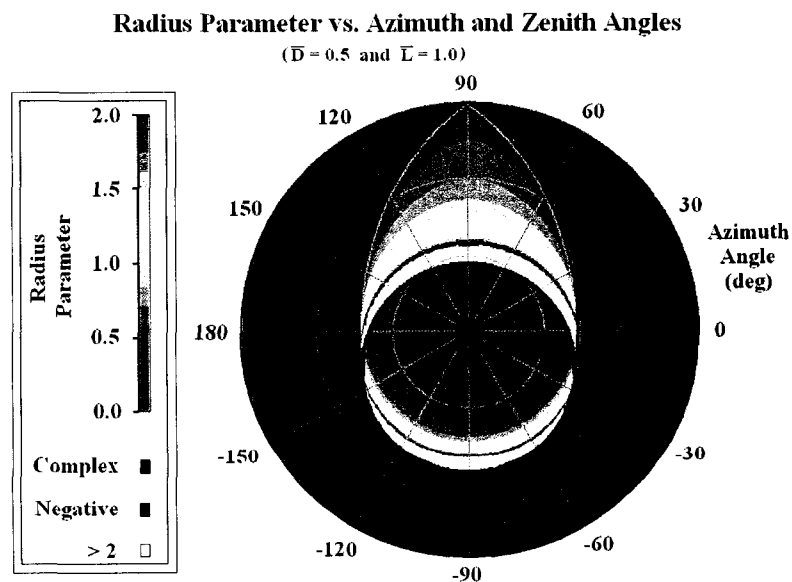


Figure 3.12 — Unified Solution for Radius Parameter.

Table 3.1 demonstrates the changes in the behavior of the scheme with varying geometrical parameters. As before, the baseline parameter and the projection parameter are used to drive the values of aim angle and fan angle.

Table 3.1 — Radius Parameter Measurements.

Projection Parameter $\bar{L}$	Baseline Parameter $\bar{D}$		
	0.25	0.50	0.75
0.50			
0.75			
1.00			
2.00			
5.00			

Color Code:  $\bar{R} = 0$  0.5 1.0 1.5 2.0 complex negative  $>2$

### 3.2.7 Measurement Limits and Camera Field of View

The plots in the previous section show that for any arrangement of the baseline parameter and the projection parameter, there will be areas of potential view of the camera that will not require image capture (there is no point in collecting data from areas of the CCD array that do not contain valid radius measurements). Areas where the solution will be negative or complex do not need to be bounded in the camera's field of view. This is important since camera parameters can be set to limit the field of view, and limiting the field of view to valid solutions maximizes the usage of the available camera resolution. In addition to these considerations, it may be advantageous to truncate the capacity of the system to measure radii outside certain limits; that is, we may want to limit valid solutions if the radius measurements are beyond what is practical for the pipe being measured. By changing the zoom level of the camera, a field of view can be selected that bounds the desired limits of the physical coordinate system. Most cameras produce a rectangular image; therefore, a rectangular region in the contour plots should be chosen. Given these considerations, a method of identifying desirable limits to the camera's field of view will be established.

In the horizontal direction, it is desirable that the edge of the field of view lies on or outside the envelope defined by a zero discriminant. This leads to the beige bounds in Figure 3.13. The lower bound in the vertical direction does not need to include areas which will yield a negative radius parameter. Therefore, it does not need to be below the lower reaches of the frontier where the denominator becomes zero. Thus, the lower bound is set at this point. If the aim of the camera is assumed to be fixed perpendicular to

the baseline  $\bar{D}$  and the camera has an axisymmetric lens and sensor setup, this sets the upper bound automatically by symmetry.

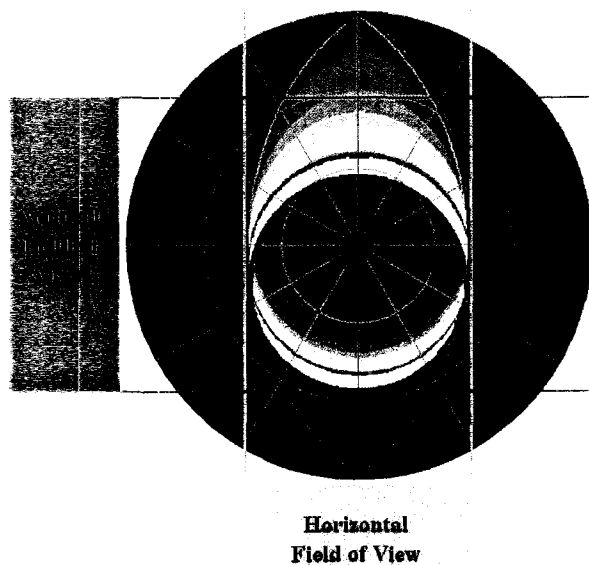


Figure 3.13 — Limits on Field of View.

To check this upper bound for measurement limitations, a geometrical representation of the upper image boundary will be examined. Setting the lower bound as shown in Figure 3.13 implies the condition shown in Figure 3.14 wherein the lower ray of the camera's FOV is parallel with the lower ray of the projected laser cone.

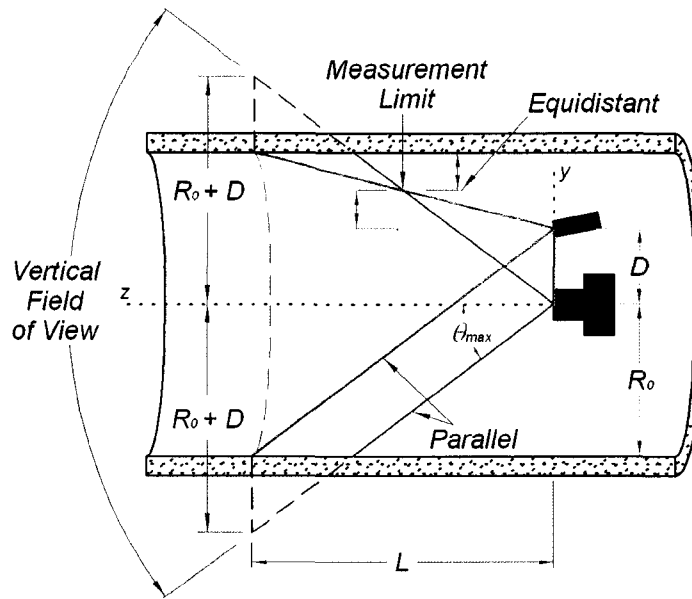


Figure 3.14 — Field of View and Implications.

The rays of the FOV will intersect the nominal measurement plane (the plane perpendicular to the pipe axis a distance  $L$  from the camera) at a distance of  $R_o + D$  from the pipe axis. On the upper ray of the FOV, the measurement limit will occur at its intersection with the laser cone. By simple geometry this can be seen to occur halfway (radially) between the point of projection of the laser cone and the nominal location of the pipe wall. Thus, the minimum radius parameter that the system will be capable of measuring at an azimuth angle of  $90^\circ$  (straight upward) is given by equation (3-37).

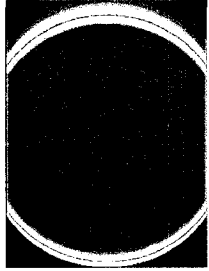
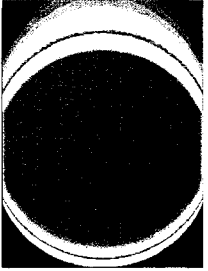
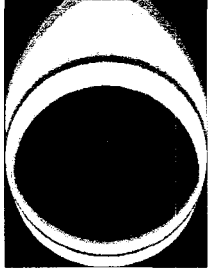
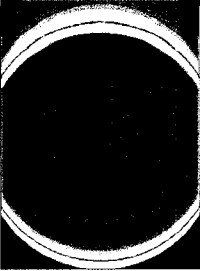
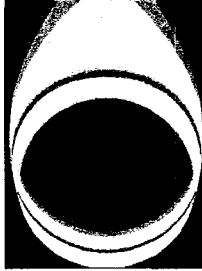
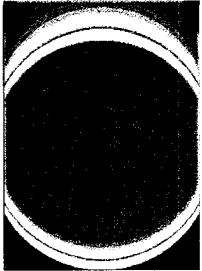
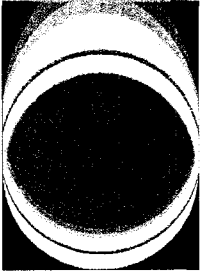
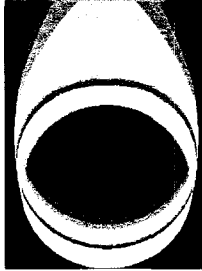
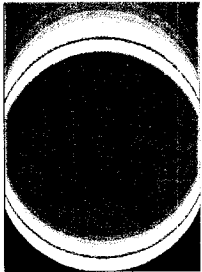
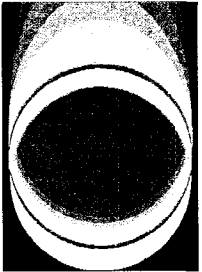
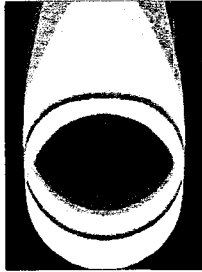
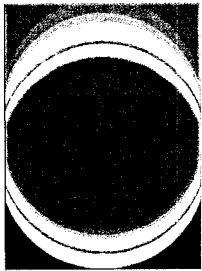
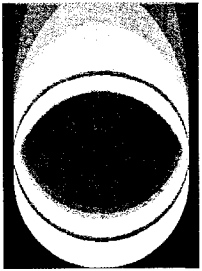
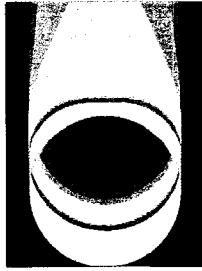
$$\bar{R}_{\min} \Big|_{\phi=\pi/2} = \bar{D} + \frac{1-\bar{D}}{2} = \boxed{\frac{\bar{D}+1}{2}} \quad (3-37)$$

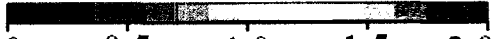
This occurs at a zenith angle given by equation (3-38).

$$\theta_{\max} = \alpha + \psi \quad (3-38)$$

This limit of measurement is not likely to be a serious limitation. The absolute minimum measurement of radius parameter even conceivable at this azimuth angle is  $1 - \bar{D}$ , and this is not practically achievable due to non-negligible physical size of the laser module and its supporting hardware. Table 3.2 presents contour plots of radius parameter truncated to fields of view appropriate to their geometrical arrangements. These plots were prepared assuming a camera with an aspect ratio of 4:3 rather than using the beige bounds of Figure 3.14.

Table 3.2 — Measurements with Limited Field of View.

Projection Parameter $\bar{L}$	Baseline Parameter $\bar{D}$		
	0.25	0.50	0.75
0.50	 ↑ FOV 136° ↓	 ↑ FOV 143° ↓	 ↑ FOV 148° ↓
0.75	 118°	 127°	 134°
1.00	 103°	 113°	 121°
2.00	 64°	 74°	 82°
5.00	 28°	 33°	 39°


■ complex negative
□ >2

Color Code:  $\bar{R} = 0$    0.5   1.0   1.5   2.0

### 3.3 Uncertainty Analysis

Uncertainty in an indirect measurement system (one which involves a calculation based on other measurements) can be evaluated using the formula given by (3-39).

$$U[M(x_1, x_2, \dots, x_n)] = \sqrt{\left(\frac{\partial M}{\partial x_1} \cdot U[x_1]\right)^2 + \left(\frac{\partial M}{\partial x_2} \cdot U[x_2]\right)^2 + \dots + \left(\frac{\partial M}{\partial x_n} \cdot U[x_n]\right)^2} \quad (3-39)$$

In this equation,  $M$  is a measurement calculated as a function of  $n$  variables and  $U[ ]$  denotes uncertainty of the quantity in the brackets. Note that the formula for the radius parameter is a function of five variables: zenith angle ( $\theta$ ), azimuth angle ( $\phi$ ), baseline parameter ( $\bar{D}$ ), aim angle ( $\alpha$ ), and fan angle ( $\psi$ ). Following the uncertainty evaluation formula in equation (3-39), the uncertainty of the measurement can be expressed in equation (3-40).

$$U[\bar{R}] = \left[ \left( \frac{\partial \bar{R}}{\partial \theta} \cdot U[\theta] \right)^2 + \left( \frac{\partial \bar{R}}{\partial \phi} \cdot U[\phi] \right)^2 + \left( \frac{\partial \bar{R}}{\partial \bar{D}} \cdot U[\bar{D}] \right)^2 + \left( \frac{\partial \bar{R}}{\partial \alpha} \cdot U[\alpha] \right)^2 + \left( \frac{\partial \bar{R}}{\partial \psi} \cdot U[\psi] \right)^2 \right]^{\frac{1}{2}} \quad (3-40)$$

The partial derivatives in equation (3-40) will be taken, and reasonable values of the uncertainties in the variables will be identified.

#### 3.3.1 Evaluation of Partial Derivatives

The partial derivatives of equation (3-36) will now be taken. Since this function is not continuous at its inversion frontier, it will not be differentiable at those points. Thus, the derivatives must be defined in a piecewise fashion similar to equation (3-36). Since the derivatives turn out the same for both pieces of the function except for differences in signs at certain points, those points will be identified with  $\pm$  symbols. This

means a sum is to be used for the first piece (where  $\theta > \theta|_{\text{denominator}=0}$ ), and a difference is to be used for the second piece (where  $\theta < \theta|_{\text{denominator}=0}$ ). The derivative of the radius parameter with respect to zenith angle is given by equation (3-41).

$$\frac{\partial \bar{R}}{\partial \theta} = \bar{D} \cdot \left[ \frac{B^* \pm \cos(\psi) \cdot \sqrt{\text{discriminant}}}{\text{denominator}} \cdot \cos(\theta) + \frac{\sin(\theta)}{2} \cdot \left( \frac{2 \cdot \sin(\phi) \cdot \cos(\theta) \cdot (\cos^2(\alpha) - \sin^2(\psi)) - \sin(\theta) \cdot \sin(2\alpha)}{\text{denominator}} \pm \frac{\cos(\psi) \cdot \sin(2\theta) \cdot (\sin^2(\psi) \cdot \sin^2(\phi) + \cos^2(\alpha) \cdot \cos^2(\phi))}{\text{denominator} \cdot \sqrt{\text{discriminant}}} \right) - \frac{B^* \pm \cos(\psi) \cdot \sqrt{\text{discriminant}}}{\text{denominator}^2} \cdot \sin(\theta) \cdot \left( \sin(2\alpha) \cdot \cos(2\theta) \cdot \sin \phi + \sin(2\theta) \cdot (\cos^2(\alpha) - \sin^2(\alpha) \cdot \sin^2(\phi)) \right) \right] \quad (3-41)$$

The partial derivative of radius parameter with respect to azimuth angle is given by equation (3-42).

$$\begin{aligned}
\frac{\partial \bar{R}}{\partial \phi} = \bar{D} \cdot \sin(\theta) \cdot \left[ \frac{\cos(\phi) \cdot \sin(\theta) \cdot (\cos^2(\alpha) - \sin^2(\psi))}{denominator} \right. \\
\pm \frac{\cos(\psi) \cdot \sin^2(\theta) \cdot \sin(2\phi) \cdot (\cos^2(\alpha) - \sin^2(\psi))}{2 \cdot denominator \cdot \sqrt{discriminant}} \\
\left. - \frac{B^* \pm \cos(\psi) \cdot \sqrt{discriminant}}{denominator^2} \cdot \left( \frac{\sin(2\alpha) \cdot \sin(2\theta) \cdot \cos(\phi)}{2} \right. \right. \\
\left. \left. - \sin^2(\alpha) \cdot \sin^2(\theta) \cdot \sin(2\phi) \right) \right] \quad (3-42)
\end{aligned}$$

The partial derivative of the radius parameter with respect to the baseline parameter is given by equation (3-43).

$$\frac{\partial \bar{R}}{\partial D} = \sin(\theta) \cdot \frac{B^* \pm \cos(\psi) \cdot \sqrt{discriminant}}{denominator} \quad (3-43)$$

The partial derivative of the radius parameter with respect to the aim angle is given by equation (3-44).

$$\begin{aligned}
\frac{\partial \bar{R}}{\partial \alpha} = \bar{D} \cdot \sin(\theta) \cdot & \left[ \frac{\cos(\theta) \cdot \cos(2\alpha) - \sin(\phi) \cdot \sin(\theta) \cdot \sin(2\alpha)}{\text{denominator}} \right. \\
& \pm \frac{\cos(\psi) \cdot \cos^2(\phi) \cdot \sin^2(\theta) \cdot \sin(2\alpha)}{2 \cdot \text{denominator} \cdot \sqrt{\text{discriminant}}} \\
& - \frac{B^* \pm \cos(\psi) \cdot \sqrt{\text{discriminant}}}{\text{denominator}^2} \cdot \left( \sin(2\theta) \cdot \sin(\phi) \cdot \cos(2\alpha) \right. \\
& \left. \left. + \sin(2\alpha) \cdot \left( \cos(2\theta) + \cos^2(\phi) \cdot \sin^2(\theta) \right) \right) \right] \quad (3-44)
\end{aligned}$$

The partial derivative of the radius parameter with respect to the fan angle is given by equation (3-45).

$$\begin{aligned}
\frac{\partial \bar{R}}{\partial \psi} = \bar{D} \cdot \sin(\theta) \cdot & \left[ - \frac{\sin(\phi) \cdot \sin(\theta) \cdot \sin(2\psi) \pm \sin(\psi) \cdot \sqrt{\text{discriminant}}}{\text{denominator}} \right. \\
& \pm \frac{\cos(\psi) \cdot \sin(2\psi) \cdot \left( \cos^2(\phi) + \sin^2(\phi) \cdot \cos^2(\theta) \right)}{2 \cdot \text{denominator} \cdot \sqrt{\text{discriminant}}} \\
& \left. + \frac{B^* \pm \cos(\psi) \cdot \sqrt{\text{discriminant}}}{\text{denominator}^2} \cdot \sin(2\psi) \right] \quad (3-45)
\end{aligned}$$

Each partial derivative quantifies the weight that a given parameter's uncertainty will have on the overall uncertainty in the radius parameter.

The uncertainty in a given parameter is a function of many variables and often boils down to the precision to which the laser profiler was fabricated. Thus, the uncertainty of a given parameter will vary from system to system. Although the equations developed can effectively account for any level of uncertainty, particular values that are believed to be reasonable for the fabrication techniques used to construct profilers are assumed to allow for visualization of the “typical” uncertainty that could be expected from a commercial system.

### 3.3.2 Uncertainty in Geometric Parameters

The length measurements used to define the non-dimensional length parameters  $\bar{L}$  and  $\bar{D}$  are assumed to have an uncertainty of  $\pm 0.1\%$  of the nominal pipe radius. This uncertainty corresponds to  $\pm 0.006''$  for a 12'' diameter pipe or  $\pm 0.024''$  for a 48'' diameter pipe. This assumption will allow a prediction to be made as to the accuracy of the measurement system without performing any experiments.

The aim and fan angles are given in terms of baseline and projection parameters in equations (3-11) and (3-14). Once again, these are measured quantities which will be measured indirectly, so equation (3-39) should be applied. The uncertainty in aim angle is given by equation (3-46).

$$U[\alpha] = \sqrt{\left(\frac{\partial \alpha}{\partial \bar{D}} U[\bar{D}]\right)^2 + \left(\frac{\partial \alpha}{\partial \bar{L}} U[\bar{L}]\right)^2} \quad (3-46)$$

The uncertainty in fan angle is given by equation (3-47).

$$U[\psi] = \sqrt{\left(\frac{\partial \psi}{\partial \bar{D}} \cdot U[\bar{D}]\right)^2 + \left(\frac{\partial \psi}{\partial \bar{L}} \cdot U[\bar{L}]\right)^2} \quad (3-47)$$

The values of  $U[\bar{D}]$  and  $U[\bar{L}]$  will be assumed to be 0.001 ( $\pm 0.1\%$ ) based on the discussion in the previous paragraph. So, all that remains is evaluation of the partial derivatives. The partial derivative of the aim angle relative to the baseline parameter is given by equation (3-48).

$$\frac{\partial \alpha}{\partial \bar{D}} = \frac{\bar{L} \cdot (1 + \bar{L}^2 + \bar{D}^2)}{(\bar{L}^2 + \bar{D}^2 - 2 \cdot \bar{D} + 1) \cdot (\bar{L}^2 + \bar{D}^2 + 2 \cdot \bar{D} + 1)} \quad (3-48)$$

The partial derivative of aim angle relative to projection parameter is given by equation (3-49).

$$\frac{\partial \alpha}{\partial \bar{L}} = \frac{\bar{D} \cdot (1 - \bar{L}^2 - \bar{D}^2)}{(\bar{L}^2 + \bar{D}^2 - 2 \cdot \bar{D} + 1) \cdot (\bar{L}^2 + \bar{D}^2 + 2 \cdot \bar{D} + 1)} \quad (3-49)$$

The partial derivative of the fan angle relative to baseline parameter is given by equation (3-50).

$$\frac{\partial \psi}{\partial \bar{D}} = \frac{-2 \cdot \bar{L} \cdot \bar{D}}{(\bar{L}^2 + \bar{D}^2 - 2 \cdot \bar{D} + 1) \cdot (\bar{L}^2 + \bar{D}^2 + 2 \cdot \bar{D} + 1)} \quad (3-50)$$

The partial derivative of the fan angle relative to projection parameter is given by equation (3-51).

$$\frac{\partial \psi}{\partial \bar{L}} = \frac{\bar{D}^2 - \bar{L}^2 - 1}{(\bar{L}^2 + \bar{D}^2 - 2 \cdot \bar{D} + 1) \cdot (\bar{L}^2 + \bar{D}^2 + 2 \cdot \bar{D} + 1)} \quad (3-51)$$

Substitution of equations (3-48) and (3-49) into equation (3-46) yields equation (3-52).

$$U[\alpha] = \left[ \left( \frac{\bar{L} \cdot (1 + \bar{L}^2 + \bar{D}^2)}{(\bar{L}^2 + \bar{D}^2 - 2 \cdot \bar{D} + 1) \cdot (\bar{L}^2 + \bar{D}^2 + 2 \cdot \bar{D} + 1)} U[\bar{D}] \right)^2 + \left( \frac{\bar{D} \cdot (1 - \bar{L}^2 - \bar{D}^2)}{(\bar{L}^2 + \bar{D}^2 - 2 \cdot \bar{D} + 1) \cdot (\bar{L}^2 + \bar{D}^2 + 2 \cdot \bar{D} + 1)} U[\bar{L}] \right)^2 \right]^{\frac{1}{2}} \quad (3-52)$$

Using the assumption that  $U[\bar{D}]$  and  $U[\bar{L}]$  are 0.001, the graph shown in Figure 3.15 depicting the estimated uncertainty in aim angle was prepared.

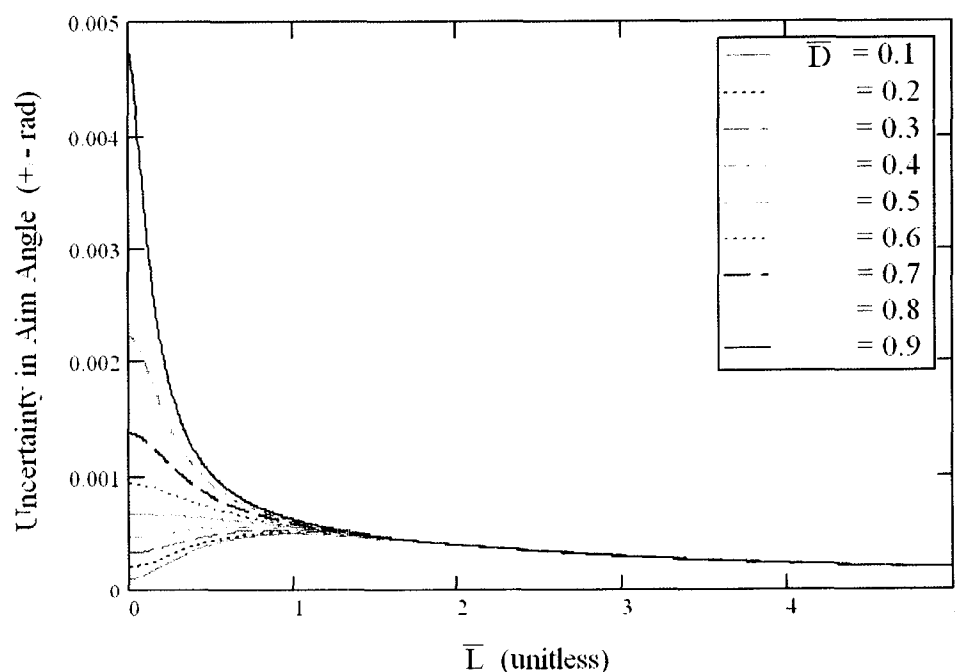


Figure 3.15 — Estimated Uncertainty in Aim Angle.

Substitution of equations (3-50) and (3-51) into equation (3-47) yields equation (3-53).

$$U[\psi] = \left[ \left( \frac{-2 \cdot \bar{L} \cdot \bar{D}}{(\bar{L}^2 + \bar{D}^2 - 2 \cdot \bar{D} + 1) \cdot (\bar{L}^2 + \bar{D}^2 + 2 \cdot \bar{D} + 1)} \cdot U[\bar{D}] \right)^2 + \left( \frac{\bar{D}^2 - \bar{L}^2 - 1}{(\bar{L}^2 + \bar{D}^2 - 2 \cdot \bar{D} + 1) \cdot (\bar{L}^2 + \bar{D}^2 + 2 \cdot \bar{D} + 1)} \cdot U[\bar{L}] \right)^2 \right]^{\frac{1}{2}} \quad (3-53)$$

This equation may be used to produce the graph in Figure 3.16.

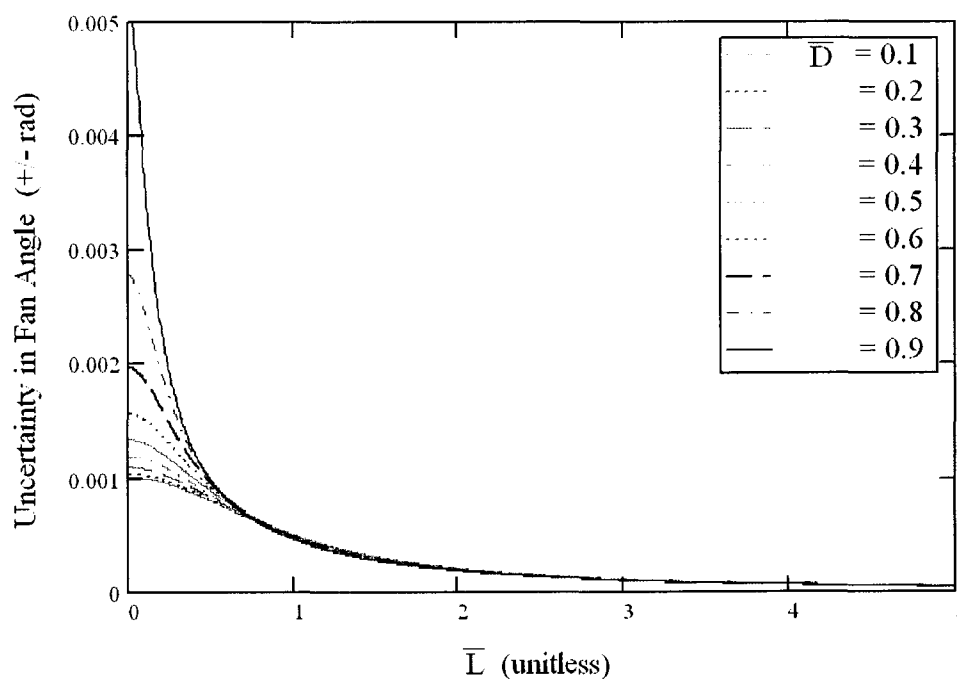


Figure 3.16 — Estimated Uncertainty in Fan Angle.

The expressions developed here for uncertainty in aim and fan angle will be substituted into equation (3-40) to estimate the overall uncertainty that can be expected for this measurement system.

### 3.3.3 Uncertainty in Camera Parameters

One of the most important drivers of the total uncertainty in a laser triangulation measurement system is the uncertainty of the location of the peak of the Gaussian profile of the laser line. Work has already been performed regarding these uncertainties as discussed in Chapter two, and it has been determined that the uncertainty in the fractional pixel number can be given by equation (3-54).

$$U[p/a] = \sqrt{\frac{\lambda^2 f_0^2}{2\pi\phi^2 a^2}} \quad (3-54)$$

In this equation,  $\lambda$  is the wavelength of the projected light,  $f_0$  is the focal length of the camera,  $\phi$  is the diameter of the lens, and  $a$  is the size of a pixel. The cameras which will be used in later analysis have CCD sensors with a size of 1/3" and have 1024 pixels along this length. Therefore, the size of each pixel is approximately  $3.255 \times 10^{-4}$ ". The wavelength of the laser modules which will be used is 650nm. For the measurement systems discussed in this work, a large depth of field is needed to keep the laser line in focus over all the measurement range in question. To achieve an adequate measurement range, a lens with a large f-number is needed. Since f-numbers are most commonly set at powers of  $\sqrt{2}$ , only these values will be considered. As f-numbers increase, less light can be collected by the camera due to a shrinking aperture; therefore, the f-number cannot increase without bounds. One of the largest useful f-numbers for image sensors (before too little light is let through the aperture) is an f-number of 32. For the sake of the analyses in this work, an f-number of 32 will be assumed; thus, equation (3-55) may be stated.

$$\frac{f_0}{\phi} = 32 \quad \Rightarrow \quad \frac{f_0^2}{\phi^2} = 1024 \quad (3-55)$$

Taking all these parameters into equation (3-54), the pixel location uncertainty may be estimated as  $\pm 1.0036$  pixels. For simplicity, the uncertainty in the location of the laser line will be taken as one pixel in any direction.

As stated in Section 3.2.4, the value of the zenith angle associated with a particular pixel is related to that pixel's radius from the center of the image. Equation (3-15) is left very general so as to allow for different kinds of axisymmetric lenses. For the purpose of estimating uncertainty, a linear relationship will be assumed, according to the Equidistant Camera Model. The relationship may be stated by equation (3-56):

$$\theta = \frac{FOV}{n} \cdot r \quad (3-56)$$

where  $FOV$  represents the field of view of the camera in a particular direction (measured in radians),  $n$  represents the number of pixels that exist in the image along that direction, and  $r$  represents the radius (in pixels) of the pixel in question from the center of the image. Again utilizing equation (3-39), the uncertainty of zenith angle can be stated in terms of pixel identification uncertainty  $U[r]$  as shown in equation (3-57)

$$U[\theta] = \frac{FOV}{n} \cdot U[r] \quad (3-57)$$

The direction for FOV is chosen along the long dimension of the image, in which case the value of FOV is given by equation (3-58).

$$FOV = 2 \cdot \theta_{\max} \quad (3-58)$$

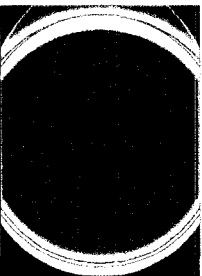
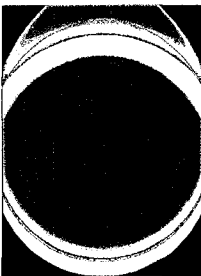
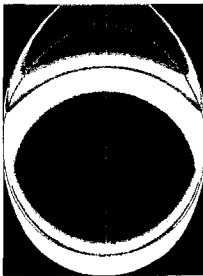
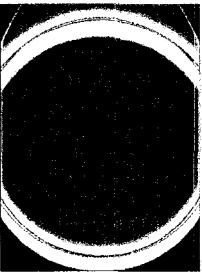
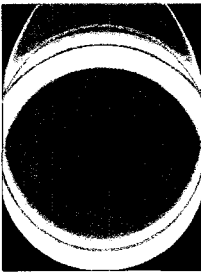
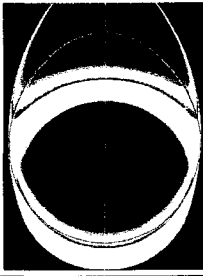
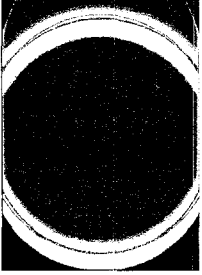
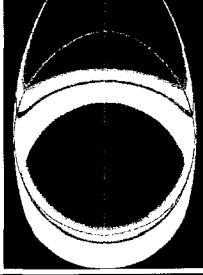
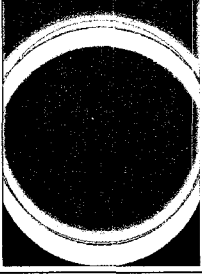
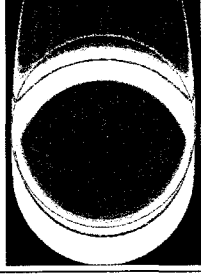
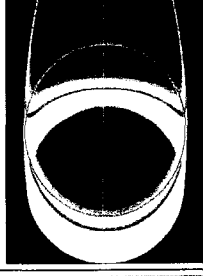
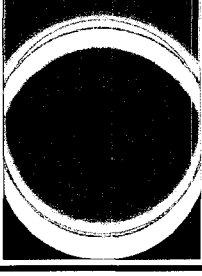
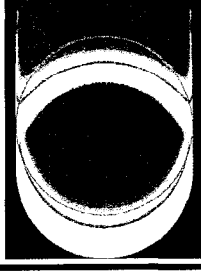
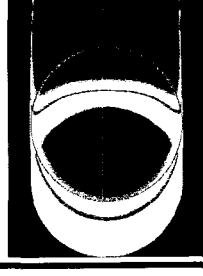
where  $\theta_{\max}$  is given in equation (3-38). The uncertainty in azimuth angle (in radians) can be approximated by the pixel identification uncertainty divided by the radius of that pixel from the center of the image, as shown in equation (3-59).

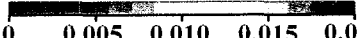
$$U[\phi] = \frac{U[r]}{r} \quad (3-59)$$

### 3.3.4 Overall Uncertainty

All parameters needed to specify uncertainty have now been addressed. Substitution of the appropriate equations into equation (3-40) will yield an expression for uncertainty. Contour plots describing uncertainty in terms of a typical image frame are given in Table 3.3. The thin gray line overlaid on the contour plots represents the location in the image which represents a radius parameter of unity, or the expected value of radius parameter.

Table 3.3 — Uncertainty in Radius Parameter.

Projection Parameter $\bar{L}$	Baseline Parameter $\bar{D}$		
	0.25	0.50	0.75
0.50			
0.75			
1.00			
2.00			
5.00			

Color  
Code:  $U[\bar{R}] =$   0 0.005 0.010 0.015 0.020 complex negative > 0.020  $\bar{R} = 1$

Assuming the camera remains centered in the pipe, and the measurements do not deviate significantly from the nominal radius of the pipe, the values of uncertainty along these gray lines are the expected values of uncertainty for the measurement system with the given geometrical parameters. Practically, these assumptions are rather dubious, but will nevertheless be useful in demonstrating the general uncertainty profile around the domain of possible azimuth angles for a set of expected measurements from a theoretical image. Figure 3.17 shows a plot of expected uncertainty versus azimuth angle for a baseline parameter  $\bar{D}$  of 0.5 and a projection parameter  $\bar{L}$  of 1.0.

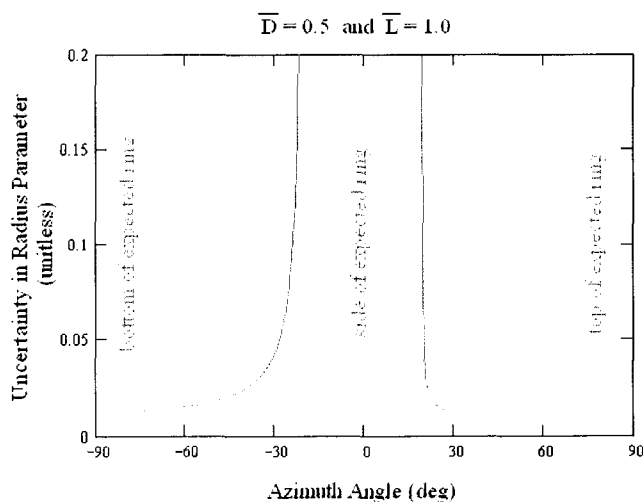


Figure 3.17 — Expected Uncertainty Profile.

It is quickly noted that the uncertainty in this measurement system becomes infinite near the sides of the expected measurement ring. Practically this means that it is impossible to use this method without modification to achieve complete profiles of pipes.

### 3.3.5 Modification to Method

A simple method of modification to this method of laser triangulation is necessary so as to achieve a scheme in which a profile of the entire circumference of the pipe can be

attained. Simply adding another laser module to the system offset by  $90^\circ$  around the axis of the pipe could theoretically accomplish this goal. The areas along one projected laser line which yield results with high uncertainty would be discarded, and the measurements from the other laser line with lower uncertainties would be used. Figure 3.18 shows a front view of such a system.

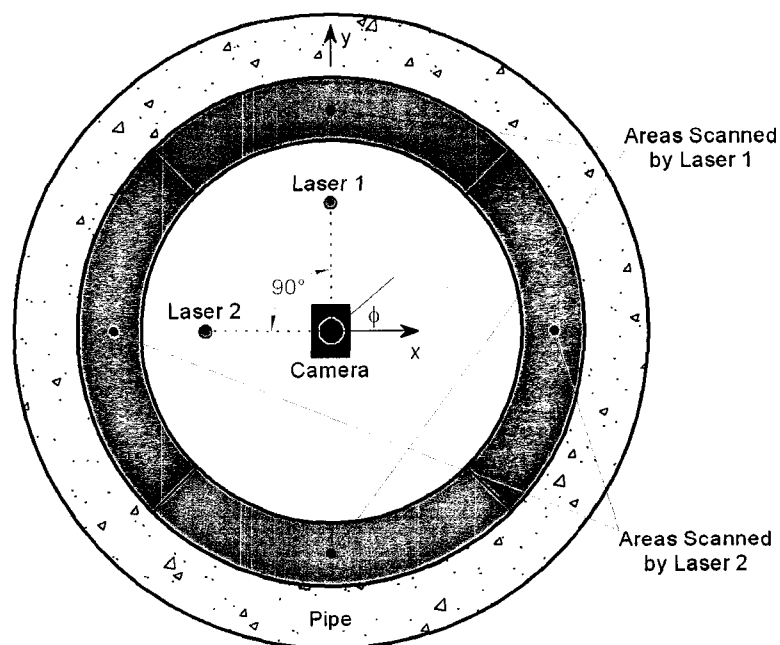


Figure 3.18 — Two-Laser Conical System.

The composite uncertainty profile (neglecting possible effects of asymmetric camera aspect ratios) for a system like this would be constructed of two profiles like the one shown in Figure 3.17, where the best case is always selected. Figure 3.19 shows this composite profile.

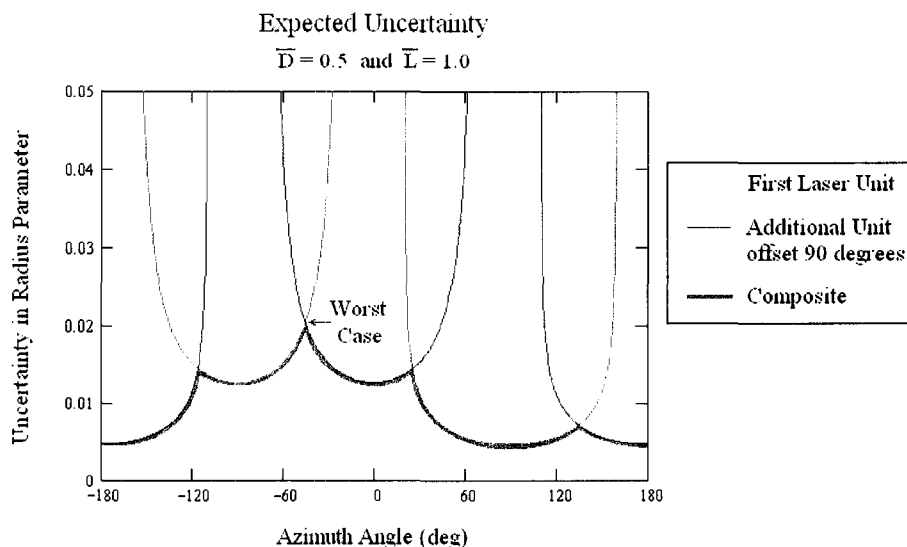


Figure 3.19 — Composite Uncertainty Profile.

For the composite uncertainty profile, the worst uncertainty is seen at an azimuth angle of -45 degrees. This point where the zenith angle is set at the value that causes the radius parameter to be unity, and the azimuth angle is set at the value that causes the most uncertainty in the system will be used as the basis by which the system will be optimized. It should be kept in mind that without the second laser unit, the uncertainty would be unbounded on certain parts of the measurement ring. The second laser unit may pose problems in image processing.

### 3.4 Design Process

Until this point in the analysis, the geometrical parameters which define the specific arrangement of the system have not been fixed. Certain values have been adopted at various points throughout the analysis for illustrative purposes but not for prescriptive purposes. Now the attempt will be made to identify values of these parameters which yield the most desirable measurement system.

To identify the nature of the relationship between the geometrical parameters and uncertainty, Figures 3.20 and 3.21 were prepared using the formulas derived in Section 3.3 and its subsections.

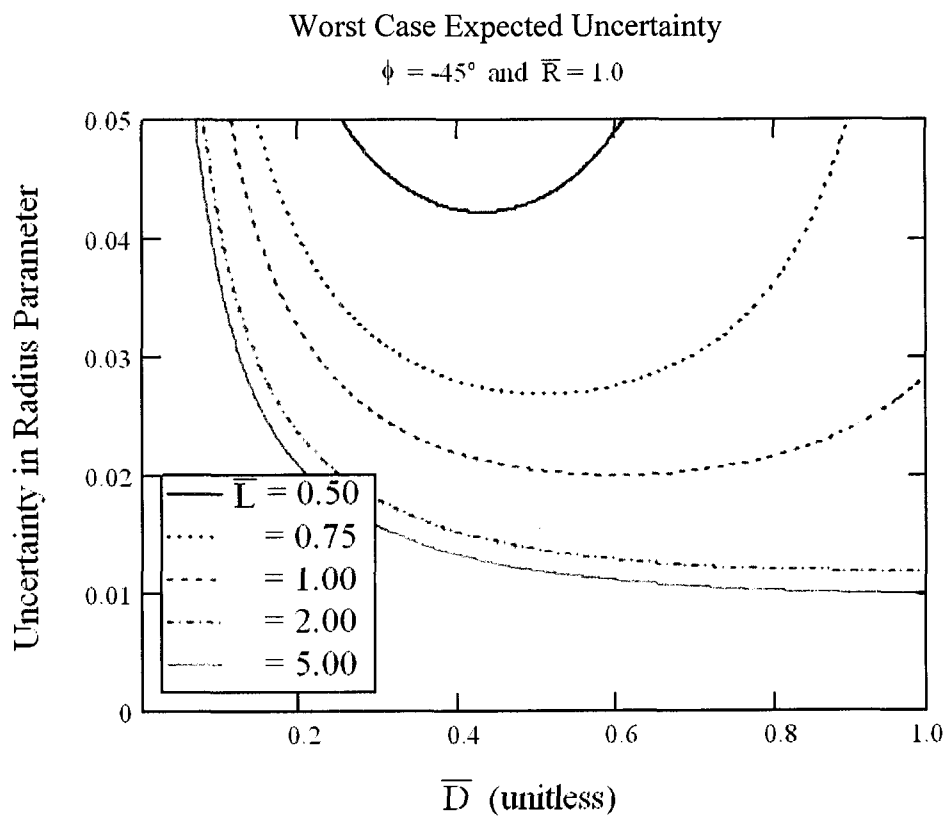


Figure 3.20 — Uncertainty Versus Baseline Parameter for Dual Laser System.

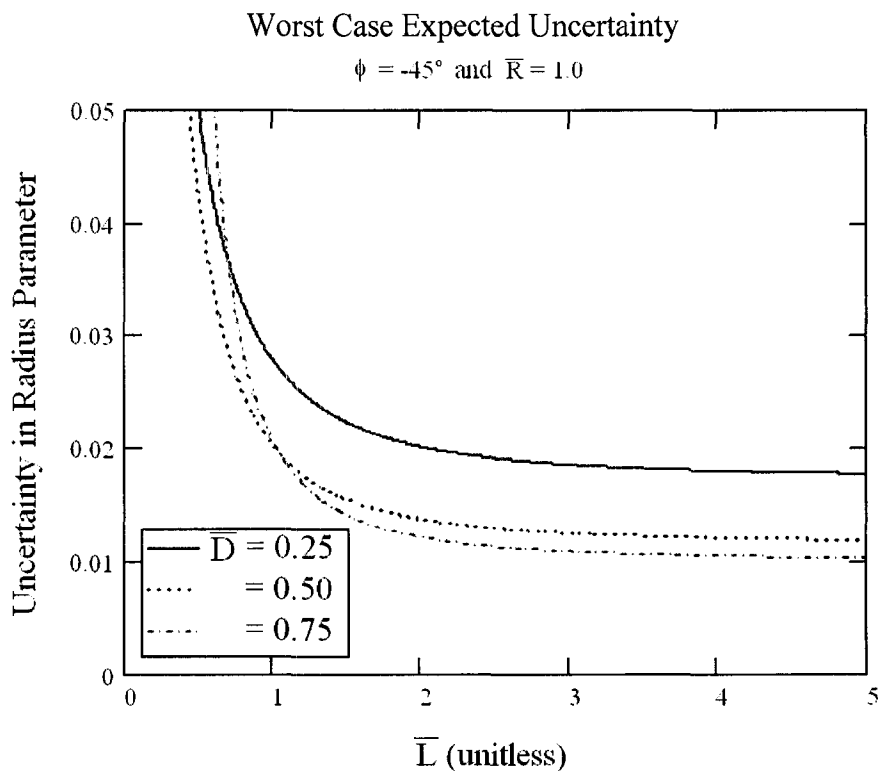


Figure 3.21 — Uncertainty Versus Projection Parameter.

It is quickly seen that the expected accuracy of this measurement system improves as the projection parameter increases. However, the rate at which accuracy improves decreases as the projection parameter increases. When the projection parameter is set at about two (about one pipe diameter) or higher, the same effect is seen for accuracy versus baseline parameter. Larger baseline parameters produce better accuracies. However, as the projection parameter decreases, increasing the baseline parameter beyond a certain point causes the accuracy of the system to degrade.

### 3.4.1 Projection Parameter

For the projection parameter, the larger the selected value, the narrower the fan angle will be. As the fan angle becomes narrower, it tends to make successive measurements based on slices of light which are increasingly nearer to parallel with the

pipe wall. Several problems then arise which are not covered in the mathematics of this problem as posed.

- The system becomes very sensitive to misalignments of the robot in the pipe
- The zoom level of the camera becomes very high (larger lenses necessary)
- Occlusion of smaller features beyond larger ones becomes a greater problem

As a result of these characteristics of large projection parameters, the design strategy is to select a projection parameter which is large enough to eliminate a significant majority of uncertainty in the measurement system, but no larger. From Figure 3.21, it is clear that a projection parameter of at least 2.0 is needed to avoid the high uncertainties associated with low projection parameters. Likewise, projection parameters greater than 2.0 begin to make the conical profiling setup impractical. Consequently, a projection parameter of 2.0 is adopted as a desirable system configuration to minimize uncertainty, and a projection parameter of 2.0 is utilized for the remainder of this chapter.

### **3.4.2 Baseline Parameter**

As the selected value of baseline parameter increases, so does the minimum measurable radius parameter at the crown of the pipe (see Section 3.2.7). Furthermore, if the pipe is crushed beyond a certain point, the laser apparatus will collide with the obstruction and hinder the progress of the measurement platform. Thus, a tradeoff must be made between accuracy and measurement range. Here, the value for the baseline parameter will be selected to eliminate a large majority of uncertainty, but not to increase the minimum measurable pipe crown outside desired limits. The graph in Figure 3.22 plots the effects of these competing considerations assist in developing a beneficial profiler design.

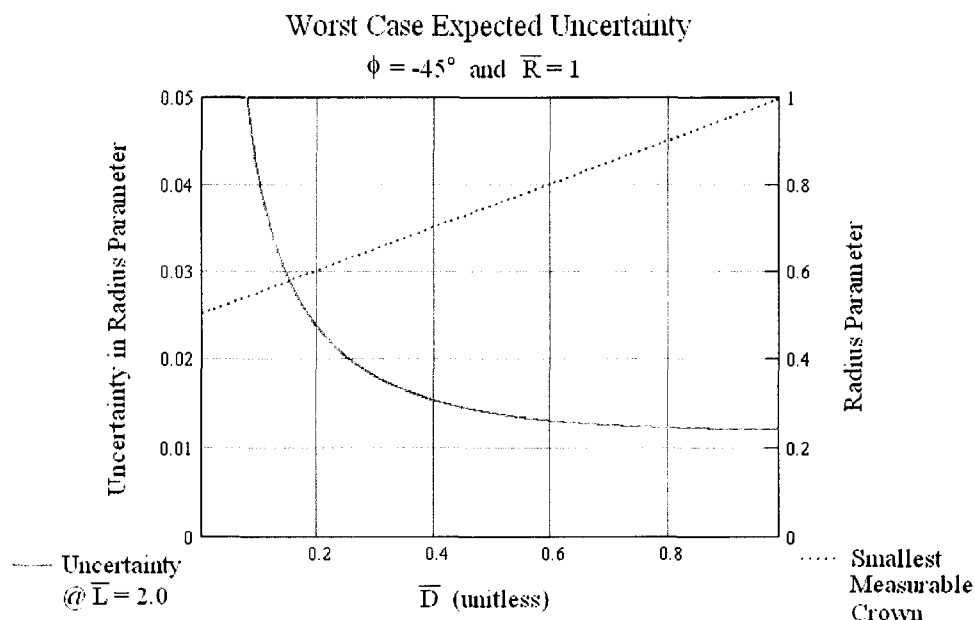


Figure 3.22 — Design Tradeoff.

Looking at the red solid curve, it is fairly intuitive that if the baseline parameter falls below approximately 0.4, the accuracy begins to degrade very quickly. The dotted blue curve, however, shows how the minimum measurable radius parameter at the crown of the pipe gets so large as the baseline parameter increases that very little inward deflection can actually be measured if the baseline parameter is too large. A choice of baseline parameter between 0.4 and 0.6 will allow 20 to 25 percent deflections at the crown to be measured at an uncertainty of approximately 1.3 to 1.5 percent of nominal radius.

### 3.4.3 Resulting System Characteristics

The design process followed thus far assumes measurements will be taken in the vicinity of the nominal pipe radius. Now that the issue of geometrical parameters has been addressed, it will be useful to characterize the resulting measurement uncertainties in terms of the values of the measurements themselves. The plot of Figure 3.23

illustrates how uncertainty in measured radius parameter varies as the value of measured radius parameter along the azimuth angle of  $-45^\circ$  for different values of the baseline parameter.

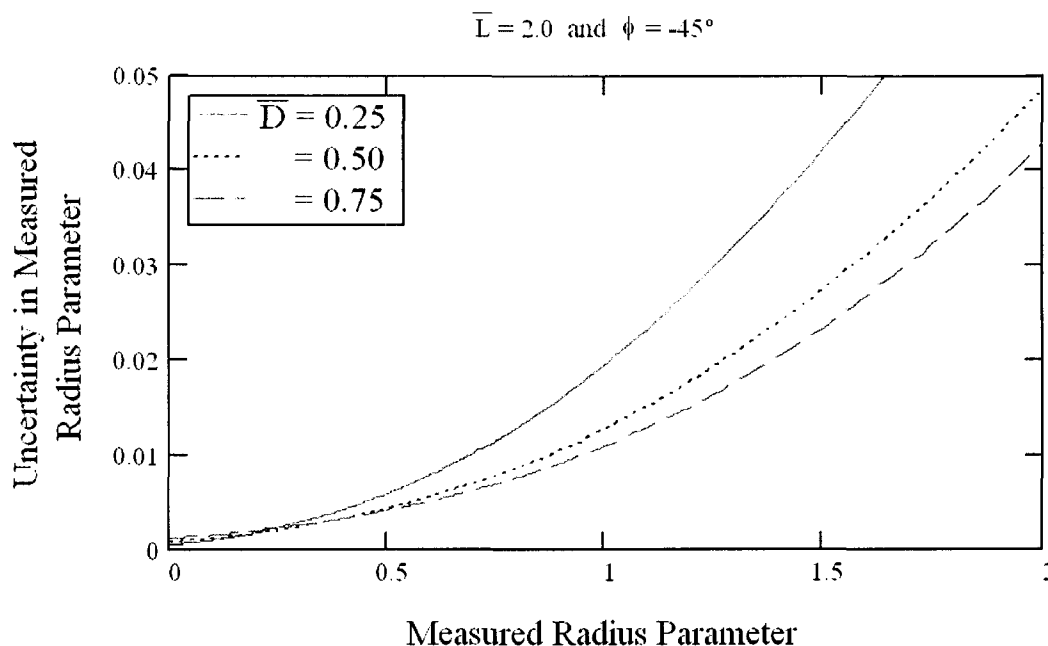


Figure 3.23 — Uncertainty Versus Measurement.

The measurement accuracy tends to degrade quite rapidly as the measurement itself increases. At a baseline parameter of 0.5, the uncertainty has increased to nearly 5% of nominal pipe radius when the measurement is 2.0. Under ideal circumstances, measurements of radius parameter may never reach a value of 2.0; however, given the fact that the mobile system may experience misalignments, this magnitude of radius parameter should still be considered.

The major conclusion of the uncertainty analysis presented above is that the conical triangulation scheme breaks down when only one laser is utilized; however, conical systems can produce reasonably accurate results when two laser units are

employed. However, systems involving two conical lasers have not been developed. Moreover, the addition of the second laser significantly increases the complexity of the hardware and software platforms. Due to these difficulties and the limited accuracy that could be expected from a dual conical system, no results for an actual implementation of the dual conical system are presented in this work; that is, the system has limited promise for practical use when compared to the triangulation configurations presented in later chapters.

### **3.5 Observations**

Before the theoretical work presented here was completed, some preliminary experiments were performed using a single conically projected laser system. The investigation revealed some problems that prompted the analytical treatment presented in this chapter. This section will outline some of the experimental results that led to the discovery that a single conical laser system is not well suited to pipe profiling.

#### **3.5.1 Profiling Apparatus**

Rather than building the apparatus aboard a mobile vehicle with wheels or skids, the apparatus was built on a linear track capable of traversing a length of pipe. This method was used to ensure precise system alignment during the profiling runs. The camera was mounted to a small two axis stage and a small tilt table to allow for precise camera alignment. The laser projector was also mounted to a two-axis stage and a tilt table. Figure 3.24 shows the apparatus as it was constructed.

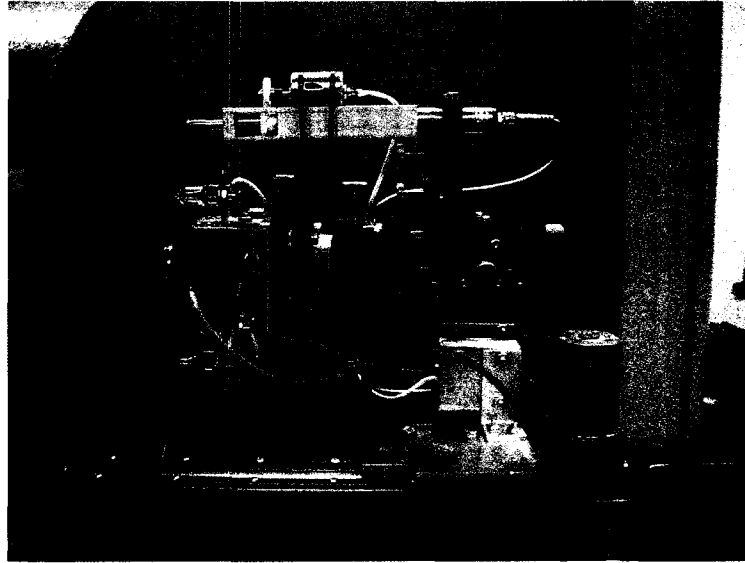


Figure 3.24 — Conical Profiling Apparatus.

The camera used had a resolution of 1024 x 768 and was configured with a fisheye lens. The custom built laser projector utilized a diode laser directed through a tube and reflected from an angled mirror. The tube and angled mirror were supported on precision ball bearings and were spun by a DC electric motor. The fan angle of the laser projector could be adjusted by bending the mirror attachment as needed. The entire process of image collection was automated using LabVIEW.

### 3.5.2 Collected Images

Many images were collected using this system. The characteristics of the images collected provided first clues that the single conical laser system may not have adequate potential for accuracy. Figure 3.25 shows one of the images collected (the discontinuity in the laser liner at the invert is caused by the laser line striking the linear track).

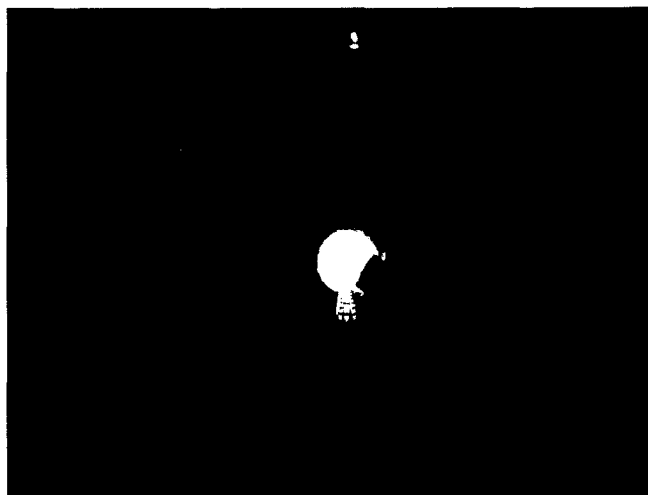


Figure 3.25 — Image Collected Over Track.

The pipe being profiled here is a 12" pipe, and the height of the track is about 0.8". This is about a 7% deflection, and should register fairly significantly in the image. Figure 3.26 shows a close up of the laser line on the right side of the track.



Figure 3.26 — Pixel Detail Over Track.

Note that the center of the laser line is only offset by about 7 pixels between the top of the track and the line on the pipe wall. This means that each pixel here represents about 1% of pipe diameter, or about 0.12".

Although this is not rigorous experimental proof of the inadequacy of this method, it was compelling enough to lead to a decision on the part of the research team that new triangulation configurations should be pursued.

### 3.6 Conclusions

Equations were developed to model the behavior of a conical laser projection scheme for pipe profiling. The model was then analyzed using error propagation techniques to assess its potential for accuracy. In this analysis, certain reasonable values were selected for uncertainties in the parameters used in the measurement computation. Different values could be used, and different results would be seen. The general form and procedure is demonstrated using reasonable but arbitrary values of parameter uncertainty. This analysis indicates that a system that uses a single conical laser has infinite uncertainty along certain azimuth angles and is thus not suited for commercial use. While the results are greatly improved when two conical lasers are employed, the resulting two-laser system would require significantly more complex hardware and software platforms. Moreover, even when a two-laser system is used to fill in the regions of the scan with unbounded uncertainty, the accuracy of the system is still fairly poor. Other triangulation methods are better suited for pipe scanning, as discussed in the following chapters.

CHAPTER 4

ANALYTICAL EVALUATION OF  
TRIANGULATION ACCURACY  
FOR PERPENDICULAR PLANE  
LASER PROFILERS

**4.1 Introduction**

Two of the most popular wastewater pipe profiling instruments commercially available utilize a plane of laser light set perpendicular to the axis of the camera and the axis of the pipe [12,15]. In this configuration, the camera takes images of the resulting ring-shaped laser stripe, and a computer processes the images to make measurements of pipe radius. The manufacturers of these profilers publish system accuracies, but many of the details of how the accuracy figures were obtained are either not specified or specified to a limited degree. A documented analytical method of estimating the accuracy theoretically possible for this family of profilers is needed. This chapter provides such an analytical method based on error propagation theory. Here, certain values of uncertainty in the parameters which define the system are reasonably estimated, and these values are embedded into a Kline-McClintock uncertainty analysis to estimate overall system accuracy.

## 4.2 Derivation of Triangulation Equations

To analytically assess the uncertainty in the perpendicular plane profiling scheme, equations must be derived describing the behavior of the measurement system. A spherical coordinate camera model will be utilized to characterize the geometry of the triangulation scheme. The model developed will incorporate the degree of misalignment of the camera with the laser module. Appropriate zoom levels of the camera will be defined based on the desired measurement ranges and camera-laser spacing. Finally, visualizations of the resulting measurements will be demonstrated using color contour plots.

### 4.2.1 Geometrical Assumptions

A laser module which projects a  $360^\circ$  plane of laser light radially from its axis is placed a distance  $D$  away from the camera along the axis of the camera. The system is intended to measure a pipe with a nominal radius of  $R_0$ . For the purposes of this analysis, the camera axis and the laser point of projection will coincide with the axis of the pipe. The camera will capture images of the laser ring as it illuminates the pipe wall, and the coordinates of the intersection of the laser and the pipe will be stored as spherical world coordinates: the azimuth angle  $\phi$  and the zenith angle  $\theta$ . Note that the initial use of spherical coordinates to describe pipe coordinates follows the approach outlined in Chapter three. A diagram of the triangulation setup is shown in Figure 4.1.

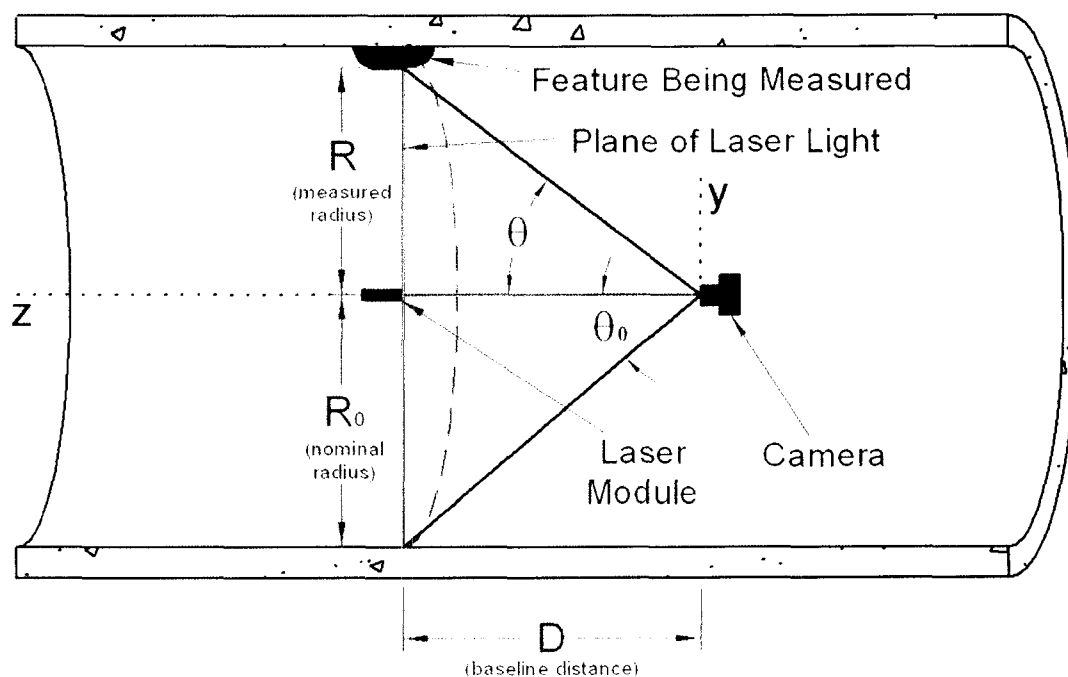


Figure 4.1 — Perpendicular Plane Triangulation Setup.

As demonstrated in Chapter three, the length dimensions of the system will be non-dimensionalized by dividing by the nominal pipe radius. Thus, the baseline parameter will be defined as the ratio of the baseline distance to the nominal pipe radius in equation (4-1).

$$\bar{D} = \frac{D}{R_0} \quad (4-1)$$

The radius parameter will be defined as the ratio of the measured radius to the nominal pipe radius in equation (4-2).

$$\bar{R} = \frac{R}{R_0} \quad (4-2)$$

## 4.2.2 Laser Misalignment

Given the potential for the laser module to be placed quite far from the camera, it may have the potential to become misaligned angularly. Since the error propagation analysis techniques which will be employed require mathematical definition of all sources of uncertainty, this misalignment will be defined as shown in Figure 4.2.

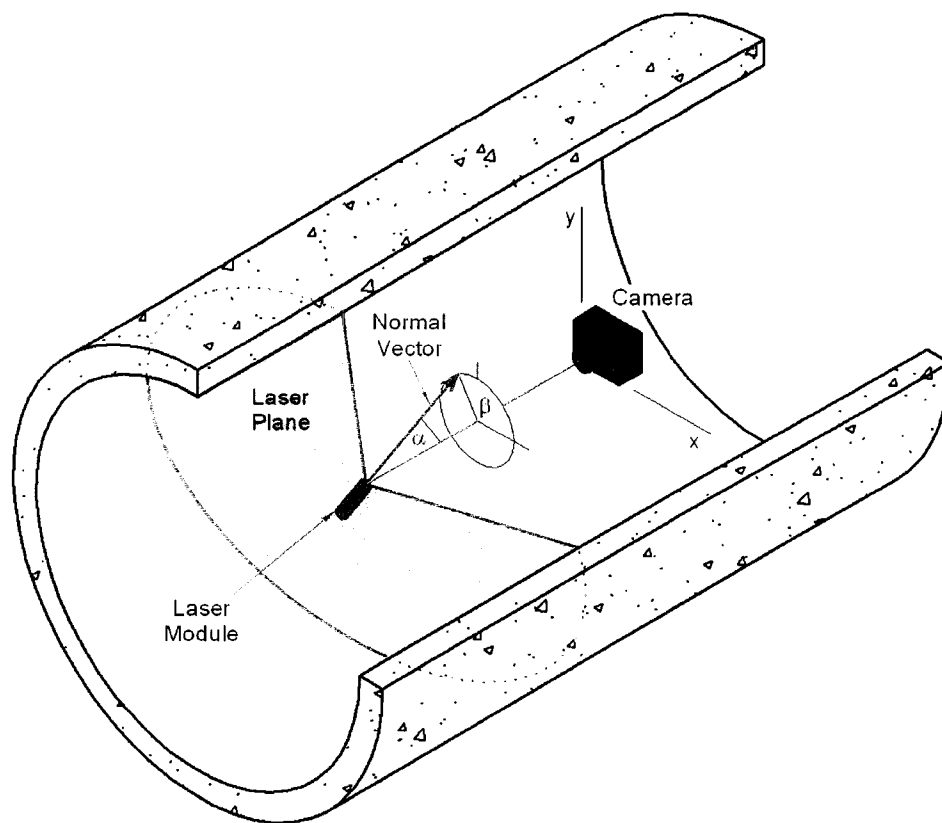


Figure 4.2 — Laser Module Misalignment.

The angle  $\alpha$  shown is the angular deviation of a normal vector of the laser plane from the axis of the camera. This is the quantity that specifies the magnitude of the angular misalignment. The angle  $\beta$  is the angle from the  $x$ - $z$  plane to the plane which contains both the camera axis and the normal vector to the plane of laser light. This is the quantity which specifies the direction of angular misalignment.

### 4.2.3 Triangulation Equations

The equation of a plane parallel to the  $x$ - $y$  plane, and offset by  $D$  units in the positive  $z$  direction is  $z = D$ . Rotation of this plane about the  $y$  axis by an angle of  $\alpha$  yields equation (4-3).

$$z = x \cdot \tan(\alpha) + D \quad (4-3)$$

Rotation of this plane about the  $z$  axis by an angle of  $\beta$  yields equation (4-4).

$$z = [x \cdot \cos(\beta) + y \cdot \sin(\beta)] \cdot \tan(\alpha) + D \quad (4-4)$$

This equation can be related to the spherical camera coordinates by the transformation equations (4-5), (4-6) and (4-7).

$$x = d \cdot \cos(\phi) \cdot \sin(\theta) \quad (4-5)$$

$$y = d \cdot \sin(\phi) \cdot \sin(\theta) \quad (4-6)$$

$$z = d \cdot \cos(\theta) \quad (4-7)$$

In these equations,  $d$  is the straight line distance from the entrance pupil of the camera to the point in question on the laser plane (the upper blue line in Figure 4.1). Substitution of these equations into equation (4-4) yields equation (4-8).

$$d \cdot \cos(\theta) = [d \cdot \cos(\phi) \cdot \sin(\theta) \cdot \cos(\beta) + d \cdot \sin(\phi) \cdot \sin(\theta) \cdot \sin(\beta)] \cdot \tan(\alpha) + D \quad (4-8)$$

Simplification and solution for  $d$  yields equation (4-9).

$$d = \frac{D}{\cos(\theta) - \tan(\alpha) \cdot \sin(\theta) \cdot [\cos(\phi) \cdot \cos(\beta) + \sin(\phi) \cdot \sin(\beta)]} \quad (4-9)$$

The measured radius of this system is simply the distance  $d$  times the sine of the zenith angle, as shown in equation (4-10).

$$R = d \cdot \sin(\theta) = \frac{D \cdot \sin(\theta)}{\cos(\theta) - \tan(\alpha) \cdot \sin(\theta) \cdot [\cos(\phi) \cdot \cos(\beta) + \sin(\phi) \cdot \sin(\beta)]} \quad (4-10)$$

Dividing the left and right sides of this equation by the nominal radius and substituting equations (4-1) and (4-2) into equation (4-10) results in an expression for the radius parameter as shown in equation (4-11).

$$\bar{R} = \frac{\bar{D} \cdot \sin(\theta)}{\cos(\theta) - \tan(\alpha) \cdot \sin(\theta) \cdot [\cos(\phi) \cdot \cos(\beta) + \sin(\phi) \cdot \sin(\beta)]} \quad (4-11)$$

Dividing numerator and denominator by  $\cos(\theta)$ , and applying trigonometric identities yields equation (4-12).

$$\bar{R} = \bar{D} \cdot \tan(\theta) \cdot \left( \frac{1}{1 - \tan(\alpha) \cdot \tan(\theta) \cdot \cos(\phi - \beta)} \right) \quad (4-12)$$

The expression in parentheses on the right of the above equation is of particular interest. Notice that the expression assumes a value of 1 when  $\alpha = 0$ . Therefore, if there is no misalignment of the laser module, the formula for radius parameter reduces to equation (4-13).

$$\bar{R} \Big|_{\text{zero misalignment}} = \bar{D} \cdot \tan(\theta) \quad (4-13)$$

which is a solution which can be verified by inspection of Figure 4.1. The expression  $\cos(\phi - \beta)$  in the denominator varies from one when  $\phi = \beta$  to negative one when  $\phi = \beta \pm 180^\circ$ , and is zero when  $\phi = \beta \pm 90^\circ$ . This expression has interesting properties that relate exclusively to misalignment and will be called the *misalignment factor* and denoted by the variable  $M$  as in equation (4-14).

$$M = \left( \frac{1}{1 - \tan(\alpha) \cdot \tan(\theta) \cdot \cos(\phi - \beta)} \right) \quad (4-14)$$

Therefore, the radius parameter may be expressed as equation (4-15).

$$\bar{R} = \bar{D} \cdot \tan(\theta) \cdot M \quad (4-15)$$

If the profiling instrument includes provisions to track the misalignment of the laser unit, these misalignments may be fed into the measurement scheme through the misalignment factor. Otherwise, the scheme will be required to assume zero misalignment (even if this may not be the case) and suffer greater uncertainty if misalignment does exist.

#### 4.2.4 Measurement Limits and Camera Field of View

It is important to decide on an appropriate field of view for the camera so that its resolution may be advantageously utilized. A large field of view may provide for a more complete range of measurements; however, the measurements will be less accurate. Conversely, a small field of view can provide more accurate measurements, but the measurement range will be reduced.

For pipe profiling, it cannot be guaranteed that the profiling platform will actually remain on the center axis of the pipe. One of the more extreme cases of radial offset

occurs when the entrance pupil of the camera is nearer to the pipe wall than to the center axis. In this case, assuming the pipe is not heavily deformed, the maximum radius parameter which can be measured will be about two (one diameter). It is unlikely that the measurement platform would be offset to this degree; thus, the extra range would act as a buffer for possible outward deformations occurring simultaneously with extreme misalignments. Thus, the outer limit of desired measurements will be set at  $\bar{R}_{\max} = 2$ . This outer limit of measuring capacity can be varied if the user finds that more or less range is needed, but for the sake of the accuracy analysis, this reasonable outer limit will be adopted. A formula for the field of view implied by this assumption is given by equation (4-16).

$$FOV = 2 \cdot \tan^{-1}\left(\frac{\bar{R}_{\max}}{D}\right) = 2 \cdot \tan^{-1}\left(\frac{2}{D}\right) \quad (4-16)$$

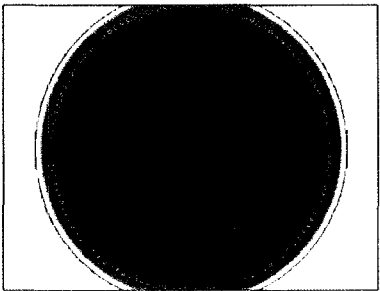
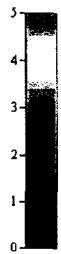
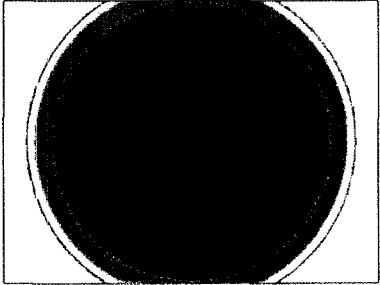
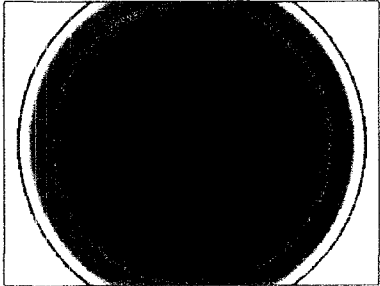
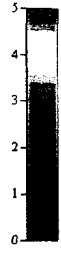
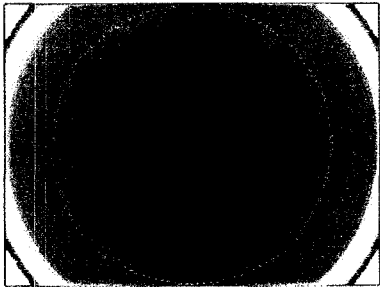
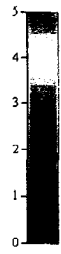
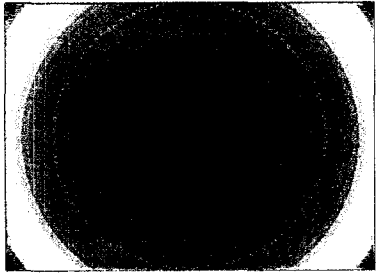
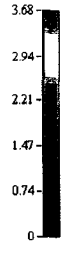
This field of view does not yet have a specified direction. Since the camera will be assumed to have an aspect ratio of 4:3, there will be areas of the picture that measure more range than other areas. It is unknown which direction pipe deformations will occur relative to the camera; thus, to maintain at least an  $\bar{R}_{\max} = 2$  range of measurement in all directions, the field of view given above must be for the shorter image axis; that is, the axis associated with the “3” of the 4:3 aspect ratio.

#### 4.2.5 Visualization of Measurements

The nature of the solution obtained in equation (4-15) will be visualized using polar plots. As in Chapter three, the rectangular coordinates in the polar plots correspond to pixel coordinates in images acquired using this system, while the colors at particular

coordinates describe the radius parameter measurement. Table 4.1 shows several of these plots for varying baseline parameter.

Table 4.1 — Visualization of Measurements.

Baseline Parameter $\bar{D}$	Contours of Radius Parameter In Image Space		
0.50	↑ FOV 152° ↓		
0.75	↑ FOV 139° ↓		
1.00	↑ FOV 127° ↓		
2.00	↑ FOV 90° ↓		
5.00	↑ FOV 44° ↓		
Legend: $\overline{R}=2$ $\overline{R}=1$ $>5$			

### 4.3 Uncertainty Analysis

The method followed in chapter three will be used to estimate the accuracy of the perpendicular plane method of triangulation. The variables which drive the measurement are the zenith and azimuth angles of the camera, the baseline distance, and any angular misalignment of the laser unit. Expressing the uncertainty of the radius parameter measurement in terms of these variables and their uncertainties yields equation (4-17).

$$U[\bar{R}] = \left[ \left( \frac{\partial \bar{R}}{\partial \theta} \cdot U[\theta] \right)^2 + \left( \frac{\partial \bar{R}}{\partial \phi} \cdot U[\phi] \right)^2 + \left( \frac{\partial \bar{R}}{\partial \bar{D}} \cdot U[\bar{D}] \right)^2 + \left( \frac{\partial \bar{R}}{\partial \alpha} \cdot U[\alpha] \right)^2 + \left( \frac{\partial \bar{R}}{\partial \beta} \cdot U[\beta] \right)^2 \right]^{\frac{1}{2}} \quad (4-17)$$

This section is devoted to the development of the various components of this equation.

#### 4.3.1 Evaluation of Partial Derivatives

The most straightforward part of equation (4-17) is the evaluation of the partial derivatives. The partial derivative of the radius parameter with respect to the measured zenith angle is given by equation (4-18).

$$\frac{\partial \bar{R}}{\partial \theta} = \bar{D} \cdot \frac{1}{\cos^2(\theta)} \cdot M^2 \quad (4-18)$$

The partial derivative of the radius parameter with respect to the selected azimuth angle is given by equation (4-19).

$$\frac{\partial \bar{R}}{\partial \phi} = \bar{D} \cdot \sin^2(\theta) \cdot \tan(\alpha) \cdot \sin(\phi - \beta) \cdot M^2 \quad (4-19)$$

The partial derivative of the radius parameter with respect to the baseline parameter is given by equation (4-20).

$$\frac{\partial \bar{R}}{\partial \bar{D}} = \tan(\theta) \cdot M \quad (4-20)$$

The partial derivative of the radius parameter with respect to the laser plane misalignment magnitude angle is given by (4-21).

$$\frac{\partial \bar{R}}{\partial \alpha} = \bar{D} \cdot \frac{\tan^2(\theta) \cdot \cos(\phi - \beta)}{\cos^2(\alpha)} \cdot M^2 \quad (4-21)$$

The partial derivative of the radius parameter with respect to the laser plane misalignment direction angle is given by equation (4-22).

$$\frac{\partial \bar{R}}{\partial \beta} = \bar{D} \cdot \tan^2(\theta) \cdot \tan(\alpha) \cdot \sin(\phi - \beta) \cdot M^2 \quad (4-22)$$

These partial derivatives represent the influence that the uncertainty in a particular variable has on measurement accuracy. The following sections identify reasonable values for uncertainty in particular variables.

### 4.3.2 Uncertainty in Geometrical Parameters

To be consistent in the analysis across the several triangulation schemes considered here, it will again be assumed for accuracy estimation that the length measurements used to define the geometry of the system will have an uncertainty of  $\pm 0.1\%$  of the nominal pipe radius. Thus, the uncertainty in baseline parameter will be estimated as  $\pm 0.001$ .

The misalignment magnitude and direction will be taken as zero since they will be set as close to zero as possible during the setup of the device; also, no method of tracking the misalignment during travel is being considered here. Yet to account for the possibility of unintended misalignments, nonzero uncertainties in the misalignment angles will be considered in later sections.

### 4.3.3 Uncertainty in Camera Parameters

The camera is used in the same fashion for this triangulation scheme as for the conically projected laser scheme. Thus, the rationale behind the uncertainty estimations given in Chapter three apply to this system. The uncertainty in the zenith angle is a function of the field of view, the camera resolution, and the estimated pixel uncertainty. This is expressed with equation (4-23).

$$U[\theta] = \frac{FOV}{n} \cdot U[r] \quad (4-23)$$

In this equation,  $FOV$  is the field of view of the camera corresponding to the shorter image axis, and  $n$  is the number of pixels along that axis. The azimuth angle uncertainty is a function of the field of view, the zenith angle, the camera resolution, and the pixel uncertainty. This is given by:

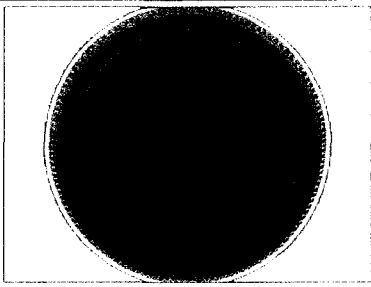
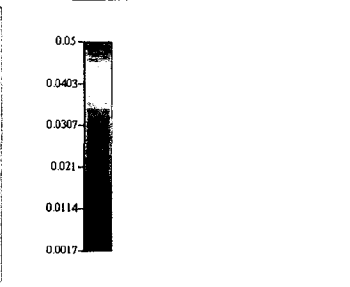
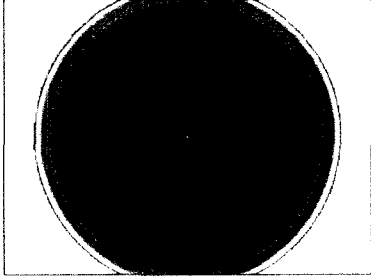
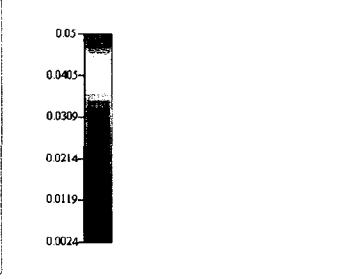
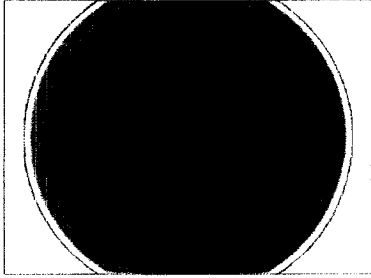
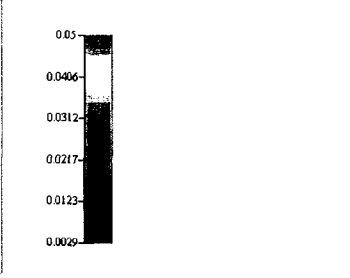
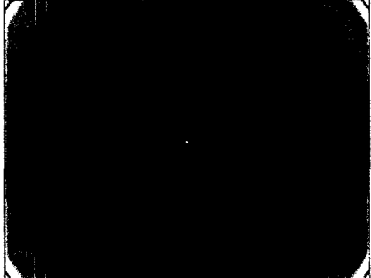
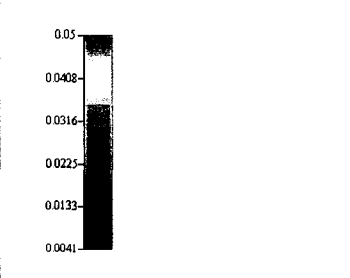
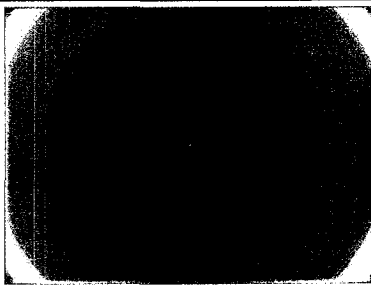
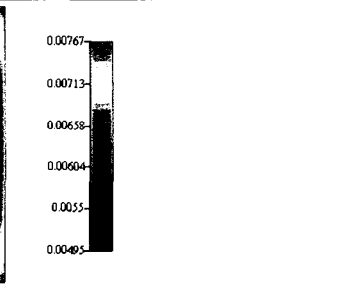
$$U[\phi] = \frac{FOV}{n \cdot \theta} \cdot U[r] \quad (4-24)$$

All angle measurements are specified in radians. For the same reasons given in Chapter three, for estimation purposes, the pixel uncertainty will be taken as one, and the camera resolution across the shorter axis will be taken as 768.

#### 4.3.4 Overall Uncertainty Visualization

Now that all the terms in equation (4-17) have been addressed, plots may be constructed describing measurement uncertainty versus location in the collected image. Table 4.2 shows contour plots similar to those of Table 4.1 with the exception that they describe uncertainty rather than the measurement itself. The solid and dotted lines overlaid in the contour plots represent the location in the images where radius parameter assumes the value of one and two, respectively. Carefully note the differences in scales on the individual contour plots provided in Table 4.2.

Table 4.2 — Uncertainty Visualization.

Baseline Parameter $\bar{D}$	Contours of Uncertainty in Radius Parameter In Image Space	
0.50		
0.75		
1.00		
2.00		
5.00		
Legend: $\bar{R} = 2$ $\bar{R} = 1$ $> 0.05$		

It is quickly observed that uncertainty seems to decrease as baseline parameter lengthens. However, other considerations also need to be evaluated when designing a profiling system for use in pipes. In any case, the images presented above demonstrate that the uncertainties in the measurements are axisymmetric about the center of the image. This being the case, it is no longer necessary to consider a range of values for azimuth angle, and it is possible to focus on how accuracy changes relative to radial location in the image.

#### 4.3.5 Overall Uncertainty Versus Measurement

The measurements of pipe radius parameter increase as the radial location in the image increases, as demonstrated in the figures of Table 4.1. To facilitate the understanding of the nature of this measurement system, the information regarding the radius parameter measurements and the uncertainties of those measurements can be synthesized into one descriptive chart. Figure 4.3 shows uncertainty in the radius parameter measurements versus the measurements themselves.

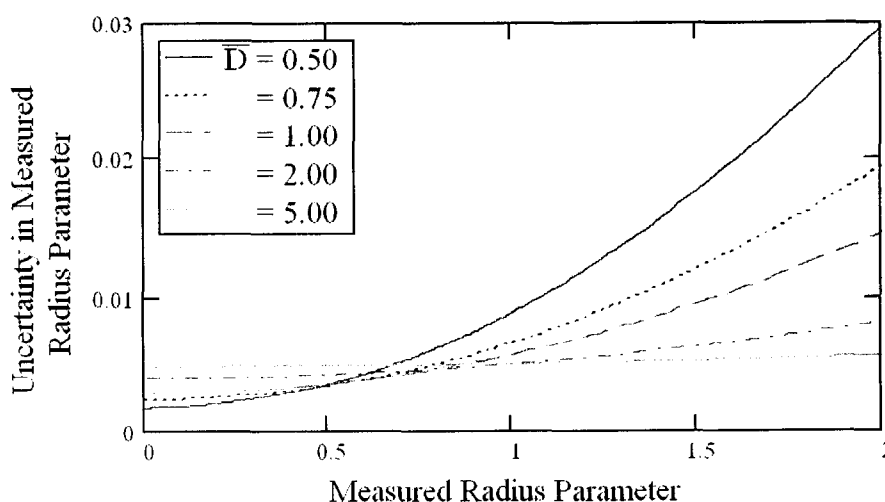


Figure 4.3 — Uncertainty Versus Measurement.

As baseline parameter increases, it seems that the uncertainty in the measurements becomes nearer to constant regardless of the value of the radial measurement. The uncertainty also seems to decrease with increasing baseline parameter in the vicinity of expected measurements ( $\bar{R} = 1$ ). These are both desirable effects, so a significant motivation should exist to increase the baseline parameter as far as possible without causing excessive undesirable effects from other design considerations.

#### 4.3.6 Effects of Angular Misalignment

The laser module has the potential to become misaligned during usage of the laser profiler. The impact of misalignment on measurement accuracy is investigated through equation (4-17) by setting the radius parameter  $\bar{R}$  equal to one, neglecting measurement uncertainty due to azimuth angle  $\phi$  and angle  $\beta$ , examining set values for the baseline distance  $\bar{D}$ , and allowing uncertainty in misalignment by varying misalignment angle  $\alpha$ . Figure 4.4 plots the uncertainty of the profiling system at expected measurement values ( $\bar{R} = 1$ ) versus the angle of misalignment.

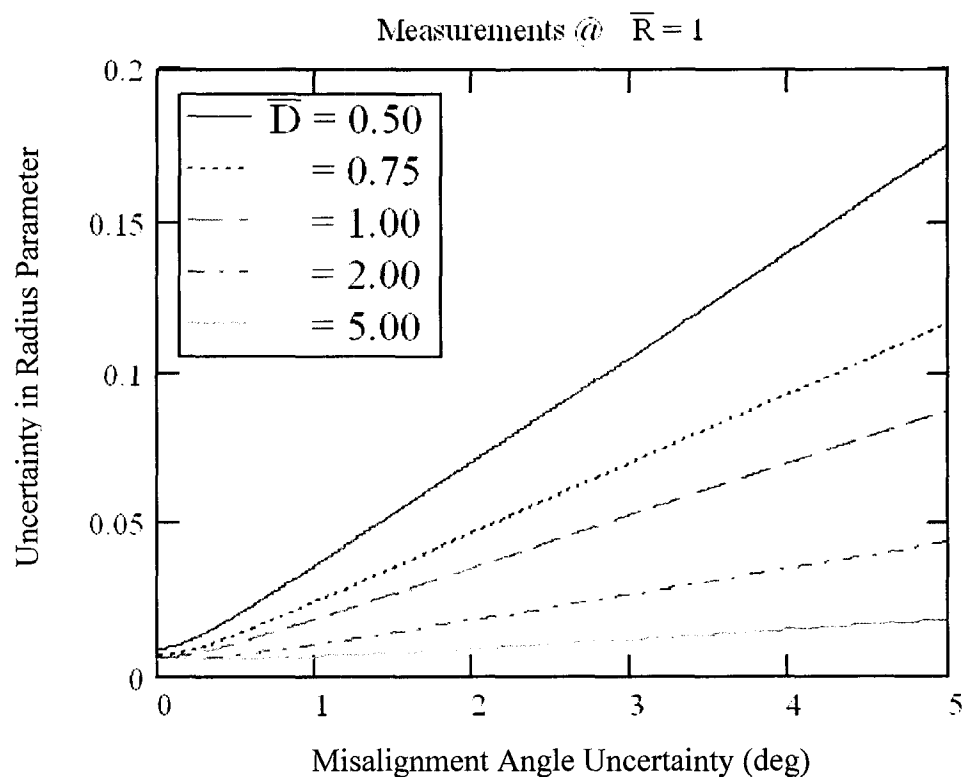


Figure 4.4 — Uncertainty Versus Misalignment.

Note that an increase in uncertainty in angular misalignment can lead to very large increases in radius parameter uncertainty for smaller values of baseline parameter. Larger values of baseline parameter, however, are much less affected by uncertainties in misalignment. This is further motivation to lengthen the baseline parameter in profiler design, as described in the following section.

#### 4.4 Design Process

The preceding sections have shown that longer baseline parameters can lead to reduced measurement uncertainty. This can be misleading, however, because other effects can begin to surface which lead to a measurement system which has undesirable characteristics. A long baseline tends to make a more unwieldy measurement robot and

can increase the occlusion effects of the system. Occlusion occurs when the laser line is no longer visible to the camera due to features on the pipe wall. Figure 4.5 demonstrates how increasing the baseline parameter can lead to more occlusion difficulties.

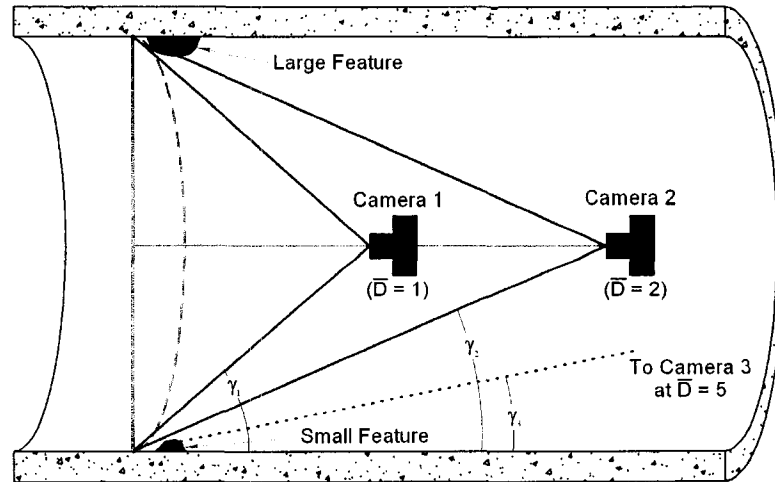


Figure 4.5 — Occlusion Effects.

The large feature shown at the crown of the pipe causes no problem for the first camera located at  $\bar{D} = 1$  but causes a problem for the second camera at  $\bar{D} = 2$ . The small feature shown in the invert of the pipe causes no problem for either the first or second cameras, but the third camera (not shown) at  $\bar{D} = 5$  experiences occlusion problems. The design strategy for this system will attempt to balance system accuracy and occlusion susceptibility.

#### 4.4.1 Occlusion Versus Accuracy

There is a critical angle at the back side of any feature which controls whether or not that feature will cause occlusion and to what degree. It is the angle between the wall of the pipe and a ray extending to the point of view of the camera. The angles  $\gamma$  in Figure 4.5 illustrate this angle. Assuming for design purposes that the host pipe has a radius of

$R_0$  and the measurement system is centered in the pipe, the value of this angle will be given by equation (4-25).

$$\gamma = \tan^{-1}\left(\frac{1}{D}\right) \quad (4-25)$$

Figure 4.6 summarizes the tradeoff between occlusion effects (note the scale on the right hand side of the plot) and system uncertainty (note the scale on the left hand side of the plot) at the expected measurement values.

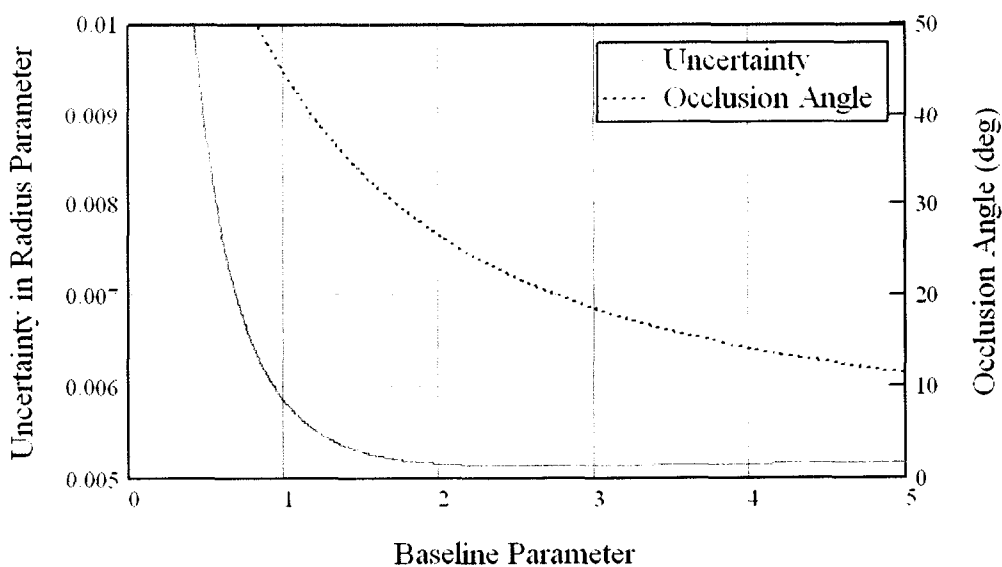


Figure 4.6 — Design Chart for Baseline Parameter.

By selecting a baseline parameter of approximately two (one pipe diameter), the expected uncertainty can be reduced to just slightly more than 0.5% of nominal pipe radius while still allowing an occlusion angle of over 25°. Of course if larger occlusion angles are required for a particular pipe, the baseline can be shortened at the cost of more

uncertainty. Such a configuration may be preferred in pipes with internal corrugations, for example.

#### 4.4.2 Physical Dimensions

Another consideration that is not negligible when evaluating a suitable baseline parameter for a measurement platform is its deployability. Profiling systems are built to be inserted into pipes at manholes. If the overall length of the profiler is too long, it may not actually fit into the pipe via the manhole. Figure 4.7 demonstrates how using a long baseline distance (the extension in front of the robot) can lead to deployment difficulties.

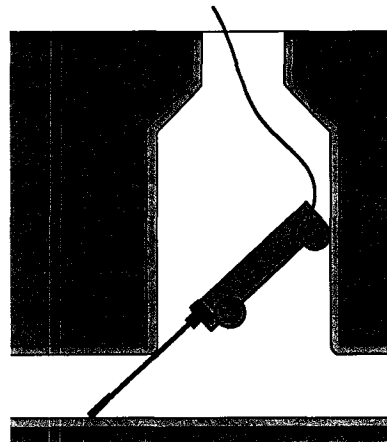


Figure 4.7 — Length Constraint for Deployment.

Of course a hinge of some kind could be fitted between the laser unit and the body of the robot, but this also opens up more potential for uncertainty. Shorter units are clearly more deployable.

#### 4.5 Conclusions

An analytical method to estimate uncertainty in perpendicular plane profiler systems has been presented. The uncertainty in the measurements tends to increase as the measurements themselves increase. Shorter baseline parameters lead to greater

uncertainty, while longer ones tend to make uncertainty more constant across radial measurement magnitudes. Uncertainties in laser plane misalignment can have large effects on measurement uncertainty, but these effects can be reduced if long baseline parameters are utilized. Other considerations such as occlusion and physical dimensions inherent in a long baseline parameter system limit the extent to which the baseline parameter can be lengthened. A baseline parameter of approximately two (the length of one nominal pipe diameter) is estimated to give a good tradeoff between accuracy and the competing effects. Given certain reasonable assumptions, the overall accuracy of perpendicular plane profiler systems near measurements of  $R_0$  is approximately 0.5% of nominal pipe radius.

CHAPTER 5

ANALYTICAL EVALUATION OF  
TRIANGULATION ACCURACY  
FOR SIDE-FACING  
LASER PROFILERS

**5.1 Introduction**

The conically projected laser light configuration and the perpendicular plane laser light configuration are designed with the camera facing down the length of the pipe. The advantage of this camera arrangement lies principally in the fact that the camera does not need to be articulated to capture the full circumference of the pipe wall. One undesirable consequence of this arrangement, however, is that much of the view of the camera becomes devoted to seeing too far down the axis of the pipe. Much of the resolution of the camera is essentially wasted because little desired information is gathered from the pixels toward the center of the image.

If the camera is aimed at the wall of the pipe, perpendicular to its axis, the entire image is useful in characterizing the condition of the pipe. The effective resolution of the images is greater, and more surface detail can be recognized. Of course, to cover the entire circumference of the pipe wall, an indexing mechanism must move the camera through a full 360° angular range, likely reducing the speed of the pipe inspection. The

possible inspection quality improvements, however, seem to make this method worthy of investigation. This chapter derives the equations required to determine pipe coordinates using side facing triangulation configurations and analyzes the uncertainty associated with system parameters.

## 5.2 Derivation of Triangulation Equations

The equations describing the behavior of a side-facing camera and laser setup will be derived based on the spherical coordinates described in Chapter three. Equations describing both non-dimensionalized radius parameter and axial location are derived. Appropriate limits of camera field of view and measurement range are identified and applied to the models. Visualizations of the measurements are then plotted versus the image coordinates to demonstrate the behavior of the system.

### 5.2.1 Geometrical Assumptions

The laser module in this arrangement is assumed to project a perfect plane of light, which will be called the laser sheet. This laser sheet will define the  $y$ - $z$  plane for the coordinate system of the measurement system as shown in Figure 5.1. The laser sheet is approximately parallel to the axis of the pipe. The axis which passes through the entrance pupil of the camera's lens and falls on the center of the image sensor will be called the axis of the camera. The plane which contains the axis of the camera and is perpendicular to the laser sheet will define the  $x$ - $y$  plane. The  $x$ - $y$  plane will be approximately perpendicular to the pipe axis. The focal point of the camera's lens is placed at a known perpendicular distance from the laser sheet; this distance is called the baseline distance and is denoted as  $D$ . The plane that is perpendicular to both the  $y$ - $z$  plane and the  $x$ - $y$  plane and contains the focal point of the camera will define the  $x$ - $z$

plane. The camera is assumed to have a planar, rectangular image sensor which is perpendicular to the center axis of the camera's lens. One of the rectangular directions of the sensor will be placed parallel to the laser sheet. The axis of the camera will form an angle of  $\alpha$  with the laser sheet. The laser module and camera assembly will incrementally rotate about the  $z$  axis so as to enable the scanning of the entire circumference of the pipe wall.

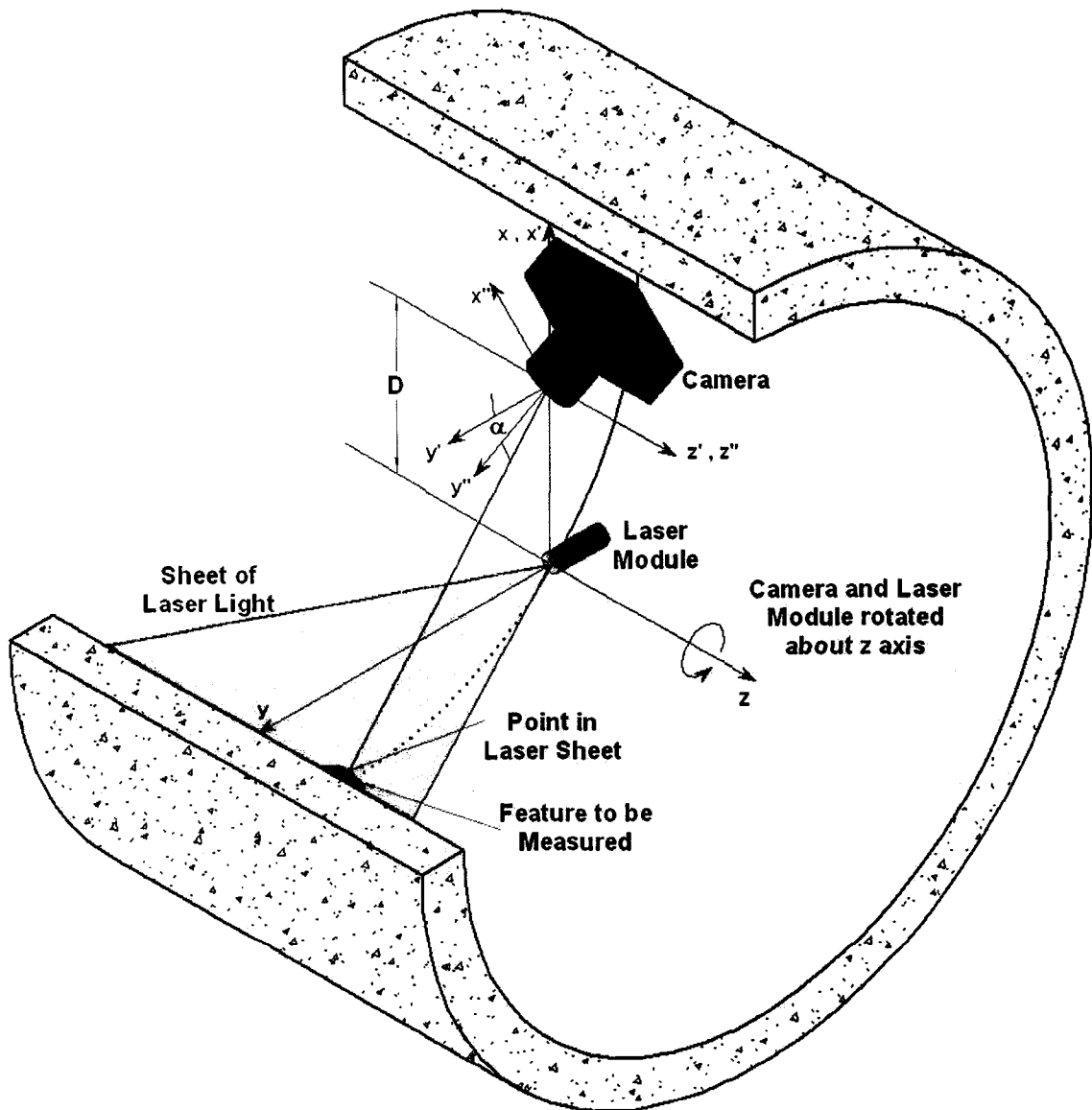


Figure 5.1 — Side-Facing Triangulation Setup.

### 5.2.2 Triangulation Equations

The equation of the laser plane in untransformed coordinates is  $x = 0$  since it is coincident with the  $y$ - $z$  plane. If the equation of this plane is expressed in terms of the primed coordinate system shown in Figure 5.1, its new equation becomes  $x' = -D$ . When the equation of the plane is then expressed in terms of the double primed coordinate system shown in Figure 5.1, it can be given by equation (5-1).

$$x'' \cdot \cos(\alpha) - y'' \cdot \sin(\alpha) = -D \quad (5-1)$$

This equation is then solved for  $y''$  and expressed as equation (5-2).

$$y'' = \frac{x''}{\tan(\alpha)} + \frac{D}{\sin(\alpha)} \quad (5-2)$$

The equation for the plane containing the laser sheet is now expressed in terms of a rectangular coordinate system with its origin at the camera's entrance pupil. Since the camera's view is based on two spherical coordinates, these rectangular coordinates must be converted to spherical coordinates. If the reference plane for azimuth angles is the  $y''$ - $z''$  plane, the conversion equations are given as equations (5-3), (5-4) and (5-5).

$$x'' = d \cdot \sin(\phi) \cdot \sin(\theta) \quad (5-3)$$

$$y'' = d \cdot \cos(\theta) \quad (5-4)$$

$$z'' = d \cdot \cos(\phi) \cdot \sin(\theta) \quad (5-5)$$

Where  $d$  is the straight line distance between the entrance pupil of the camera and the point in question on the laser sheet. Substitution of these conversion equations into equation (5-2) yields equation (5-6).

$$d \cdot \cos(\theta) = \frac{d \cdot \sin(\phi) \cdot \sin(\theta)}{\tan(\alpha)} + \frac{D}{\sin(\alpha)} \quad (5-6)$$

This equation is then solved for  $d$  as shown in equation (5-7).

$$d = \frac{D}{\cos(\theta) \cdot \sin(\alpha) - \sin(\phi) \cdot \sin(\theta) \cdot \cos(\alpha)} \quad (5-7)$$

Now the distance from the lens of the camera to a point in question on the laser sheet is known in terms of the geometrical parameters of the system and the spherical coordinate angles of the camera. To make radius measurements, it would be much more convenient to convert back to unprimed coordinates. First, the double primed coordinates are computed from the raw distance measurement in equation (5-7) using the conversion equations (5-3)-(5-5). These coordinates are listed in equations (5-8), (5-9) and (5-10).

$$x'' = \frac{D}{\cos(\theta) \cdot \sin(\alpha) - \sin(\phi) \cdot \sin(\theta) \cdot \cos(\alpha)} \cdot \sin(\phi) \cdot \sin(\theta) \quad (5-8)$$

$$y'' = \frac{D}{\cos(\theta) \cdot \sin(\alpha) - \sin(\phi) \cdot \sin(\theta) \cdot \cos(\alpha)} \cdot \cos(\theta) \quad (5-9)$$

$$z'' = \frac{D}{\cos(\theta) \cdot \sin(\alpha) - \sin(\phi) \cdot \sin(\theta) \cdot \cos(\alpha)} \cdot \cos(\phi) \cdot \sin(\theta) \quad (5-10)$$

These coordinates may be converted to single primed coordinates by rotation about  $z''$  as given in equations (5-11), (5-12) and (5-13).

$$\begin{aligned}
 x' &= x'' \cdot \cos(\alpha) - y'' \cdot \sin(\alpha) \\
 &= D \cdot \frac{\sin(\phi) \cdot \sin(\theta) \cdot \cos(\alpha) - \cos(\theta) \cdot \sin(\alpha)}{\cos(\theta) \cdot \sin(\alpha) - \sin(\phi) \cdot \sin(\theta) \cdot \cos(\alpha)} = -D
 \end{aligned} \tag{5-11}$$

$$\begin{aligned}
 y' &= y'' \cdot \cos(\alpha) + x'' \cdot \sin(\alpha) \\
 &= D \cdot \frac{\cos(\theta) \cdot \cos(\alpha) + \sin(\phi) \cdot \sin(\theta) \cdot \sin(\alpha)}{\cos(\theta) \cdot \sin(\alpha) - \sin(\phi) \cdot \sin(\theta) \cdot \cos(\alpha)}
 \end{aligned} \tag{5-12}$$

$$z' = z'' = D \cdot \frac{\cos(\phi) \cdot \sin(\theta)}{\cos(\theta) \cdot \sin(\alpha) - \sin(\phi) \cdot \sin(\theta) \cdot \cos(\alpha)} \tag{5-13}$$

Finally, the coordinates are translated along the  $x$  axis to the unprimed coordinate system as shown in equations (5-14), (5-15) and (5-16).

$$x = x' + D = 0 \tag{5-14}$$

$$y = y' = D \cdot \frac{\cos(\theta) \cdot \cos(\alpha) + \sin(\phi) \cdot \sin(\theta) \cdot \sin(\alpha)}{\cos(\theta) \cdot \sin(\alpha) - \sin(\phi) \cdot \sin(\theta) \cdot \cos(\alpha)} \tag{5-15}$$

$$z = z' = D \cdot \frac{\cos(\phi) \cdot \sin(\theta)}{\cos(\theta) \cdot \sin(\alpha) - \sin(\phi) \cdot \sin(\theta) \cdot \cos(\alpha)} \tag{5-16}$$

As expected, the  $x$  coordinate of any measured point will be zero. The  $y$  coordinate will represent a radial coordinate within the pipe, and the  $z$  coordinate will represent an axial coordinate along the pipe. Simplifying equations (5-15) and (5-16) and renaming them for the quantities they represent gives the formulas in equations (5-17) and (5-18) for radius  $R$  and axial location  $H$ .

$$R = D \cdot \frac{1 + \sin(\phi) \cdot \tan(\theta) \cdot \tan(\alpha)}{\tan(\alpha) - \sin(\phi) \cdot \tan(\theta)} \quad (5-17)$$

$$H = D \cdot \frac{\cos(\phi) \cdot \tan(\theta) \cdot \sec(\alpha)}{\tan(\alpha) - \sin(\phi) \cdot \tan(\theta)} \quad (5-18)$$

The axial location equation is of interest for the sake of locating the point being measured in the axial direction along the pipe. As wireframe models are built of the pipe wall, these values will be combined with odometry measurements to define the axial coordinates. The primary purpose of this analysis, however, is to establish the accuracy of the radial measurements. Considerations for the axial location will continue to be made, but may be less emphasized than the radius measurements. To non-dimensionalize the measurements given in (5-17) and (5-18), the equations will be divided by the nominal pipe radius  $R_0$  as demonstrated in Chapter three. This yields the non-dimensional equations for radius parameter  $\bar{R}$  and axial location parameter  $\bar{H}$  shown in equations (5-19) and (5-20).

$$\bar{R} = \bar{D} \cdot \frac{1 + \sin(\phi) \cdot \tan(\theta) \cdot \tan(\alpha)}{\tan(\alpha) - \sin(\phi) \cdot \tan(\theta)} \quad (5-19)$$

$$\bar{H} = \bar{D} \cdot \frac{\cos(\phi) \cdot \tan(\theta) \cdot \sec(\alpha)}{\tan(\alpha) - \sin(\phi) \cdot \tan(\theta)} \quad (5-20)$$

### 5.2.3 Measurement Limits and Camera Field of View

It is important to decide on an appropriate field of view for the camera so that its resolution may be advantageously utilized. A large field of view may provide for a more complete range of measurements; however, the measurements will be less accurate.

Conversely, a small field of view can provide more accurate measurements, but the range which can be measured will be reduced. Figure 5.2 illustrates how the field of view relates to the measurement range for this triangulation scheme.

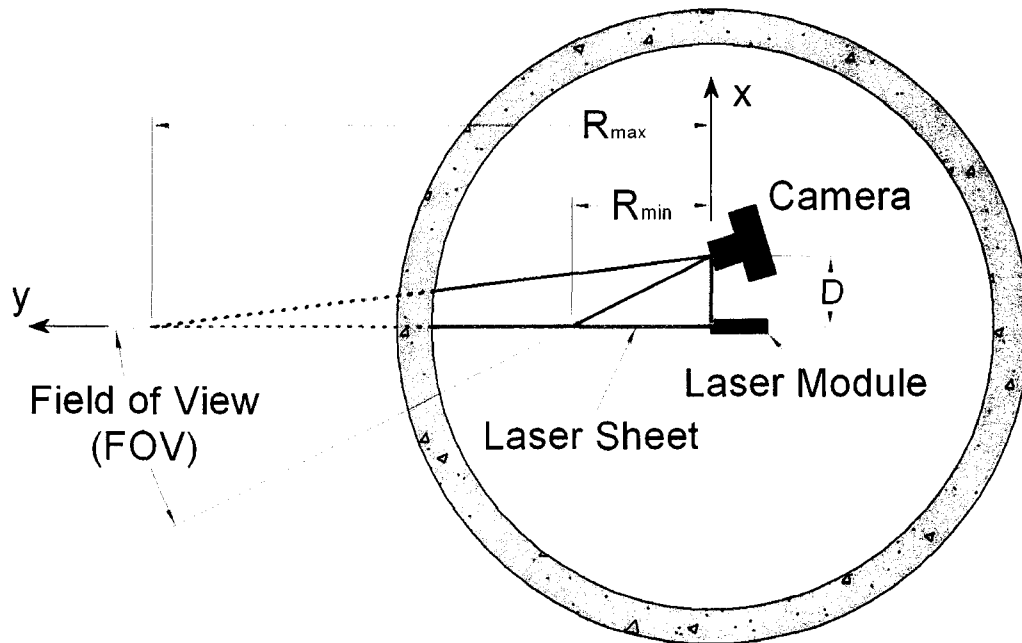


Figure 5.2 — Range of Measurement.

For pipe profiling, it cannot be guaranteed that the profiling robot will actually remain on the center axis of the pipe. One of the more extreme cases of this potential for misalignment is when the axis of rotation is placed at the pipe wall rather than the center axis. In this case, assuming the pipe is not very deformed, the maximum radius parameter which will be measured will be about two. It is unlikely that the measurement platform would be this extremely misaligned; thus, the extra range could be a buffer for possible outward deformations occurring simultaneously with extreme misalignments. Thus, the outer limit of measurements will be set at  $\bar{R}_{max} = 2$ . Expansion of the inner limit (the lower blue line in Figure 5.2) has a greater cost in terms of loss of accuracy,

since it requires a greater expansion of the field of view per unit of radial limit expansion. For the conical laser projection system, a convenient inner limit was established at half the length from the point of laser projection to the expected location of the pipe wall. A similar method is proposed here. If the inner limit is set at half the distance from the focal point of the camera to the expected location of the pipe wall, an expression for this limit is given by equation (5-21).

$$\bar{R}_{\min} = \frac{1 + \bar{D}}{2} \quad (5-21)$$

This choice for the inner limit will allow for some room for camera hardware, enhance system accuracy by effectively narrowing the field of view, and will allow for a consistent comparison between laser triangulation schemes. Given the choices of measurement limits made here, the desired field of view of the camera is simply the angle difference between the outer and inner limit angles, given with equation (5-22).

$$FOV = \tan^{-1}\left(\frac{\bar{R}_{\max}}{\bar{D}}\right) - \tan^{-1}\left(\frac{\bar{R}_{\min}}{\bar{D}}\right) \quad (5-22)$$

The aim angle needed may simply be found as the complement of the average of the outer and inner limit angles, given by equation (5-23).

$$\alpha = \frac{\pi}{2} - \frac{\tan^{-1}\left(\frac{\bar{R}_{\max}}{\bar{D}}\right) + \tan^{-1}\left(\frac{\bar{R}_{\min}}{\bar{D}}\right)}{2} \quad (5-23)$$

A plot describing the aim angle and field of view is given in Figure 5.3. Also shown in the plot is the aim angle which would place the expected measurements ( $\bar{R} = 1$ ) in the

very center of the image frame. Note that the deviation between these two angles is not very great, especially near where the two curves cross at a baseline parameter of 0.296.

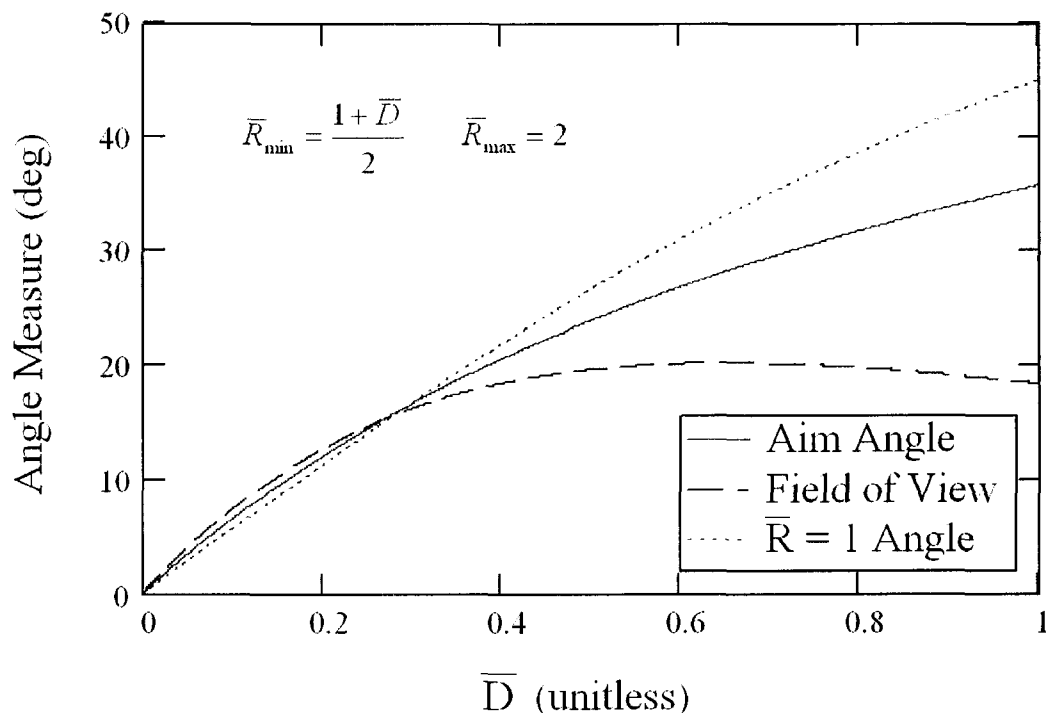
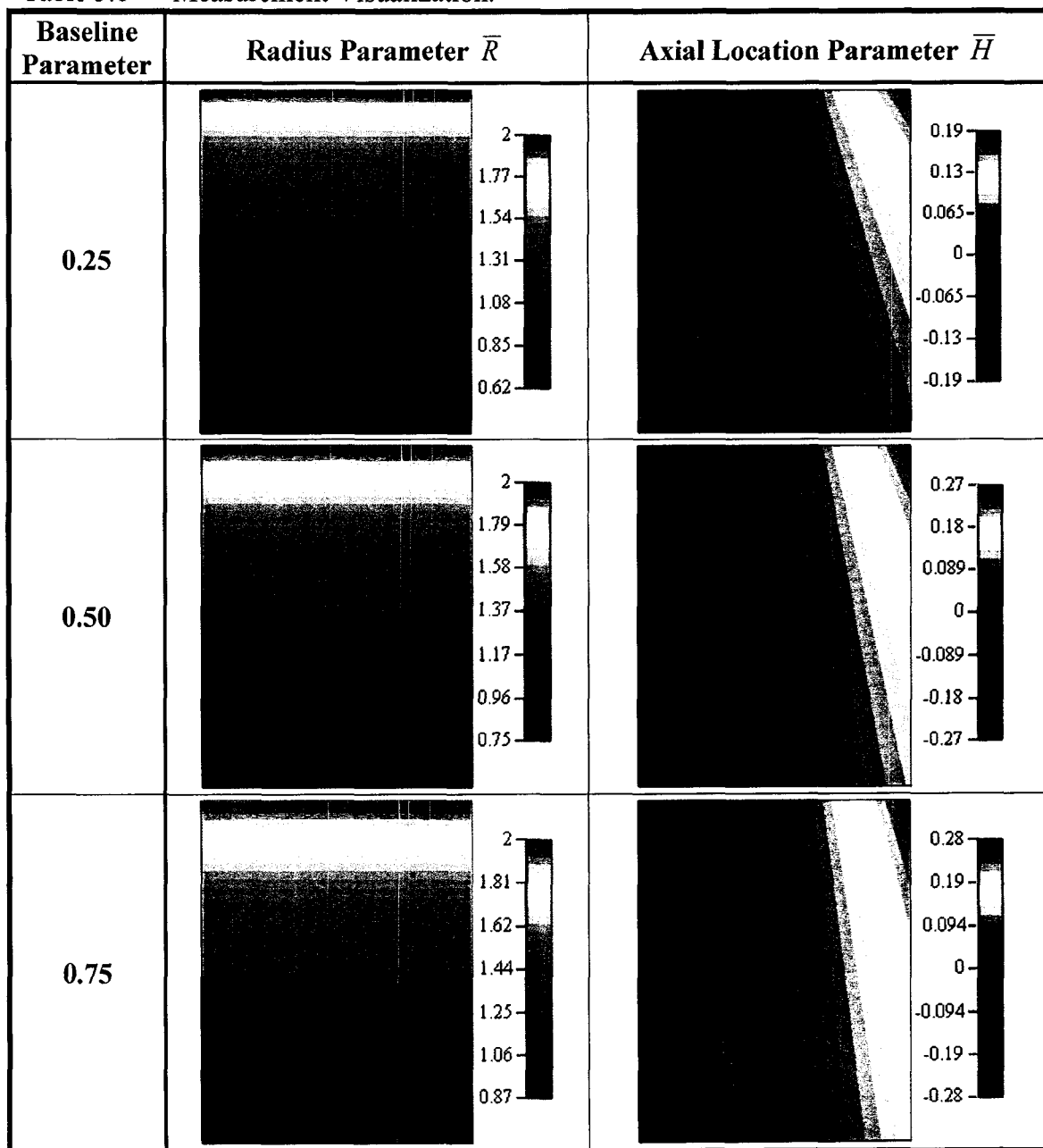


Figure 5.3 — Aim and Field of View Selection Versus Baseline Distance.

#### 5.2.4 Visualization of Measurements

Plotting equations (5-19) and (5-20) versus the zenith and azimuth angles in polar coordinates will yield contour plots which approximate image coordinates for the independent variables and whose contours represent the dependent variable (the radius parameter or axial location parameter measurements). Table 5.1 provides visualizations for values of radius parameter and axial location parameter within an image for several values of baseline parameter.

Table 5.1 — Measurement Visualization.



Note that the contour plots for each parameter are not strong functions of the baseline parameter.

### 5.3 Uncertainty Analysis

The method followed in Chapter three will be used to estimate the accuracy of the side-facing method of triangulation. The variables which drive the measurement are the zenith and azimuth angles of the camera, the baseline distance, and the aim angle of the camera. Expressing the uncertainty of the radius parameter measurement in terms of these variables and their uncertainties yields equation (5-24).

$$U[\bar{R}] = \sqrt{\left(\frac{\partial \bar{R}}{\partial \theta} \cdot U[\theta]\right)^2 + \left(\frac{\partial \bar{R}}{\partial \phi} \cdot U[\phi]\right)^2 + \left(\frac{\partial \bar{R}}{\partial D} \cdot U[D]\right)^2 + \left(\frac{\partial \bar{R}}{\partial \alpha} \cdot U[\alpha]\right)^2} \quad (5-24)$$

Similarly, the uncertainty in the axial location parameter may be evaluated by equation (5-25).

$$U[\bar{H}] = \sqrt{\left(\frac{\partial \bar{H}}{\partial \theta} \cdot U[\theta]\right)^2 + \left(\frac{\partial \bar{H}}{\partial \phi} \cdot U[\phi]\right)^2 + \left(\frac{\partial \bar{H}}{\partial D} \cdot U[D]\right)^2 + \left(\frac{\partial \bar{H}}{\partial \alpha} \cdot U[\alpha]\right)^2} \quad (5-25)$$

This section is devoted to the development of the various components of these equations.

#### 5.3.1 Evaluation of Partial Derivatives

The most straightforward elements of equations (5-24) and (5-25) to evaluate are the partial derivatives. The partial derivatives of the radius and axial location parameters with respect to the zenith angle of the camera are given by equations (5-26) and (5-27).

$$\frac{\partial \bar{R}}{\partial \theta} = \bar{D} \cdot \frac{\sin(\phi)}{\cos^2(\theta) \cdot \cos^2(\alpha)} \cdot \frac{1}{(\tan(\alpha) - \sin(\phi) \cdot \tan(\theta))^2} \quad (5-26)$$

$$\frac{\partial \bar{H}}{\partial \theta} = \bar{D} \cdot \frac{\cos(\phi) \cdot \sin(\alpha)}{\cos^2(\theta) \cdot \cos^2(\alpha)} \cdot \frac{1}{(\tan(\alpha) - \sin(\phi) \cdot \tan(\theta))^2} \quad (5-27)$$

The partial derivatives of the radius and axial location parameters with respect to the azimuth angle of the camera are given by equations (5-28) and (5-29).

$$\frac{\partial \bar{R}}{\partial \phi} = \bar{D} \cdot \frac{\cos(\phi) \cdot \tan(\theta)}{\cos^2(\alpha)} \cdot \frac{1}{(\tan(\alpha) - \sin(\phi) \cdot \tan(\theta))^2} \quad (5-28)$$

$$\frac{\partial \bar{H}}{\partial \phi} = \bar{D} \cdot \frac{\tan(\theta)}{\cos(\alpha)} \cdot \frac{\tan(\theta) - \tan(\alpha) \cdot \sin(\phi)}{(\tan(\alpha) - \sin(\phi) \cdot \tan(\theta))^2} \quad (5-29)$$

The partial derivatives of the radius and axial location parameters with respect to the baseline distance are given by equations (5-30) and (5-31).

$$\frac{\partial \bar{R}}{\partial \bar{D}} = \frac{1 + \sin(\phi) \cdot \tan(\theta) \cdot \tan(\alpha)}{\tan(\alpha) - \sin(\phi) \cdot \tan(\theta)} \quad (5-30)$$

$$\frac{\partial \bar{H}}{\partial \bar{D}} = \frac{\tan(\theta) \cdot \cos(\phi)}{\cos(\alpha)} \cdot \frac{1}{\tan(\alpha) - \sin(\phi) \cdot \tan(\theta)} \quad (5-31)$$

The partial derivatives of the radius and axial location parameters with respect to the aim angle are given by equations (5-32) and (5-33).

$$\frac{\partial \bar{R}}{\partial \alpha} = -\bar{D} \cdot \frac{1}{\cos^2(\alpha)} \cdot \frac{\sin^2(\phi) \cdot \tan^2(\theta) + 1}{(\tan(\alpha) - \sin(\phi) \cdot \tan(\theta))^2} \quad (5-32)$$

$$\frac{\partial \bar{H}}{\partial \alpha} = -\bar{D} \cdot \frac{\tan(\theta) \cdot \cos(\phi)}{\cos(\alpha)} \cdot \frac{\sin(\phi) \cdot \tan(\theta) \cdot \tan(\alpha) + 1}{(\tan(\alpha) - \sin(\phi) \cdot \tan(\theta))^2} \quad (5-33)$$

These partial derivatives represent factors that describe how much influence an uncertainty in any one variable affects the overall uncertainty of the method. The following sections will describe how reasonable values are chosen for estimation of uncertainty in the individual variables.

### 5.3.2 Uncertainty in Geometrical Parameters

To be consistent in the analysis across the three triangulation schemes considered, the length measurements defining the geometry of the system will have an assumed

uncertainty of  $\pm 0.1\%$  of the nominal pipe radius. Thus, the uncertainty in baseline parameter will be estimated as  $\pm 0.001$ .

A formula for the aim angle has been given by equation (5-23). To estimate uncertainty, the method outlined in Section 3.3 will again be utilized. Taking the partial derivative of the aim angle with respect to the maximum measurement range yields equation (5-34).

$$\frac{\partial \alpha}{\partial \bar{R}_{\max}} = -\frac{\bar{D}}{2 \cdot (\bar{D}^2 + \bar{R}_{\max}^2)} \quad (5-34)$$

And, taking the partial derivative of the aim angle with respect to the baseline parameter yields equation (5-35).

$$\frac{\partial \alpha}{\partial \bar{D}} = \frac{5 \cdot \bar{R}_{\max} \cdot \bar{D}^2 + 2 \cdot \bar{D}^2 + 2 \cdot \bar{R}_{\max} \cdot \bar{D} + 2 \cdot \bar{R}_{\max}^2 + \bar{R}_{\max}}{2 \cdot (\bar{D}^2 + \bar{R}_{\max}^2) \cdot (5\bar{D}^2 + 2\bar{D} + 1)} \quad (5-35)$$

These partial derivatives are used in equation (5-36) to estimate the uncertainty in the aim angle.

$$U[\alpha] = \sqrt{\left( \frac{\partial \alpha}{\partial \bar{R}_{\max}} \cdot U[\bar{R}_{\max}] \right)^2 + \left( \frac{\partial \alpha}{\partial \bar{D}} \cdot U[\bar{D}] \right)^2} \quad (5-36)$$

Taking  $U[\bar{R}_{\max}]$  as 0.001 and assuming  $\bar{R}_{\max}$  is to be 2 results in the plot shown in Figure 5.4 that describes the uncertainty in aim angle as a function of baseline parameter.

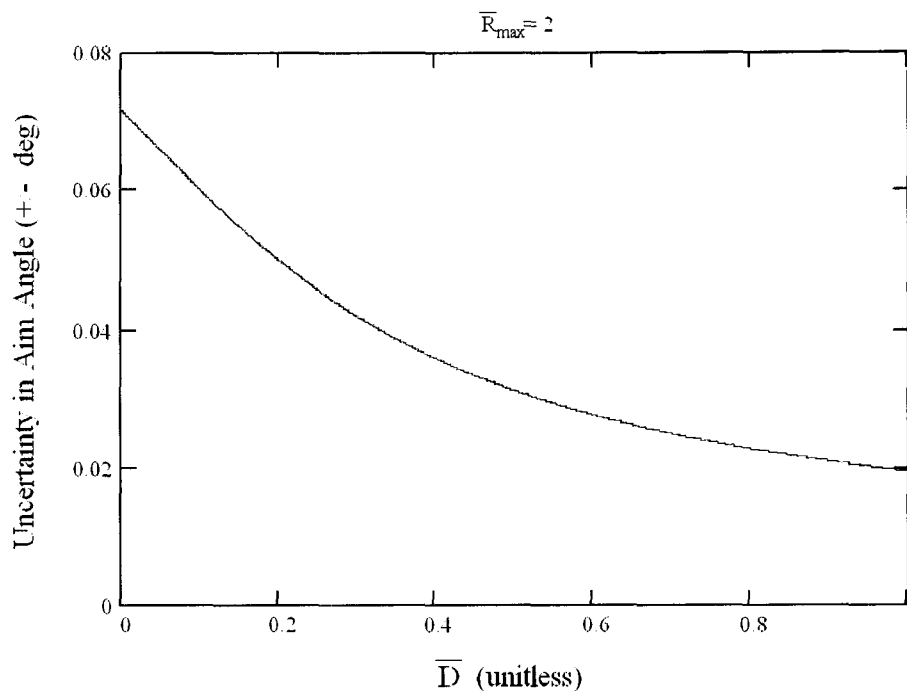


Figure 5.4 — Uncertainty in Aim Angle.

### 5.3.3 Uncertainty in Camera Parameters

The camera is used in the same fashion for this triangulation scheme as for the conically projected laser scheme. Thus, the rationale behind the uncertainty estimations given in Chapter three also apply to this system. The uncertainty in the zenith angle is a function of the field of view, the camera resolution and the estimated pixel uncertainty. This is expressed using equation (5-37).

$$U[\theta] = \frac{FOV}{n} \cdot U[r] \quad (5-37)$$

where  $FOV$  is the field of view of the camera across the longer image axis, and  $n$  is the number of pixels along that axis. The azimuth angle uncertainty is a function of the field of view, the zenith angle, the camera resolution, and the pixel uncertainty. This is given by equation (5-38).

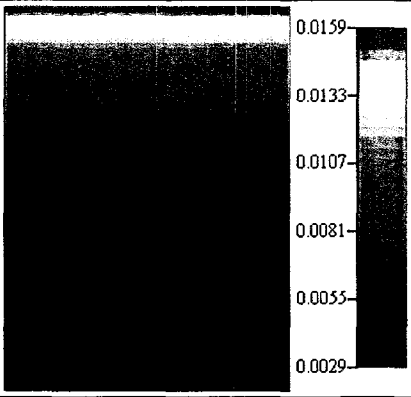
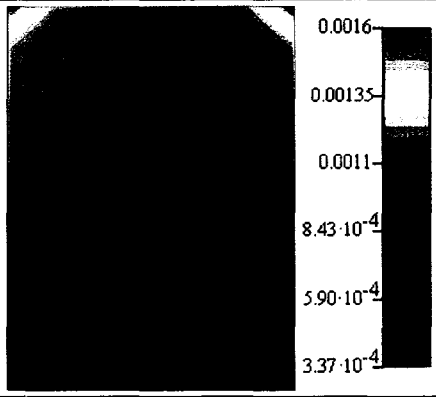
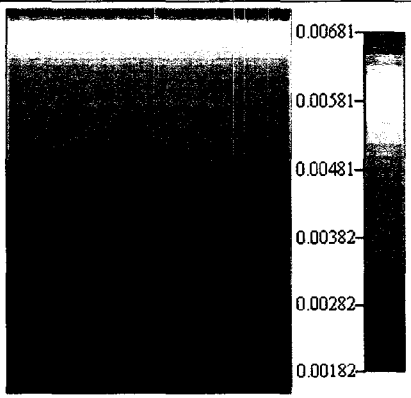
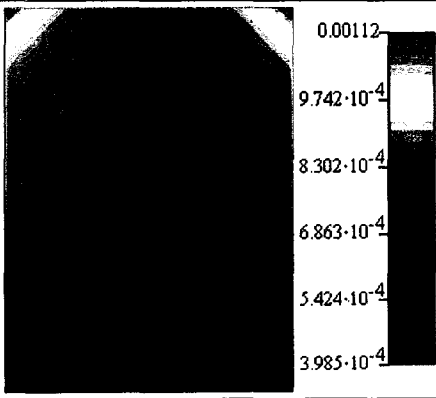
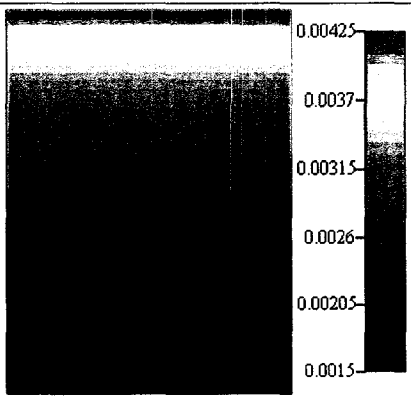
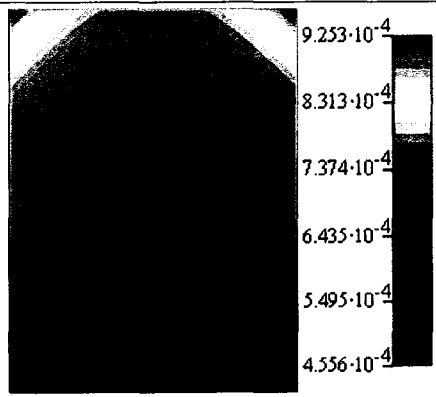
$$U[\phi] = \frac{FOV}{n \cdot \theta} \cdot U[r] \quad (5-38)$$

Here, all angles are measured in radians. For the same reasons given in Chapter three, for estimation purposes, the pixel uncertainty will be taken as one, and the camera resolution across the long axis will be taken as 1024.

#### **5.3.4 Overall Uncertainty**

Using the equations in the preceding section, contour plots describing predicted uncertainty may be prepared. Again the axes of the contour plot represent locations in images collected by the camera. Table 5.2 shows predicted uncertainty in radius parameter and axial location parameter for given locations in collected images for several values of baseline parameter.

Table 5.2 — Uncertainty Visualization.

Baseline Parameter	Radius Parameter Uncertainty $U[\bar{R}]$	Axial Location Parameter Uncertainty $U[\bar{H}]$
0.25		
0.50		
0.75		

Uncertainty in the side facing triangulation scheme is clearly less for inward pipe deflections (radial measurements where  $\bar{R}$  is less than one) than for outward pipe deflections. Also, more accurate measurement is associated with larger baseline distances because the larger aim angle provides more vertical pixel variation for a given  $\bar{R}$ .

Referring to the contour plots for  $U(\bar{H})$ , it is clear that better measurement accuracy occurs near the center of the image where the number of CCD pixels per unit pipe surface area is greater; however, the amount of uncertainty in  $\bar{H}$  is very small.

### 5.3.5 Measurement Uncertainty Versus Measurement

A good method of characterization of the nature of the uncertainty in the radius parameter is to compare it with the measurement itself. Since the radius parameter measurements and the uncertainties in these measurements change very little along the horizontal axis of the images (see Tables 5.1 and 5.2), only a slice of the image vertically through one edge will be considered. Figure 5.5 shows this comparison of measurements and their uncertainties for three values of baseline parameter.

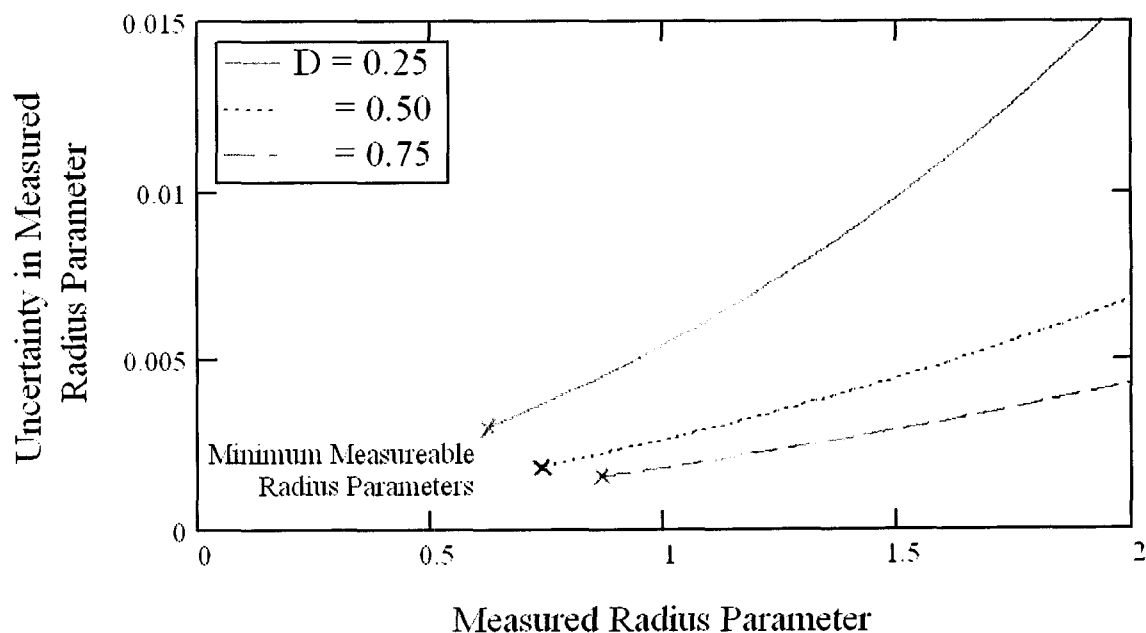


Figure 5.5 — Uncertainty Versus Measurement.

When larger baseline parameters are used, the uncertainty in the method can be reduced. The points where each curve terminates on their left ends are significant because they represent the limits on the minimum measurement that can be made for each

baseline parameter given the assumptions of Section 5.2.3. The inner limit tends to increase as baseline parameter increases, so if a narrower inner limit is needed, a smaller baseline parameter may be required.

#### 5.4 Measurement System Design

As suggested in the previous section, the essence of the tradeoff which must be considered for the design of this measurement system is a choice between smaller minimum measurable radius parameters and greater measurement accuracy; Figure 5.6 illustrates these competing effects.

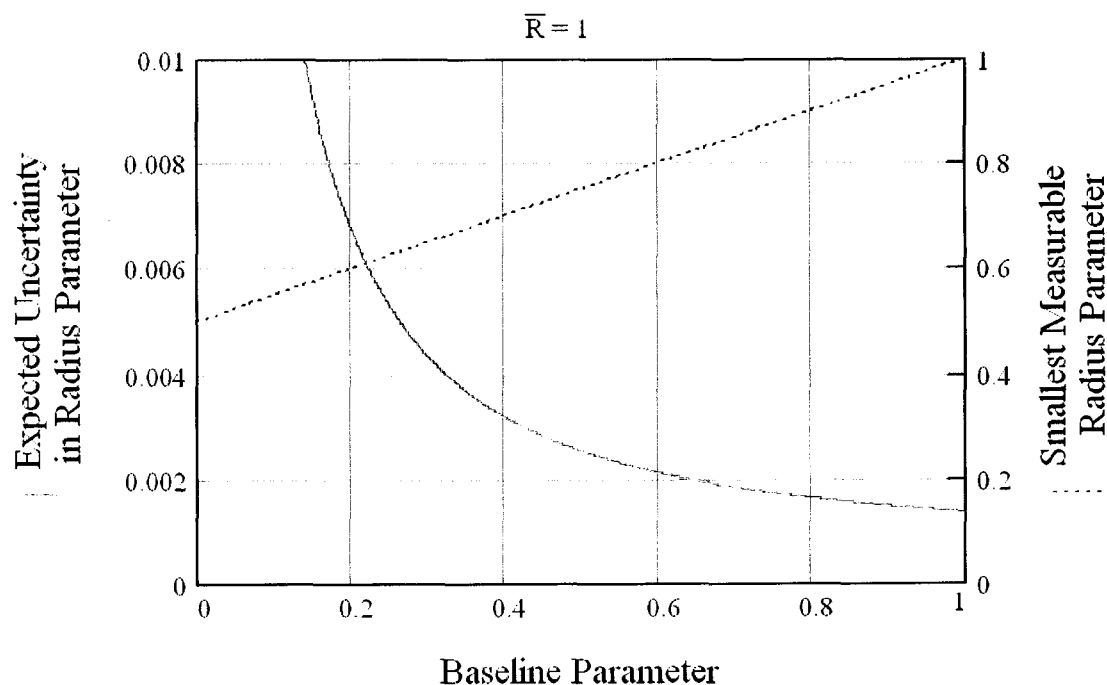


Figure 5.6 — Design Chart for Baseline Parameter.

When selecting a desirable baseline parameter, a vertical line of a proposed value of baseline parameter can be placed on the chart, and the uncertainty expected in the vicinity of  $\bar{R} = 1$  may be read from the red curve and the left vertical scale. This is

evaluated concurrently with the smallest measurable radius parameter read from the dotted blue curve and the right vertical scale. A choice of baseline parameter somewhere between 0.3 and 0.5 would give uncertainties in the range of 0.25-0.50% of nominal radius and allow for measurements as small as 65-75% of nominal radius. This method appears to offer very good accuracy and measurement range.

### **5.5 Conclusions**

Equations have been derived to predict the behavior of a side-facing profiling system. Limits on the measurement range were applied set the aim angle and the field of view for the camera. An uncertainty analysis was performed on the system, and the predicted uncertainties were presented as a function of the radial measurements. Design tradeoffs based on uncertainty and measurement limits have been identified; larger baseline distances result in greater system accuracy but reduced measurement range. The predicted uncertainty of the system is very good, providing uncertainties of approximately 0.25% to 0.50% of nominal radius while allowing for measurements as small as about 65% to 75% of nominal radius. The small values of uncertainty predicted for this method may not be enough to justify the extra time it may take to perform scans of the pipe because of the angular articulation required by this method.

CHAPTER 6

OBTAINING PIPE PROFILES USING THE  
PERPENDICULAR PLANE PROFILING  
METHOD

**6.1 Introduction and Overview**

This chapter describes the development and testing of a physical model of the perpendicular plane profiling method. A camera model was identified, and suitable values were chosen to define the geometry of the triangulation configuration. The resulting physical system was fabricated and mounted on linear slides to allow for axial movement of the camera-laser system inside a “test pipe.” The camera-laser system was indexed axially along the pipe using a lead screw driven by a stepper motor; the electromechanical system, including image capture, was automated using LabVIEW. The captured images were processed using machine vision techniques developed in LabVIEW to extract pipe wall coordinates based on camera calibration. Finally, the results were plotted in three dimensions with color gradients to visualize the profiles obtained. Each of these steps was performed for nominal baseline distances of 3 inches, 6 inches, 12 inches and 30 inches corresponding to baseline parameters of 0.5, 1.0, 2.0 and 5.0, respectively; the nominal measuring radius was 6 inches in every case. Profiling

trials were performed for each of these baseline distances, and profiles from each were reported separately.

## 6.2 Extrinsic Camera Calibration

This section is devoted to selecting a suitable camera and lens model to describe the relationship between light trajectory angles and pixel coordinates.

### 6.2.1 Calibration Methodology

Lens and camera systems are typically designed to follow one of a few standard models. Each of these models relates image coordinates to angles describing the trajectory of incoming light. In each case, the azimuth angle describing the incoming trajectory will directly correspond to an azimuth angle in the image (see section 3.2). The models differ in how the angle of an incoming light ray off of the optical axis (the zenith angle) relates to the radius of the resulting illuminated pixel in the image from the image center.

The five common lens models to relate zenith angle  $\theta$  to image radius  $r$  are provided in equations (6-1), (6-2), (6-3), (6-4) and (6-5).

*Perspective Projection:*

$$\theta(r) = \tan^{-1}\left(\frac{r}{k}\right) \quad (6-1)$$

*Stereographic Projection:*

$$\theta(r) = 2 \cdot \tan^{-1}\left(\frac{r}{k}\right) \quad (6-2)$$

*Equidistant Projection:*

$$\theta(r) = \frac{r}{k} \quad (6-3)$$

*Sine-Law Projection:*

$$\theta(r) = \sin^{-1}\left(\frac{r}{k}\right) \quad (6-4)$$

*Equi-Solid Projection:*

$$\theta(r) = 2 \cdot \sin^{-1}\left(\frac{r}{k}\right) \quad (6-5)$$

Here,  $k$  is a camera calibration factor that varies with camera zoom. Each of these camera models is designed to be inserted into the profiling model developed in Chapter four. Note that for contour plots presented in Chapters three through five, the equidistant model was applied due to its simplicity and generally good correspondence with actual lenses. When the camera models above are inserted into equation (4-13), the resulting profiling models may then be given with equations (6-6), (6-7), (6-8), (6-9) and (6-10).

*Perspective Projection:*

$$R = D \cdot \tan\left(\tan^{-1}\left(\frac{r}{k}\right)\right) = D \cdot \frac{r}{k} \quad (6-6)$$

*Stereographic Projection:*

$$R = D \cdot \tan\left(2 \cdot \tan^{-1}\left(\frac{r}{k}\right)\right) \quad (6-7)$$

*Equidistant Projection:*

$$R = D \cdot \tan\left(\frac{r}{k}\right) \quad (6-8)$$

*Sine-Law Projection:*

$$R = D \cdot \tan\left(\sin^{-1}\left(\frac{r}{k}\right)\right) \quad (6-9)$$

*Equi-Solid Projection:*

$$R = D \cdot \tan\left(2 \cdot \sin^{-1}\left(\frac{r}{k}\right)\right) \quad (6-10)$$

The camera calibration to be performed will take data from a physical system in which good approximations are known for baseline distance  $D$  and the pixel normalization factor  $k$  (which is a function of the field of view of the camera). The data which will be collected will be the radius of a point in world coordinates and the corresponding radius of the same point in pixel coordinates. A curve will then be fit to the data, and the optimized parameters of this fit will give more suitable values for the baseline distance and the pixel normalization factor.

### **6.2.2 Calibration Fixture**

To verify the behavior of the camera-lens system, a calibration stand was constructed such that a camera could be held stationary a set distance away from a precisely prepared target. The target consisted of concentric rings at even two inch diameter intervals. Threaded rods were used to provide for accurate spacing between the camera and the target. Three pieces of rod were used which allowed for adjustment to the perpendicularity of the camera's axis to the target. The feet of the rods were not affixed to the board to which the target was glued so that the camera could be easily translated parallel with the target. Figure 6.1 shows the calibration setup with the attached camera. The calibration stand was designed to be fully adjustable for baseline distances between 0 and 30 inches.

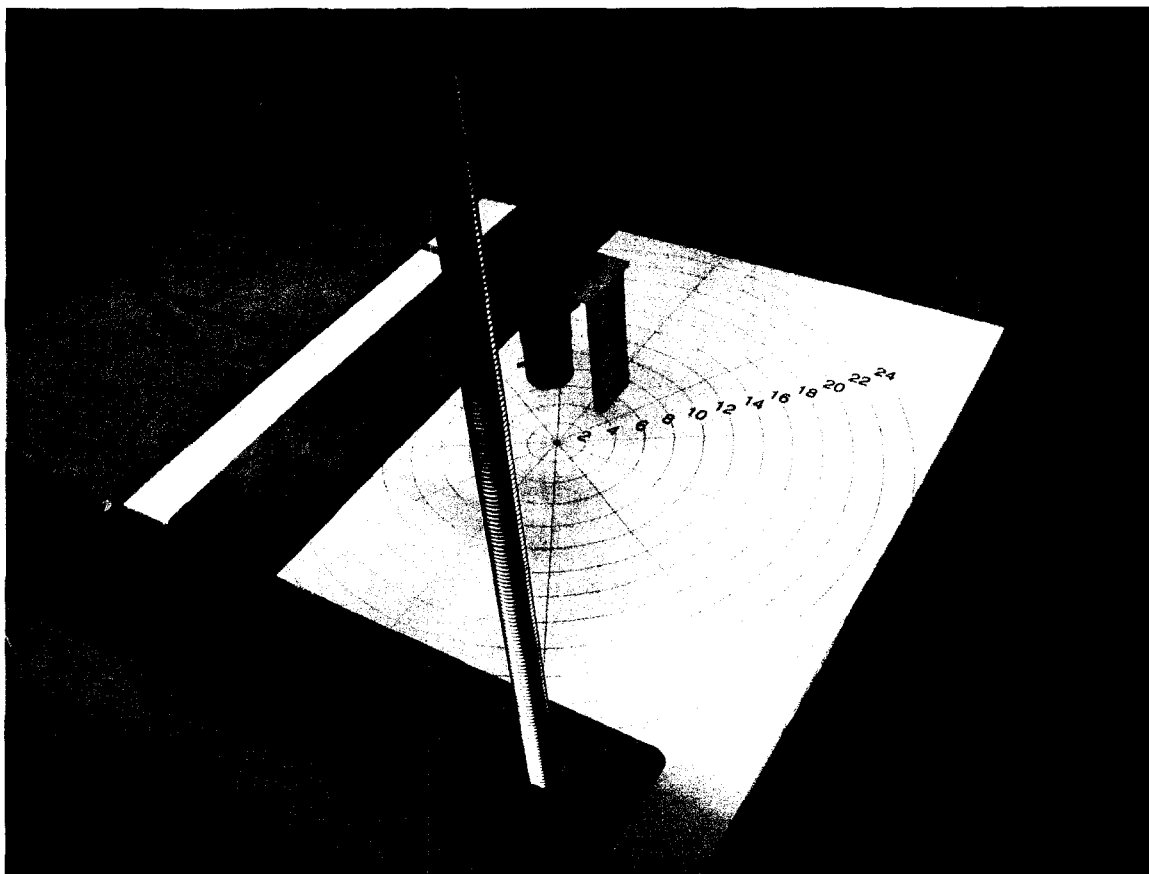


Figure 6.1 — Camera Calibration Stand.

### 6.2.3 Calibration Images and Data

Calibration data was required at all four of the baseline distances considered. Therefore, the stand was positioned and aligned at four different locations to obtain calibration photographs. Each time, the stand was checked for alignment of the camera's optical axis with the center of the target, the perpendicularity of the camera with the target, and the field of view was set such that the 24 inch circle was inscribed within the frame. The baseline distance was set as the distance between the front edge of the lens and the target, with the assumption that the calibration procedure would determine the actual baseline distance to the entrance pupil. Using this setup, images were obtained of the target as shown in Figure 6.2.

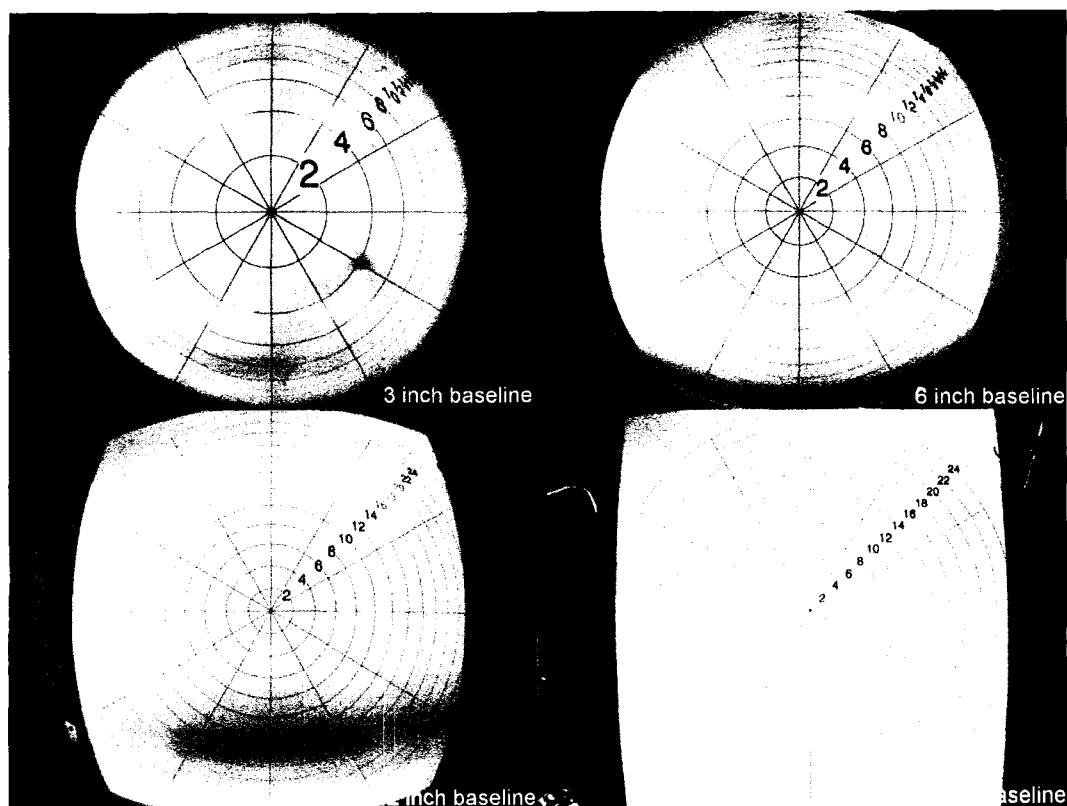


Figure 6.2 — Calibration Images.

For each image, the center of the image was taken as the point where the radial lines converged. Pixel radii were found along the rightward horizontal radial line for each location where it intersected a concentric circle. The pixel radius values were paired with their corresponding target radius values and recorded. This was repeated for the leftward horizontal line and the vertical radial lines. The plot in Figure 6.3 shows the target radius values plotted versus the pixel radius values for all four images.

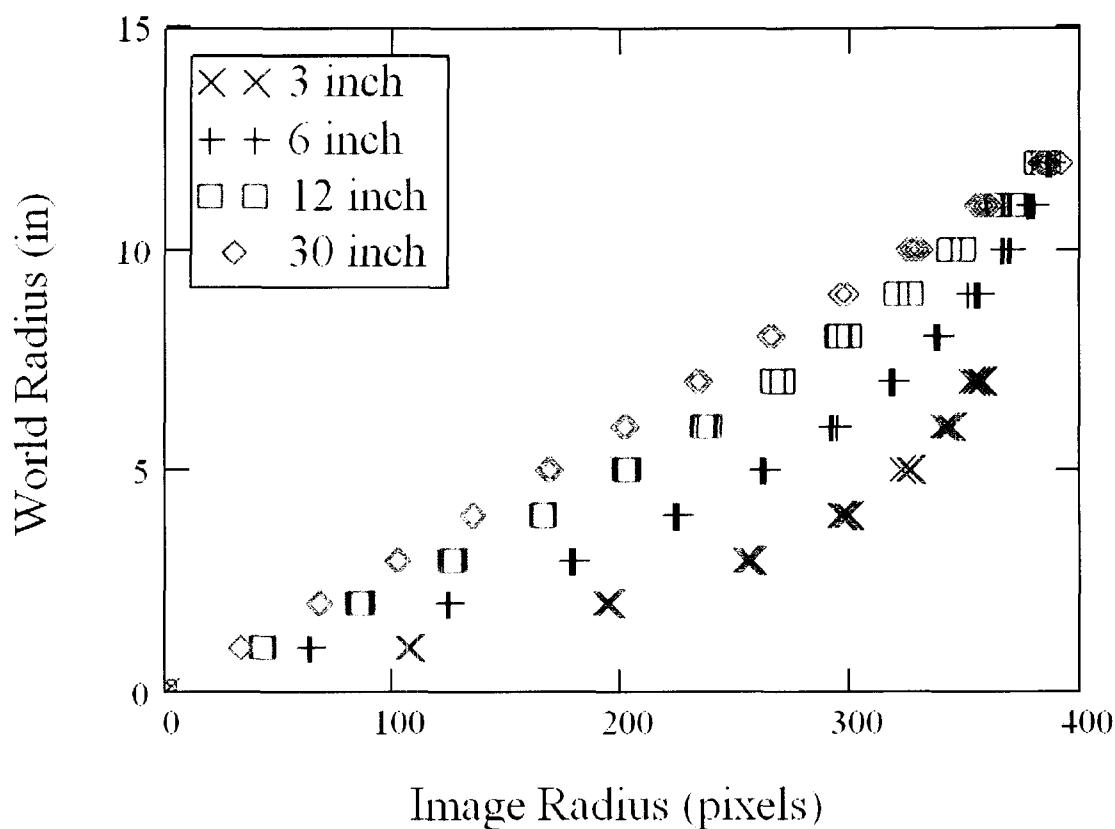


Figure 6.3 — Extrinsic Camera Calibration Data.

The presence of several markers at each general location in this plot is an artifact of using four radial lines in the images of Figure 6.2. The use of four radial lines should help to account for small errors due to small misalignments, misidentification of pixel locations, or other unidentified errors during the calibration process.

#### 6.2.4 Curve Fitting

The data in the above plot was fit to identify the most appropriate camera model to be used for this system as well as the best values for the parameters in that model. An algorithm known as the Levenberg-Marquart method was applied to compare each of the measurement models given in equations (6-6) through (6-10) with the data collected. The model with the best curve fit would be taken as the most appropriate model. Figure 6.4

shows the curve fits for the perspective projection model (the most commonly used camera model).

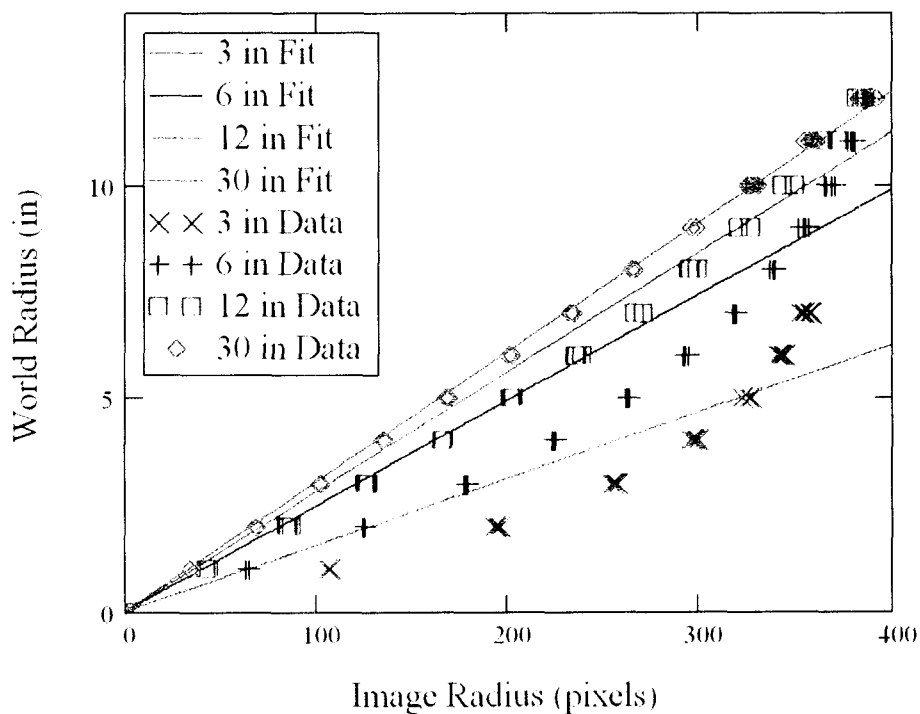


Figure 6.4 — Perspective Projection Fit.

This figure illustrates the inadequacy of the perspective projection camera model, especially for wide fields of view (shorter baseline lengths). This camera model forms straight linear relationships between the radius (in pixels) of a detected line in the image versus its actual world radius. As the baseline lengths involved with this measurement scheme get shorter, the field of view needs to be wider resulting in very non-linear behavior. The short baseline lengths possible with this measurement model can therefore not be correctly modeled with the perspective projection model.

The remaining four models provide for curvature in the relationship between image radius and world radius and therefore have more potential to accurately model the

camera used in this system. Figures 6.5 through 6.8 show the curves of fits for the remaining four models.

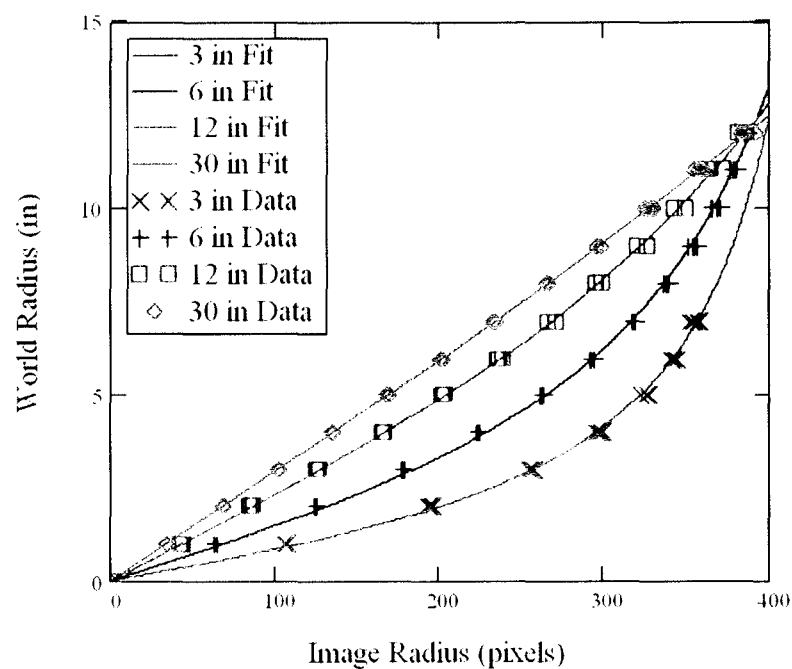


Figure 6.5 — Stereographic Curve Fit.

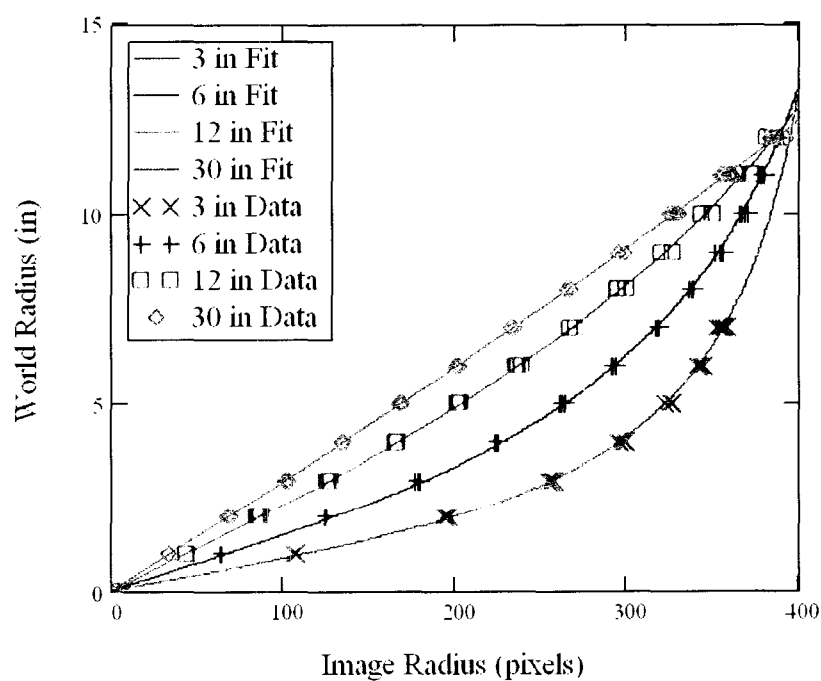


Figure 6.6 — Equidistant Curve Fit.

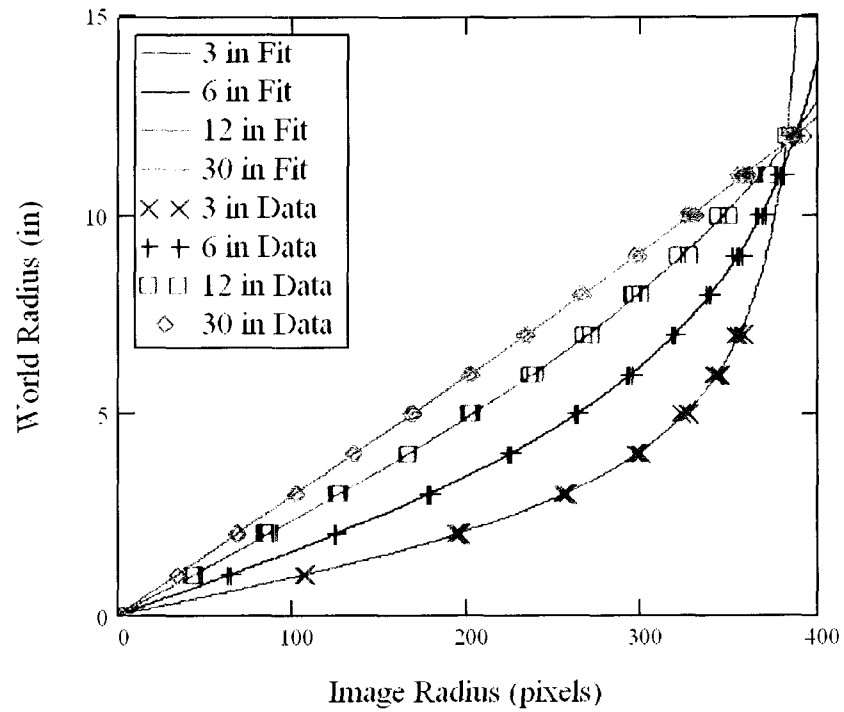


Figure 6.7 — Sine-Law Curve Fit.

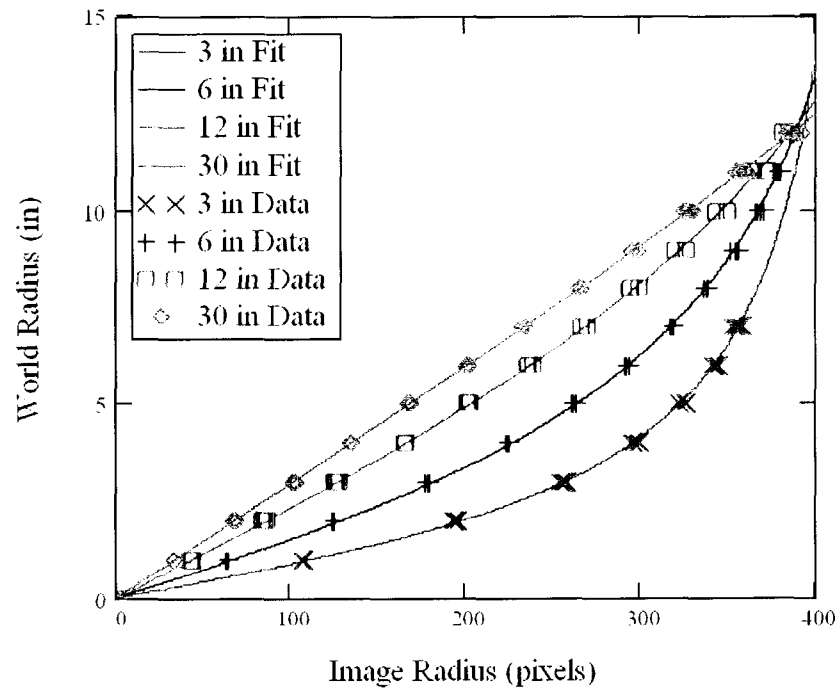


Figure 6.8 — Equi-Solid Curve Fit.

To objectively evaluate which of the models is most suitable, the root mean squared error (RMSE) was computed for each fit and for each baseline length. Table 6.1 summarizes these errors and the model parameters calculated by the fitting algorithm.

Table 6.1 — Fitted Curve Parameters and Errors.

Model		Nominal Baseline Length			
		3 inch	6 inch	12 inch	30 inch
<b>Perspective</b> $R = D \cdot \frac{r}{k}$	$D$ (in)	4.035	7.519	11.60	18.48
	$k$ (pixels)	259.0	304.2	413.6	608.2
	RMSE (in)	0.887	1.298	0.607	0.127
<b>Stereographic</b> $R = D \cdot \tan\left(2 \cdot \tan^{-1}\left(\frac{r}{k}\right)\right)$	$D$ (in)	1.871	3.746	8.397	24.10
	$k$ (pixels)	465.2	529.6	742.3	1646
	RMSE (in)	0.109	0.136	0.106	0.051
<b>Equidistant</b> $R = D \cdot \tan\left(\frac{r}{k}\right)$	$D$ (in)	2.394	4.724	10.06	28.02
	$k$ (pixels)	287.5	325.3	442.3	956.6
	RMSE (in)	0.097	0.115	0.104	0.051
<b>Sine-Law</b> $R = D \cdot \tan\left(\sin^{-1}\left(\frac{r}{k}\right)\right)$	$D$ (in)	3.574	6.850	13.10	34.36
	$k$ (pixels)	399.3	446.3	571.0	1173
	RMSE (in)	0.088	0.084	0.101	0.051
<b>Equi-Solid</b> $R = D \cdot \tan\left(2 \cdot \sin^{-1}\left(\frac{r}{k}\right)\right)$	$D$ (in)	2.658	5.207	10.83	29.80
	$k$ (pixels)	628.0	708.5	950.3	2035
	RMSE (in)	0.092	0.106	0.103	0.051

The RMSE error and the value of  $D$  are both used to evaluate the appropriateness of the fits. Table 6.1 shows that in every case, the Sine-Law model provides for the lowest RMSE error of any of the models. Examination of the computed distances  $D$  also reveals that the Sine-Law model provides the best match to the nominal baseline lengths. This, along with the high quality of the fit depicted in Figure 6.7, indicate that the Sine-Law model is most suitable for accurately relating image pixel radius to the real world radius.

### 6.3 Profiling

Using the calibration parameters determined above for the Sine-Law model, the measurement system was tested in an actual section of pipe to verify its validity. A laser projector and camera were oriented relative to each other as specified by the definition of this measurement setup provided in Chapter four. The setup was passed along a section of pipe with detectable features, and images were collected and saved at 0.1 inch axial increments. The images were processed using automated LabVIEW modules, and the location of the laser line was detected for each image.

#### 6.3.1 Profiling Methodology

Pipe profiles were collected using a cylindrical coordinate system with two length values (radius  $R$  and axial position  $H$ ) and one angle  $\phi$ , as shown in Figure 6.9.

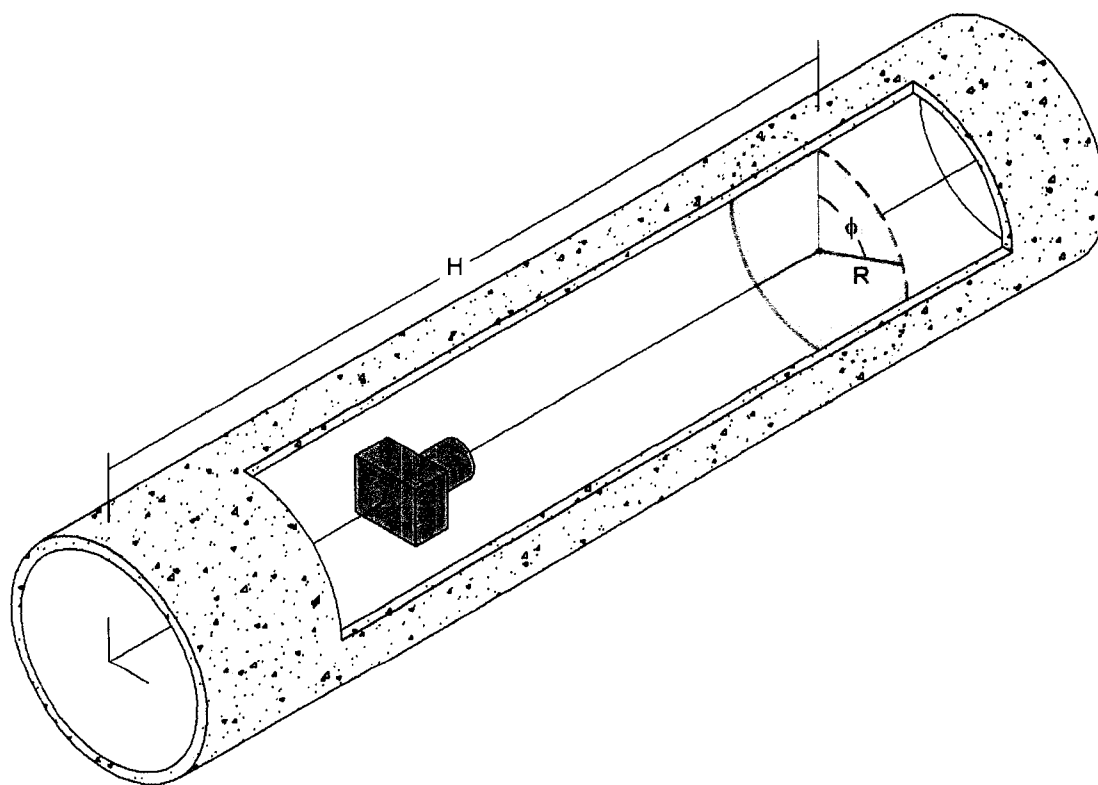


Figure 6.9 — Coordinates for Profiling.

For commercial profilers, the axial position  $H$  would be determined by odometry attached to the robot wheels or by measuring the length of the robot's tether. In the laboratory measurements collected here, the axial position was precisely set by a stepper motor and lead-screw arrangement described later. The angle  $\phi$  corresponds to the angular location of a measurement around the circumference of the internal pipe wall measured relative to the upward vertical line. The radius  $R$  was determined by relating the pixel coordinate to the real-world coordinate using the Sine-Law model. Collecting all three of these cylindrical coordinates results in a single spatial data point defining the wall of the pipe; plotting all of the collected data points results in a wireframe model of the pipe.

### **6.3.2 Hardware and Automated Axial Position**

The perpendicular plane profiling method called for a laser plane to be projected at a specified spacing in front of the camera. To accomplish this, an adjustable rail was constructed. The rail was built on linear bearings and included a slot cut along its length to allow the camera and the laser to be properly positioned relative to each other and locked in place. Figure 6.10 shows the camera and laser projector affixed to the rail.

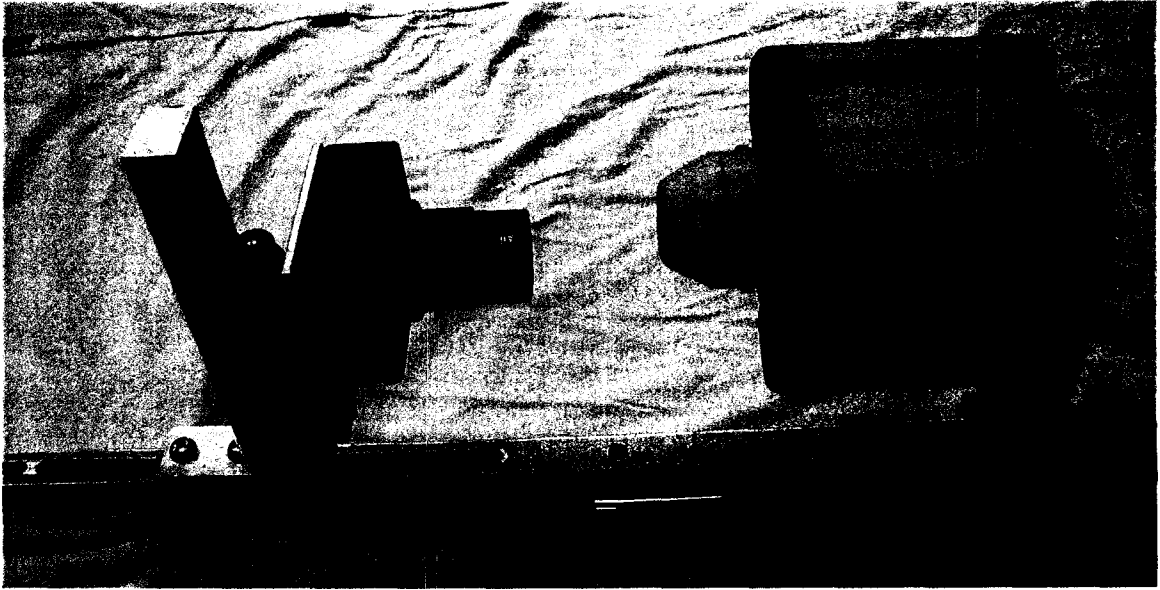


Figure 6.10 — Rail for Holding Camera and Laser.

The length of the rail was set to allow for baseline lengths ranging from 3 inches to 30 inches. Figure 6.11 shows the rail with the camera and laser placed at the baseline distances implemented for these experiments.

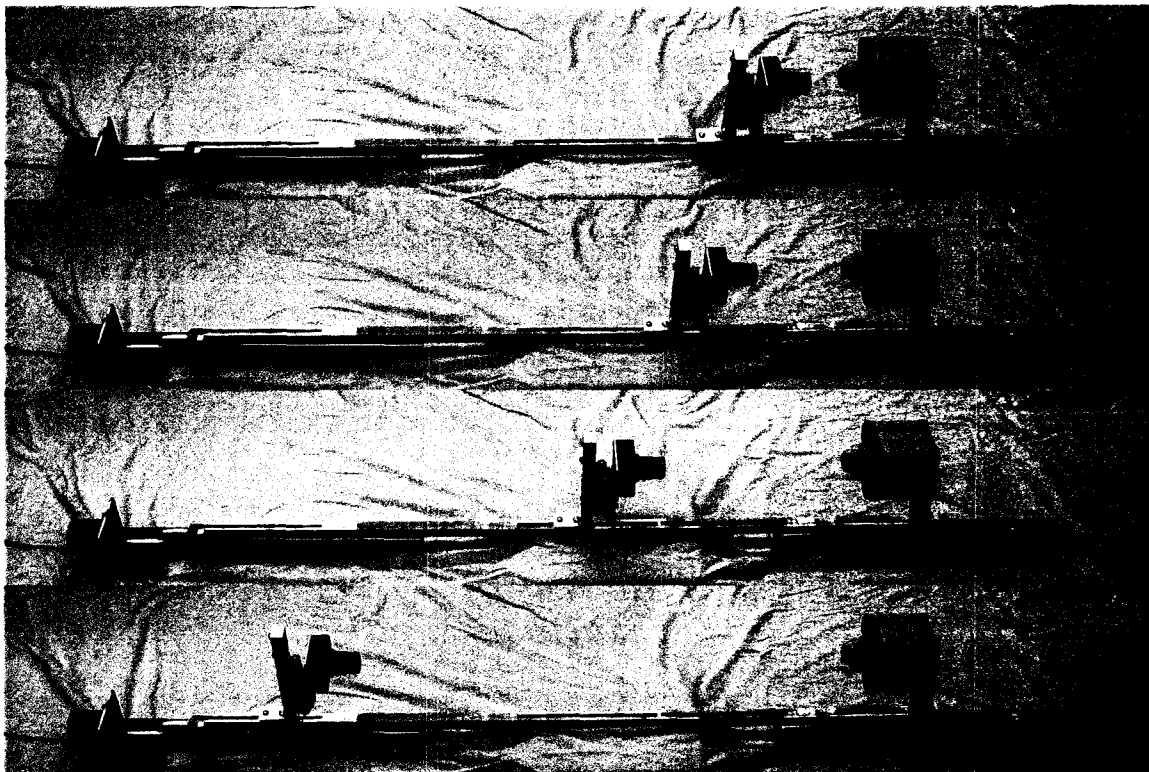


Figure 6.11 — Rail Spacings of 3, 6, 12 and 30 Inches (Top to Bottom).

The measurement system was incrementally translated along the axis of the pipe section to be profiled. To facilitate this motion, a precision carriage advancing system was implemented. The system consisted of the linear bearings on which the measurement system was fixed, a lead screw driven by a stepper motor, and a stepper motor driver interfaced with a data acquisition board controlled with LabVIEW. Figure 6.12 shows the automated axial positioning hardware.

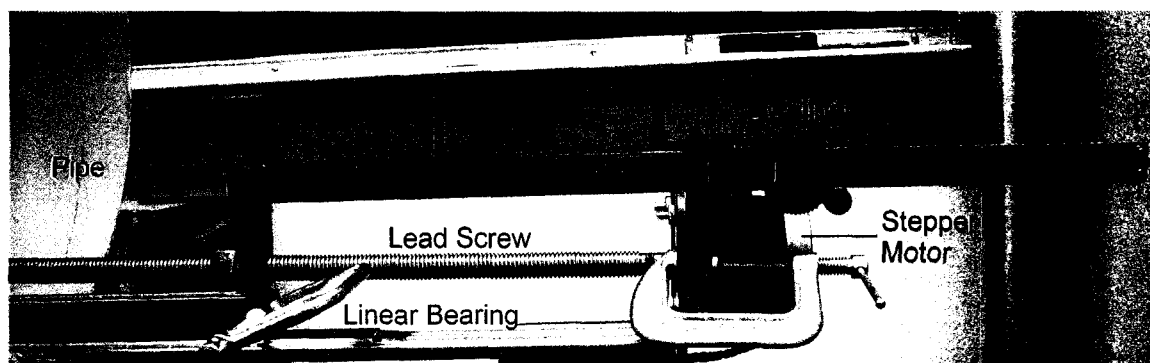


Figure 6.12 — Axial Positioning System.

The lead screw had a pitch of 13 threads per inch, and the stepper motor indexed 200 full steps per revolution. Thus, each step of the stepper motor was equivalent to an axial motion of 0.000385" of the measurement system. This axial measurement was verified using digital caliper. To obtain the desired increments of axial position, the stepper motor was instructed by the LabVIEW VI to step 260 steps for every profiling increment. Each step of the stepper motor was accomplished by sending the stepper motor driver one full digital clock cycle on its CLOCK input. The stepper motor also had a DIRECTION input so as to allow for motor reversal; however, the LabVIEW control VI (the LabVIEW Virtual Instrument program that controls the hardware) did not need to change this input. The following section will describe the control of the image collection process.

### 6.3.3 Image Collection

A LabVIEW VI was written to automate the image collection process. A total of four scans of the same section of pipe were performed, each scan with a different baseline length. The front panel of the VI provides an interface for a user to edit parameters which control how the VI executes and to monitor the output of the image collection

process. Figure 6.13 shows the front panel for the VI which controlled the image collection.

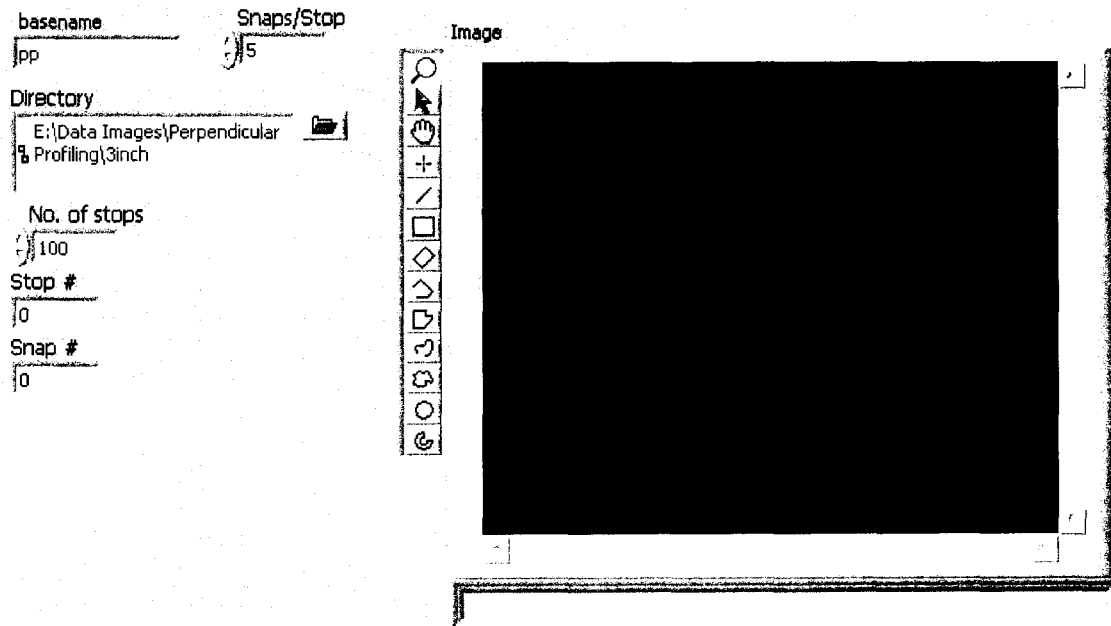


Figure 6.13 — Front Panel of Image Collection VI.

The user is allowed to control the “basename” (the filename of each image before indices are added), the “Snaps/Stop” parameter (number of pictures taken at each stop), the Directory where the images will be stored, and the “No. of Stops” (the total number of locations where images will be collected). The VI automatically adds indices to each image filename based on the axial position of the camera-laser platform. This automated process, which does not require input from the user, is completed through the Block Diagram of the VI which is provided in Figure 6.14.

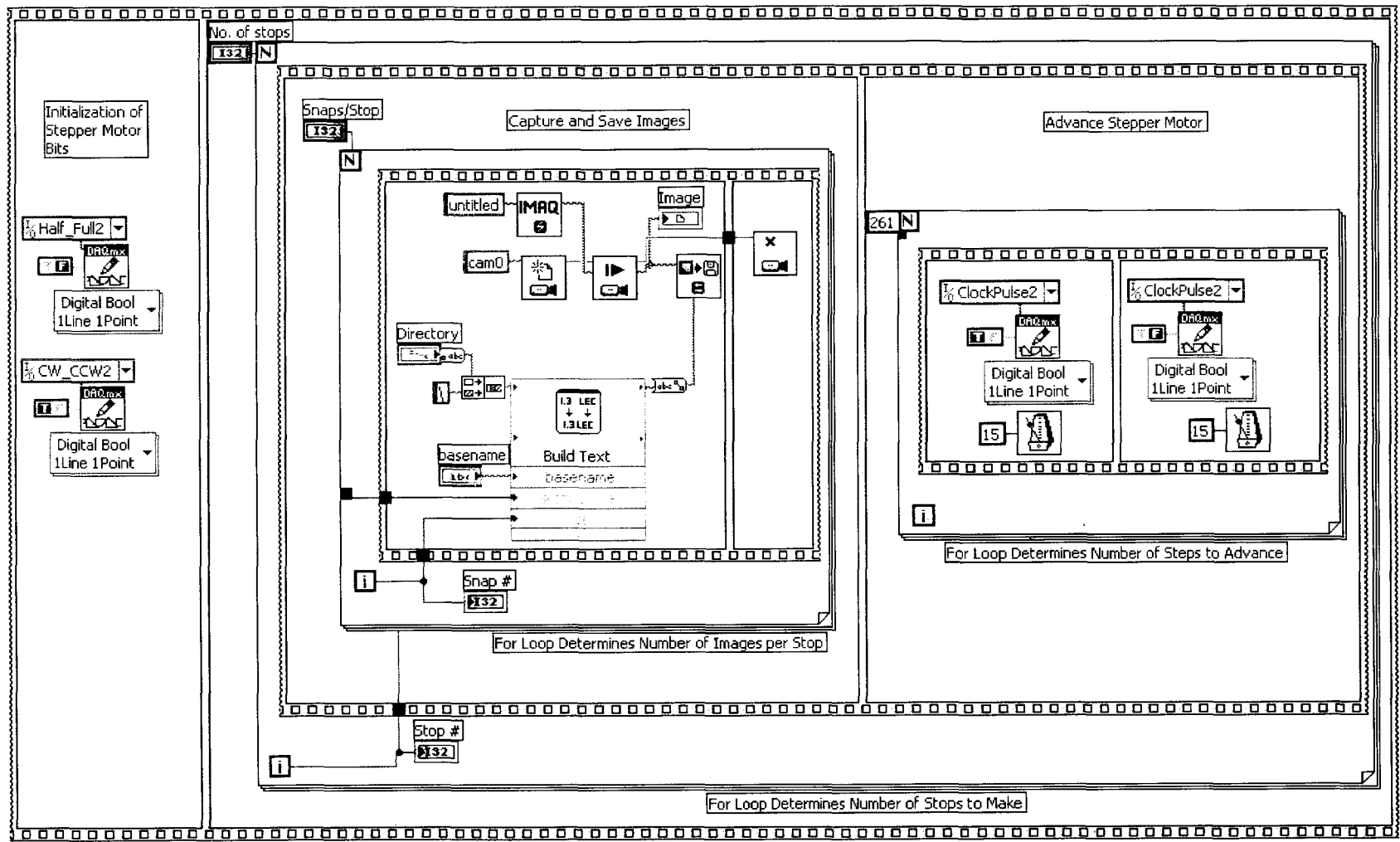


Figure 6.14 — Block Diagram of the Image Collection VI.

The first action performed by the VI is the initialization of control bits for the stepper motor that define the direction of rotation and control whether the stepper motor increments a full step or a half step for each clock pulse. The next action initiates a loop which controls the what happens at each stop of the carriage. During each iteration of this loop, a set of images is captured, and the stepper motor advances the carriage to the next stop. The “Build Text” block on the diagram is responsible for creating the filename for each image, including its indices. The filenames have the form *Directory\basename stopnumber index.png*, where *stopnumber* is a three digit integer representing the incremental carriage position and *index* is a one digit integer that keeps track of each image taken at a particular carriage stop (1<sup>st</sup> picture, 2<sup>nd</sup> picture, etc). The images at a particular *stopnumber* should all look the same; multiples were only taken for data redundancy.

#### **6.3.4 Image Processing**

The collected images were processed to extract coordinates defining the intersection of the laser line with the pipe wall. The desired data from each image is an array of ordered pairs defining the angular location (in radians) and the radius (in pixels) of the laser line relative to the center of the image. To accomplish this processing, a VI was written in LabVIEW, using several built in image processing and data analysis functions. Figure 6.15 shows the front panel of the image processing VI.

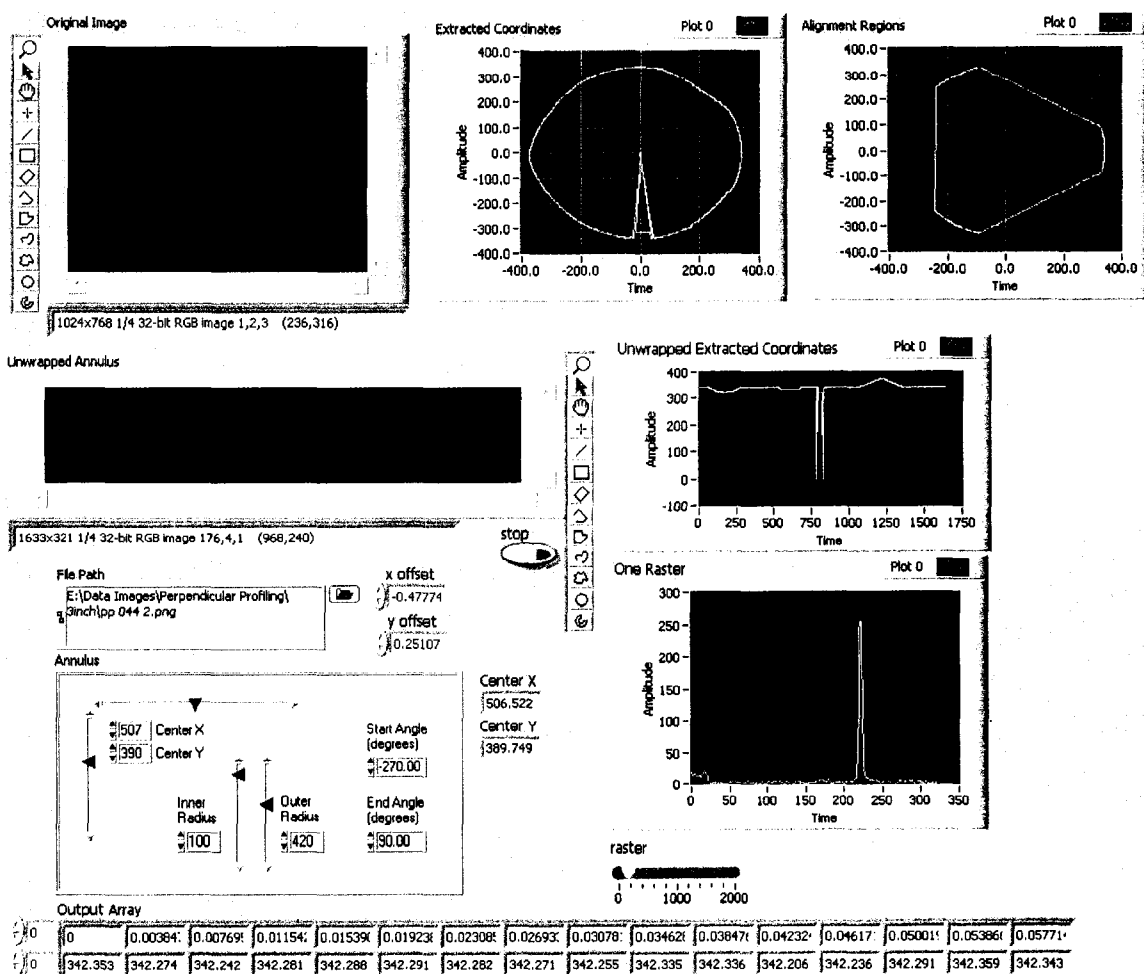


Figure 6.15 — Front Panel of Image Processing VI.

The front panel shows the original image, an unwrapped annulus, the detected line in that annulus, the re-wrapped detected line, and the alignment regions used to locate the center of the detected profile. The “File Path” box allows for a particular image file to be selected for processing, and the “Annulus” box allows the user to set the initial parameters for the annulus and monitor the progress of the center-finding algorithm.

The block diagram of the image processing VI has several modules associated with it. Figure 6.16 shows the block diagram used for image processing.



On the upper left portion of the VI diagram, the image is opened and passed to the initial processing steps. These steps include unwrapping an annulus, converting the image datatype to numerical arrays, and extracting one raster of red values in the unwrapped image. Next, the peak finding algorithm is employed to find the center of the laser line for each raster. The detected peaks are then passed to a process that identifies the image center of the detected profile. This new image center is used as a reference point to unwrap the original image again, finding new data points which define the location of the laser line. The iterative process is repeated until there is less than half a pixel of error between the calculated center of the profile and the center chosen for the annulus. After convergence, the output array will contain values of pixel radius versus angular location. The following sections describe the image processing process in detail.

#### **6.3.4.1 Initial Processing**

Before any other transformations are performed on the images, they are processed by unwrapping an annulus from within the original image which contains the laser line. The annulus can then be displayed as a rectangular image. Each vertical raster of the unwrapped image represents a radial line from the center of the original image. There are approximately 1500 of these vertical rasters in the unwrapped annulus. Initially, the center of the annular ring is selected arbitrarily somewhere near the center of the frame. (A process for more accurately determining the center of a profile will be discussed later.) Once the annulus is unwrapped, LabVIEW image processing functions are utilized to change the image datatype to a 2D numerical array (with each element representing a pixel). A cluster of three eight bit color values exists at each pixel, corresponding to red intensity, green intensity and blue intensity. Since this algorithm identifies a red line

within the image, the red values are isolated raster by raster. One vertical raster (a 1D array) of red values is passed to the peak finding algorithm at a time.

#### **6.3.4.2 Peak Finding**

A built-in LabVIEW function identifies peaks in each 1D array of data by fitting parabolas to the red pixel intensities. Two parameters define the behavior of the peak finding routine. First, a window width is specified that defines the number of red pixel intensity values to use in fitting each parabola. The window is moved along one pixel at a time until the entire vertical raster has been traversed. For example, a window of 10 red pixel intensities would be used to fit 191 individual parabolas for a vertical raster containing 200 values. The second parameter defining the behavior of the peak finding routine is a threshold that sets the minimum parabola height to consider as a peak. The threshold corresponds to a red pixel intensity level that would indicate the presence of the laser line. Any location where the fitted parabola reaches a height above the threshold value is identified as a peak. If proper values are selected for the width and the threshold, then each raster to be scanned should return only one peak. Through trial and error, it was discovered that a width of 8 data points and a threshold of 45 (out of 0-255) for the red pixel intensity yielded good results. Using these values with the experimental apparatus, there were a few occasions when zero or multiple peaks were identified, usually due to occlusion. In these cases a value of -1 is written to the stored data file for easy removal during post-processing.

#### **6.3.4.3 Center Finding**

The section of pipe on which the tests were performed was intentionally constructed with three general angular regions where no features were located. These

regions were to be utilized to evaluate the center of a profile. The plot titled “Alignment Regions” on the front panel shown in Figure 6.15 shows the orientation of these featureless angular regions. The long straight lines located at one o’clock, five o’clock, and nine o’clock represent areas not included in the centering evaluation while the arcs at three o’clock, seven o’clock, and eleven o’clock represent the areas used for the centering of the profile. An application of Green’s theorem was used to evaluate the centroid of the three arcs. Green’s theorem takes an ordered set of points and evaluates the centroid of the polygon that they define. Green’s theorem is given by equations (6-11) and (6-12).

$$x_C = -\frac{\frac{1}{6} \sum (y_{i+1} - y_i)(x_i^2 + x_i x_{i+1} + x_{i+1}^2)}{\frac{1}{2} \sum (y_i + y_{i+1})(x_{i+1} - x_i)} \quad (6-11)$$

$$y_C = \frac{\frac{1}{6} \sum (x_{i+1} - x_i)(y_i^2 + y_i y_{i+1} + y_{i+1}^2)}{\frac{1}{2} \sum (y_i + y_{i+1})(x_{i+1} - x_i)} \quad (6-12)$$

Recall that the center of the unwrapped annulus was only estimated to perform these calculations. Based on the location of the centroid of the profile given by these equations, an estimate of the true centroid of the profile may be determined by subtracting the estimated center coordinates from the evaluated centroid. This process gives the new location in the image about which the annulus will again be unwrapped. Since a new location is being used to unwrap the annulus, the centroid evaluation must be performed to determine if the offsets used in the last iteration were adequate. The centroid evaluation is considered to have converged when less than a half pixel of difference exists between two successive iterations.

#### 6.3.4.4 Real-Time Visualization and Output

Once the true center of the profile is determined, the identified laser line can be visualized on the front panel of the VI in two ways. The window called “Unwrapped

Extracted Coordinates” provides a view of the peak intensity of the laser line in unwrapped form. The base line (not including the features) is seen to be very flat. This indicates that the center of the profile is being used for the annulus unwrapping step. The other visualization provides a view of the profile after “re-wrapping” it back to its original circular form. One may note that the detected profile matches the laser line profile in the “Original Image” window (with the exception of a few locations where a laser peak was not identified near a discontinuity in the profile). This provides confidence that the profile detection has been successful.

A partial listing of the “Output Array” is provided at the bottom of the window in Figure 6.15. The top row represents angular values of each identified pixel (measured in radians), and the bottom row represents the distance in pixels from the center of the image to the identified pixel.

#### **6.3.4.5 Parsing Multiple Images**

Not all of the identified pixels are utilized to construct a 3D model of the pipe wall. Only specified angular increments are needed, and the rest of the points are ignored. Also, since each image only represents one slice of the pipe, more than one image must be considered to build a complete wireframe model of the pipe wall. The VI described above for determining the location of the laser line was embedded as a sub-VI into the VI shown in Figure 6.17 to perform the parsing.

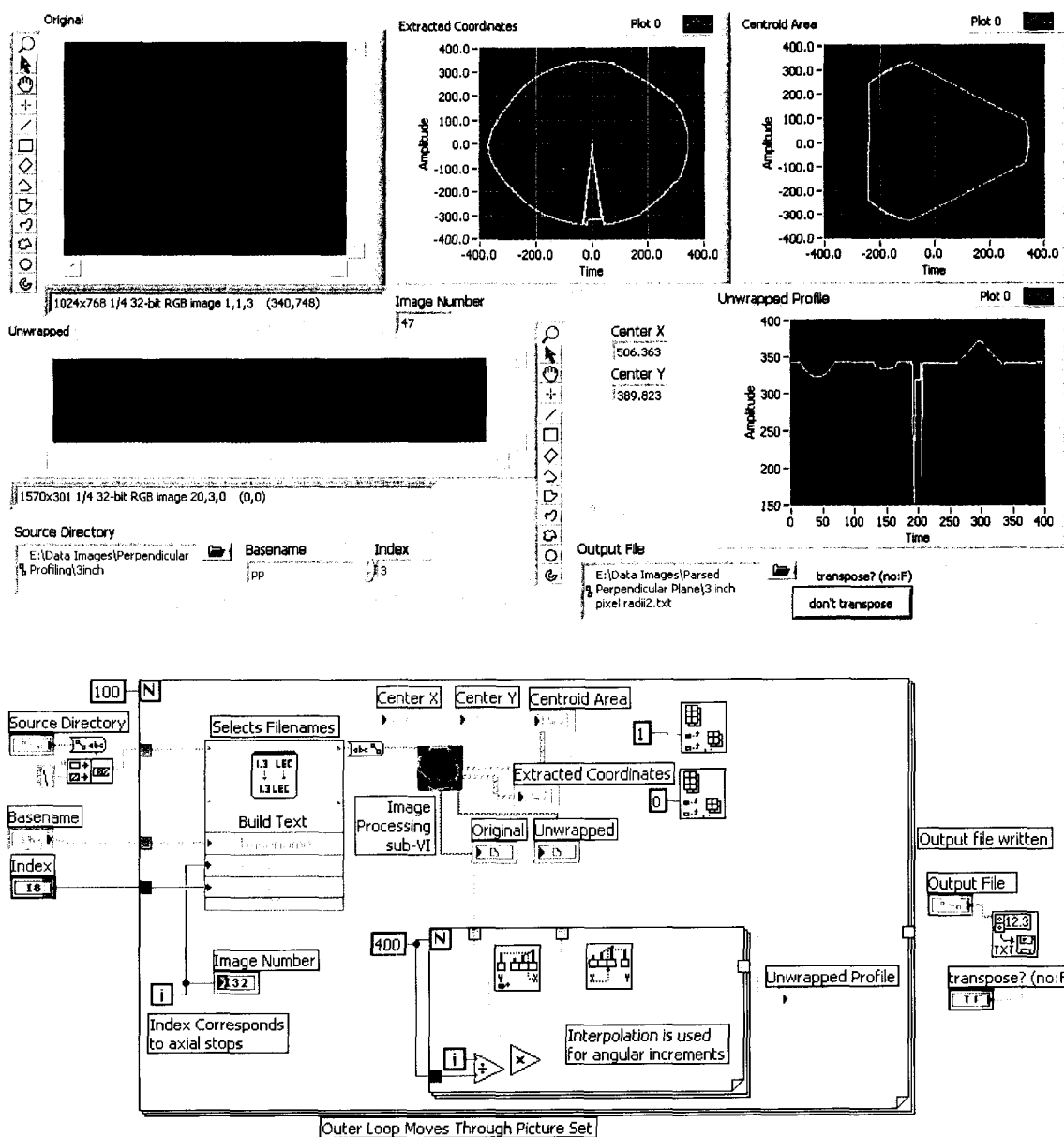


Figure 6.17 — Parsing Multiple Images VI.

Most of the output on the front panel of this VI comes directly from the image processing VI described in the previous section. Hence, as a set of pictures is parsed, the user can monitor the progress. The output of this VI is a two-dimensional array of pixel radius coordinates. These pixel radii are placed in the two-dimensional array according to their angular and axial coordinates. Each column of pixel radii corresponds to one

reduced ring of data taken from a single image; therefore, the column location of a particular pixel radius value indicates its axial increment number. The row location of a particular pixel radius value corresponds to the angular increment number for that value. The number of angular increments are reduced to 400 (from about 1600 rasters analyzed by the image processing VI), or about  $0.9^\circ$  per increment. Since the pipe has a radius of about six inches, this means that the circumferential arc length increment will be very close to 0.1 inch. This corresponds well with the 0.1 inch axial increment which was used between successive rings during data collection.

### **6.3.5 Application of Calibration**

The image processing steps described until now return image radii of the detected laser line. To return useful measurements to the user, these pixel radii must be converted to real units of length describing pipe radius. The sine-law model is applied to the pixel radii to yield these real measurements. A VI was written which sorts through the collected data, throwing out invalid data and applying the sine-law calibration to all valid data. Figure 6.18 shows the front panel and block diagram of the calibration VI.

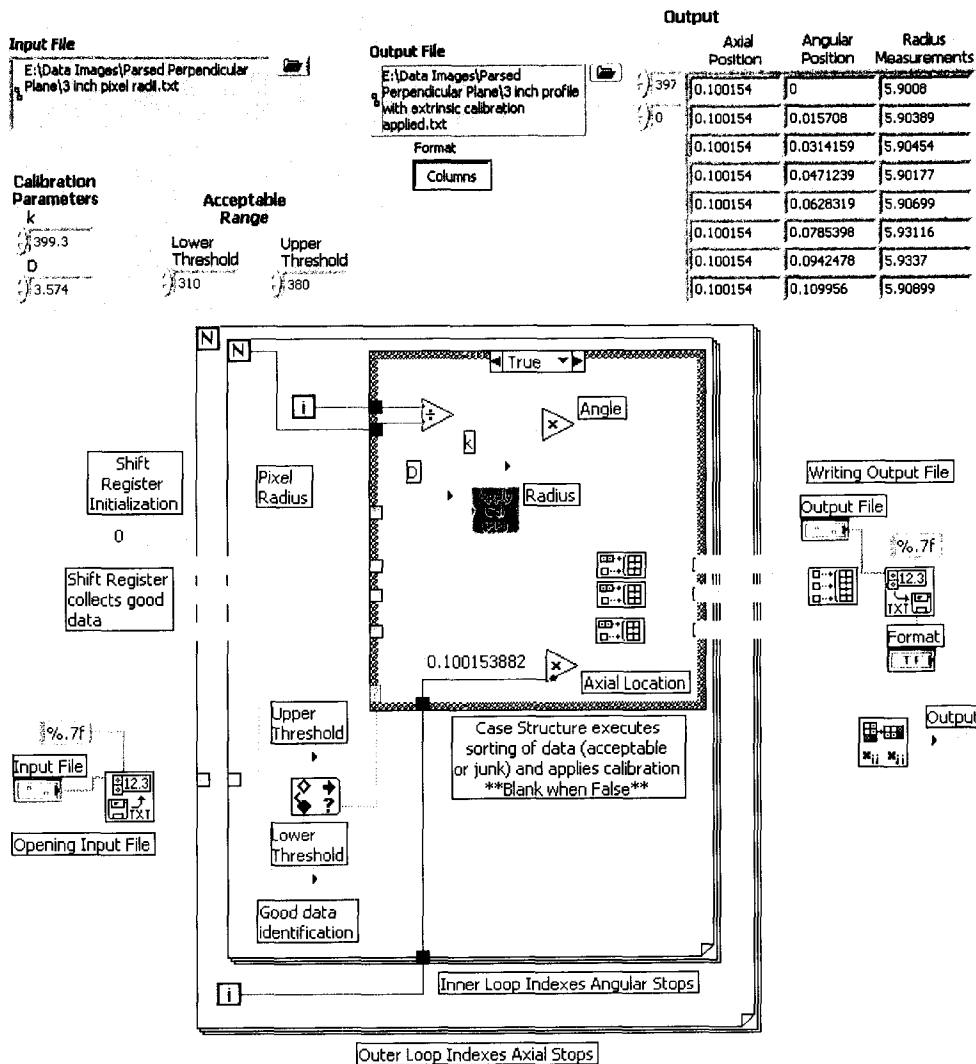


Figure 6.18 — Calibration VI.

The processed data is stored in an array of ordered triples. The first element of each triple is the distance along the axis of the pipe, the second is the angle around the circumference of the pipe wall and the third is the measured radius at that point. These ordered triples are stored in a text file to be used by other VIs.

### 6.4 Profile Visualization

Another VI was written to visualize the data stored in a text file of ordered triples. The front panel and block diagram of this VI is shown in Figure 6.19.

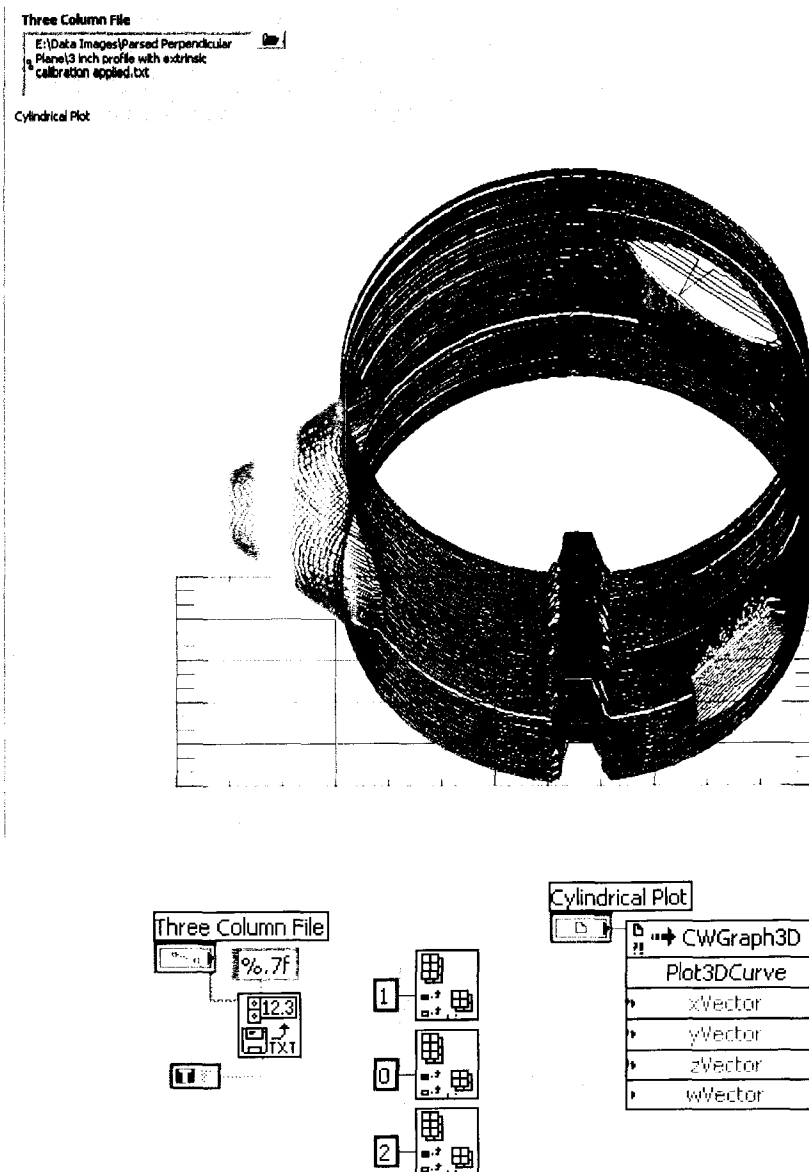


Figure 6.19 — Profile Visualization VI.

The block diagram shows how the file with three columns of data is opened, split into three separate vectors of data, and fed to the LabVIEW plotting package. The LabVIEW package for 3D plotting is called CWGraph3D; the package provides many options for displaying three and four dimensional data. The user may dynamically rotate the view for inspection of details, and the package can display point clouds, lines, or

surfaces. The line option is shown in Figure 6.19. A pipe geometry with a conical protrusion was profiled using the prototype system developed, as shown in Figure 6.20. Comparing the profile in Figure 6.19 with the actual pipe geometry in Figure 6.20 visually confirms the functionality of the profiling apparatus and the associated LabVIEW VIs.



Figure 6.20 — Pipe Test Section.

#### 6.4.1 Output for Various Baseline Lengths

The LabVIEW VIs discussed above were developed to utilize any baseline distance. Four different sets of data were collected for the 3, 6, 12 and 30 inch baseline distances. Three-dimensional views of all four sets of collected data are shown in Figure 6.21.

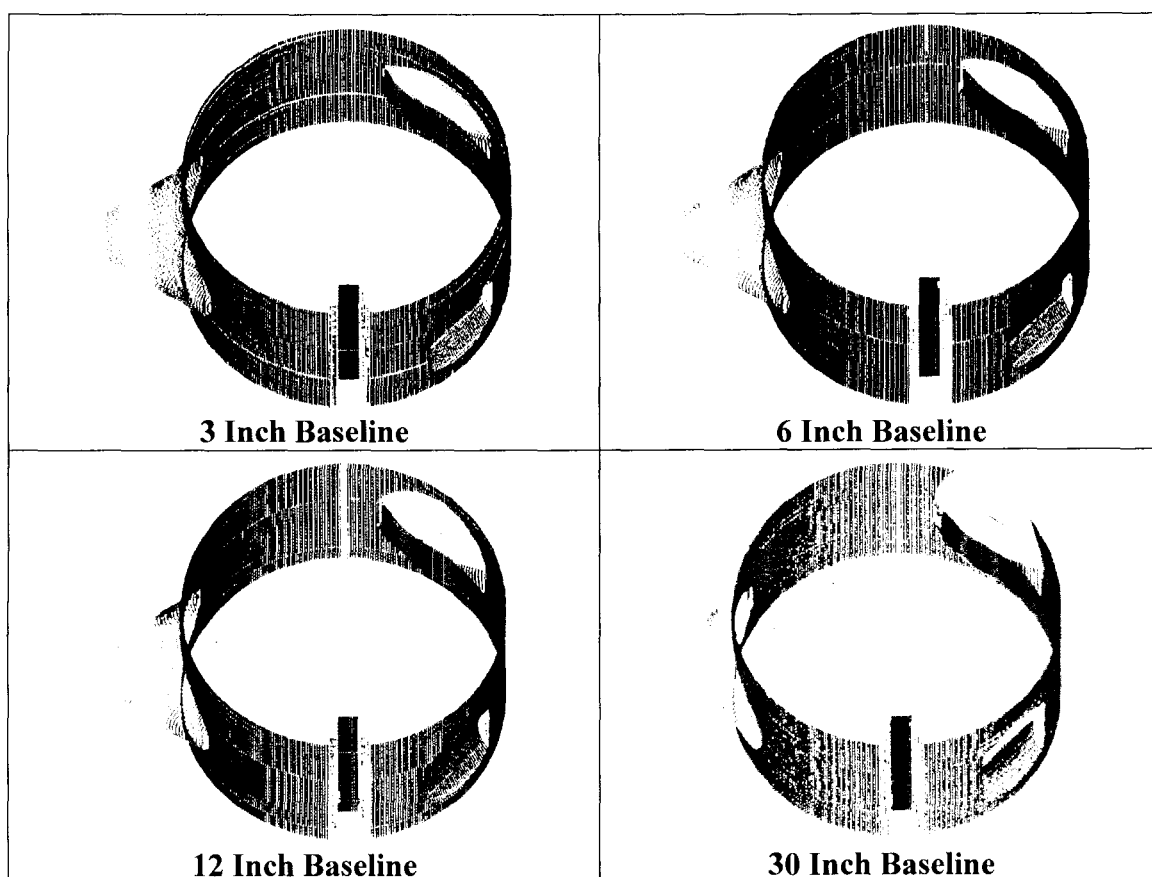


Figure 6.21 — Three Dimensional Visualizations.

The ridge seen at the bottom of the pipe corresponds to the rail that transports the camera-laser unit. The other features were intentionally added to the pipe to demonstrate the capabilities and limitations of the measurement system. One of the limitations is occlusion, which is most evident in the 30 inch baseline profile.

#### 6.4.2 Observations

Two observations are evident when examining the output from the visualization VI. Probably the more obvious of the two is the issue of occlusion. Figure 6.22 shows the profile visualizations from the front and the top. The top view clearly shows that as the baseline length increases, the tendency of the system to fail to capture the full extent and details of the protruded region also increases. Chapter four discusses the theory

behind this tendency. The other observation to be noted is that the shorter the baseline length, the more “noisy” the profile appears. When looking at the profiles from the front, this can be seen in a thicker line of points representing the pipe wall. From the top view, if the right and left tangential edges are examined closely, it appears that there is less consistency as the baseline length shortens. This effect, and how it pertains to accuracy of the system will be examined further in Chapter eight.

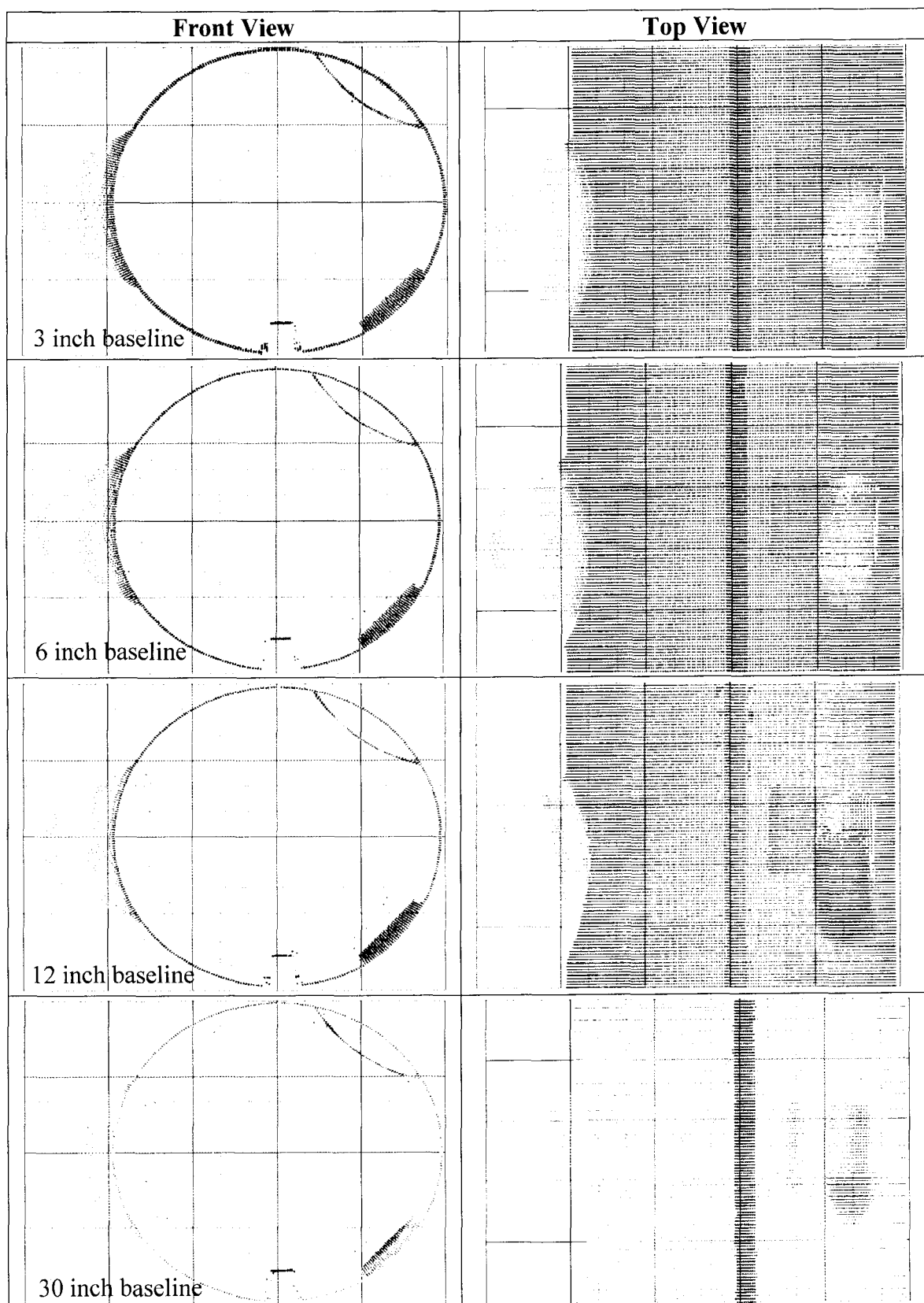


Figure 6.22 — Top and Front Views of Profiles.

## 6.5 Conclusions

A system to profile a pipe using the perpendicular plane profiling method was constructed and demonstrated. The camera used in each setup was calibrated using a special stand that facilitated the comparison of target coordinates with image coordinates. The calibrated camera along with a laser that generates a radial plane of laser light were assembled to a specially constructed rail and automated carriage advance system. Custom VIs were prepared to collect images, parse the images, and display the resulting profiles. The profiles obtained correctly reflect the shape of the pipe, and the expected occlusion effects from the long baseline setups were noted. The perpendicular profiling equations derived in Chapter four seem to accurately reflect the behavior of the measurement system.

## CHAPTER 7

# OBTAINING PIPE PROFILES USING THE SIDE-FACING PROFILING METHOD

### **7.1 Introduction and Overview**

A side-facing laser pipe profiler was fabricated and tested to evaluate the performance of the side-facing profiling model described in Chapter five. The model adopts an origin, called the entrance pupil, located relative to physical features of the camera using an experimental procedure. A rotating profiling head (camera and laser) was designed to allow for the accurate placement of the entrance pupil relative to the axis of rotation and the orientation of the laser plane. Once this head was set up properly, it was mounted to a specially prepared calibration fixture to adjust its field of view and to associate image coordinates with pipe radii. The profiling head was then affixed to the moveable rail described in Chapter six, and the same section of pipe was scanned. The images collected from this scan were stored, analyzed, and rendered using specially designed LabVIEW image processing routines similar to those in Chapter six.

### **7.2 Determining the Location of the Entrance Pupil**

The triangulation scheme developed in Chapter five is predicated on the assumption that the camera uses a single viewpoint. For the lenses being used in this experiment, this is a good assumption, yet for any particular lens, determining the location of this point is

not trivial. This single point of view of the camera is called the entrance pupil. It represents the origin of the spherical coordinate system used to relate pixel coordinates to world coordinates.

### 7.2.1 Methodology

One method to locate the entrance pupil involves rotating the camera about a known axis and taking pictures of two objects at differing depths away from the lens. By tracking the relative motion of the two objects as the camera rotates, it can be determined whether the pivot point lies behind or in front of the entrance pupil. Figure 7.1 illustrates the effect that will be observed when the pivot point lies behind the entrance pupil.

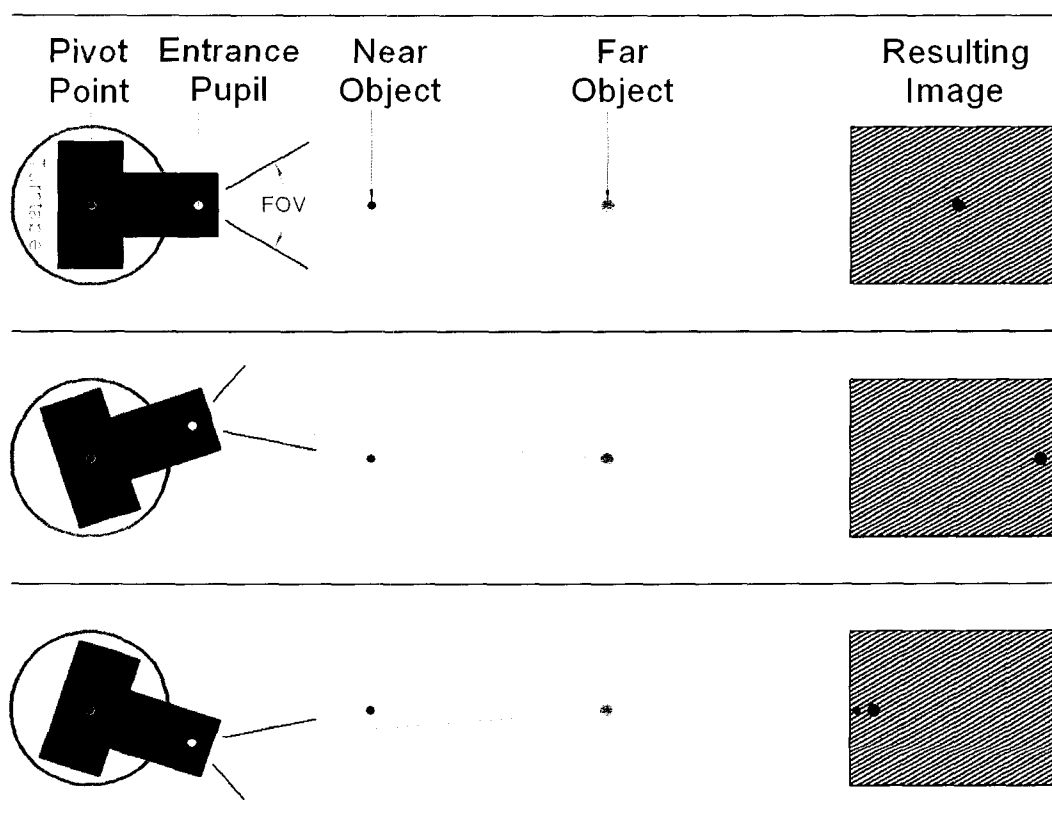


Figure 7.1 — Pivoting Behind Entrance Pupil.

A rotation about an axis behind the entrance pupil implies both a rotation and a translation of the entrance pupil. As such, objects closer to the camera will appear to change locations more rapidly than objects farther away.

The opposite effect will be noticed when the pivot point lies in front of the entrance pupil. Figure 7.2 illustrates this effect.

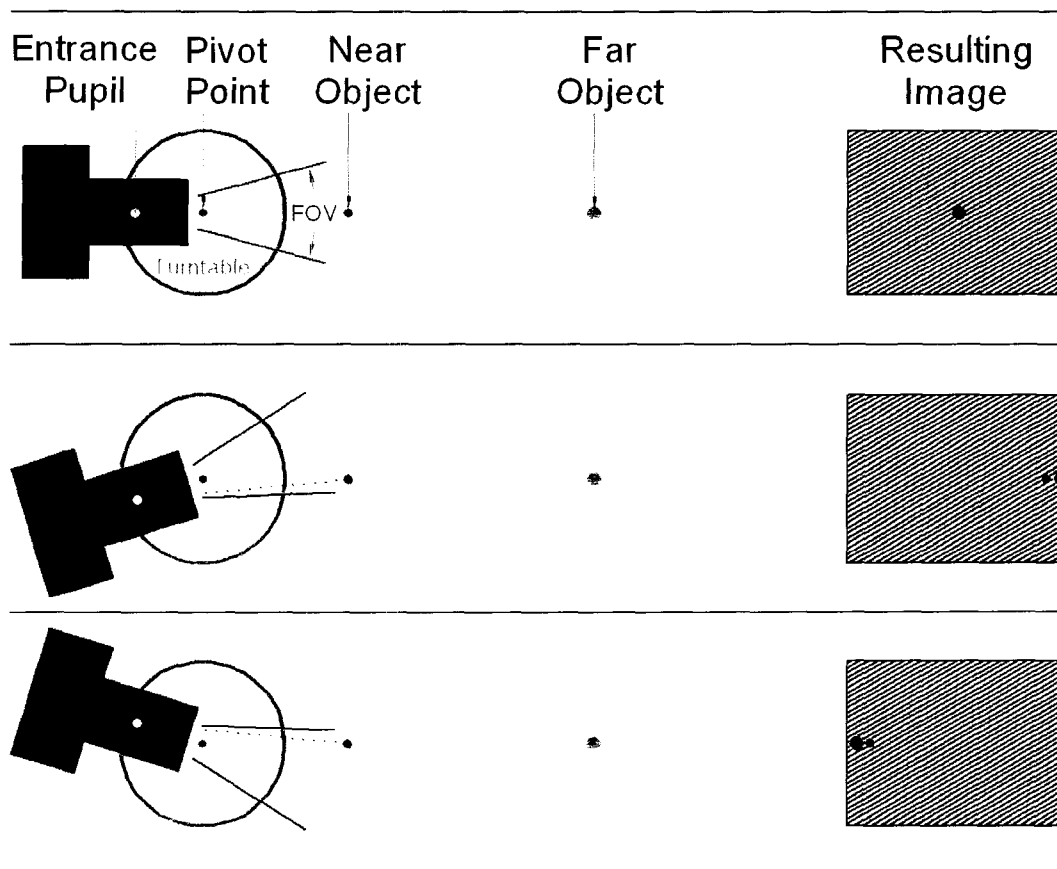


Figure 7.2 — Pivoting In Front of Entrance Pupil.

As the camera is rotated in this scenario, the entrance pupil still translates as it rotates, but in the opposite direction as before. This will cause closer objects in captured images to move less rapidly than more distant objects. The location of the pivot point

may be found by iteratively moving the pivot point until the near and far objects align in the image throughout the range of rotation.

### 7.2.2 Testing Fixture

To perform the procedure described above, a fixture was built that would move the camera about a known axis while capturing images of two pins at different distances from the camera. The fixture used for this procedure is shown in Figure 7.3.

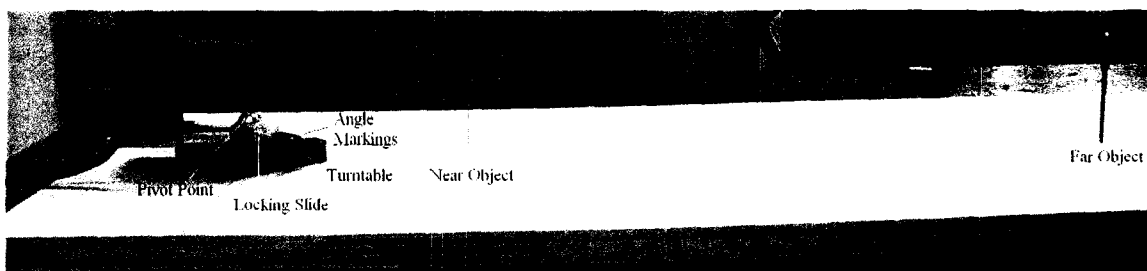


Figure 7.3 — Fixture for Determining the Location of the Entrance Pupil.

This fixture allows a user to affix the camera to the turntable such that the axis of rotation of the turntable intersects the axis of the lens while allowing the user to adjust where the axis of rotation of the turntable lies along the length of the lens. The locking slide mechanism can then be locked using the screw shown at the pivot point. The turntable is then rotated to both limits of the camera's field of view, and the relative motion of the near and far objects is observed.

### 7.2.3 Procedure

At the first stage of the process of finding the entrance pupil, the pivot point was found to lie to the rear of the entrance pupil. Note how the closer object moves farther in the captured images than the more distant object in Figure 7.4.

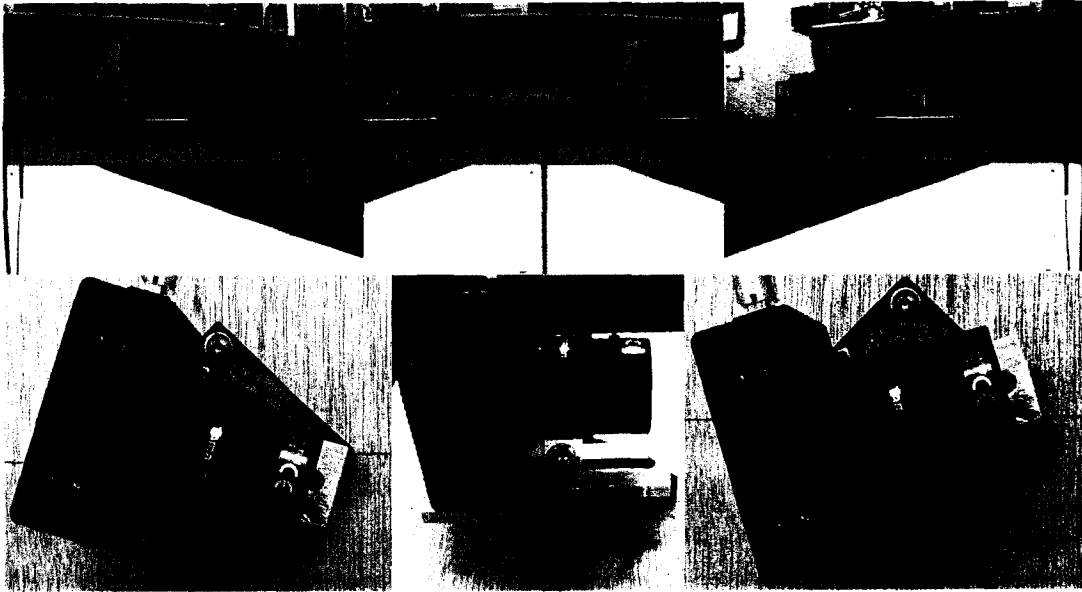


Figure 7.4 — Pivot Behind Pupil.

The locking slide mechanism was released and slid backwards. At the new location, the pivot point was found to be in front of the entrance pupil. Note how the closer object does not move as far as the more distant object in the captured images of Figure 7.5.

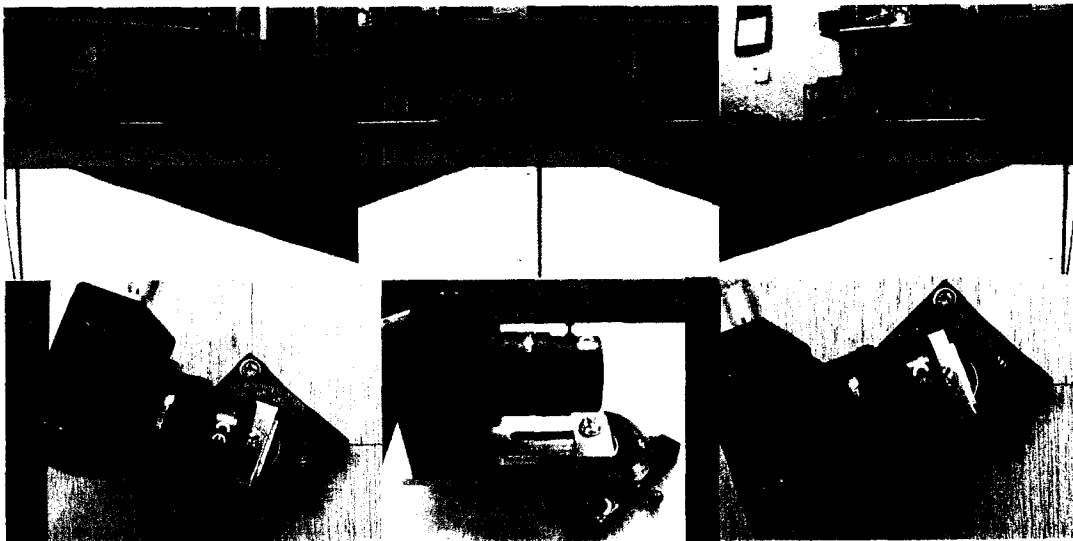


Figure 7.5 — Pivot In Front of Pupil.

The location of the entrance pupil was now bounded within the range of the locking slide mechanism. The process of determining the exact location of the entrance pupil was iterative; for each iteration, the locking slide mechanism was moved in the direction determined by the last iteration. The location of the entrance pupil was determined to be found when no difference in the relative movement of the near and far objects could be detected in the captured images. Figure 7.6 shows the results of this process.

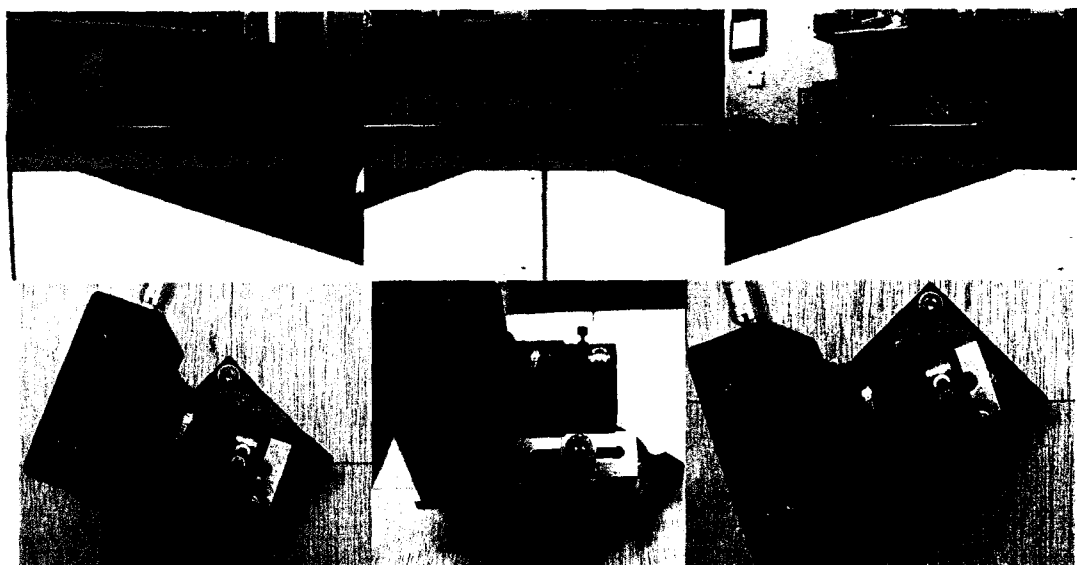


Figure 7.6 — Axis of Rotation Coincides with the Entrance Pupil.

Notice that the near and far objects travel together as the camera is rotated. This means that the entrance pupil has been found.

### 7.3 Rotating Profiling Head

The measurement head used to make the measurements is designed to match as closely as possible with the model described in Chapter five. This model specifies a head

that is capable of precise rotation so as to allow for measurements of the entire circumference of the pipe wall. It also specifies that the origin of the camera should lie in a plane which has two constraints. The first of these constraints is that the plane should contain the axis of rotation of the measurement head. The second constraint is that the plane should be perpendicular to the plane of the projected laser.

### 7.3.1 Physical Arrangement

The profiling head is constructed of aluminum. The laser projector is mounted such that the laser plane it produces passes through the axis of rotation. It is mounted such that the exit aperture is located just slightly behind the axis of rotation to make it easier to verify that the laser plane it produces passes through the axis of rotation. Above the laser projector, there is a wing into which several holes are drilled. These holes are drilled in a plane that is perpendicular to the laser plane and passes through the axis of rotation. The holes are drilled at distances of 1.8, 2.4, 3.0, and 3.6 inches away from the axis of rotation. These distances were chosen to correspond with  $\bar{D}$  values of 0.3, 0.4, 0.5, and 0.6, respectively, for a nominal pipe radius of 6 inches. The holes are tapped to accept the screw from the locking slide mechanism described in section 7.2.2. Figure 7.7 shows the geometry of the arrangement of the rotating head fixture.

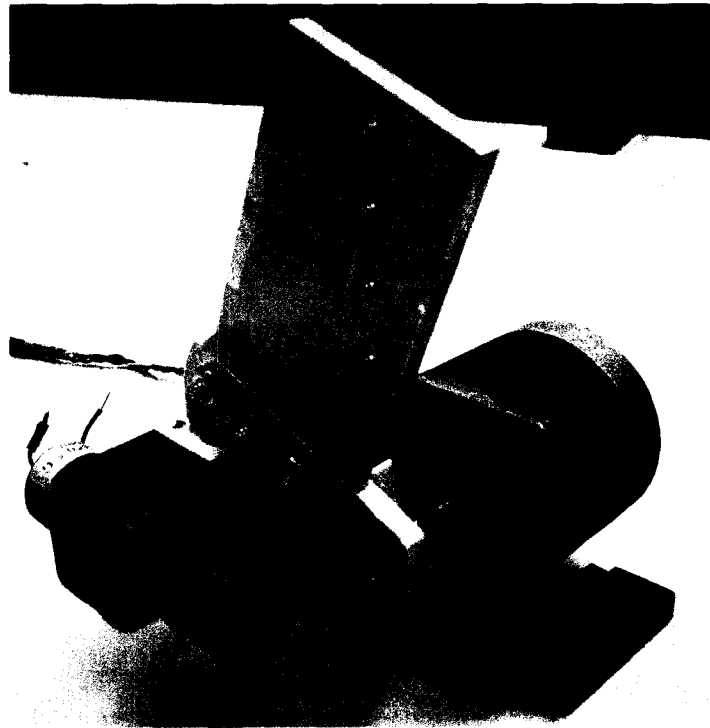


Figure 7.7 — Rotating Profiling Fixture.

The locking slide mechanism used in the location of the entrance pupil is used to precisely place the entrance pupil of the camera in the desired plane. When the entrance pupil is found, the precise distance from the front of the slide to the clamp is found using a dial caliper with a depth probe. The camera and locking slide assembly is then affixed to the wing of the rotating profiling fixture. Before the slide is locked down with the locking screw, the dial caliper is used to set the same distance between the pieces of the locking slide as determined in the entrance pupil location step. Thus, the camera is located such that its entrance pupil is directly over the tapped hole in the wing. Figure 7.8 shows the procedure for precisely setting the location of the entrance pupil of the camera relative to the laser projector and the axis of rotation.

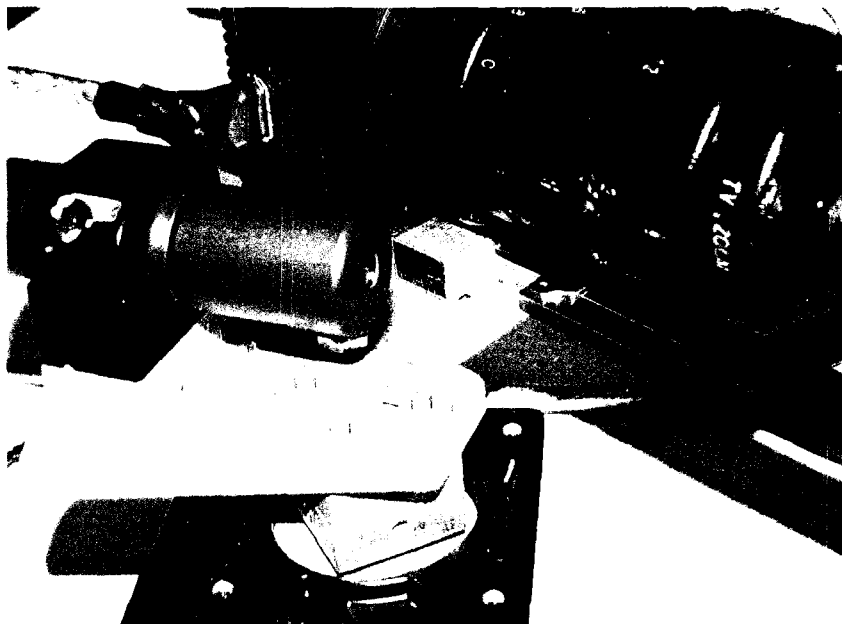


Figure 7.8 — Setting the Location of the Entrance Pupil.

### 7.3.2 Angular Indexing

The entire profiling head, which is set up according to the assumptions made in Chapter five, must be indexed precisely about its axis of rotation. To accomplish this, the head is attached to a stepper motor. The stepper motor is constructed to step 200 full steps per revolution, or 400 half steps. When used in the half-stepping mode, this implies an angular increment of  $0.9^\circ$ . If the radius measurements being taken are approximately 6 inches, this angular increment implies a circumferential increment of approximately 0.1 inch. This size of a measurement grid is expected to yield sets of radius data which capture the desired scale of features (about 1 inch).

### 7.4 Extrinsic Measurement Calibration

A relationship between the location of a laser line in an image and the range of that laser line to the target must be determined. It would be extremely difficult to construct the profiling head to precise enough tolerances to completely rely on the setup

functioning as predicted from the profiling models developed in Chapter five. The actual baseline lengths, field of view, camera aim angle, and other constraints are not known well enough from the fabrication process of the profiling head to trust that the design dimensions are the actual dimensions. To determine closer values to these actual parameters, a calibration procedure was performed. By correlating distance measurements made using a caliper with the images collected with the camera, the fixed parameters for the profiling model were determined. This correlation was performed by fitting a curve to the image coordinates of a point on a laser line to the corresponding geometrical position.

#### **7.4.1 Calibration Methodology**

The indexing profiling head is rigidly fixed to a stand such that the laser plane is parallel with the base of the stand. The camera is located above the laser projector. Also affixed to the base of the stand is a precision linear sliding bearing. The sliding portion of this bearing holds a target with a flat surface facing the measurement head. This surface is perpendicular to the laser plane and parallel with the axis of rotation of the indexing profiling head. The sliding bearing constrains the motion of the target to be parallel with the laser plane and perpendicular to the axis of rotation. Figure 7.9 illustrates this arrangement.

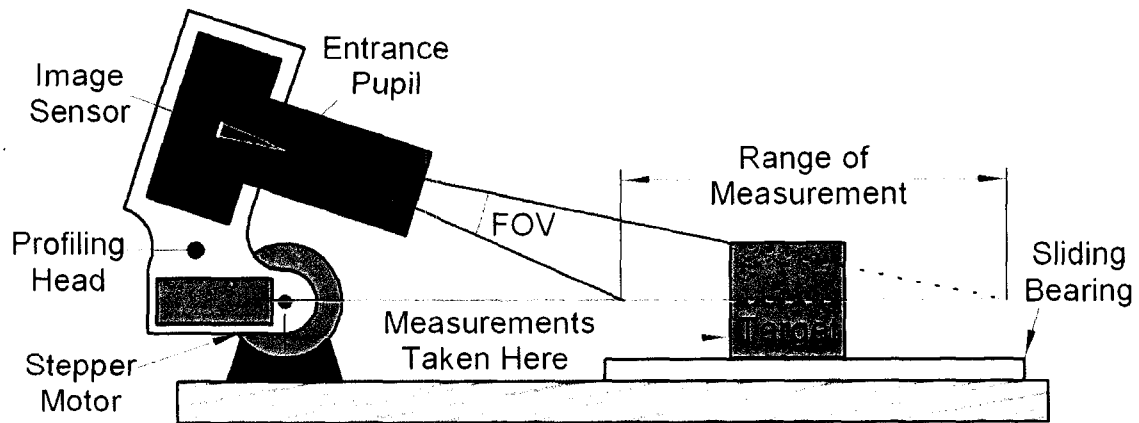


Figure 7.9 — Side-Facing Calibration Setup.

Before calibration data can be taken, the field of view (FOV) and the aim angle of the camera must be set. The aim angle is first iteratively set until an image of the laser line on the target at the farthest desired measurable range is the same distance from the center of the image as an image of the laser line on the target at the nearest desired measurable range. Next, the field of view is set such that an image of the laser line on the target at the farthest desired measuring range is located on the edge of the image. The first step can then be repeated, and the process iterated until the aim angle and the field of view of the camera are set according to the model in Chapter five.

Once these parameters are set, the calibration procedure can be performed. The target is moved incrementally from the near measurement limit to the far measurement limit. The location of each incremental stop is set by a caliper. At each stop, an image is taken and saved with a filename that indicates the range at which it was taken. The location of the laser line within each image is later determined using a peak-finding algorithm. These locations are plotted versus the ranges with which they are associated. A curve is fit to the data to determine the most suitable values for the parameters in the

profiling model developed in Chapter five. The determination of the best parameters for this model constitutes the output of this calibration procedure.

#### **7.4.2 Calibration Fixture**

To perform the calibration tests, a fixture was constructed. This fixture was constructed on a  $\frac{3}{4}$  inch thick plywood base. One edge of the plywood was very straight and served as a reference line for collecting perpendicular measurements. The stepper motor bracket was screwed to the base using a square to ensure that the shaft of the stepper motor was perpendicular to the edge of the base. Next, the slide was aligned parallel with the edge of the base and screwed down. The target was then aligned perpendicular to the slide and screwed to the moving part of the slide. A ruler printed on white paper was glued to the surface of the target. The ruler was divided into 20 divisions per inch and was designed for two purposes. The first purpose was to ensure that as the slide was moved, that the laser line maintained its location on the target. This verified that the target was translating parallel with the laser plane. The other purpose was to provide a reference for the physical width associated with a particular horizontal line within an image. Figure 7.10 shows the calibration fixture.

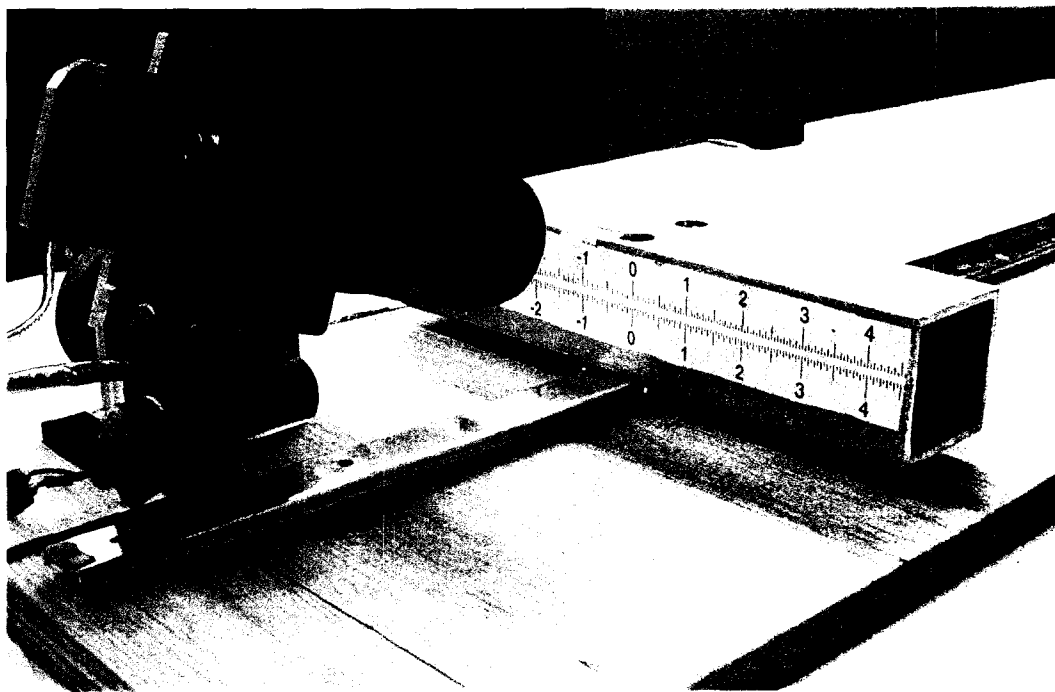


Figure 7.10 — Side-Facing Calibration Fixture.

As the calibration was performed, distance measurement defining the separation of the camera and the target were taken on the back side of the liner slide to provide for increased accuracy (it is difficult to measure from the entrance pupil to the target). To accurately set up the system, an internal divider was set at a known span, and the target was placed at that range from the shaft of the stepper motor. The distance between the two pieces of the linear slide was then measured, and the additive constant needed to relate the backside measurement with the desired measurement was determined. Figure 7.11 shows the steps involved in this process.

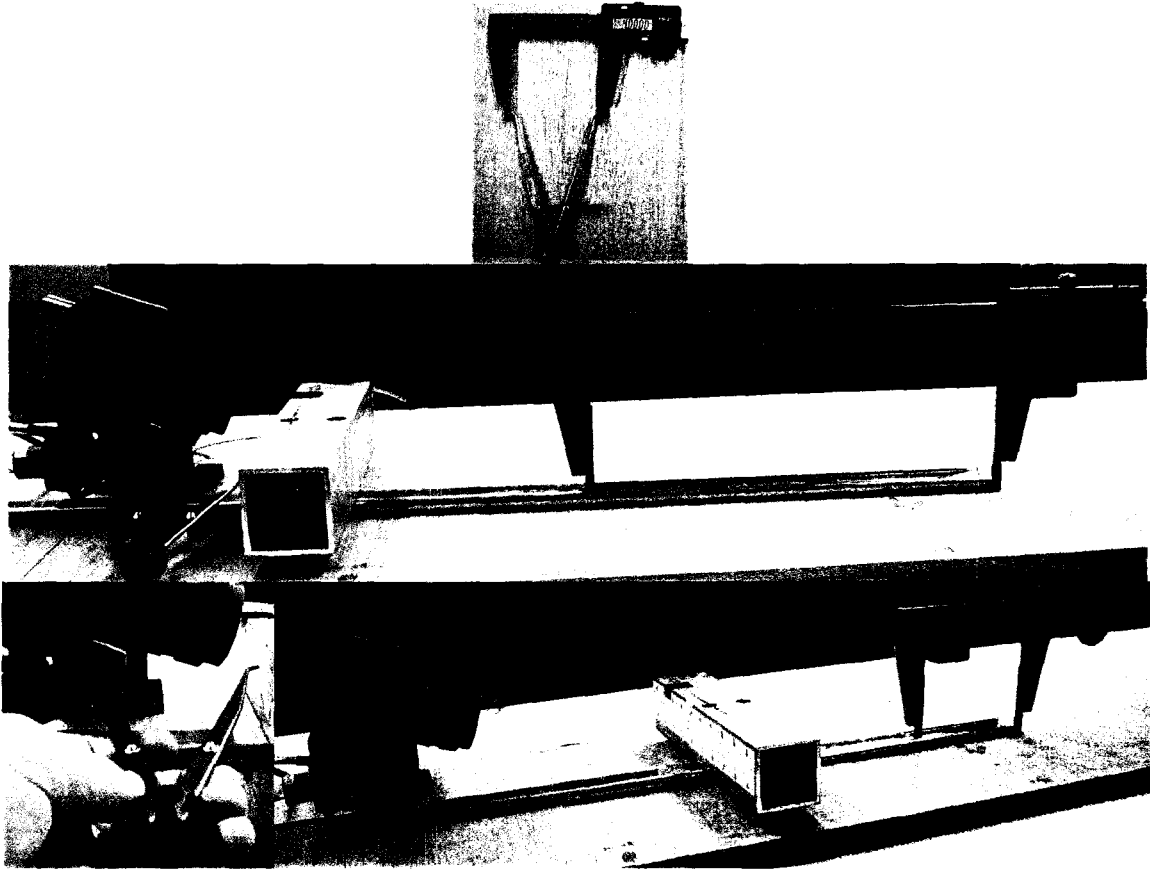


Figure 7.11 — Collecting Measurements for Calibration.

#### 7.4.3 Calibration Images and Data

To aid in the process of collecting the needed images and extracting the needed information, VIs were prepared in LabVIEW. The first of these VIs was a tool to assist in the process of collecting the calibration images. The front panel of the calibration image collection tool is shown in Figure 7.12.

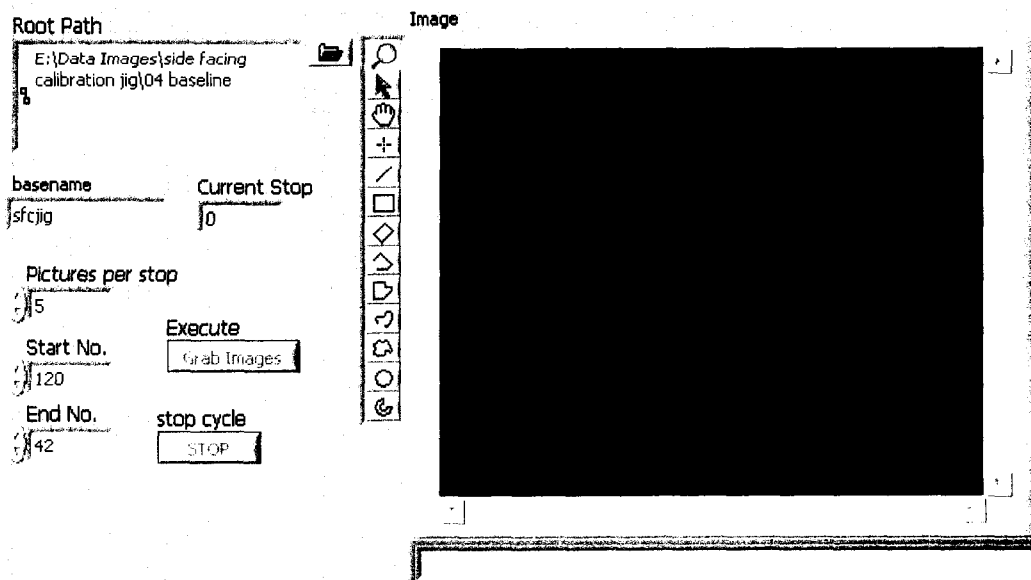


Figure 7.12 — Calibration Image Collection Tool.

On the front panel, the user can enter a root directory where the images collected will be stored, and a basename which serves as the filename onto which indices will be added to distinguish the multiple images to be collected. The user may also enter the beginning and ending image indices. In the example in Figure 7.12, the user has chosen to save images with indices between 42 and 120. These were chosen such that the indices would represent the number of 0.1 inch increments of range from the axis of rotation of the measurement head to the target. At an index of 120, the range is 12 inches, and at an index of 42, the range is 4.2 inches. The user may also specify the number of images to be snapped per stop for redundancy in image data. The front panel provides feedback on the current stop number and the most recent image snapped. The button labeled “Grab Images” on the front panel is the interface that by which the user instructs the VI to snap the images at the current stop. After the images are collected, the “Current Stop” value is updated, and the VI waits for the user to set the next range on the

calibration fixture. When the user has repositioned the calibration fixture and specified the new image index, the “Grab Images” button may be pressed, and the next set of images will be collected. The programming of the VI is set up such that the first image captured at each stop will have room lighting turned on, and the remaining images will only have laser illumination. The block diagram of this VI is shown in Figure 7.13.

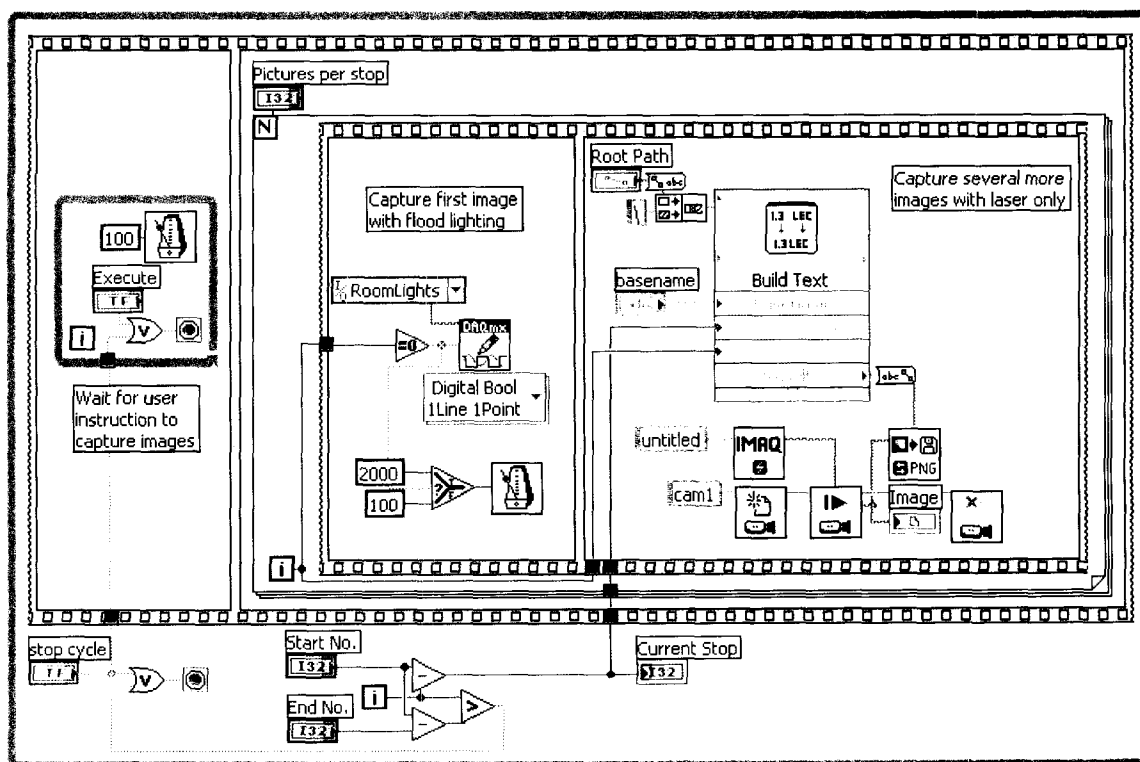


Figure 7.13 — Calibration Tool Block Diagram.

The images captured using the calibration image collection tool had to be processed to determine the location of the laser line at each stop. Since the location of the laser line in an image was a process that would also have to be performed when the profiling of a pipe was undertaken, a special sub-VI was prepared to accomplish this step. The VI scans each raster of an image and locates the highest peak of red intensity values

in each raster based on parabola fitting as described in Chapter six. The fractional pixel location where this peak is located within the raster is then stored in an array. If no peak is found in a raster, a value of -1 is entered in the array. This sub-VI accepts a name and directory path of an image file as an input and provides a one dimensional array as an output. The indices of this array correspond to the rasters of the source image, and the entries in the array correspond with the identified pixel location of the laser line. Secondary outputs of this sub-VI are the original image with the identified location of the laser line overlaid in blue, and a monitor of how many peaks are being found. The front panel and block diagram of the “Find Array of Peaks” sub-VI is shown in Figure 7.14.

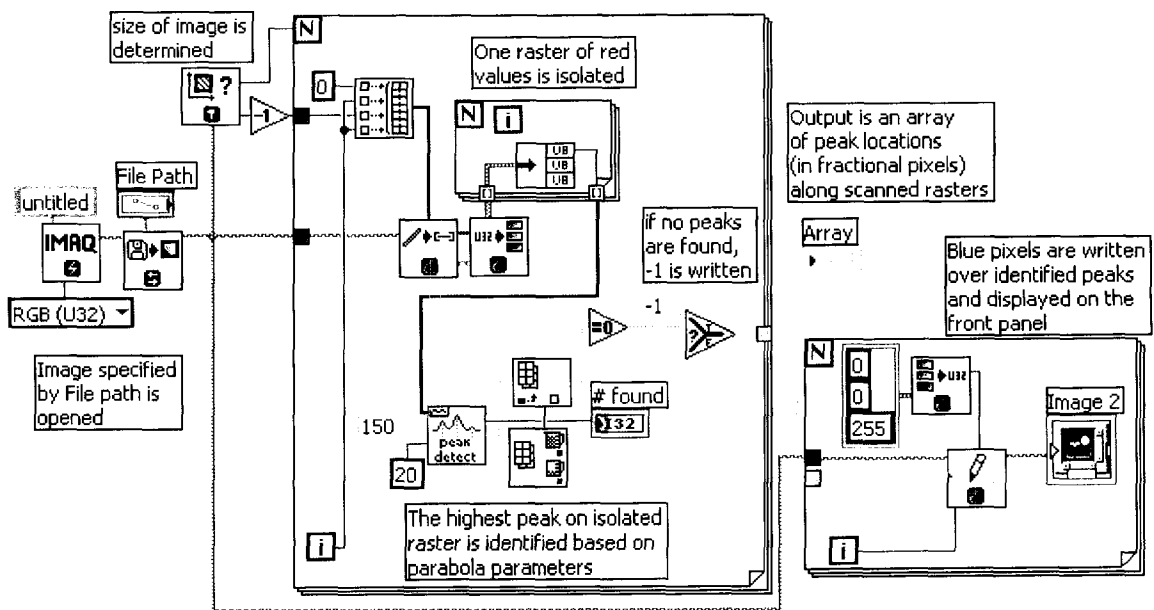
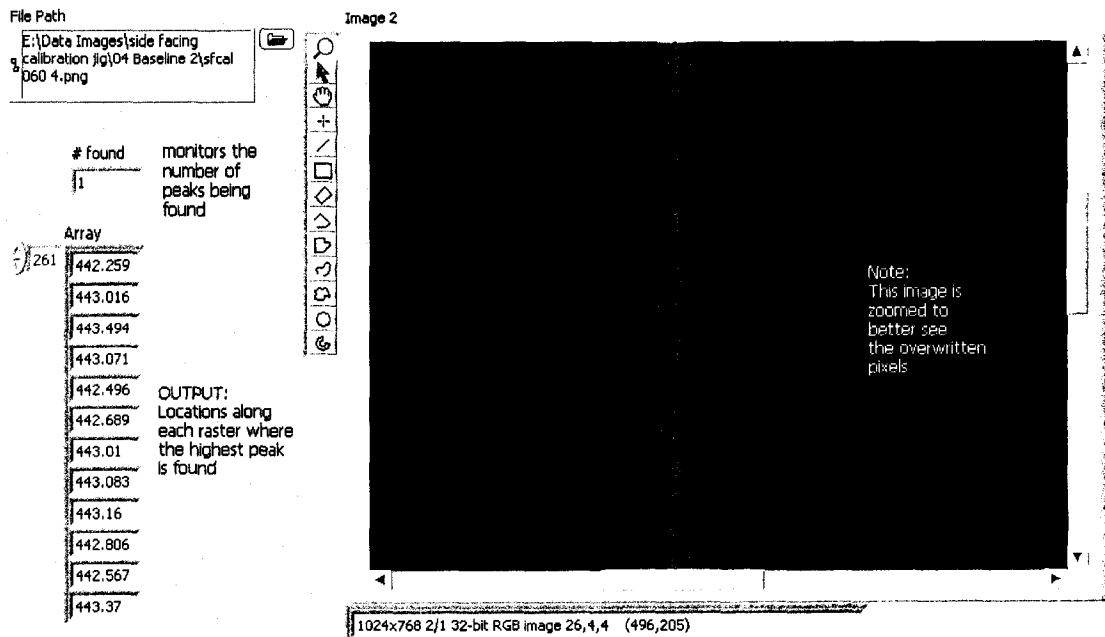


Figure 7.14 — Peak Finding Sub-VI.

Multiple images were collected for the calibration of the profiling head. A VI was prepared that parses through this set of images, calling the “Find Array of Peaks” sub-VI for each image and assembling the data into a single file. Some of the parameters

are similar for this VI as for the calibration tool VI. It allows the user to select a directory where the images to be parsed are located and select a basename and index range for the images to be parsed. The user can specify the name and path of the file into which the data will be written, and the orientation of this two dimensional data file. To monitor the progress of the parsing VI, there is a field that tells the user which stop is being processed and the filename and path of the image file that is currently being evaluated. This image is displayed for the user to monitor during the process. Figure 7.15 shows the front panel and block diagram of the calibration image parsing VI.

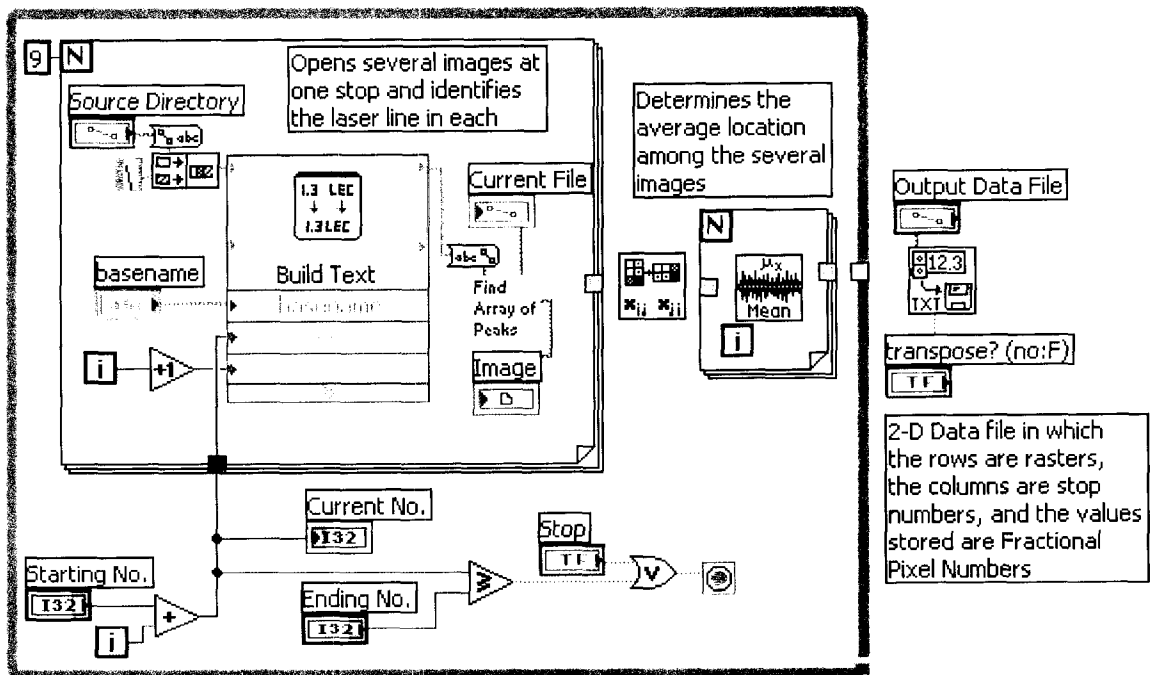
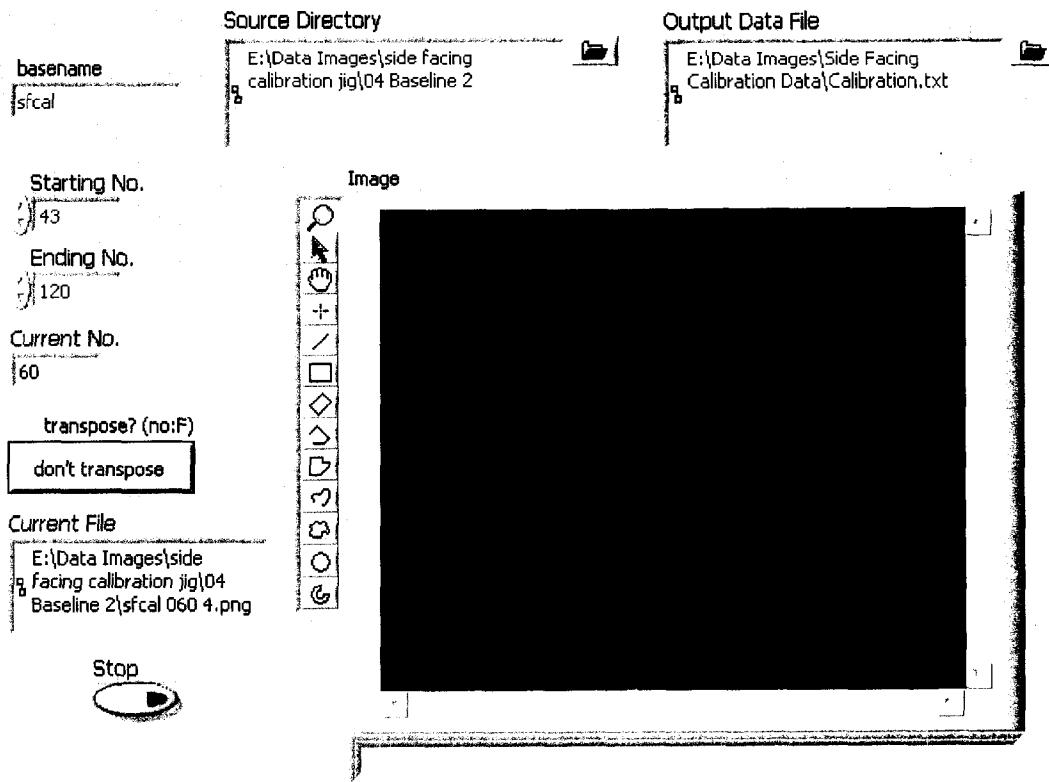


Figure 7.15 — Calibration Image Set Parsing VI.

The block diagram of the calibration image parsing VI shows the steps that are performed during the parsing. The images at a particular stop which only contain laser illumination are sequentially opened, and the line location extracted. The one dimensional arrays passed from the peak finding routine are stacked into a two dimensional array for a particular stop. The laser line locations in corresponding rasters of images taken at the same stop are averaged to yield a value that is less affected by speckle. Finally, all of the processed data is stored into a two dimensional array in which the rows represent rasters, the columns represent range stops, and the values stored represent fractional pixel numbers within a raster. The relationship between the range stops and the pixel numbers will be the basis for calibration of the profiling head.

#### 7.4.4 Calibration Curve Fitting

Once the calibration images were processed to determine the location of the laser line in the center of each image, these locations could be compared with the ranges to the target. The first step in making this comparison was to plot the ranges to the target versus the location in the image, measured in pixels. The next step was to perform a regression analysis on the data to identify suitable values for fixed parameters in the model developed in Chapter five as expressed with equation (5-17). This general model may be reduced if certain simplifications are adopted. The first simplification is to only consider pixels along a line which bisects the longer axis of the image. This simplification leads to values of  $\phi$  of either  $0^\circ$  or  $180^\circ$ , and if this is the case, the equation can be reduced to equation (7-1).

$$R = D \cdot \frac{1 + \tan(\theta) \cdot \tan(\alpha)}{\tan(\alpha) - \tan(\theta)} \quad (7-1)$$

If the equidistant camera model is used, (the equidistant model is acceptable because of small fields of view) then the zenith angle may be evaluated using equation (7-2).

$$\theta = f \cdot r \quad (7-2)$$

where  $f$  is a constant which quantifies the zoom level of the camera and  $r$  is the radius of an identified pixel from the center of the image. In practice, it is much more common to set up the coordinate system of an image relative to the upper left hand corner. For the images taken for calibration of the profiling head, it is assumed that the left side of the images will have a zero coordinate, and this coordinate will be called  $p$ . The horizontal direction of the camera has 1024 pixels, and the center pixel will be taken as pixel number 512. Thus, the image radius along a central horizontal axis may be expressed with equation (7-3).

$$r = p - 512 \quad (7-3)$$

If equations (7-2) and (7-3) are substituted into equation (7-1), then equation (7-4) may be defined as the working model for the calibration of the measurement system.

$$R = D \cdot \frac{1 + \tan[(p - 512) \cdot f] \cdot \tan(\alpha)}{\tan(\alpha) - \tan[(p - 512) \cdot f]} \quad (7-4)$$

For this model, the calibration fixture yielded paired values of  $R$  and  $p$ , and a curve was fit to this data to determine appropriate values of  $D$ ,  $\alpha$ , and  $f$ . Since this is not a very standard model on which to perform a regression, a generalized curve fitting technique was adopted. The *genfit* function in Mathcad is a curve fitting routine based on the Levenberg-Marquart algorithm. It requires the input of the partial derivatives of the model with respect to each of the variables for which values are to be determined. It also requires that initial guesses be provided for each of the variables to be fitted. The partial

derivatives of equation (7-4) with respect to  $D$ ,  $\alpha$ , and  $f$  are given with equations (7-5), (7-6), and (7-7), respectively.

$$\frac{\partial R}{\partial D} = \frac{1 + \tan[(p - 512) \cdot f] \cdot \tan(\alpha)}{\tan(\alpha) - \tan[(p - 512) \cdot f]} \quad (7-5)$$

$$\frac{\partial R}{\partial \alpha} = -D \cdot (1 + \tan^2(\alpha)) \cdot \frac{1 + \tan^2[(p - 512) \cdot f]}{[\tan(\alpha) - \tan[(p - 512) \cdot f]]^2} \quad (7-6)$$

$$\frac{\partial R}{\partial f} = D \cdot [1 + \tan^2[(p - 512) \cdot f]] \cdot \frac{(1 + \tan^2(\alpha)) \cdot (p - 512)}{[\tan(\alpha) - \tan[(p - 512) \cdot f]]^2} \quad (7-7)$$

The measurement head was constructed to give a baseline distance  $D$  of about 2.4 inches. The aim angle  $\alpha$  desired for this baseline distance is read off of Figure 5.3 to be about 20.5°. The factor  $f$  will be approximately the field of view divided by the number of horizontal pixels, or about 0.018 degrees per pixel. Using these initial guesses, the genfit procedure was performed, and the best fit values were determined for the parameters in question. These values are given in Table 7.1.

Table 7.1 — Designed Versus Actual Parameters.

Calibration Parameter	Initial Guess / Design Value	Actual Value from Regression
Baseline Distance, $D$	2.4 in	2.355 in
Aim Angle, $\alpha$	20.5°	19.9°
Zoom Factor, $f$	0.018°/pixel	0.0175°/pixel

When the measurement model is then plotted along with the original data, a visualization of the appropriateness of the fit can be seen. Since the differences between the locations of the points plotted and the fitted line are so small, these differences were plotted against a second vertical axis with a different scale. The differences were found to be approximately centered about a value of zero, and the magnitude of the differences

tended to increase for larger measurement distances. Figure 7.16 shows the calibration data with the fitted measurement model and the error between these two values at each calibration point. Here, each green dot represents the error between a calibration data point and the curve fit to the data (depicted by the corresponding blue circle).

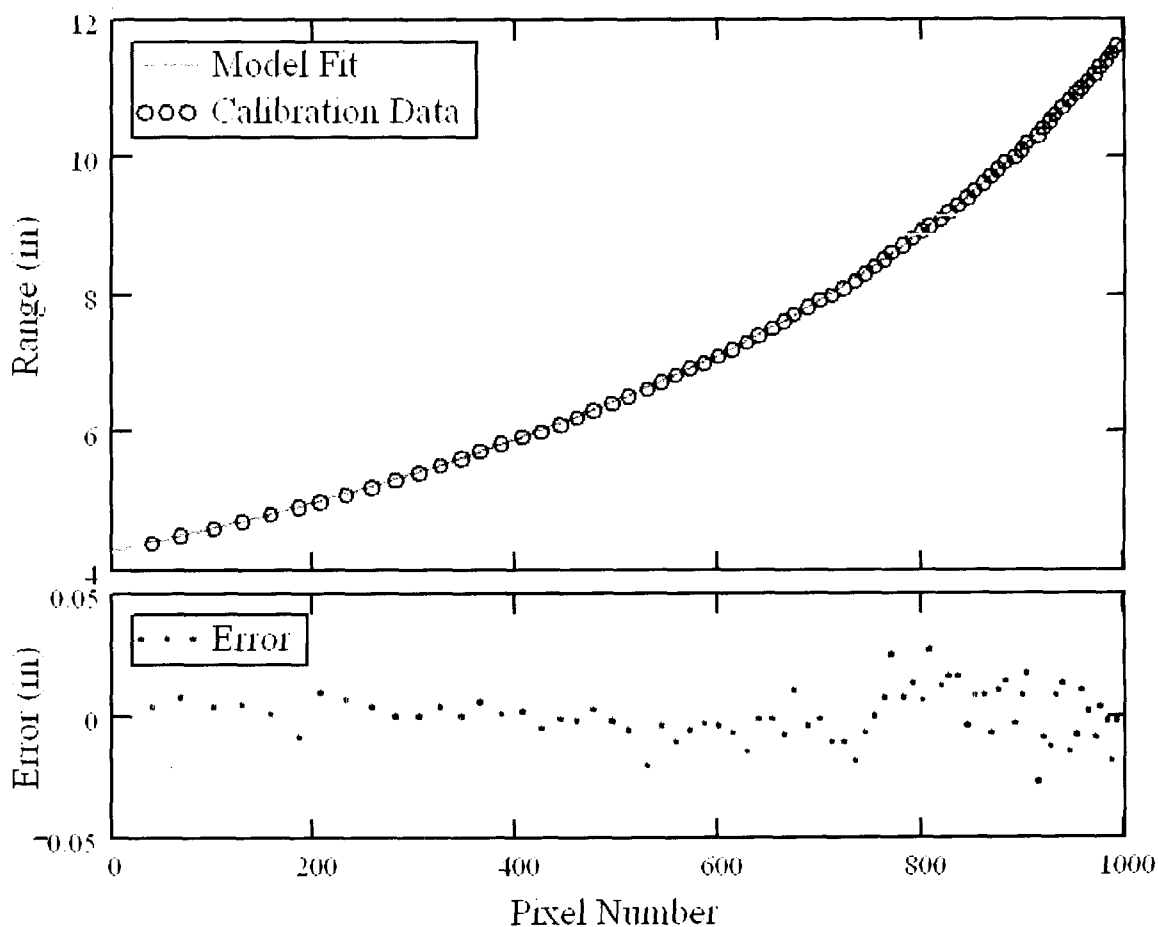


Figure 7.16 — Side-Facing Measurement Calibration.

As a measure of the goodness of this fit, a root mean squared error value was calculated by taking the geometric mean of the all the errors of all the calibration points from the fitted calibration function. This computed root mean squared error for Figure 7.16 was 0.0102 inches.

## 7.5 Profiling

Using the parameters found in the calibration procedure, the profiling head was tested in the same section of pipe scanned in Chapter six. The head was set up to scan around the circumference of the pipe wall at discrete axial increments. An image was collected and saved at each axial and angular increment. The images were processed to locate the center of the laser line using specially prepared image processing VIs in LabVIEW. Finally, the calibration information was applied to yield cylindrical coordinates describing the profile of the pipe.

### 7.5.1 Profiling Methodology

The same cylindrical coordinate system as was used for the profiling described in Chapter six was used to describe the profile obtained using the side-facing profiling method. In the case of the side-facing profiling method, the angular location of the radius measurements being taken is set by the stepper motor upon which the measurement head is mounted. In the perpendicular plane method, each image provided radius measurements for the entire circumference of the pipe at a single axial location. With the side-facing method, radius measurements are taken for a small range of axial locations, but only a single angular location. At each axial stop, a set of images is collected in which each image is taken at a different angular increment, where the angular increments span the circumference of the pipe. After all of the images are collected, they are processed and assembled into a set of ordered triples, just as in Chapter six. This set of ordered triples can then be plotted using the same tools used in Chapter six.

### 7.5.2 Hardware

The indexing profiling head previously described was affixed to the same axial positioning system described in Chapter six. For this system, both the stepper motor which controls axial position and the stepper motor which controls angular positioning had to be interfaced with the automated collection VI. Stepper motor drivers were connected to each motor such that only two bits (step and direction) of input were required from the DAQ card for each motor.

The entire profiling head was mounted on a two directional stage to enable a fairly close center alignment within the pipe. This alignment was performed by rotating the profiling head to a few angular locations around the circumference of the pipe and checking sample images at those locations to ensure that the laser line was located in the same place within the images. The stage was adjusted as necessary to align the measurements within the pipe. Figure 7.17 shows the profiling head and all the supporting hardware in the pipe, ready to perform a scan.

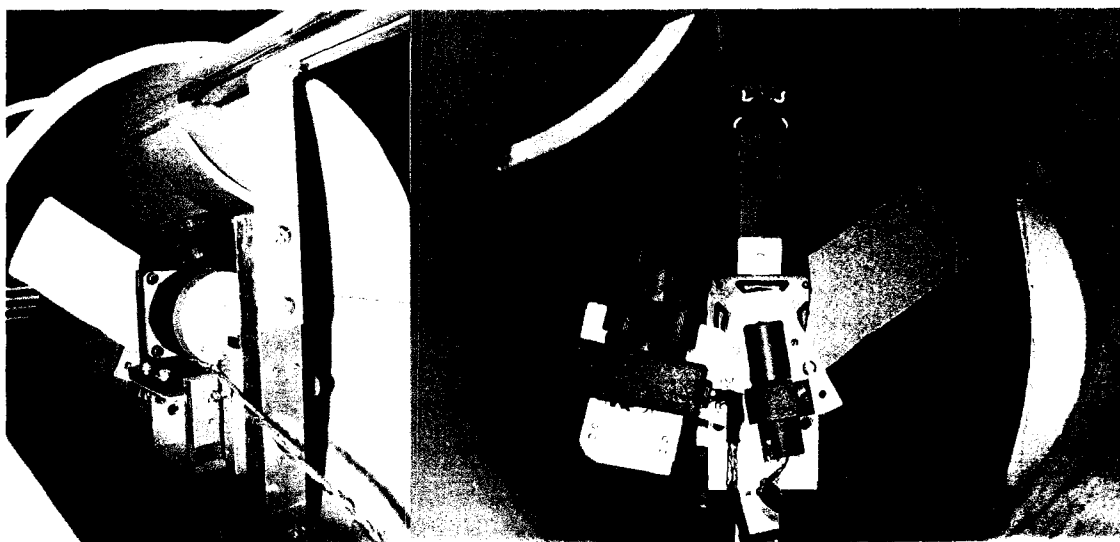


Figure 7.17 — Profiling Hardware.

### 7.5.3 Image Collection

The process of collecting the images required for the construction of a profile was automated using a LabVIEW VI. This VI was prepared to automatically index the axial and angular position of the profiling head, and capture images in the locations needed. Figure 7.18 shows the front panel of this VI.

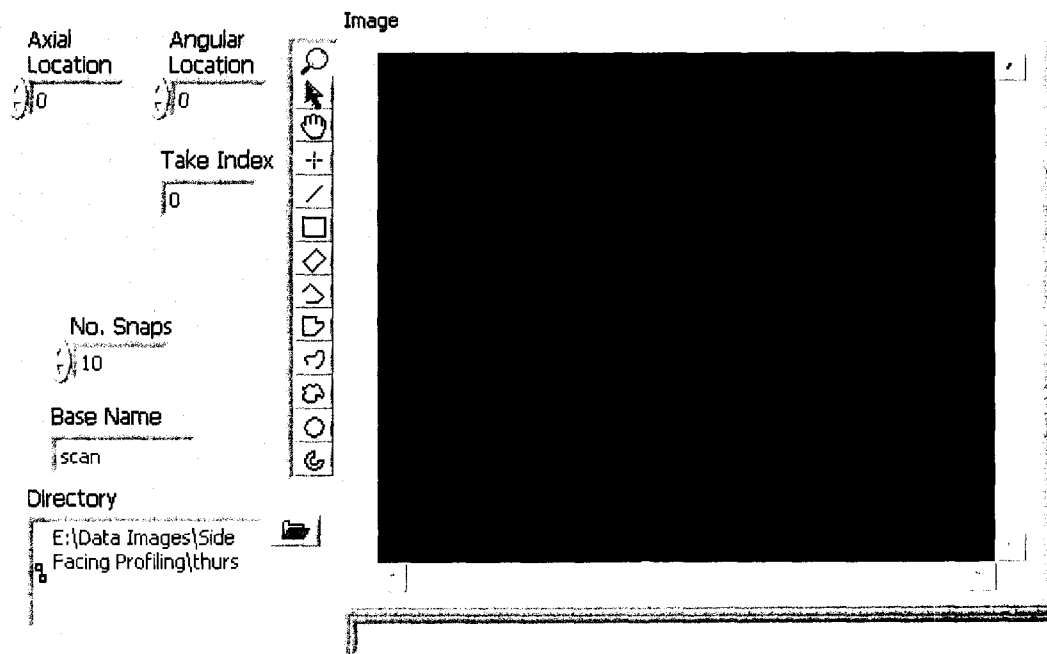


Figure 7.18 — Front Panel of Image Collection VI.

The user may enter the beginning axial and angular indices, the number of images to snap per discrete location, the base filename onto which the indices will be added for individual image filenames, and the directory into which the images will be stored. The format of a filename of an image is *basename aaa bbb c.png*, where *aaa* is the axial location index, *bbb* is the angular location index, and *c* is the take index (for multiple images taken at each stop). The user may monitor the progress of the collection process by looking at the Axial Location, Angular Location, and Take Index boxes, since these

boxes update as the process is performed. The user may also monitor the images which are being collected using the display on the right side of the front panel. The details of the programming of this VI can be seen in its block diagram shown in Figure 7.19.

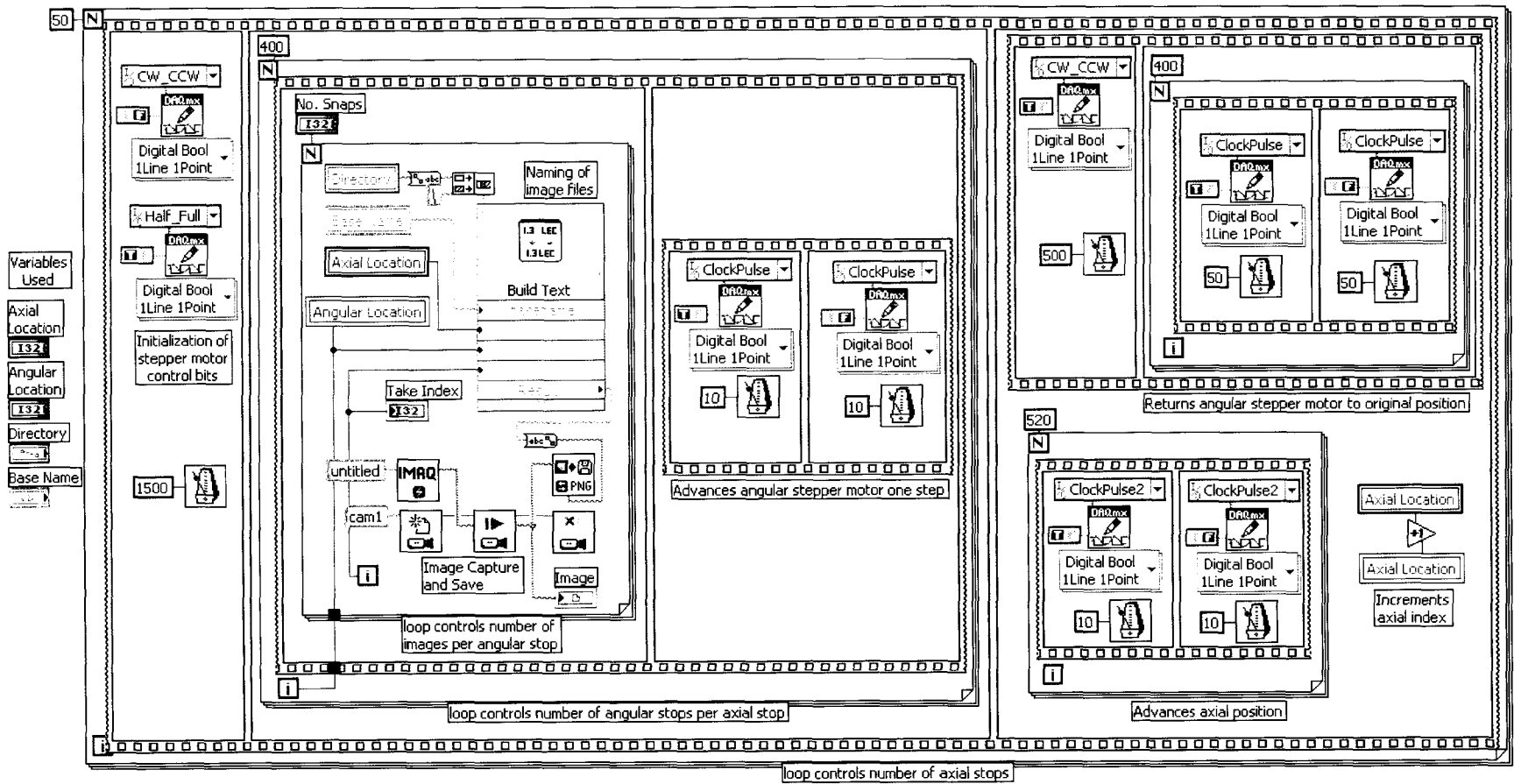


Figure 7.19—Block Diagram of Image Collection VI.

The outer loop of this VI controls the number of rings of images to collect. Inside this loop is a sequence structure that defines the steps of the process for each ring. The first step is the initialization of stepper motor control bits. The next step contains a loop that controls how many angular stops will be processed (400 stops), and what happens at each stop. The final step returns the angular indexing stepper motor to its original location (to unwind the wires to the camera and laser) and moves the axial positioning stepper motor 520 steps (0.2in) to its next stop, while incrementing the axial location index.

At each angular stop, a sequence structure is used to define the steps of the process. The first step contains a loop which controls the number of images that will be taken at each stop. Inside this loop, there is a sub-VI which builds the text needed to name an individual image filename with its indices included. Commands are also included in this loop that execute the capture of the image and save it to the hard drive. The next frame of the sequence structure advances the angular positioning stepper motor a half step to prepare the head to take its next image or set of images. The total number of images snapped by the execution of this VI is the product of the number of rings, the stops per ring, and the number of images per stop. For 10 images per stop, 400 stops per ring, and 50 rings, a total of 200,000 images are collected by the execution of this VI.

#### **7.5.4 Parsing Images**

The many image files collected by the Image Collection VI had to be automatically processed to determine the location of the laser line within each image. To accomplish this task, a VI was implemented which cycled through a set of images and applied the previously described “Find Array of Peaks” sub-VI to each image. This VI

runs through a number of rings of images, extracting the pixel location of the laser line in each raster of each image. Each image produces a one-dimensional array of pixel locations, so the multiple images comprising one ring produces a set of 400 one-dimensional arrays. The “Parse Rings” VI combines these 400 one-dimensional arrays in each ring into one two-dimensional array for each ring. These arrays are stored in data files which may be viewed with a spreadsheet program. The index included in the filename of each data file indicates the index of the ring from which it was generated. Figure 7.20 shows the front panel and block diagram of the “Parse Rings” VI.



to start (in the “Current Ring” field). The user may also choose the directory and base name of the output files in the “Destination Files” field. The user may monitor the progress of the process by looking at the “Current Ring” field, the “Angular Stop” field and the “Image” indicator which shows the user the most recent image file to be processed. On the block diagram, the dataflow can be seen. An outer loop steps through multiple rings of images. The individual images in each ring are then stepped through one at a time with the inner loop. The appropriate filename is selected for each image and passed to the “Find Array of Peaks” VI. This VI outputs the image for the user to monitor along with a one dimensional array containing peak locations. The loop tunnel which passes these one dimensional arrays employs automatic indexing to assemble the two dimensional array which is passed to the sub-VI which writes the data file for the current ring. After this file is written, the axial index is incremented, and the VI is ready to process another ring. This continues until all the rings have been processed.

#### 7.5.5 Application of Calibration

Two sets of world coordinates are needed from each of the parsed ring data files. The first set of coordinates describes the radius of the pipe relative to the angular and axial locations. The other set of coordinates describes the axial offset from the axial location of the profiling head. If equations (7-2) and (7-3) are substituted into equations (5-17) and (5-18), equations (7-8) and (7-9) are obtained.

$$R = D \cdot \frac{1 + \sin(\phi) \cdot \tan(f \cdot r) \cdot \tan(\alpha)}{\tan(\alpha) - \sin(\phi) \cdot \tan(f \cdot r)} \quad (7-8)$$

$$H = D \cdot \frac{\cos(\phi) \cdot \tan(f \cdot r) \cdot \sec(\alpha)}{\tan(\alpha) - \sin(\phi) \cdot \tan(f \cdot r)} \quad (7-9)$$

The value of the azimuth angle  $\phi$  of a point in an image can be found in terms of the radius in the image and the vertical location in the image using trigonometry. Figure 7.21 shows the image coordinates.

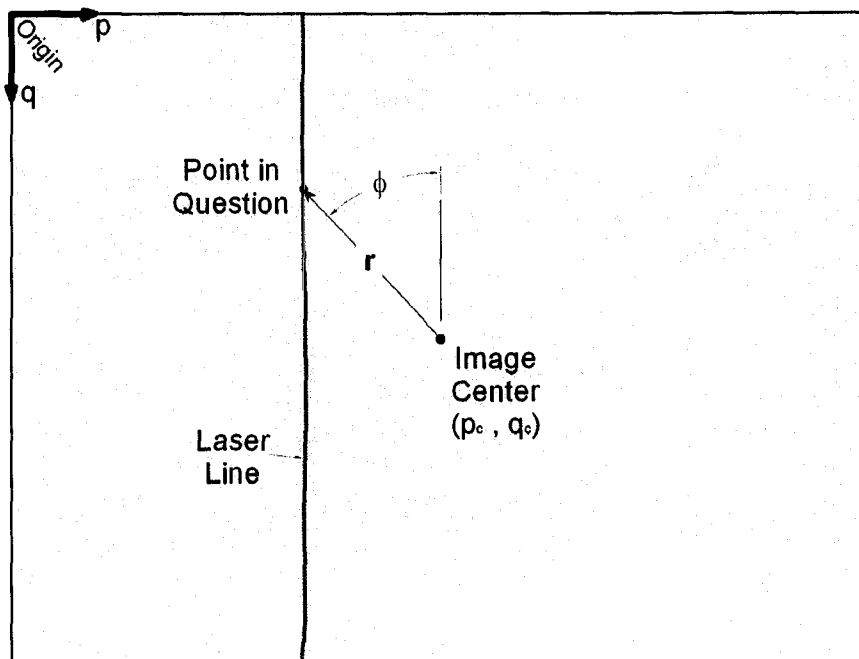


Figure 7.21 — Image Coordinates of a Point on the Laser Line.

If  $p$  is the pixel coordinate in the horizontal direction,  $q$  is the pixel coordinate number in the vertical direction, and  $p_c$  and  $q_c$  are the centers of the image in the vertical and horizontal directions, respectively, then the azimuth angle is given by equation (7-10).

$$\phi = \tan^{-1} \left( \frac{p_c - p}{q_c - q} \right) \quad (7-10)$$

By the Pythagorean Theorem, the image radius is given by equation (7-11).

$$r = \sqrt{(q_c - q)^2 + (p_c - p)^2} \quad (7-11)$$

Thus, by substitution of equations (7-10) and (7-11) into equations (7-8) and (7-9), equations (7-12) and (7-13) are obtained, describing the radius and axial offset in terms of the identified pixel coordinates.

$$R = D \cdot \frac{1 + \sin\left(\tan^{-1}\left(\frac{p_c - p}{q_c - q}\right)\right) \cdot \tan\left(f \cdot \sqrt{(q_c - q)^2 + (p_c - p)^2}\right) \cdot \tan(\alpha)}{\tan(\alpha) - \sin\left(\tan^{-1}\left(\frac{p_c - p}{q_c - q}\right)\right) \cdot \tan\left(f \cdot \sqrt{(q_c - q)^2 + (p_c - p)^2}\right)} \quad (7-12)$$

$$H = D \cdot \frac{\cos\left(\tan^{-1}\left(\frac{p_c - p}{q_c - q}\right)\right) \cdot \tan\left(f \cdot \sqrt{(q_c - q)^2 + (p_c - p)^2}\right) \cdot \sec(\alpha)}{\tan(\alpha) - \sin\left(\tan^{-1}\left(\frac{p_c - p}{q_c - q}\right)\right) \cdot \tan\left(f \cdot \sqrt{(q_c - q)^2 + (p_c - p)^2}\right)} \quad (7-13)$$

The calibration curve which was fit in Section 7.4.4 determined values for the baseline distance  $D$ , the aim angle  $\alpha$ , and the zoom factor  $f$  for the particular profiling head being used. The camera used for the profiling had a sensor with 1024 pixels in the horizontal direction and 768 pixels in the vertical direction; so, the center pixels were taken as 512 and 384, respectively. When all these values are substituted into equations (7-12) and (7-13), the final expressions for the radius and axial offset are given by equations (7-14) and (7-15), respectively.

$$R = 2.355 \sin \cdot \frac{1 + \sin\left(\tan^{-1}\left(\frac{512 - p}{384 - q}\right)\right) \cdot \tan\left(0.0175 \cdot \sqrt{(384 - q)^2 + (512 - p)^2}\right) \cdot 0.362}{0.362 - \sin\left(\tan^{-1}\left(\frac{512 - p}{384 - q}\right)\right) \cdot \tan\left(0.0175 \cdot \sqrt{(384 - q)^2 + (512 - p)^2}\right)} \quad (7-14)$$

$$H = 2.355 \text{ in} \cdot \frac{\cos\left(\tan^{-1}\left(\frac{512-p}{384-q}\right)\right) \cdot \tan\left(0.0175 \cdot \sqrt{(384-q)^2 + (512-p)^2}\right) \cdot 1.064}{0.362 - \sin\left(\tan^{-1}\left(\frac{512-p}{384-q}\right)\right) \cdot \tan\left(0.0175 \cdot \sqrt{(384-q)^2 + (512-p)^2}\right)}$$

(7-15)

These two equations were implemented in a LabVIEW VI to calculate the actual coordinates of the pipe wall using the data from the parsed images. The front panel of the VI is shown in Figure 7.22.

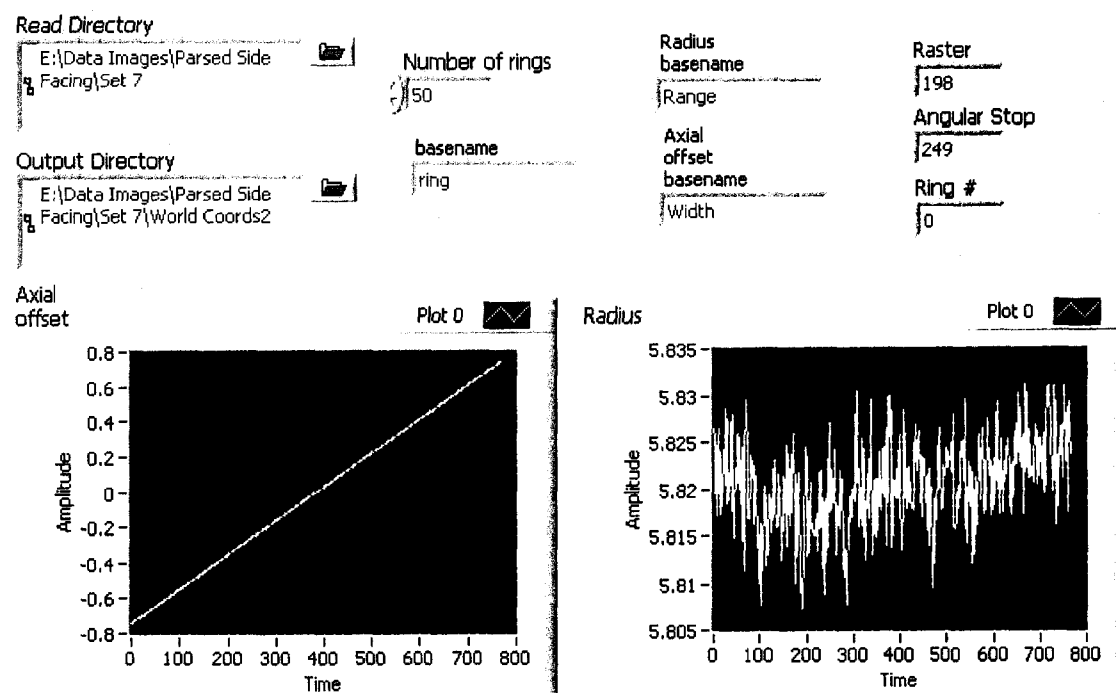


Figure 7.22 — World Coordinate Calculation VI Front Panel.

The user may choose the directory where the data from the parsed images are stored, the base name of these data files, and the number of these files for which the calculations are to be performed. The user may also specify the base names of the output files, one base name for the files containing radius coordinates, and another base name

for the files containing the axial offset coordinates. To monitor the progress of the VI, the user may check the indices of the current raster, angular stop and axial stop (“Ring #”). As the VI calculates the world coordinates, these coordinates are displayed in graphs on the front panel. The vertical axis of these graphs has units of inches, and the horizontal axis of these graphs is quantified using raster coordinates. Note that the noise in the radius coordinate measurement has a magnitude of approximately 0.01 inch. This gives an initial idea of the magnitude of the uncertainty in the measurements of radius for this system. The details regarding the application of the calibration information to the pixel location data can be seen in the block diagram shown in Figure 7.23.

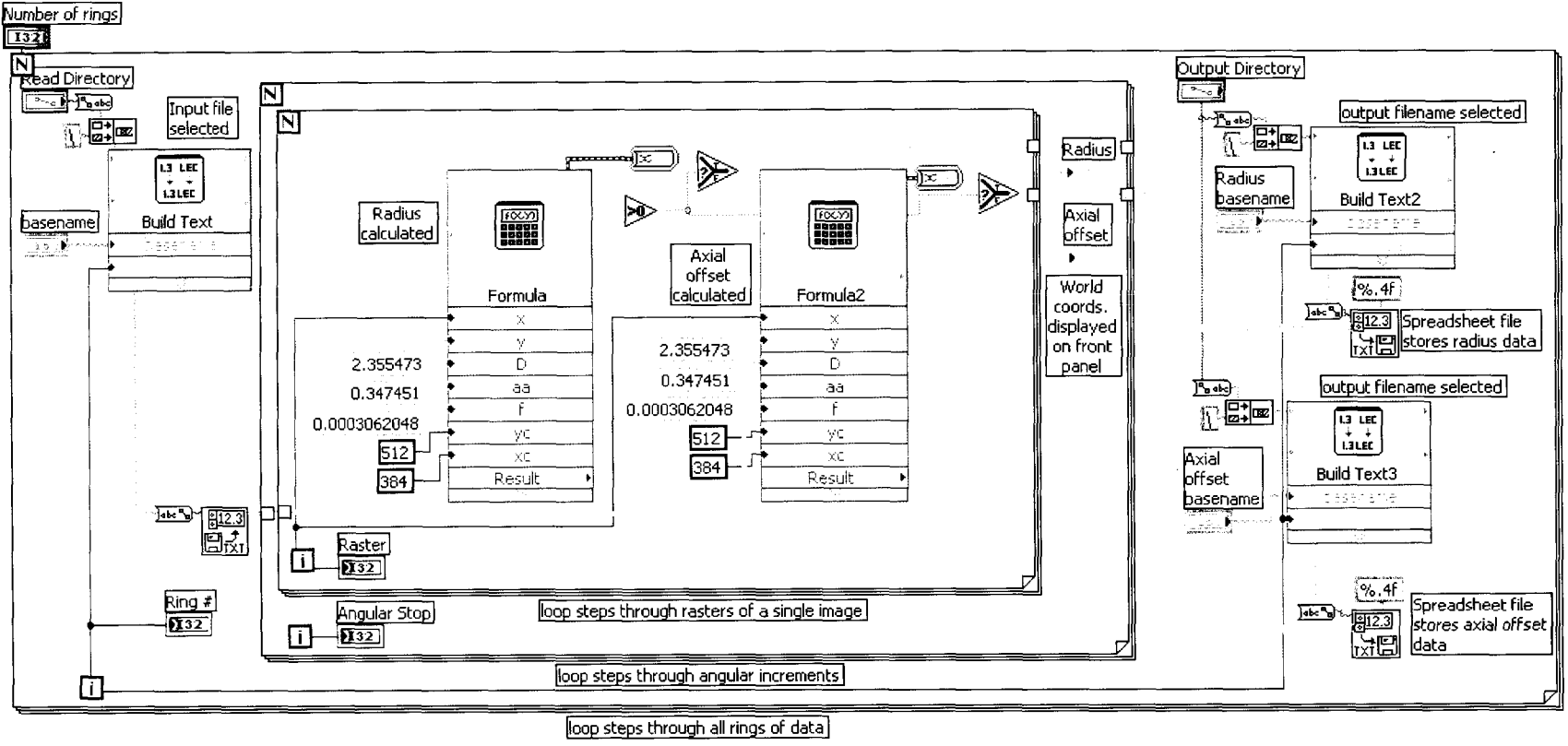


Figure 7.23 — World Coordinate Calculation VI Block Diagram.

The outer loop of this VI controls the number of pixel location data files that will be processed. Each time the loop iterates, another data file is opened, and the information in that data file is passed through two loops. These loops step through each angular index and raster of information stored in the data file. The formula blocks inside these loops are where equations (7-14) and (7-15) are applied to the pixel location data, one point at a time. Since values of -1 were written in the pixel location data file to indicate a failure to find a peak, this VI also checks for negative input values, and passes the -1 value into the new files wherever they are found. As the calculated coordinates are passed out of the indexing loops, they are re-assembled into two dimensional data arrays. These two dimensional data arrays have rows that are organized by angular index, columns that are organized by raster number, and entries that represent radius values (in inches) for one of the arrays, and axial offset (in inches) for the other array. These arrays are then stored into two files with indices in the filenames denoting the axial stop from which those calculated coordinates originated. The outer loop is then ready to execute its next iteration. The result of running this VI is the creation of two world coordinate files for each pixel location data file.

#### **7.5.6 Removal of Invalid Data and Calculation of Independent Coordinates**

After the calculation of world coordinates from the pixel locations, the data had to be further processed for accurate display. The two files with radius and axial offset values had these values stored versus the angular index and the raster number. Multiple files were used to represent multiple rings. Values of -1 were stored in the files for locations where the peak finding algorithm could not identify the laser line. To display a cloud of points with accurate dimensions representing only the valid data, a VI was

prepared that used the many data files to produce a single data file with invalid points removed. This data file was designed to be a list of ordered triples representing the axial coordinate, the angular coordinate, and the radius coordinate, respectively.

During the image collection process, more rings of data were collected than were actually needed to fully profile the whole pipe. Significant overlap existed in the view of the camera from one ring to another. These extra rings were taken for possible use in later projects. The VI which was prepared to create the list of ordered triples was also designed to reduce the number of these rings that had to be considered by utilizing more of the width of the camera's view. The front panel of this VI is shown in Figure 7.24.

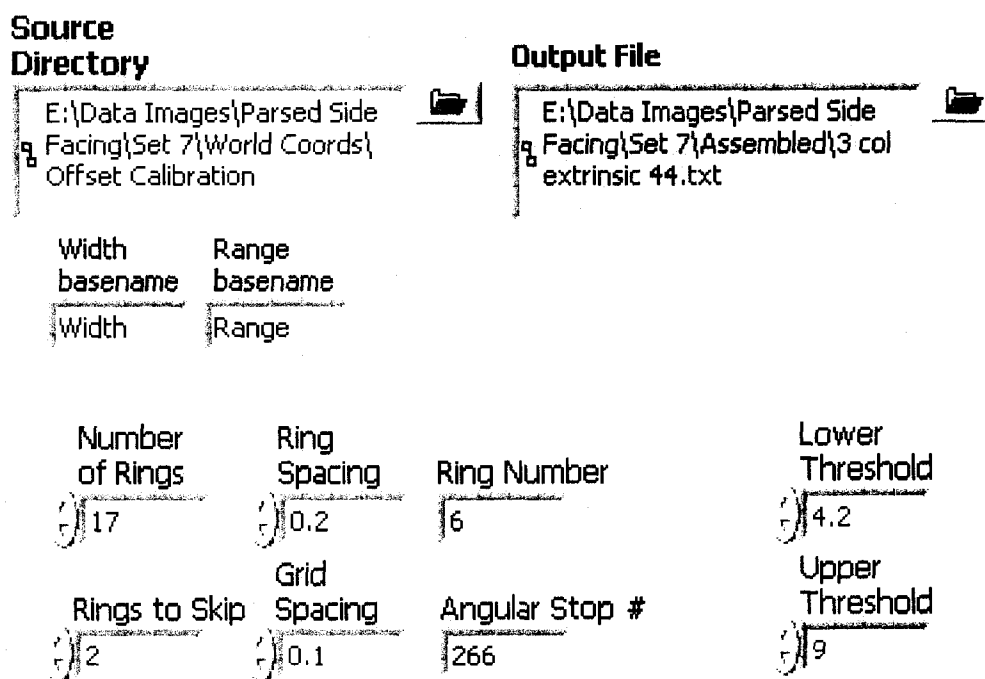


Figure 7.24 — Front Panel of Data Sorting VI.

The user may enter the directory where the source data files are stored, the base names of the axial offset (“Width basename”) and radius (“Range basename”) data files, and the sorting parameters. The sorting parameters included the total number of rings of

data to sort through (“Number of Rings”), the physical spacing represented by the axial index (Ring Spacing), the number of rings to skip between successive data rings (“Rings to Skip”), and the desired axial distance between adjacent points (“Grid Spacing”). The user also specifies a range of radius values to which the output will be limited (“Upper Threshold” and “Lower Threshold”). As long as the lower threshold is set higher than -1, the invalid data will automatically be excluded. The name of the output file is specified in the “Output File” field.

Internally, the data sorting VI performed several processes. The block diagram of the data sorting VI is shown in Figure 7.25.

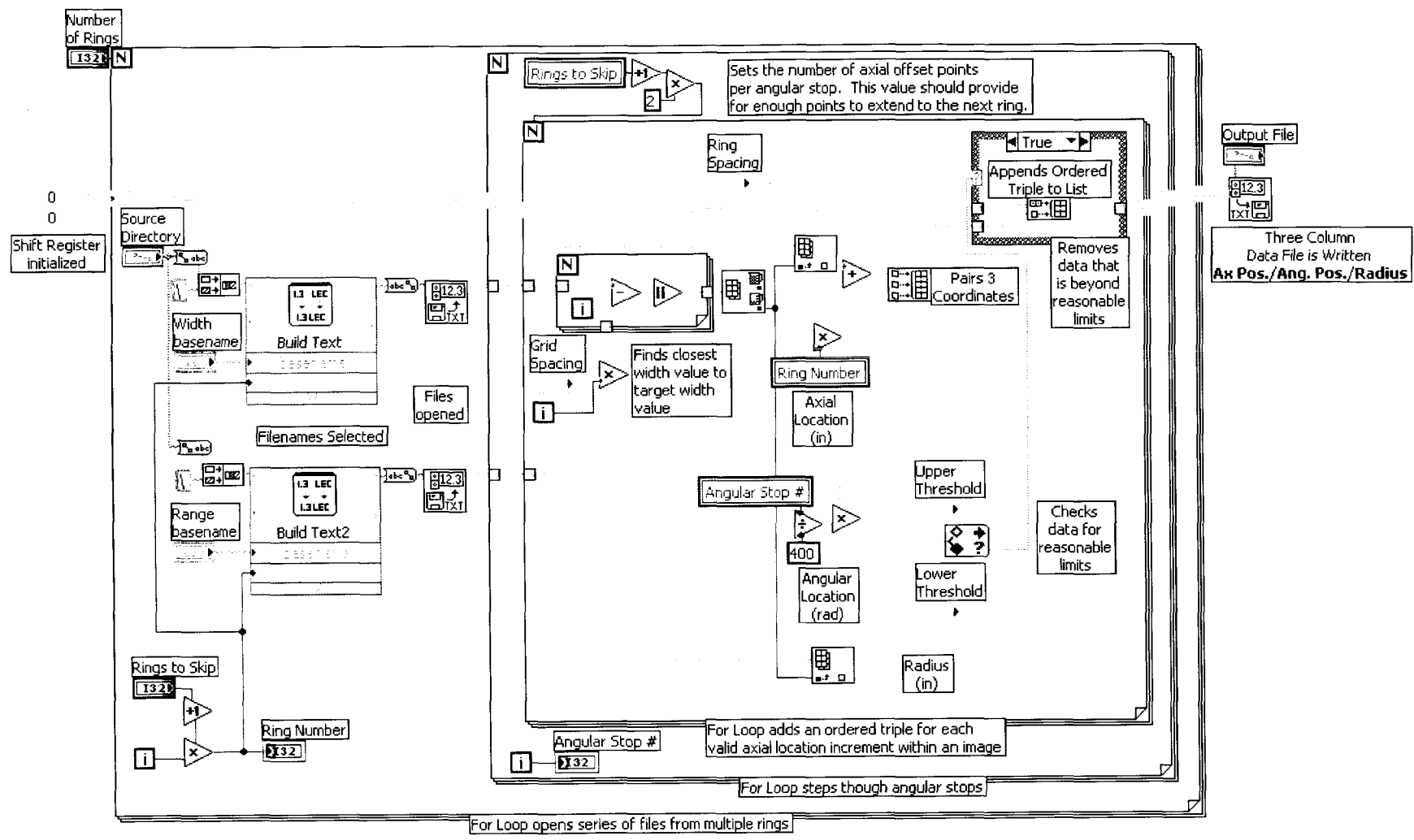


Figure 7.25 — Data Sorting VI Block Diagram.

The outer loop steps through multiple data files from multiple rings of data. Each ring of data is then passed to an indexing loop that extracts the information from individual angular stops. At each angular stop, enough axial points must be considered to extend to the start of the next ring. A loop is used to identify multiple points at a spacing specified by “Grid Spacing” for which coordinates would be included in the list of point cloud coordinates. The axial offset for each point is added to the axial location of the profiling head to yield the axial location of the measurement. The angular location in radians is calculated from the angular index based on the number of angular stops per full circle. The radius at these coordinates is then examined, and if it lies within the specified bounds, then this ordered triple is added to the list by a conditional structure in the upper right corner. This process continues through all the angular stops for all the rings of data to be used.

### **7.6 Profile Visualization**

To verify the validity of the methods used for the calculation of the coordinates of the inner surface of the pipe, the same VI was used to visualize the data as was used in Chapter six. This VI accepts a list of ordered triples and displays it in three dimensions as a point cloud. Figure 7.26 shows the front panel and block diagram for the visualization VI.

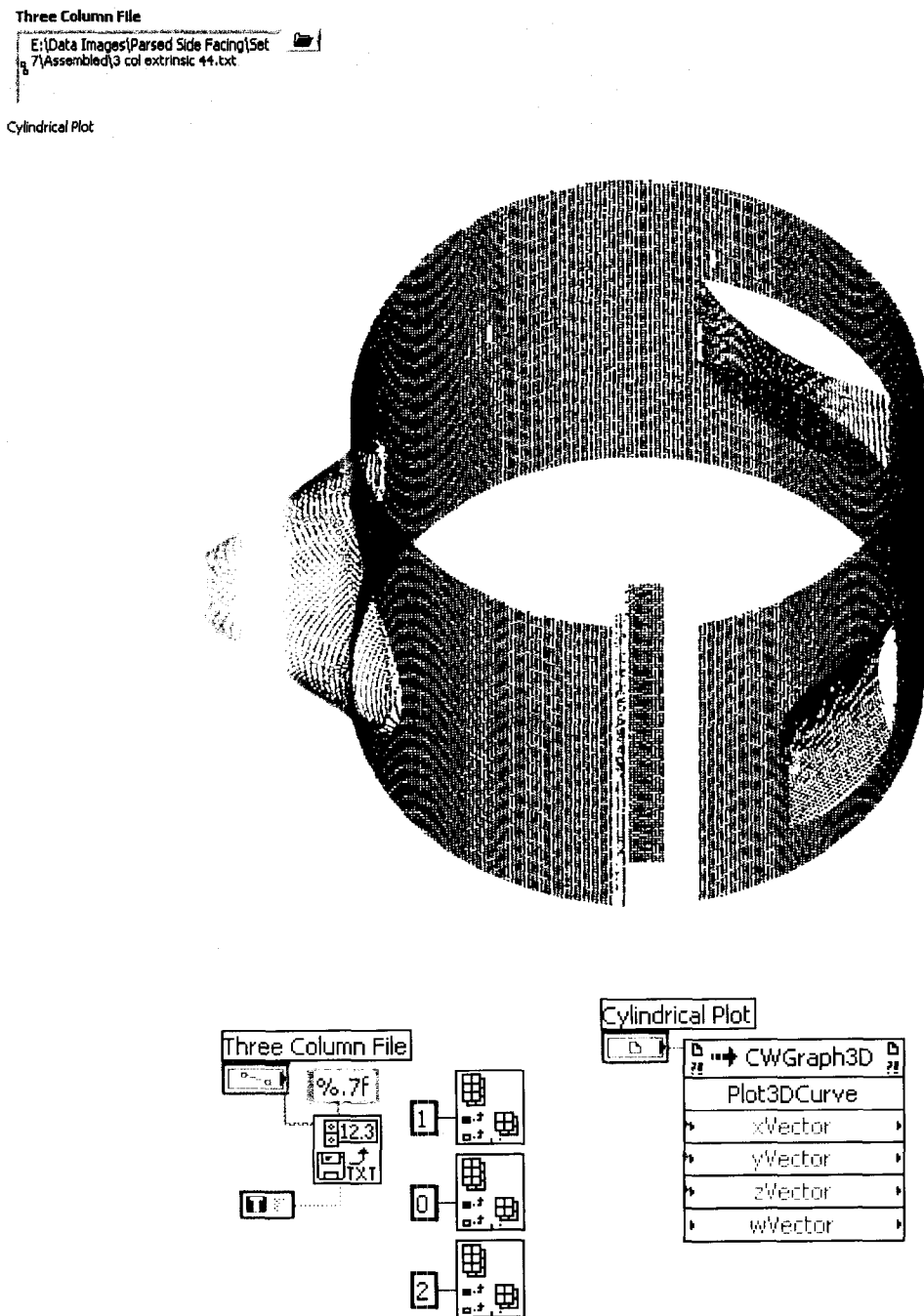


Figure 7.26 — Profile Visualization VI.

The three column file containing the axial position, angular position and radius coordinates is read and displayed on the front panel. The profile can be manipulated with the user's mouse to re-orient it, zoom in and out, and pan left, right, up and down. Many

options are available to the user to manipulate the graph using the CWGraph3D interface discussed in Chapter six. Front and top views of the profile obtained with the side facing method are shown in Figure 7.27.

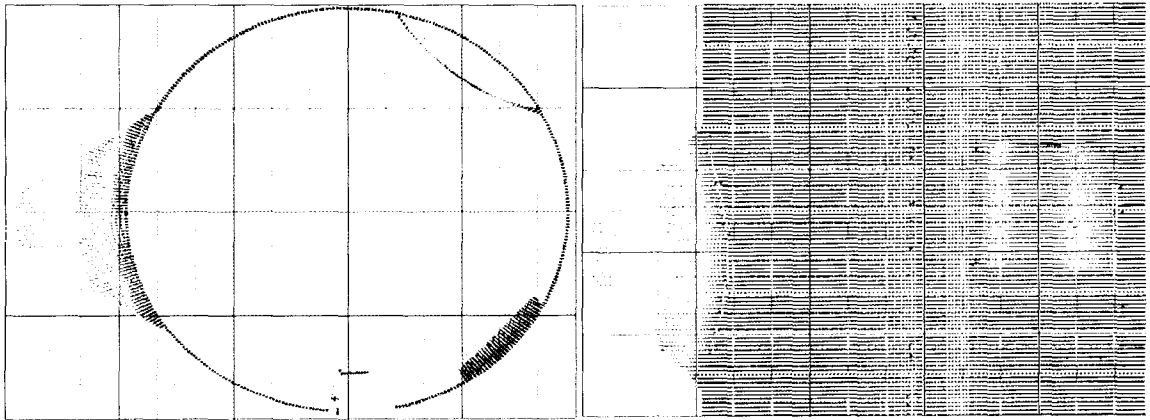


Figure 7.27 — Front and Top Views of Profile.

For both of these figures, the minor grid represents a one inch spacing increment. A few observations may be noted by looking at these visualizations. The first is that there occlusion is not a significant problem (as it was for the perpendicular plane profiling method). Some occlusion may be noted in the front view, just to the right of the rail, which is seen at the bottom. This occlusion is expected, since the rail represents such a sharp change. The next observation is that the dimensions obtained using the side-facing profiling method match quite well with the dimensions obtained using the perpendicular plane method in Chapter six. This provides some confidence that both methods must have merit, although a thorough examination of the accuracy of both methods is provided in Chapter eight. A small amount of noise can be seen slightly to the left of the rail; this effect is caused by the linear bearings possessing specular reflective properties.

## 7.7 Conclusions

A system capable of profiling the inner wall of a section of pipe using the side-facing profiling method was constructed and demonstrated. An extrinsic calibration was performed on the measurement system using a specially constructed calibration apparatus. A calibration curve based on the theory from Chapter five was fit to data relating world radii to pixel locations in images. Hardware and control software was set up to index the measurement system around a center axis and along the length of the section of pipe. Software was also set up to capture images at each angular and axial stop. Additional LabVIEW software was developed to parse the images, extract the coordinates of the laser line, apply the calibration data, and form a set of coordinates describing the inner surface of the pipe. LabVIEW graphing tools were adapted for viewing the profile, and the resulting profile appeared to represent the physical model quite well. Chapter eight will provide a quantitative comparison of the physical model and the laser profiling results detailed in Chapters six and seven.

## CHAPTER 8

# COMPARISON OF LASER-BASED PROFILES WITH TACTILE MEASUREMENTS

### **8.1 Introduction and Overview**

An automated tactile measurement system was designed and fabricated to provide physical measurements of the test section of pipe profiled in Chapters six and seven. Computing the difference between the physical measurements and the pipe measurements obtained using the perpendicular plane and side facing laser triangulation systems allows the measurement error of these profiling systems to be determined. Quantifying the measurement error of the profiling systems provides a mechanism for evaluating the analytical profiling models developed in Chapters four and five as well as the uncertainty of the methods.

### **8.2 Automated Tactile Profile Measurements**

Approximately 40,000 radius measurements of the test pipe were required to provide for meaningful comparison with the laser profiling results. This large number of measurements precluded the use of manual methods for procurement of the data. As such, a method of automatic data collection had to be devised. The device was to operate without human supervision, be capable of taking measurements of the pipe at an accuracy

on the order of 0.001 inches, and be capable of storing the data automatically. The features to be measured in the section of pipe in question were not well suited to a constant contact sort of tactile measurement because of abrupt changes in the radius of the test pipe. To accomplish the measurements, the same axial and angular positioning equipment described in Chapter seven was used in conjunction with a positional-feedback linear actuator with a probe tip attached to its end.

### **8.2.1 Hardware**

The linear actuator used for the measurement of the pipe radii was actuated pneumatically. A pneumatic cylinder was used so that a low enough pressure could be applied to the cylinder to allow for very low force measurements. By adjusting the air pressure applied to the cylinder, the force output of the cylinder could be controlled. A relatively new family of pneumatic cylinders, made by Bimba® Manufacturing, have recently become available. In addition to functioning as ordinary pneumatic actuators, these cylinders incorporate a built-in linear potentiometer. The potentiometer is capable of outputting a voltage signal that is proportional to cylinder extension. In this manner, an automatically controlled system can receive positional feedback regarding the process being performed. Figure 8.1 shows a pneumatic cylinder with integrated positional feedback [61].

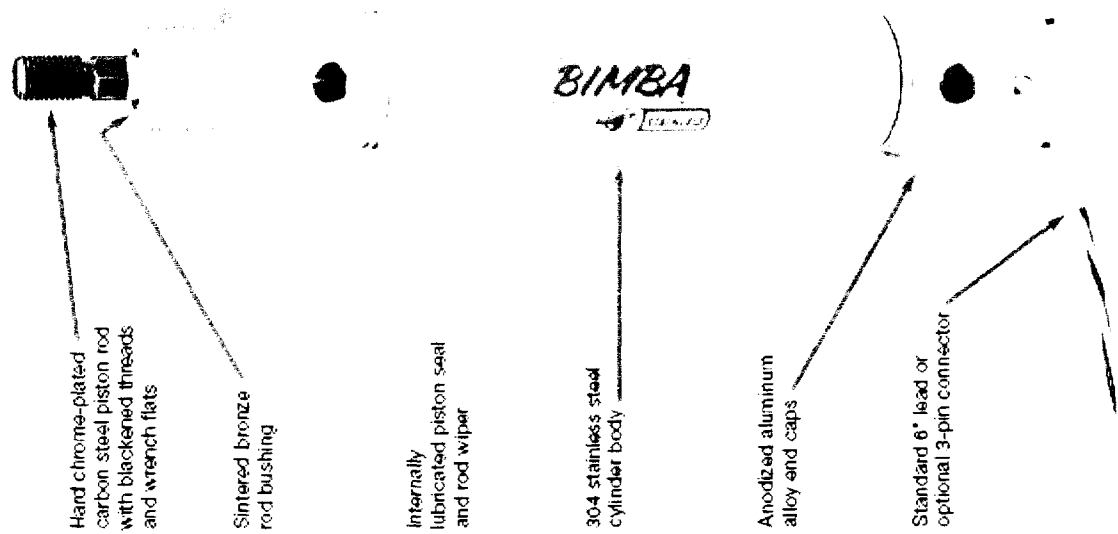


Figure 8.1 — Positional Feedback Air Cylinder.

Since low measuring forces were desired and measuring force is proportional to the cross-sectional area of the cylinder, the smallest diameter bore (1.0625 inches) offered by Bimba® was selected. Bimba® also offered several types of mounting options, of which the Block Mount appeared to be the most suitable for the mounting needs of this system. A low friction option was also available and was specified to minimize the air pressure needed just to overcome internal friction in the cylinder.

To mount the cylinder to the stepper motor shaft of the positioning system, a custom bracket was fabricated. The bracket was constructed of 0.5 inch thick aluminum plate to provide adequate stiffness to minimize measurement error due to system compliance. The bracket was designed to offset the front of the cylinder from the axis of rotation of the stepper motor enough to ensure that the cylinder would not interfere with any of the features in the section of pipe to be measured. Figure 8.2 shows the cylinder mounted to the bracket and the stepper motor.

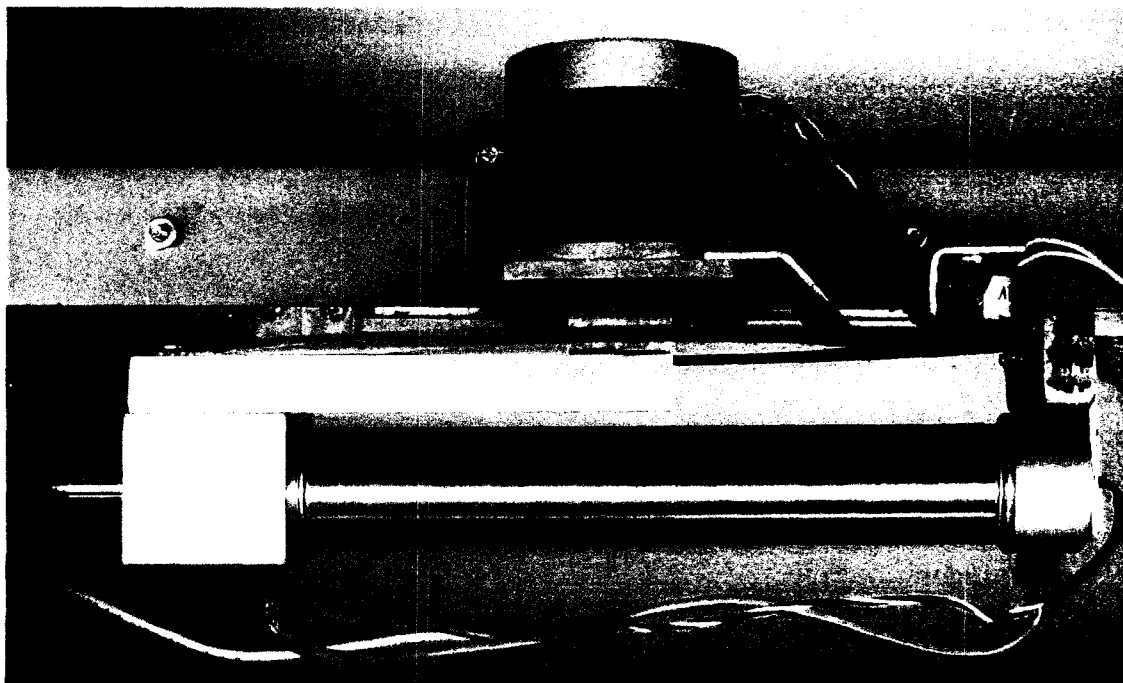


Figure 8.2 — Top View of Tactile Hardware.

A brake system was also added to the tactile measurement system. Since some of the measurements would be taken on sloping surfaces, this would induce a moment about the axis of the stepper motor shaft. The stepper motor being used had enough holding torque to hold a system stationary when little or no external force was applied to it, but not enough holding torque to resist the moments induced by the probe. A circular steel disk was fabricated to be connected to the bracket which held the cylinder. An electromagnet was procured, and a bracket was designed to position it next to the steel disk. By energizing the electromagnet, the bracket and cylinder may be locked firmly in place, and when the electromagnet is de-energized, the stepper motor is free to increment the orientation of the probe. Figure 8.3 shows a rear view of the tactile measurement system as it was deployed in the section of pipe to be measured.

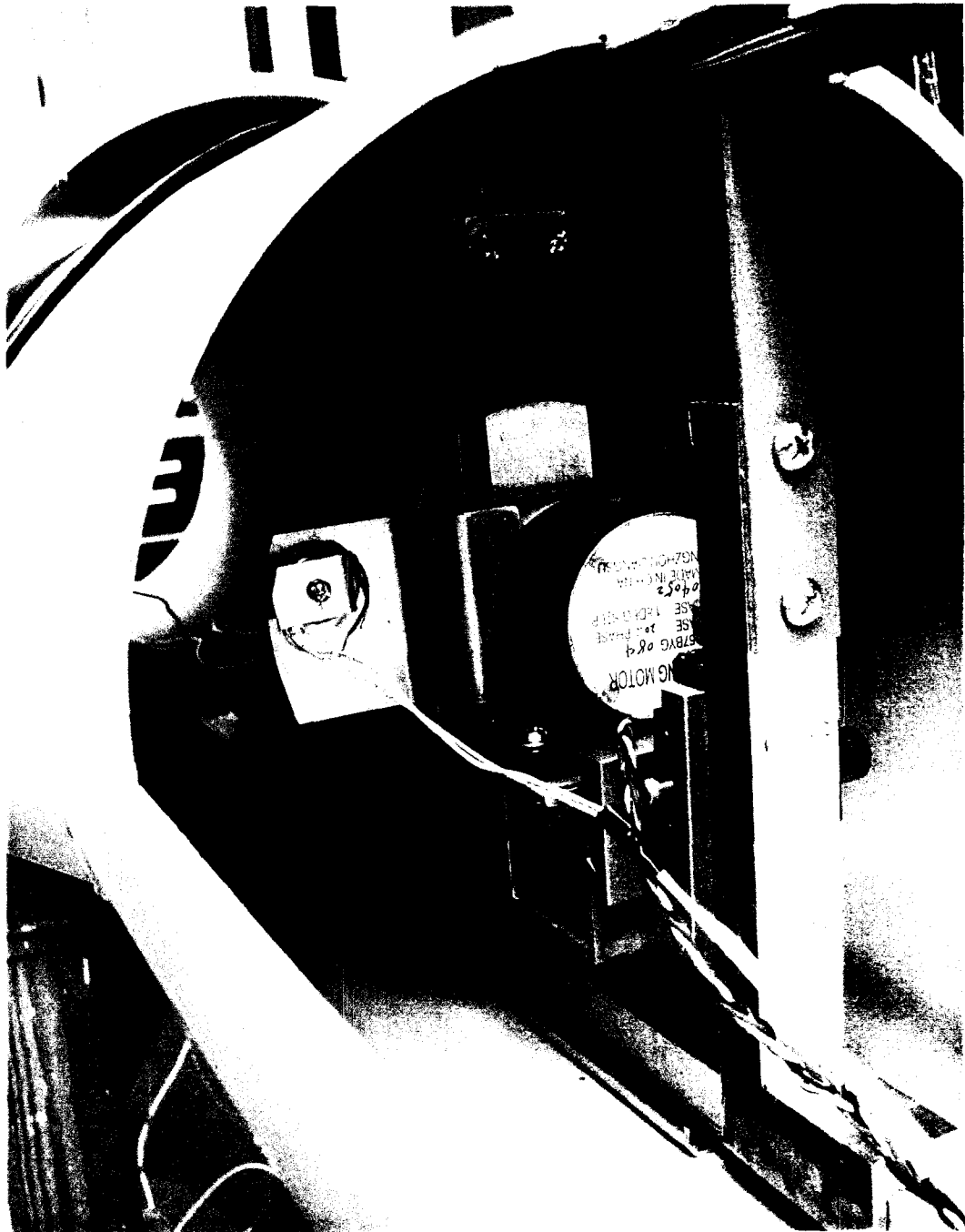


Figure 8.3 — Tactile Measurement Hardware.

The leads connecting the stepper motor coils and the electromagnetic brake were routed out the rear of the pipe, while the pneumatic hoses and the signal wire were routed out the front of the pipe. As with the side-facing measurement system, the entire head

was mounted on a stage by which the axis of the stepper motor could be placed quite near the center of the pipe.

### **8.2.2 Control and Automation**

The control of the tactile measurement device was accomplished using LabVIEW and a National Instruments 6025E data acquisition card. The digital outputs of the data acquisition card could not source more than about 25 milliamps of current at 5 volts. This current capacity and voltage was adequate for control of the stepper motor control boards, but was insufficient to supply power to the electromagnet or to the control valves for the actuation of the pneumatic cylinder. To supply the correct voltage at an adequate current capacity to the electromagnet and the control valves, an external power supply was utilized. The power supply was set to supply about 12 volts, to match the requirements of the control valves, the electromagnet and the stepper motors. Current from this power supply to the control valves and electromagnet was switched using cascaded transistor/relay circuits. The voltage signal from the cylinder by which the measurements were made was routed to an analog input on the data acquisition board. A schematic of the automated tactile measurement system is shown in Figure 8.4.

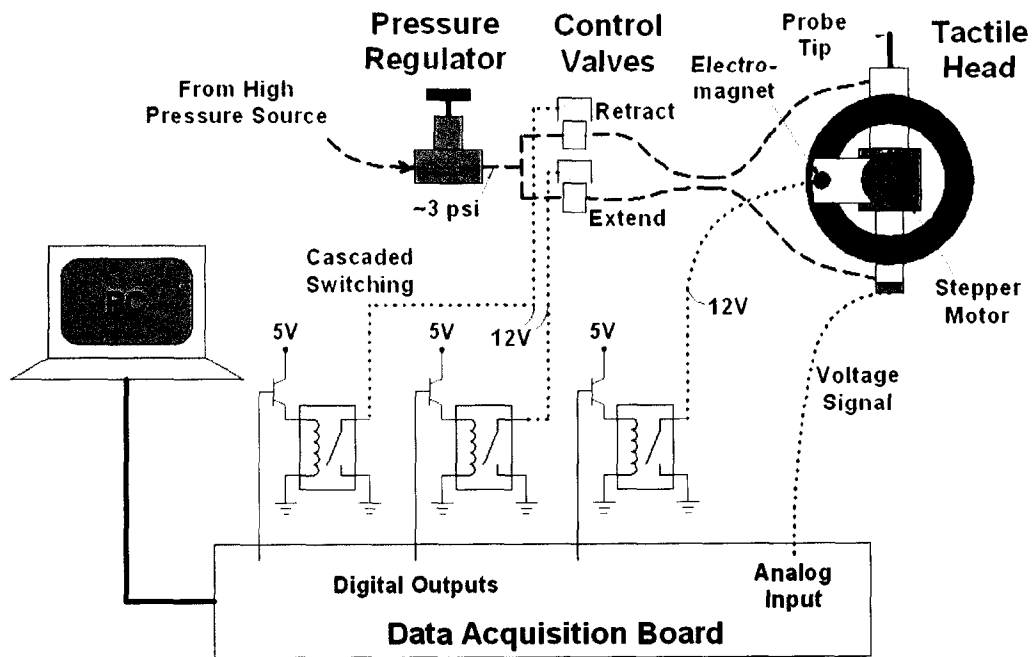


Figure 8.4 — Schematic of Tactile Measurement System.

The pressure required for the extension and retraction of the air cylinder was about 3 psi. To supply this pressure, a precision pressure regulator was used. The pressure regulator stepped the pressure down from about 120 psi to about 3 psi. The control valves were designed to apply pressure to their respective sides of the pneumatic cylinder when activated, and to vent their respective sides of the cylinder to the atmosphere when not activated. Thus, when both valves are not active, the rod of the cylinder is free to move, only being restricted by its own friction. The pressure regulator and control valves are shown in Figure 8.5.

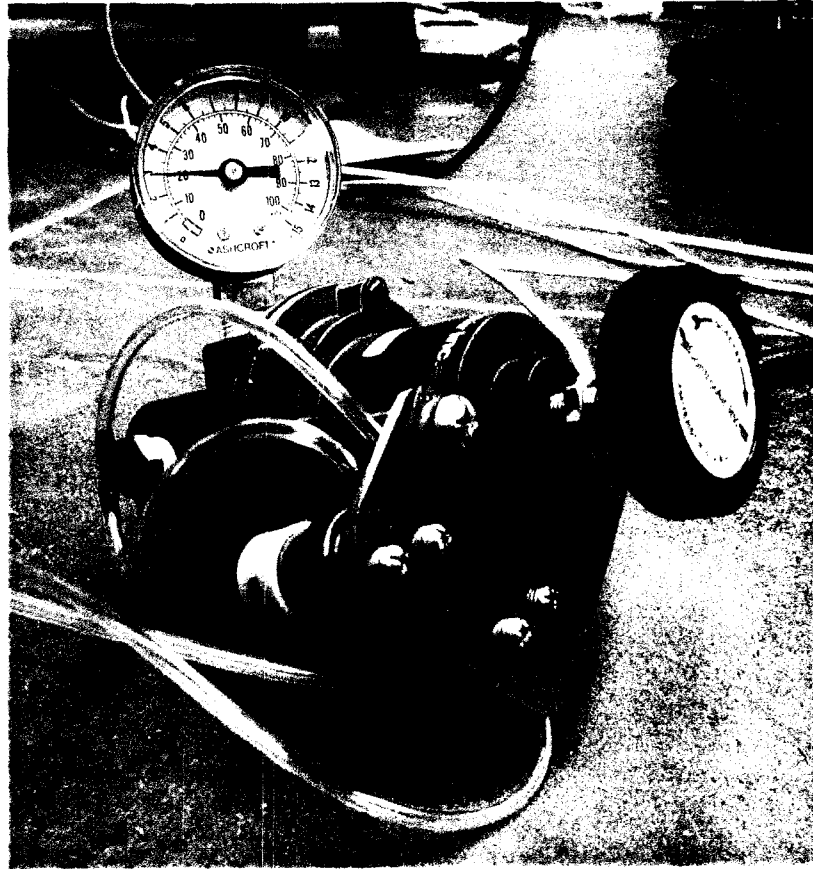


Figure 8.5 — Pneumatic Control Components.

The automation of the measurement collection process was accomplished using a LabVIEW VI. This VI was responsible for controlling the hardware for locating the measurement probe, for controlling the extension and retraction of the measurement probe, and for collection of the measurement data. The front panel of the tactile experiment control VI is shown in Figure 8.6.

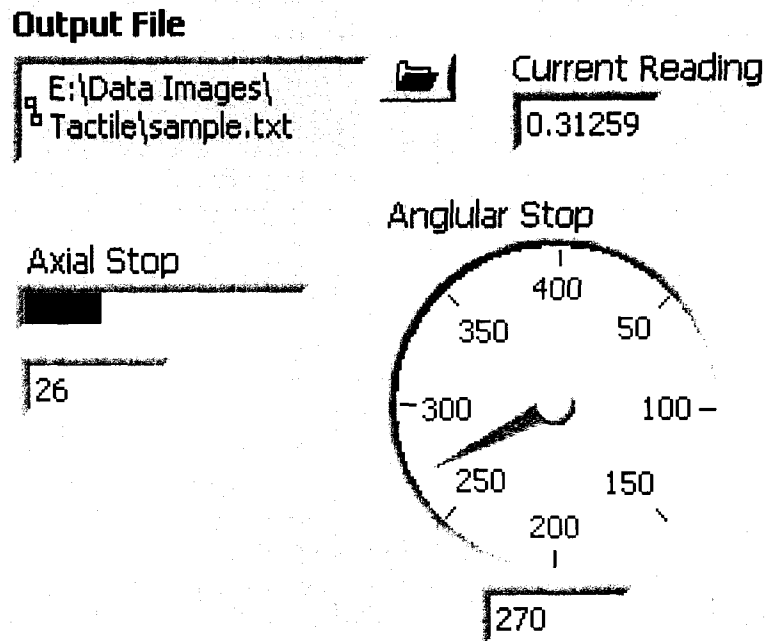
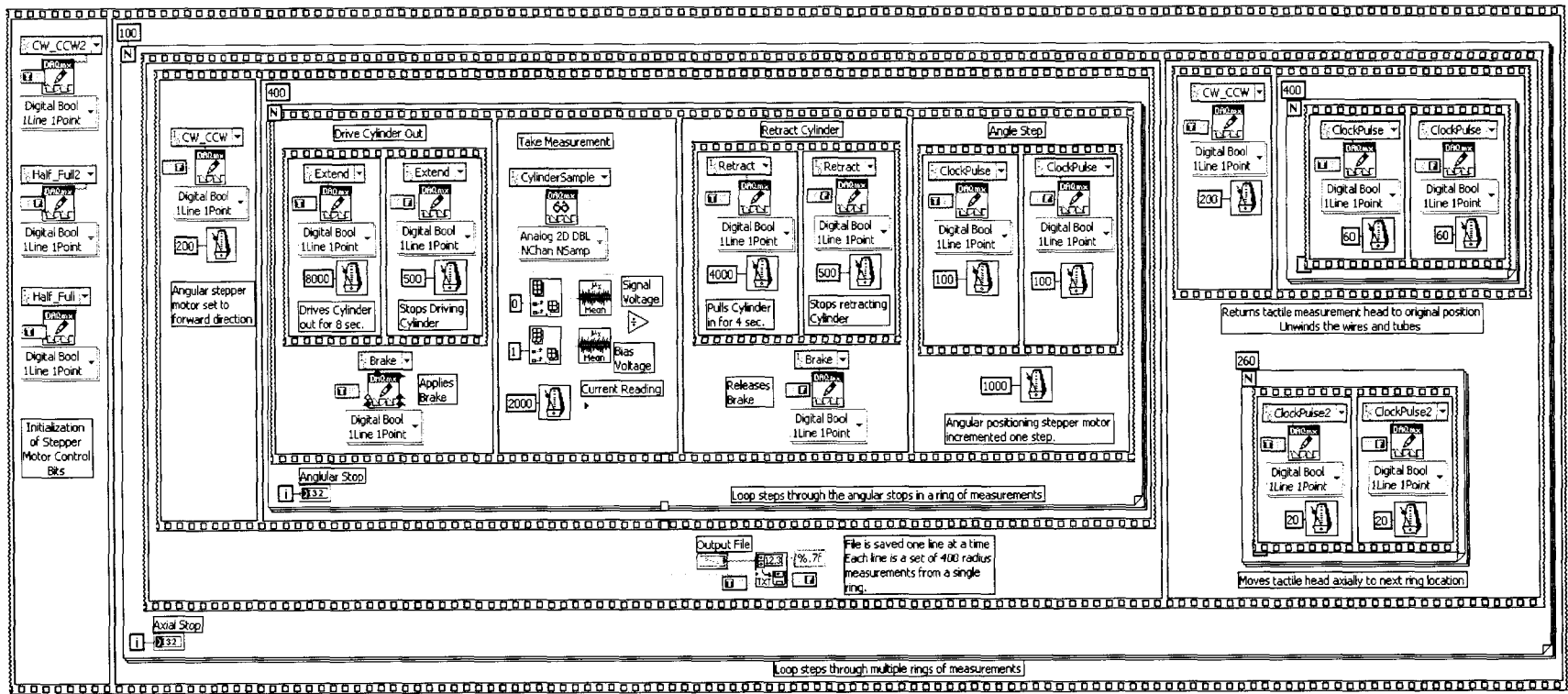


Figure 8.6 — Tactile Experiment VI Front Panel.

On the front panel the user may specify the path and filename of the data file to be written using the tactile measurements. As the tactile experiment progresses, the user may monitor its progress using indicators on the front panel. There is a bar indicator which represents the axial location index, a dial indicator which represents the angular index, and a number readout representing the raw data coming from the measurement probe. The details of the programming process is shown in the block diagram in Figure 8.7.



The first step performed by the VI is the initialization of the stepper motor control bits. Next, a loop which controls the number of rings of measurements is entered. At each ring, a number of steps are performed. First, the direction of the angular indexing stepper motor is set to forward. Next, the valve which applies pressure to the back of the cylinder is opened, the electromagnetic brake is applied, and the cylinder drives outward. Eight seconds are allowed for the probe to contact the pipe wall. When the probe contacts the pipe wall it stops. After eight seconds, the pressure is allowed two seconds to be released to prepare for taking the measurement. Next, the measurement is taken. Voltages at two analog inputs are recorded at a rate of 1000 samples per second for one second. One of the voltages represents the bias voltage across the entire cylinder potentiometer, and the other voltage is the signal voltage from the wiper of the potentiometer. The average of the 1000 signal voltages measured is divided by the average of the 1000 bias voltages measured to obtain a raw number proportional to probe extension. The conversion of this raw number to actual length measurements will be accomplished using data from a calibration which is described in Section 8.2.3. When the measurement has been taken, the raw number is displayed on the front panel and appended to a one dimensional array of measurements from that ring. The cylinder is then retracted for four seconds, the electromagnetic brake is released, and the angular positioning stepper motor increments one step. This process is performed at 400 angular stops per axial stop. When all 400 measurements are taken, the one-dimensional array of measurements is appended as a new line in a two-dimensional data file. The angular positioning stepper motor then returns the probe to its starting position, and the axial positioning stepper motor advances the measurement system to its next axial stop. These

stops are placed every 0.1 inch. The VI is made to collect 100 axial stops (rings) but can be aborted by the user while still retaining up to the most recent ring of measurements in the data file.

### 8.2.3 Calibration of Tactile System

The raw data collected by the tactile experiment VI are numbers proportional to the extension of the probe at each stop. To turn this raw data into meaningful values, a calibration procedure was performed on the positional feedback cylinder. The cylinder was set up to be measured using a digital caliper with an accuracy of 0.0005 inches. The measured probe extension would then be compared with the signal sent from the cylinder, and a relationship would be defined. Figure 8.8 shows the cylinder set up to be measured by the digital caliper.

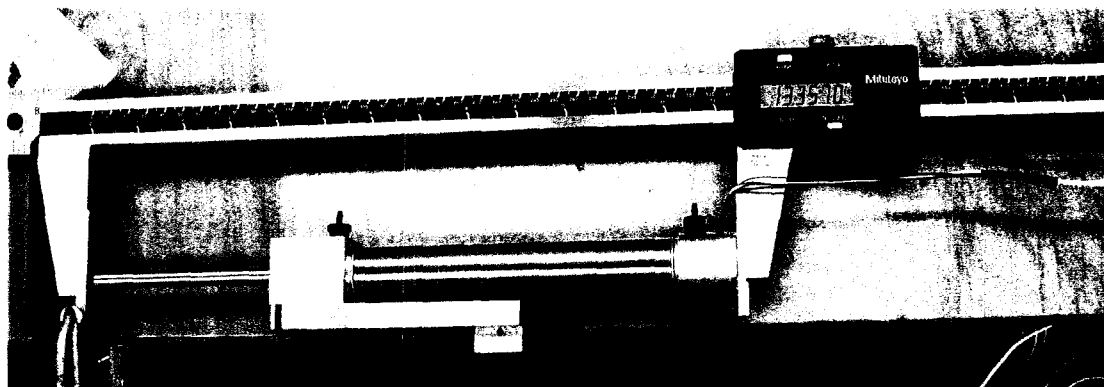


Figure 8.8 — Tactile Calibration Measurements.

The signal voltage output was divided by the bias voltage, just as in the case of the tactile experiment. The overall length measurements from the caliper were plotted against this raw unitless output from the cylinder, and a least squares line was fit to the data. The plot and fitted line are shown in Figure 8.9.

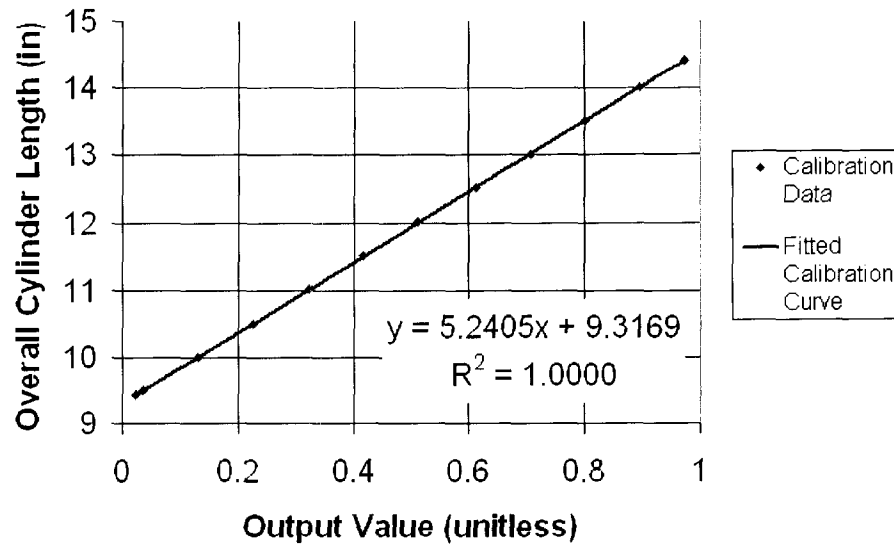


Figure 8.9 — Tactile Probe Calibration.

The measurements that are desired from the tactile system are radii from its axis of rotation. Thus, the main value of interest from the calibration curve is the slope which represents the number of inches implied by a change of one unit of raw output. The y-intercept value of the curve is a function of the chosen origin of the cylinder, which for the calibration was chosen at the very rear. To find the correct y-intercept value for the pipe measurements, the system was set up in the pipe, and radii were measured to points on the pipe wall which were diametrically opposed. This diameter was then measured with the same calipers used for the calibration procedure. To find the correct intercept value  $b$ , Equation (8-1) is employed.

$$b = \frac{\text{Diameter Measured with Caliper}}{2 \cdot \text{Slope from Calibration} \cdot (\text{Raw Measurement 1} + \text{Raw Measurement 2})} \quad (8-1)$$

It was found that the correct y-intercept value for the probe measuring radii from the axis of rotation of the angular stepper motor was 4.5706 inches. Therefore, the relationship

used to convert the raw measurements to actual radius measurements is given by equation (8-2).

$$Radius = (5.2405 \cdot Raw + 4.5706)(inches) \quad (8-2)$$

This relationship was applied to all of the raw data collected to convert it to real radius measurements. The real radius measurements were stored in a spreadsheet file with the same two dimensional formatting as was used for the raw data.

#### **8.2.4 Visualization**

To check the validity of the profiles obtained, a VI which plots radii versus axial position and angular position was prepared. Similar commands were used for this VI as for the visualization VIs in Chapters six and seven. Since a two dimensional data file was the source of the profile rather than a list of ordered triples, a slightly different form of the command was used. This alternate form accepts two one-dimensional arrays as the independent coordinates, and a two-dimensional array as the dependant coordinates. The front panel and block diagram of the profile visualization VI is shown in Figure 8.10.

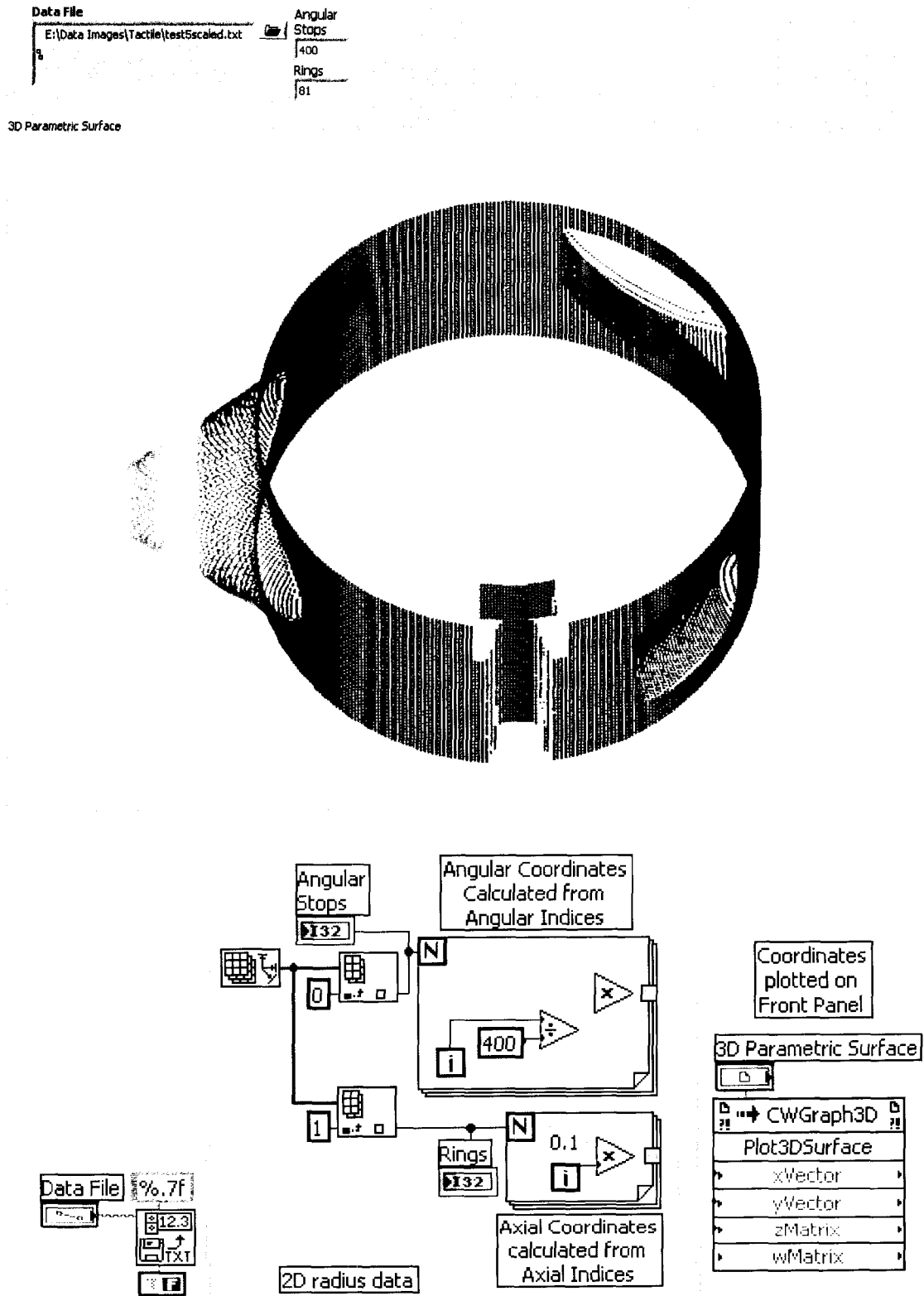


Figure 8.10 — Visualization Front Panel and Block Diagram.

There are some items in this profile that are worthy of note. Near the back end of the profile at the bottom, the profile of the rail looks different than the rest of the rail. This is due to a problem that occurred during the profiling process. The probe tended to get stuck in the extended position at the edges of the rail. The automated data collection VI was modified slightly to exclude these areas from measurement; therefore, this data is not valid. Other areas that are not valid include regions where there are sharp changes in radius. Since the tip of the probe had a distinct size, there were times when other parts of the probe would contact the pipe wall instead of the tip. When this occurs, the measurements obtained are invalid. When the tactile measurements are compared with other measurements, these points have to be removed from consideration.

### **8.3 Conditioning of Profiles**

It cannot be assumed that the points on the pipe wall which were measured using the laser based methods exactly correspond to the points measured with the tactile system. Pieces of hardware may have been shifted slightly when re-assembled for the tactile measurements after the laser measurements were completed. Comparing multiple profiles from multiple scans of the same pipe in practical profiling situations requires a degree of conditioning of the profiles to be able to compare them. Some ways that the profiles might need to be conditioned are by translating and rotating individual rings to find where they best align. Scaling of the data might also be employed to reduce systematic error due to errors in calibration. LabVIEW was used to prepare a utility by which conditioning of the profiles could be performed manually by a user. Ultimately, some of the methods used to manually condition the profiles for comparison may have

application for automated conditioning algorithms. The conditioning VI front panel and block diagram are shown in Figure 8.11.

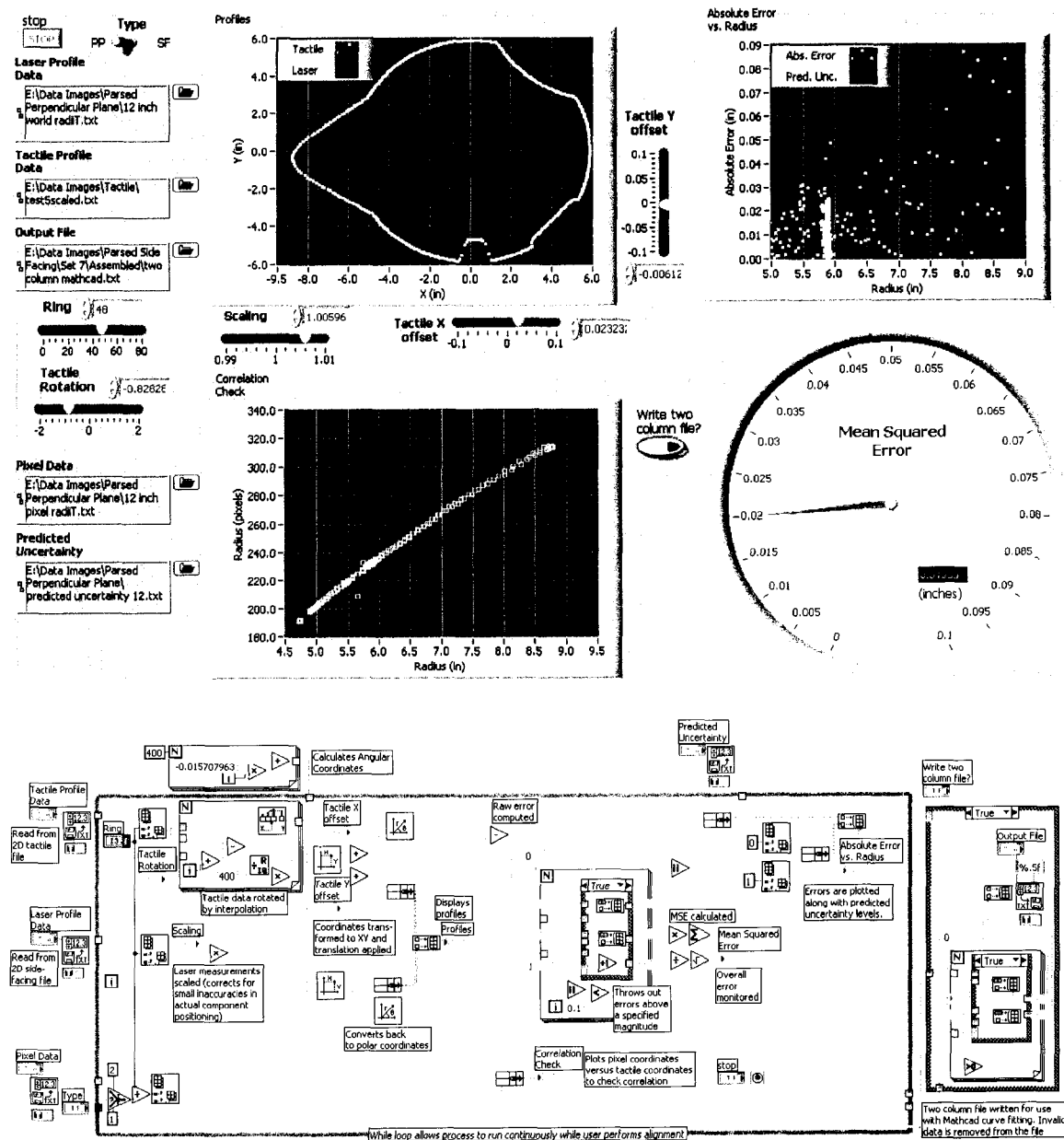


Figure 8.11 — Data Conditioning VI.

The data conditioning VI performed several transformations of the data which will be described in Sections 8.3.1 through 8.3.3.2. The VI simultaneously computed

errors which could be used to guide the user to the most appropriate alignment of the data.

### 8.3.1 Rotation by Interpolation

It could not be guaranteed that the profiles from two sources would align rotationally about the axis of the pipe. The data from one source had to be rotated to match the other. In the case of the profiles obtained using the tactile device and the laser scanning devices described in Chapters six and seven and Section 8.2, there were 400 measurements taken about the circumference of the pipe wall. To make a point to point comparison between the 400 radius measurements, the tactile data was rotated using interpolation between adjacent radius values. A fractional angular index offset was defined and added to each angular index. The interpolation rotation was performed according to equation (8-3).

$$R_i^{new} = R_{i+a} = (1-a) \cdot R_i + a \cdot R_{i+1} \quad (8-3)$$

The  $R$  values refer to radius values at their respective indices, and the  $a$  value refers to the fraction of an index between two radius measurements. The rotation actually occurs when the interpolated value is assigned to the location in the array formerly occupied by the non-interpolated value. A built-in LabVIEW interpolation function was used to interpolate between radius values at successive angular indices. A special quotient function was used to circulate the value at the end of the input array back to the beginning, or vice-versa. The interpolated values then formed a new array of radius measurements which were rotated about the central axis.

### **8.3.2 Translation Using Coordinate Transformations**

After the tactile data was rotated to best match the laser profiling data, a set of translations were applied to the tactile data. The data was originally in the form of cylindrical coordinates, with each ring representing a set of polar coordinates. The polar coordinates were transformed to Cartesian coordinates using a built-in LabVIEW function. Once the coordinates were defined as two arrays of Cartesian coordinates (horizontal and vertical), translating the coordinates in either direction was simply a matter of adding a constant value to all the elements in the appropriate array. These constant values are adjusted by the user of the VI to best match the laser profiling data, again using the mean-squared error value as a guide. The user adjusts the translational offsets by sliding the appropriate bars on the screen until the error between the two profiles is minimized. Both profiles are seen on the display, and the translation is shown in real time as the user slides the sliders.

### **8.3.3 Intrinsic Calibration Corrections**

The rotation and translation of the tactile coordinates do not change the magnitude of the measurements, but simply move it around to better match the set of laser based measurements. It was noticed, however, that there were issues in the matter of the scaling of one profile relative to the other. Since the tactile measurements are the more reliable values, these should not be scaled to match the laser based measurements, rather, the laser based measurements should be scaled to reflect the tactile measurements. Ideally, no scaling should be necessary to match up the two profiles, since a calibration was already performed on each laser profiling system. However, in practice, small errors occurred in each case that should be corrected to make valid conclusions about the

accuracies of each system. The adjustments to the scaling of the measurements based on a comparison with the tactile measurements may be thought of as an intrinsic calibration procedure.

### **8.3.3.1 Perpendicular Plane Method**

In the case of the perpendicular plane method, the source of the scaling error is entirely due to the difficulty in precisely positioning the camera and the laser plane projector at the correct baseline distance from each other. The focus and zoom adjustments on the lens used had set screws to lock them in position; therefore, no appreciable scaling error would have occurred from a change in adjustment to one of the lens parameters. Recalling the expressions obtained for the radius measurements, the baseline distance  $\bar{D}$  only appeared as a coefficient multiplying the remaining terms in the expression. The consequence of this arrangement is that adjustments may be made to the baseline distance simply by applying a linear scaling factor to the final calibrated radius measurements. This factor is applied to the laser based measurements in the conditioning VI via the slider on the front panel called “Scaling.” As with the rotation and translation transformations, the user may adjust the scaling while monitoring the resulting profiles and the mean-squared error between the profiles. For the perpendicular plane method, these transformations yield profiles that are worthy of comparison for the purpose of verification of the validity of the uncertainty assessments prepared in Chapter four.

### **8.3.3.2 Side-Facing Method**

The side-facing method posed a larger problem in the area of scaling. The first attempts at using a linear factor for scaling as with the perpendicular plane method yielded results that could be corrected for certain radius measurements but not others. It

was concluded that the zoom of the lens, the aim angle of the camera, the baseline distance of the camera, or any combination of the three, had been inadvertently changed slightly between the calibration process and the profiling. In practice, these are issues that would not be likely to emerge for a commercialized profiler and thus should not be considered as factors for the uncertainty of the method itself. Therefore, to make an error analysis possible, an intrinsic calibration was performed in which the raw pixel data was compared with the tactile measurements, and a new calibration curve was fit. The conditioning VI was modified to include the capability of exporting a list of ordered pairs of coordinates, with invalid data removed. Each pair included a pixel location from the original image processing, and the corresponding tactile measurement for that pixel location. The list was written to a file which was accessible using Mathcad. The same general curve fitting procedure described in Chapter five was applied to the data, and another curve was fit. The data and the fitted curve are shown along with the original extrinsic calibration curve in Figure 8.12.

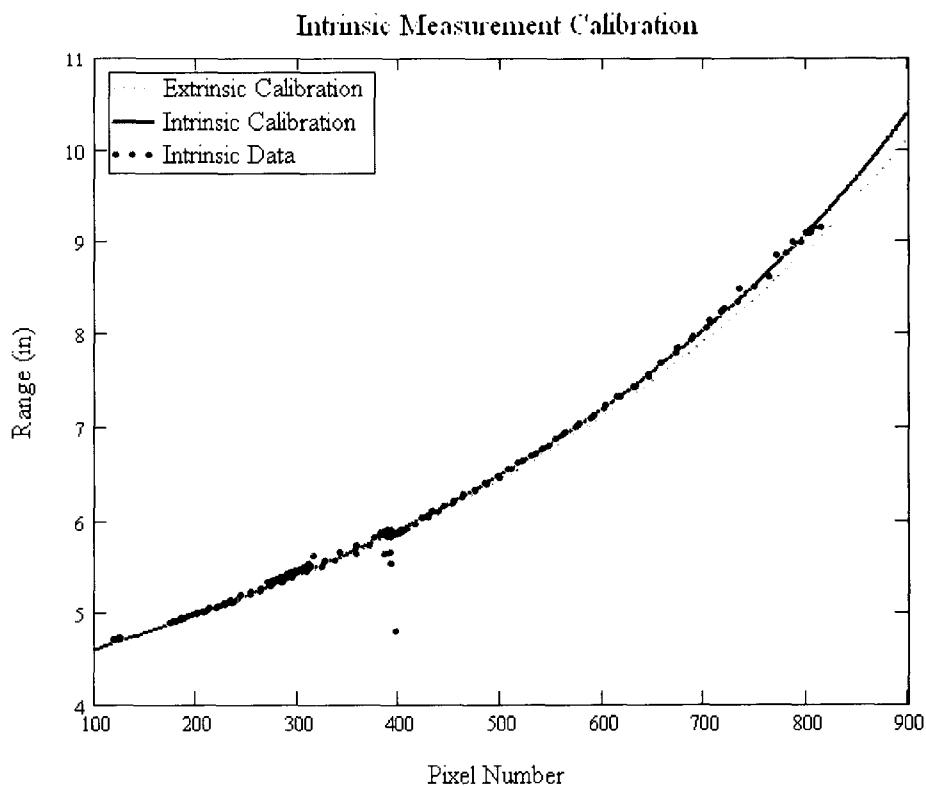


Figure 8.12 — Intrinsic Calibration Curve Fit.

The parameters obtained from the curve fit in the extrinsic calibration are compared with those obtained using the intrinsic calibration in Table 8.1.

Table 8.1 — Extrinsic Versus Intrinsic Calibration.

<b>Calibration Parameter</b>	<b>Extrinsic</b>	<b>Intrinsic</b>	<b>Percent Change</b>
Baseline Distance, $D$	2.355 in	2.359 in	0.15%
Aim Angle, $\alpha$	19.9°	19.8°	-0.68%
Zoom Factor, $f$	0.0175°/pixel	0.0180°/pixel	2.58%

It is apparent from the results of the regression on the intrinsic data that the primary parameter that changed between the calibration and the profiling was the zoom factor. The lens which was used for this profiling did not have set screws to lock its adjustments; therefore, it is quite possible that the zoom adjustment was altered. Once

the corrected calibration parameters were found, the World Coordinate Calculation VI described in Chapter seven was used to create a new two dimensional file with calculated radius coordinates as its entries.

### 8.3.4 Summary of Necessary Conditioning

To line up two profiles with each other for the sake of comparison with one another, several steps had to be performed. The tactile based profiles had to be rotated and translated to best fit the laser based profiles. Scaling operations also had to be performed on the laser based measurements to correct for small errors resulting from problems in the execution of the experimentation. A summary of the conditioning performed on each profile is provided in Table 8.2.

Table 8.2 — Conditioning Performed by Profile.

Triangulation Scheme	$\bar{D}$	$D$ (in)	Rotation (°)	Horizontal Translation (in)	Vertical Translation (in)	Scaling Multiplier
Perpendicular Plane	0.5	3	0.964	0.0374	0.0061	0.997
	1.0	6	0.818	0.0232	-0.0102	1.005
	2.0	12	0.563	0.0111	-0.0102	1.006
	5.0	30	1.036	0.0131	0.0163	0.997
Side-Facing	0.4	2.4	0.964	-0.0192	0.0306	Curve Fit

## 8.4 Error Analysis

The purpose of the error analysis in this section is to provide a general indication as to whether or not the analytical predictions of uncertainty provided in Chapters four and five could be confirmed experimentally. Much more rigorous statistical analysis of the data could be performed, but is not the key focus of this analysis. An analysis scheme by which individual rings were isolated and analyzed was followed. By performing the analysis in such a way, the same VI as was used to condition the profiles could be used to

provide enough information to compare the behavior of the real systems with the predicted uncertainties.

#### **8.4.1 Quantification of Measurement Error**

The Data Conditioning VI shown in Figure 8.11 was designed to evaluate and display measurement errors in a descriptive way. Several steps were performed to most appropriately display error. The first step to be performed was the calculation of the error itself. To perform this calculation, the Cartesian coordinates used for the transformations described in Section 8.3 are first converted back to polar coordinates. The resulting data consists of arrays of 400 radius measurements each, one array coming from the laser based measurements, and the other array coming from the tactile measurements. The physical source of corresponding elements of these arrays each has a common physical origin; thus, the difference between corresponding elements represents the error in the measurements. The measurements taken by the tactile device are assumed to be totally reliable, and the laser based measurements are compared to the tactile measurements. An array of raw error is produced by taking the difference in the arrays. This raw error includes all of the elements in both arrays, including the measurements flagged as invalid. To exclude the invalid measurements, as well as the measurements probably taken by a part of the tactile probe other than the tip, all quantities of error greater than 0.15 inches were excluded. This value was chosen because it was sufficiently greater than any of the predicted uncertainties, and seemed to exclude most of the points which would obviously qualify as outliers. This yielded a set of error values which would be used for analysis.

The first type of analysis performed on the data was a calculation of the mean squared error. The mean squared error (MSE) is calculated using equation (8-4).

$$MSE = \sqrt{\frac{1}{n} \sum_{i=1}^n (R_i^{laser} - R_i^{tactile})^2} \quad (8-4)$$

The mean squared error provides an estimation of the overall error of the method and conditions under investigation. It is closely related to standard deviation which is one of the typical methods of quantifying uncertainty of a set of data. The values obtained from the MSE may be compared with the predicted values of uncertainty to make conclusions about the validity of the analytical uncertainty evaluation.

Another type of analysis which will be performed is a direct comparison of the error data with the predicted uncertainty versus the radii being measured. Recall from Chapters four and five that the uncertainties predicted were functions of the magnitude of the measurements themselves. These predicted uncertainty profiles were plotted as lines on error versus radius measurement plots for comparison with the error data. This visualization will allow for conclusions to be drawn about the similarity of the nature of the experimental error to the predicted behavior as the radius measurements change.

#### **8.4.2 Perpendicular Plane Error**

It was found that the behavior of the perpendicular plane profiling systems closely followed the predicted behavior. As longer baseline lengths were used, the overall error of the system was reduced, although occlusion effects were increased. It was also observed that the error of the measurement system increased for larger radial measurements, with a generally acceptable correlation with the predicted behavior.

### 8.4.2.1 Error Versus Baseline Distance

As the laser and tactile profiles were conditioned to best match each other, the MSE was monitored as well as the error versus radius. The user would adjust the various parameters until the MSE was the lowest value for which the error versus radius looked most suitably distributed. The MSE at this point was then recorded. The MSE values obtained experimentally were then plotted along with the predicted uncertainty for each baseline length. This plot is shown in Figure 8.13, with both the absolute and parametric forms of the axes displayed.

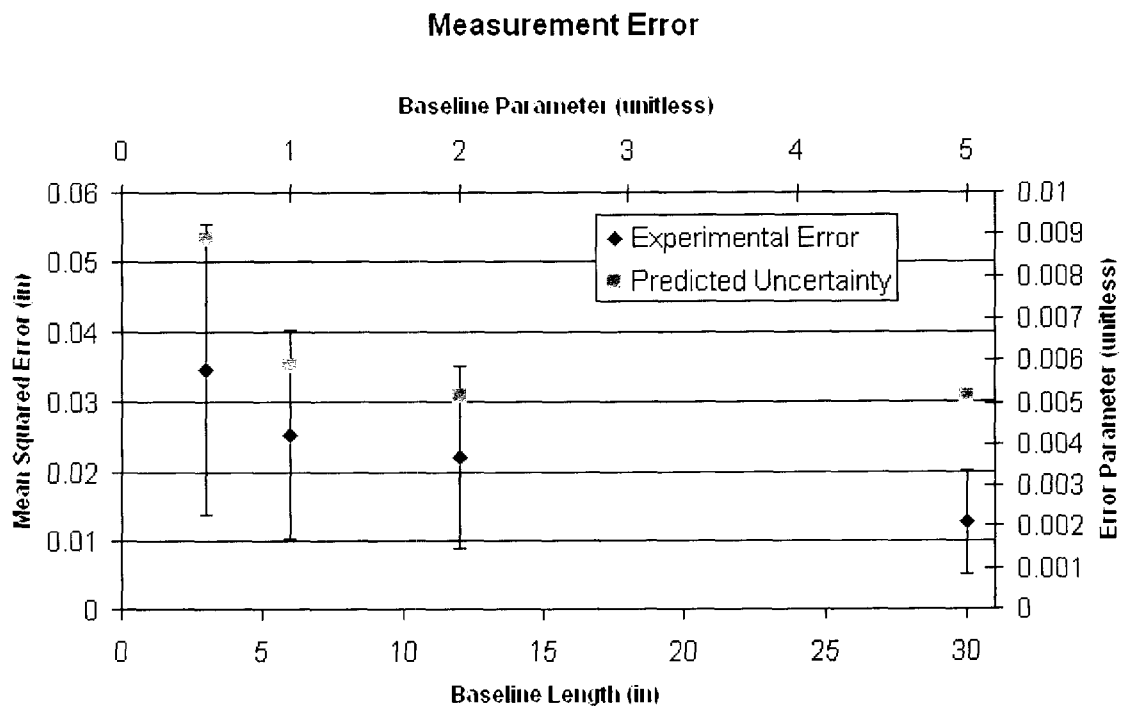


Figure 8.13 — Experimental Error Comparison.

Overall the shapes of the two curves coincide very well, although the magnitude of the predicted uncertainties are about one and a half times the actual observed MSE. It would be expected for the observed MSE to be smaller than the predicted uncertainty

because the predicted uncertainty is designed to better approximate the worst-case errors than the average error. The standard deviation of the absolute errors for each baseline length was about 60% of each MSE. If the worst case error is approximated as being one standard deviation greater than the MSE (see the bars on Figure 8.13 for one standard deviation above and below the MSE), this means that the predicted uncertainty is very close to the worst case error. Table 8.3 summarizes the comparison between the approximate worst-case error, and the predicted uncertainty for each tested baseline length.

Table 8.3 - Predicted Uncertainty and Worst-Case Error for Perpendicular Plane Method.

<b>Baseline Parameter</b>	<b>Baseline Length (in)</b>	<b>Predicted Uncertainty (in)</b>	<b>Approximate Worst-Case Error (in)</b>	<b>Percent Difference (% of error)</b>	<b>Percent Difference (% of <math>R_0</math>)</b>
0.5	3	0.0532	0.0554	4%	0.04%
1.0	6	0.0351	0.0404	14%	0.09%
2.0	12	0.0308	0.0352	13%	0.07%
5.0	30	0.0309	0.0203	-42%	-0.18%

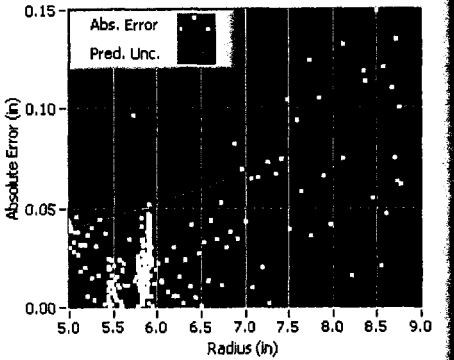
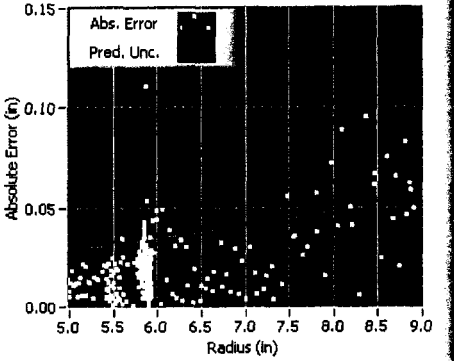
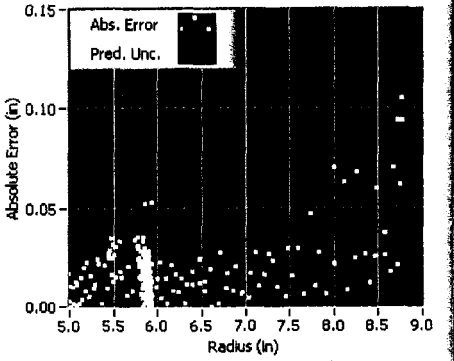
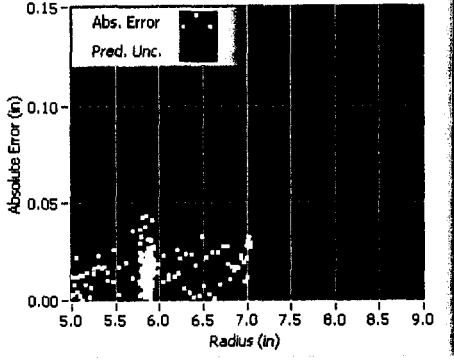
The baseline length for which the analytical method provided the worst prediction was for the longest baseline length. It appears that the predicted limit to accuracy as baseline length increases cannot be confirmed with this experiment. There are some issues, however, that may be at work that would argue that the predicted limiting effect may not be invalid. More error is observed in all cases when the radius measurements increase. The particular section of pipe which was scanned had fairly abrupt changes in cross-section; thus, occlusion was a large factor for the long baseline length. The occlusion kept large radius values from being measured, thereby reducing the average amount of error observed. If the same radial magnitudes could have been measured, the errors observed would very likely have been larger, and it may have been possible to

observe the predicted effect of the limit on accuracy. In any case, the remaining values predicted for uncertainty are very close to the actual observed values of approximate worst-case error. This generates confidence that the analytical method and the assumptions used in Chapter four are useful.

#### **8.4.2.2 Error Versus Radius**

It is slightly more difficult to break out the effect that the magnitude of the measurements has on the error of the measurements. To demonstrate the effect, a chart was provided on the front panel of the same VI that allows the user to see the errors of the measurements versus the radii themselves. In Figure 8.11, this chart can be seen at the upper right. The red line in the figure represents the uncertainty predicted in the analytical treatment of uncertainty from Chapter four. Each plotted point on the chart represents one point on the pipe wall. The vertical axis gives the error of the laser based measurement, and these values are plotted against the radial measurements themselves. By displaying this information in this way, the user can visually compare the error with the predicted uncertainty. One would expect most of the points to fall somewhere between an error of zero and the analytical uncertainty curve. In general, this is how the data behave. Table 8.4 shows a sample output of this chart for each baseline length.

Table 8.4 — Errors Versus Radii.

Baseline Parameter	Baseline Length (in)	Errors and Predicted Uncertainty
0.5	3	
1.0	6	
2.0	12	
5.0	30	

In all the charts shown, there is a cluster of points just to the left of a radius value of 6.0. This cluster represents where the radius value for a majority of the measurements taken, or the radius of the pipe excluding features. For every chart, this cluster sits fairly centered between an error value of zero and the predicted uncertainty. This means that the uncertainty predictions for the expected measurement values provide a good estimation of the uncertainty at those measurement values. It can also be seen for the first three charts shown that the errors tend to increase as radius increases. This occurs in a fashion approximately as predicted. The one deviation that seems to appear in the data is the larger scale increase in error toward the higher measured radius values. This increase in error is suspected to be due to the errors induced by the change in the orientation of the measured surface relative to the camera (i.e. not perpendicular). For the last baseline length, occlusion effects exclude the collection of larger radius measurements; thus, the increase in error due to increased radius cannot be observed. Overall, the observed errors very closely resemble the predicted uncertainty for each baseline length.

#### **8.4.3 Side-Facing Error**

The size of hardware used for the side-facing method dictated that only one baseline length could be tested. The errors of the side-facing method were evaluated using the same VI as for the perpendicular plane method. Using the conditioning discussed in Section 8.3.4, the error of the side-facing method was evaluated for a baseline parameter of 0.4 (2.4 inches). The MSE was calculated to be approximately 0.0185 inches, with a standard deviation of about 0.0142 inches. Again, if the worst-case error is approximated as one standard deviation greater than the mean, this gives a worst-

case error of about 0.0327 inches. This is about 70% higher than the predicted value of 0.019 inches for this method. This could be due to the change in the zoom parameter in the camera from the designed specifications discussed in Section 8.3.3.2. Also, when the errors are plotted versus radius, it can be seen that one standard deviation greater than the mean may not be a good estimator of the worst-case error. Figure 8.14 shows the errors plotted versus radii, with the predicted uncertainty plotted as a reference.

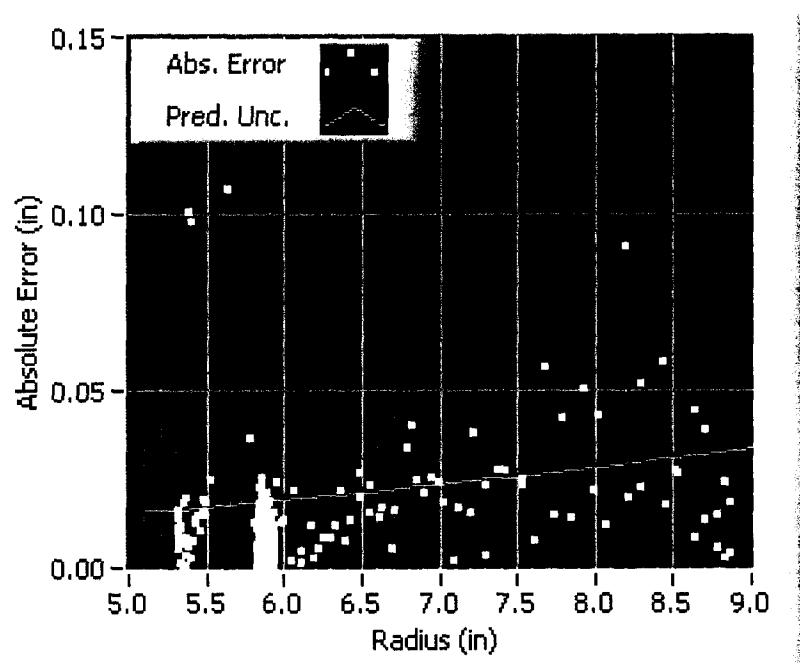


Figure 8.14 — Error Versus Radius.

Looking at the error distribution, it can be seen that most points fall within the bounds of the predicted uncertainty. The cluster of points representing the featureless radius of the pipe lies almost entirely within the bounds of the predicted uncertainty, and the uncertainty increases with radius as predicted. The error seems to increase more than predicted for larger measured radii, just as with the perpendicular plane data. Once again, it is suspected that the sloping sides of the features in the pipe induced some error

that caused this effect. Overall, however, the uncertainty prediction provides a fairly good estimator of the uncertainty in the side-facing system.

### 8.5 Conclusions

To experimentally verify the validity of the analytical estimations of laser triangulation uncertainty provided in Chapters six and seven, an accurate tactile measurement system was constructed to measure the same section of pipe as was measured by the laser profiling systems. The measurements obtained by the tactile system were taken to be completely reliable measurements, with the difference between the tactile measurements and the laser measurements taken as error on the part of the laser measurements. A special data conditioning application was created to align the data from the tactile and laser based measurements for valid comparison. Once the data was aligned for a particular ring, the error between the tactile measurements and the laser measurements was analyzed and found to generally match the predictions well. The difference between the predicted uncertainty and the first standard deviation above observed mean errors tended to be within about 14% of each other. This value is 14% of the magnitudes of the errors and uncertainties themselves. Expressed as a percentage of nominal pipe radius, the difference between error and predicted uncertainty is on the order of 0.1% of  $R_0$ . The perpendicular plane and the side-facing analytical uncertainty evaluations seem to accurately represent the nature of the uncertainty observed in the corresponding physically constructed models tested in this work.

## CHAPTER 9

### CONCLUSIONS, BROADER IMPACT AND FUTURE DIRECTIONS

#### 9.1 Research Conclusions

Buried infrastructure represents one of the public's biggest investments, yet quite frequently it receives insufficient attention. To make decisions on how to best spend limited resources, information regarding the current state of the infrastructure must be gathered. The tools available to gather helpful information have been growing in sophistication in recent years, and a technique that shows promise for widespread acceptance is laser profiling. Laser profiling most commonly uses a principle called structured light triangulation to achieve radius measurements of pipes. The measurements may then be assembled into wireframe models or point clouds in three dimensions to visualize defects and deformation. The question of the quality of the measurements obtained is of critical importance to those considering the adoption of laser profiling techniques.

The objective of this research was to develop and test an analytical method for quantifying the uncertainty inherent in laser triangulation systems for pipe profiling. Three triangulation schemes were analyzed, one utilizing a conically shaped laser mounted beside a camera, one utilizing a planar laser mounted in front of a camera and

perpendicular to the pipe axis, and one utilizing a planar laser mounted beside a side-facing camera and projected parallel to the pipe axis, as depicted in Figure 9.1.

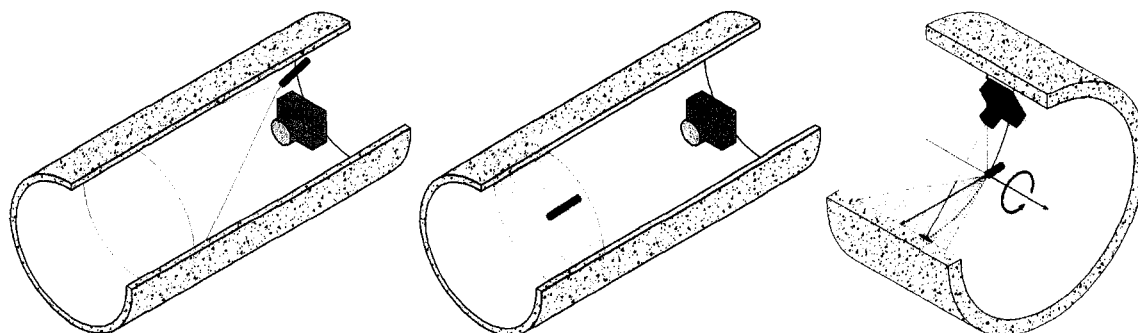


Figure 9.1 — Triangulation Schemes Studied.

Analytical models were developed characterizing the behavior of each of these schemes. Values for parameters defining the geometry of the system were left variable so as to allow for a certain degree of optimization of each design. An uncertainty analysis was performed for each scheme, and critical design tradeoffs were identified for each scheme. Physical models were constructed for the perpendicular plane and side facing profiling schemes for the purpose of comparison of the analytical models with real systems. Software was written to control the physical models and to process the data retrieved. The results obtained from the laser profiling systems were compared with measurements taken by a precise tactile measurement device. The difference between the profiling data and the tactile data was computed to quantify the profiling error, and this error was compared to the analytical uncertainty models for the perpendicular plane and side facing profiling methods. Parameters pertaining to the measurement ranges, equipment quality, and image processing were assumed at certain reasonable values.

Specific activities that were performed to achieve these outcomes composed the following research program:

- A literature review was completed that demonstrates the need for objective assessment of pipe condition and details current pipe profiler technology and research.
- Equations were derived describing the nature of the measurements taken by three structured light triangulation schemes. These equations were left independent of particular models used for real cameras so as to provide more universal application to a variety of cameras and lenses.
- Uncertainty in the measurements obtained by each measurement scheme was estimated using uncertainty propagation techniques prescribed by the Kline-McClintock method. This allows the overall uncertainty of the schemes to be estimated by estimating the uncertainty of each of the components of each equation.
- Visualizations of the predicted measurements and the uncertainties in the measurements were provided as color contour plots over the area of an image which may be collected from each measurement scheme.
- Design considerations and tradeoffs for each scheme were identified.
- Physical models of the perpendicular plane and side facing triangulation schemes were constructed and tested.
- Software was written to interface with the profiling hardware and automate the profiling process and data processing.

- A precision tactile measurement profiling tool and the accompanying software was developed to provide a set of high-confidence measurements of a test section of pipe.
- Measurements of the same section of pipe taken with two of the laser profiling schemes were aligned to and compared with the tactile measurements to calculate error.
- The error between the laser and tactile measurements was compared with the analytical uncertainty predictions, and conclusions were drawn as to the suitability of the analytical method.

It was found that the analytical predictions for uncertainty tended to lie within about 14% of the actual worst-case laser measurement error values obtained in the experiments. Expressed as a percentage of nominal pipe radius, the difference between worst-case laser measurement error and predicted uncertainty is on the order of 0.1% of nominal pipe radius.

## 9.2 Broader Impact and Future Directions

This study represents an evaluation of the fundamental minimum uncertainty achievable by laser pipe profilers. Factors such as profiler misalignment [62] or surface irregularities (such as wet pipe walls) can negatively impact the accuracy of laser profilers. Standardized field calibration procedures are also needed to ensure the scaling of the measurements obtained is accurate.

The results of the study may be of interest to the designers of laser profilers, those considering the use of laser profiling for asset management, or those attempting to determine the limitations of laser profiling. Laser profiling is becoming a standard

method of inspecting the quality of newly installed underground infrastructure in some states. Moreover, based on the increasing emphasis on asset management, laser profiling or other methods to accurately determine the geometry of existing assets is sure to become a required component of asset management plans in the future; the managers of buried infrastructure must be able to track geometrical changes of their assets to best allocate resources.

Asset managers need the capability to continuously track the geometry of buried pipes based on the cumulative knowledge obtained from multiple pipe scans. However, as seen in Chapter eight, even when scans are taken of a pipe that has not changed and even when the device taking the measurements rides on a fixed rail in the pipe, significant differences between the scans exist. These differences necessitate that multiple scans be translated, rotated and scaled on a local basis to make sure the wireframe models are appropriately coregistered. Only by properly overlaying properly coregistered models can deterioration rates be computed. The key contribution of this work is the clear development of the analytical models for three triangulation schemes and the minimum uncertainty that can be expected from these schemes based on the parameters defining the profiling systems. Knowledge of the accuracy and uncertainty of the measurement techniques coupled with proper coregistration of overlaid wireframes provides a basis for objective asset management; the development of the algorithms for automatically coregistering multiple wireframe images with known uncertainties is needed to fully integrate laser profiling into asset management.

## REFERENCES

1. Wade, M., *Controlling Inflow and Infiltration In Wastewater Collection Systems*. 2002, Wade and Associates, Inc.: Lawrence, KS.
2. EPA, *Guide For Evaluating Capacity, Management, Operation, And Maintenance (CMOM) Programs At Sanitary Sewer Collection Systems*. Office of Enforcement and Compliance Assurance, 2005, United States Environmental Protection Agency.
3. Ghosh, S., *Sewer Rehab Trends*. Trenchless Technology. May, 2006. p. 38-41.
4. Sinha, S.K. and M.A. Knight, *Intelligent System for Condition Monitoring of Underground Pipelines*. Computer-Aided Civil and Infrastructure Engineering, 2004. **19**(1): p. 42-53.
5. EPA, *Report to Congress on Impacts and Control of Combined Sewer Overflows and Sanitary Sewer Overflows*. 2004, United States Environmental Protection Agency.
6. Chae, M.J. and D.M. Abraham, *Neuro-fuzzy approaches for sanitary sewer pipeline condition assessment*. Journal of Computing in Civil Engineering, 2001. **15**(1): p. 4-14.
7. WEF, *The O & M in CMOM, in Operation & Maintenance*. 2006, Water Environment Federation.
8. Gokhale, S., J.A. Graham, and S. Bowns, *Sanitary Sewer Evaluation Surveys: Why and How (Part 1)*. Trenchless Technology. October, 2005. p. 48-56.
9. Carter&Burgess, *In the Public Interest: GASB 34/35*, in *Carter & Burgess's Quarterly*. 2002.
10. McLendon, R. *Florida Culverts & Pipe Advisory Group*. 2006 [cited 2006 12/19/2006]; Available from: <http://www.dot.state.fl.us/rddesign/dr/Advisory-Groups.htm>.
11. AZDOT, *Corrugated High Density Polyethylene Plastic Pipe General Requirements*, Highways, Roads, and Design, Editors. 2005, AZDOT.
12. Logan, G.I. and P.R. Anderson, *Lasers and machine vision for pipeline precision measurement*. 2003, Albany, Auckland, New Zealand: CleanFlow Systems Limited.
13. WRc, *Cleanflow Systems LTD: WRc Approved*. 2005, WRc: Swindon, UK.

14. Graham, J.A. *Rehabilitation of Large Concrete Sewer Interceptors with the Aid of Laser Profiling and Other Investigative and Analytical Techniques*. in *North American Society for Trenchless Technology (NASTT) NO-DIG 2006*. 2006. Nashville, TN, USA.
15. Ouellet, M. and C. Senecal. *3-D Profiling and Software Modeling for Pipe Qualification*. in *North American Society for Trenchless Technology (NASTT) No-Dig 2004*. 2004. New Orleans, LA, USA.
16. Optical-Metrology-Centre, *OMC Laser Profiler 15/50*. 2002.
17. Optical-Metrology-Centre. *OMC Project Description - Sewer Profiling*. 2006 [cited 2006 12/19/2006]; Available from: [http://www.optical-metrology-centre.com/Downloads/Projects/Project\\_Description-Sewer\\_Profiling.pdf](http://www.optical-metrology-centre.com/Downloads/Projects/Project_Description-Sewer_Profiling.pdf).
18. Clarke, T.A., *The development of an optical triangulation pipe profiling instrument*, in *Optical 3-D Measurement Techniques III*. 1995, Wichmann. p. 331-340.
19. Clarke, T.A., K.T.V. Grattan, and N.E. Lindsey. *Laser-based triangulation techniques in optical inspection of industrial structures*. 1990. San Diego, CA, USA: Published by the International Society for Optical Engineering, Bellingham, WA, USA.
20. Clarke, T.A. and N.E. Lindsey. *Triangulation based profiler*. 1990. Zurich, Switzerland: Published by the International Society for Optical Engineering, Bellingham, WA, USA.
21. RedZone-Robotics., *Responder Robotic Platform Laser Sensor 2006*, RedZone Robotics.
22. M. Buzinski, A. Levine, and W. H. Stevenson. *Performance characteristics of range sensors utilizing optical triangulation*. in *IEEE National Aerospace and Electronics Conference*, Dayton, OH, USA, 1992.
23. Henry, R. and A.R. Luxmoore, *Pipe-profiling adapter for CCTV inspection cameras: development of a pipe-profiling instrument*. *Measurement Science & Technology*, 1996. 7(4): p. 495-504.
24. Gooch, R.M., et al. *Driving a DSP Underground*. in *DSP 96 Scandanavia*. 1996. Copenhagen, Denmark.
25. Mizunuma, M., S. Ogawa, and H. Kuwano. *Deformation detection on the pipe inner wall using a laser-beam scanning displacement sensor*. in *Industrial Optical Sensing and Metrology: Applications and Integration*. 1993. Boston, MA, USA: SPIE.
26. Kirkham, R., et al., *PIRAT--A System for Quantitative Sewer Pipe Assessment*. *The International Journal of Robotics Research*, 2000. 19(11): p. 1033-1053.

27. Hartrumpf, M. and R. Munser, *Optical three-dimensional measurements by radially symmetric structured light projection*. Applied Optics, 1997. **36**(13): p. 2923.
28. Zhuang, B.H. and W.W. Zhang. *Machine vision system for inner wall surface inspection*. 1998. San Jose, CA, United States: The International Society for Optical Engineering.
29. Zhang, W.W. and B.H. Zhuang, *Non-contact laser inspection for the inner wall surface of a pipe*. Measurement Science & Technology, 1998. **9**(9): p. 1380-1387.
30. Zhang, G., J. He, and X. Li, *3D vision inspection for internal surface based on circle structured light*. Sensors and Actuators, A: Physical, 2005. **122**(1 SPEC ISS): p. 68-75.
31. Tsubouchi, T., et al. *A straight pipe observation from the inside by laser spot array and a TV camera*. 2000. Takamatsu: Institute of Electrical and Electronics Engineers Inc.
32. Forsyth, D.A. and J. Ponce, *Computer Vision, A Modern Approach*. 2003, Upper Saddle River, NJ: Prentice Hall.
33. Fleck, M.M., *Perspective Projection: The Wrong Imaging Model*. 1995, University of Iowa, Computer Science.
34. Pantsar, T. and J. Korkealaakso. *Recovery of the 3D Structure of a Sewer Pipeline Using Computer Vision*. in *International No-Dig*. 2002. Copenhagen, Denmark.
35. West, G.A.W. and T.A. Clarke. *Survey and examination of subpixel measurement techniques*. 1990. Zurich, Switzerland: Published by the International Society for Optical Engineering, Bellingham, WA, USA.
36. Mark, R.S., A.C. Timothy, and S. Tim. *Comparison of some techniques for the subpixel location of discrete target images*. 1994: SPIE.
37. Kline, S.J. and F.A. McClintock, *Describing Uncertainties in Single Sample Experiments*. Mechanical Engineering, 1953(January): p. 3-8.
38. Chowdhury, A.R. and R. Chellappa. *Statistical Error Propagation in 3D Modeling From Monocular Video*. in *Conference on Computer Vision and Pattern Recognition Workshop - Volume 8*. 2003.
39. Curless, B. and M. Levoy. *Better optical triangulation through spacetime analysis*. 1995. Cambridge, MA, USA: IEEE, Piscataway, NJ, USA.
40. Hueser, D. and H. Rothe, *Robust averaging of signals for triangulation sensors*. Measurement Science & Technology, 1998. **9**(7): p. 1017-1023.

41. Zeng, L., H. Matsumoto, and K. Kawachi, *Two-directional scanning method for reducing the shadow effects in laser triangulation*. Measurement Science and Technology, 1997. **8**(3): p. 262-266.
42. Baribeau, R. and M. Rioux, *Influence of speckle on laser range finders*. Applied Optics, 1991. **30**(20): p. 2873-2878.
43. Wikipedia. *f-number*. 2007 [cited 2007 3/12/2007]; Available from: <http://en.wikipedia.org/wiki/F-number>.
44. Dorsch, R.G., G. Hausler, and J.M. Herrmann, *Laser triangulation: fundamental uncertainty in distance measurement*. Applied Optics, 1994. **33**(7): p. 1306-1314.
45. Hausler, G., et al. *New Range Sensors at the Physical Limit of Measuring Uncertainty*. in *EOS Topical Meeting on Optoelectronics Distance Measurements and Applications*. 1997. Nantes.
46. CEITEC-CERF, *Evaluation of SSET: The Sewer Scanner and Evaluation Technology*. 2001, Civil Engineering Research Foundation.
47. Hunger, W. *PANORAMO A New Step Forward in Optical Sewer Inspection*. in *International Society of Trenchless Technology (ISTT) NO-DIG 2002*. 2002. Montreal, Canada.
48. Sinha, S.K. and F. Karray, *Classification of underground pipe scanned images using feature extraction and neuro-fuzzy algorithm*. IEEE Transactions on Neural Networks, 2002. **13**(2): p. 393-401.
49. Sinha, S.K., F. Karray, and P.W. Fieguth, *Underground pipe cracks classification using image analysis and neuro-fuzzy algorithm*. IEEE International Symposium on Intelligent Control - Proceedings, 1999: p. 399-404.
50. Sinha, S.K. and P.W. Fieguth, *Automated detection of cracks in buried concrete pipe images*. Automation in Construction, 2006. **15**(1): p. 58-72.
51. Duran, O., K. Althoefer, and L.D. Seneviratne, *Pipe inspection using a laser-based transducer and automated analysis techniques*. IEEE/ASME Transactions on Mechatronics, 2003. **8**(3): p. 401-409.
52. Duran, O., K. Althoefer, and L.D. Seneviratne. *Automated sewer pipe inspection through image processing*. 2002. Washington, DC, United States: Institute of Electrical and Electronics Engineers Inc.
53. Duran, O., K. Althoefer, and L.D. Seneviratne. *Experiments using a laser-based transducer and automated analysis techniques for pipe inspection*. 2003. Taipei, Taiwan: Institute of Electrical and Electronics Engineers Inc.

54. Duran, O., K. Althoefer, and L.D. Seneviratne. *Pipe inspection using intelligent analysis techniques with high noise-tolerance*. 2002. Lausanne, Switzerland: Institute of Electrical and Electronics Engineers Inc.
55. Duran, O., K. Althoefer, and L.D. Seneviratna. *Laser profiler model for robot-based pipe inspection*. 2004. Seville, Spain: TSI Press, Albuquerque, NM 87191, United States.
56. Duran, O., K. Althoefer, and L.D. Seneviratne. *Automated sewer inspection using image processing and a neural classifier*. 2002. Honolulu, HI: Institute of Electrical and Electronics Engineers Inc.
57. Duran, O., K. Althoefer, and L.D. Seneviratne. *A sensor for pipe inspection: Model, analysis and image extraction*. 2003. Barcelona, Spain: Institute of Electrical and Electronics Engineers Computer Society.
58. Xu, K., A.R. Luxmoore, and T. Davies, *Sewer pipe deformation assessment by image analysis of video surveys*. *Pattern Recognition*, 1998. **31**(2): p. 169-180.
59. Pan, X., T.J. Ellis, and T.A. Clarke. *Robust Tracking of Circular Features*. in *6th British conference on Machine vision*. 1995. Birmingham, United Kingdom.
60. Kolesnik, M. and G. Baratoff. *3-D interpretation of sewer circular structures*. 2000. San Francisco, CA, USA: Institute of Electrical and Electronics Engineers Inc., Piscataway, NJ, USA.
61. BIMBA. *Bimba Position Feedback Cylinders*. 2006 [cited 2006 11/09/2006].
62. Dettmer, A.J., *Position and Orientation Correction for Pipe Profiling Robots*, 2007, Ph.D. Dissertation, Louisiana Tech University.